Characterisation and Analysis of Catastrophic Landslides and Related Processes using Digital Cartographic Techniques

by

Keith Brian Delaney

A thesis
presented to the University of Waterloo
in fulfillment of the
thesis requirement for the degree of
Doctor of Philosophy
in
Earth Sciences

Waterloo, Ontario, Canada, 2014

Author's Declaration

This thesis consists of material all of which I authored or co-authored: see Statement of Contributions included in the thesis. This is a true copy of the thesis, including any required final revisions, as accepted by my examiners.

I understand that my thesis may be made electronically available to the public.

Statement Of Contributions

This thesis consists of material all of which I authored or co-authored, and will be defined here. I am the main author and contributer of all of the following thesis chapters, excluding Chapter 6: The July 2007 Rock And Ice Avalanches At Mount Steele, St. Elias Mountains, Yukon, Canada, which was co-authored by a consortium of earth scientists. In this chapter, I contributed to the ideas, format, and analysis in the main text, including the geometrics of the rock avalanche event, creation of some of the figures (e.g. 6.1, 6.5, 6.10, 6.11), and was completely responsible for the process modeling with DAN-W.

Abstract

This thesis represents a large body of work that seeks to describe, quantify, and simulate the behaviour of large rock slope failures (> 1 Mm³), in the form of landslides and rock avalanches, and their secondary processes, such as landslide-dammed lakes, utilizing remotely sensed data. Remotely sensed data includes aerial photography, high resolution satellite imagery from various platforms (e.g. LANDSAT, ASTER, EO-1, SPOT), and digital topographic elevation models of the Earth's surface (e.g. SRTM-3, ASTER GDEM2, LiDAR). This thesis focused on regions in northwest North America (British Columbia, Yukon Territory, and Alaska), and on regions in the Himalaya and Pamir Mountain chains (Tajikistan, Afghanistan, Pakistan, Tibet, and India). These study regions are each highly dynamic landscapes, where the occurrence of rock slope failures per area is higher than non-mountainous regions, and these events are aiding to the shape and profile of the landscapes and surfaces found today. This thesis focuses on: 1) the ability to accurately calculate geometrics (e.g. areas, volumes, runouts, debris depths) for large scale landslides and their associated landslide dammed lakes (e.g. areas, volumes, outbursts), utilizing data from remotely sensed sources; 2) the attempt to successfully simulate the observed dynamics for both landslide emplacement and their resulting debris deposits (DAN-W, DAN3D), and possible outburst flood scenarios (FLO2D); and, 3) attempt to quantify the kinetic and specific energy involved in rock avalanches, and how these energetics relate to fragmentation, as well as the lateral spreading and thinning of debris sheets. The river valleys of the northwest Himalayas (Pakistan and India) and the adjacent Pamir Mountains of Afghanistan and Tajikistan contain in excess of two hundred known rockslide deposits of unknown age that have interrupted surface drainage and previously dammed major rivers in the region in recent and prehistoric time. Some prehistoric rockslide dams in the northwest Himalayas have impounded massive lakes with volumes in excess of 20 Gm³. The region contains: 1) the highest rockslide dam in the world (the 1911 Usoi rockslide, Tajikistan), which impounds the current largest rockslide-dammed lake (Lake Sarez) on Earth (est. volume 17 Gm³); 2) the largest documented outburst flood (6.5 Gm³) associated with a historical rockslide dam outburst (the 1841 Indus Flood, Pakistan); and, 3) the world's most recent rockslide-dammed lake emergency, the 2010 Attabad rockslide dam on the Hunza River, in the Upper Indus basin, including the newly created Lake Gojal. By accurately quantifying the volume of an impoundment, and the downstream valley topography (DEM), floodwave scenarios can be created for various breaching situations, allowing for the delineation of downstream inundation areas, or the creation of hazard and risk scenarios. Two methods are used to

attempt to quantify the volumes of landslide-dammed lakes: 1) a contour interpolation method, focusing on the creation of contours to represent lake levels in the DEM data; and, 2) a new technique using digitized shorelines and statistical methods to obtain lake elevations on specific dates. A new technique has also been developed to quantify the larger block fragmentation from rock avalanches in the glacial environment, and a credible grain-size curve for the largest blocks can be obtained, aiding in the creation of a more complete grain-size curve for a particular event. The combination of landslides and their associated landslide dammed lakes are an important geomorphic process to study, as these events have a direct relationship to the hazard and risk faced by local communities living and working in these regions. By understanding the emplacement and deposit dynamics of large landslides and/or the outburst flood scenarios from naturally impounded reservoirs, we can attempt to reduce the direct impacts these events have to local communities.

Acknowledgements

This thesis would not have been possible without the financial, scientific, and emotional support from several people and institutions.

Financial support was provided by the Ontario Graduate Scholarship program over 3 years, which was vital to the completion of my PhD, allowing me to focus solely on my research. In the final two years of support from OGS, the funding was picked up by the TD Bank Graduate Scholarship in the Environment. Additional financial contributions came from the University of Waterloo, through the President's Graduate Scholarship. Finally, the financial support provided by Professor Evans through several TAs and RAs was fundamental to completing my PhD. I am forever grateful for all the financial support offered throughout my graduate student experience.

I would like to thank the organizers and scientists for the opportunity to participate in the prestigious International School of Landslide and Risk Assessment (LARAM), which is held annually in Ravello, Italy. Only 30 international PhD students are chosen each year, and I was honoured to be one of those students.

I would also like to acknowledge all of the teaching responsibilities given to me from the Earth and Environmental Sciences department at the University of Waterloo. Although not directly related to my thesis, I believe these experiences have been a vital part of my growth and desire to be a future faculty member, and professor. I would like to acknowledge Professor Evans, Professor Warner, Professor Saunderson, and Professor Dusseault for all their encouragement and assistance in allowing me these opportunities.

My most heartfelt and biggest thanks goes to my supervisor, Professor Evans. Without all of the scientific, academic, and moral support he has provided to me, this PhD would not have been possible. Professor Evans provided more than just motivation and guidance, but also friendship and support for all my time at the University of Waterloo and I know that my PhD would not have been as rigorous or thorough without his invaluable assistance.

Finally, I would like to thank my loving wife Jennifer and son Alexander. Without Jennifer's never-ending patience, support, and love, I do not think I would have been able to complete this extensive body of work.

To all those mentioned above, I feel that these brief words are insufficient in expressing my sincere gratitude and thanks, and I truly appreciated all the help and support.

Dedication

This thesis is dedicated to my loving wife Jennifer Delaney, son Alexander Delaney, and the rest of my amazing family.

Table of Contents

List of Figures

Mount Munday rock avalanche source area (2,830 m a.s.l.), 70 km distant to the southwest. In order to roughly estimate the temperature in the Mount Munday source area, we used a dry atmospheric lapse rate (−6.5 °C/1,000 m) applied to the elevation difference between the station and the source area. This results in a temperature reduction of ca. 16 °C for each data point recorded at the weather station. The horizontal lines are the average minimum (blue), average mean (black) and average maximum (red) temperatures obtained by the adiabatic adjustment as above for the Mount Munday source area. These values were calculated from the 1971 to 2000 climate normals for the Tatlayoko Lake climate station (Environment Canada 2012; Canadian Climate Normals or Averages 1971–2000 http://www.climate.weatheroffice.gc.ca/climate_normals/index_e.html). Black square on horizontal axis marks the date (August 12, 1997) of the Queen Bess glacier avalanche and associated moraine-dammed lake outburst at el. 1700 m a.s.l., 45 km to the SSW of the Tatlayoko Climate Station (Kershaw et al. 2005) and 54 km east of Mount Munday. Precipitation measured at Tatlayoko Lake, British Columbia, July 1–August 6, 1997 (Environment Canada 2012) is also shown (grey histogram

List of Tables

Chapter 1

Introduction

1.1 **Introduction**

Mountainous terrains in all parts of the world are subject to mass wasting events. Some of the most active locations include the North and South American Cordillera (e.g. Evans and Clague, 1999; Holm et al., 2004; Jibson et al., 2006; Lipovsky et al., 2007; Hewitt et al., 2008; Evans et al., 2009a; Harp et al., 2011; Safran at al., 2011; Guthrie et al., 2012; Petley, 2012; Schulz et al., 2012; Gorum et al., 2014; Mather et al., 2014), the Pamir and Himalaya Mountains (e.g. Heimsath and McGlynn, 2008; Dortch et al., 2009; Evans et al., 2009b; Hewitt, 2001, 2002a, 2006b, 2009a, 2009b; 2009c; Hewitt et al., 2008; Yuan et al., 2013), and the European Alps (e.g. Hewitt et al., 2008; Oppikofer et al., 2008; Deline, 2009; Fischer et al., 2010; Agliardi et al., 2013; Viero et al., 2013; Stoffel et al., 2014). These regions are specifically prone to rock avalanches, as they have high relief, often with glacially over-steepened slopes, tectonically fractured geology, and with little to no sediment or vegetation cover. Rock avalanches in mountainous regions have also been a fatal hazard suffered by local communities in many parts of the world (e.g. Petley et al., 2005; Nadim et al., 2006; Evans et al., 2009a, 2009b; Petley, 2012), initiating the creation and dissemination of various global and regional landslide hazard maps (e.g. Van Westen et al., 1999; Jibson et al,. 2000; Guzzetti et al., 2012; Bhatt et al., 2013; Fenton et al., 2013; Martha et al., 2013). Most recently, a fatal landslide has been observed in northern Afghanistan (Fig. 1.1)
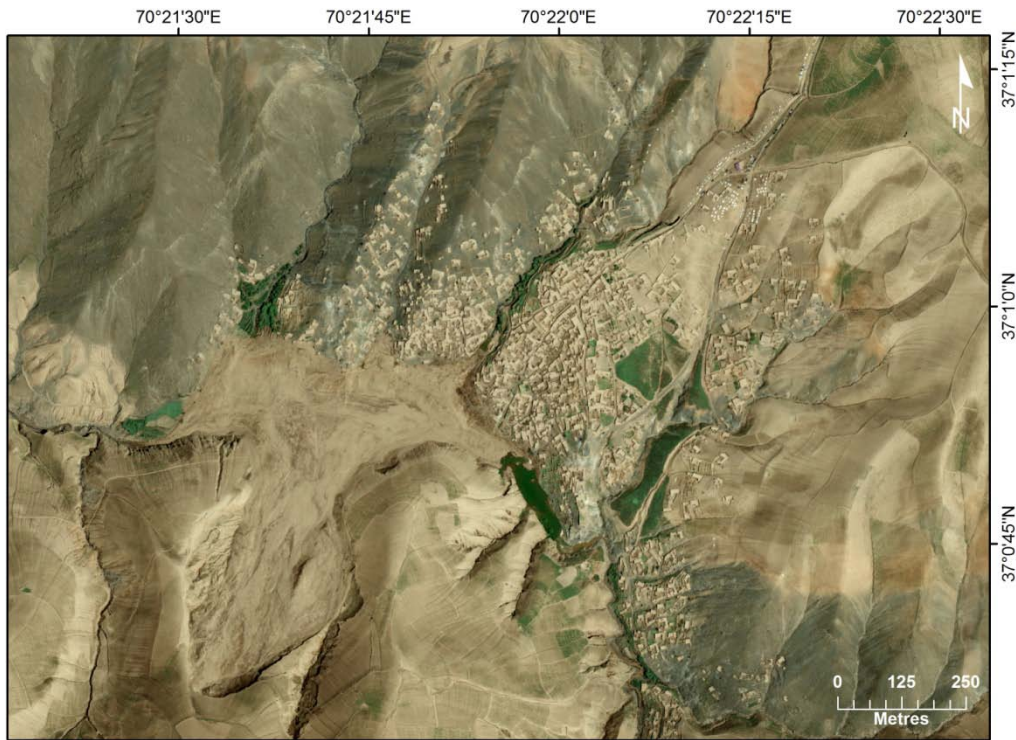
Figure 1.1: World-View 2 image taken May 5th 2014 of a fatal loess landslide in northern Afghanistan.

Rock avalanches travelling onto glaciers are of interest to Earth scientists as: 1) they commonly afford an excellent opportunity to examine rock avalanche emplacement mechanisms without substantial topographic interference in runout or additional earth materials being entrained in the debris; 2) they are an important geomorphic process in glacierised mountain environments, contributing to regional denundation and glacier sediment budgets; 3) events larger than 1 Mm³ can be accurately studied through the use of remotely sensed data; 4) the smooth topography of the glacial surface allows for improved performance in model simulations; and 5) the magnitude and frequency of these events can be analyzed for regional or global comparisons.

Although the catalysts of some rock avalanche events are not known, many of these events do have definite triggers, including earthquakes (e.g. Post, 1968; NRC, 1968; Jibson et al., 2006; Dunning et al., 2007; Owen et al., 2008; Evans et al., 2009a, 2009b; Gorum et al.,

2014) and climate warming (e.g. O'Conner and Costa, 1993; Holm et al., 2004; Huggel, 2009; Moore et al., 2009; Huggel et al., 2010a, 2010b).

Data on 48 catastrophic rock avalanches (> 1 Mm³), which occurred in the glacial environment of northwest North America (British Columbia, Yukon Territory, Alaska) since 1899 was collated (Table 1-1; Fig. 1.1), with a focus on the events occurring since the advent of the satellite era (ca. 1964). These events were identified through an extensive literature review, and through visual identification from optical satellite archives. Notably, 41 of these events could be positively identified with optical satellite imagery in the 50 year period from 1964 – 2014, and quantified with the aid of digital elevation models. At least 20 of the 48 events in our inventory of rock avalanches in northwestern North America (Fig. 1.2) were triggered by one of three major Alaskan earthquakes in 1964 (M9.2), 1979 (M7.5), and 2002 (M7.9).

Table 1-1: 48 rock avalanches occurring in northwest North America, locations shown in Figure 1.1.

	Event Location	**Date**	**Prov./State**	**Lat**	**Long**
1	Ferris Glacier	1899	BC	59 03 37.95	137 13 34.00
2	Capricorn Creek	1920s	BC	50 36 40.84	123 28 46.74
3	Devastation Glacier	1931	BC	50 36 00.24	123 32 51.00
4	Devastation Glacier	1947	BC	50 36 00.24	123 32 51.00
5	Tim Williams Glacier	1956	BC	56 32 37.29	130 00 03.58
6	Pandemonium Creek	1959	BC	52 00 13.17	125 46 51.32
7	Sherman Glacier 1	1964	AK	60 32 40.85	145 08 20.50
8	Steller 1	1964	AK	60 34 58.88	143 17 31.16
9	Allen 4	1964	AK	60 47 15.21	144 54 57.73
10	Fairweather	1964	AK	58 52 55.64	137 38 51.85
11	Schwan 1	1964	AK	60 52 43.74	145 10 46.93
12	Sioux Glacier 1	1964	AK	60 31 08.58	144 18 54.58
13	Martin River 1	1964	AK	60 36 00.37	143 39 40.17
14	Martin River 2	1964	AK	60 36 03.02	143 38 51.40
15	Martin River 3	1964	AK	60 38 23.98	143 35 01.20
16	Grewinck Glacier	1967	AK	59 36 08.28	151 04 34.36
17	Devastation Glacier	1975	BC	50 36 00.24	123 32 51.00
18	Tweedsmuir Glacier	1979	BC	59 55 27.77	138 31 32.91
19	Jarvis Glacier	1979	BC	59 28 50.35	136 34 03.23

20	Towagh Glacier	1979	BC	59 22 29.29	137 14 21.74
21	Cascade 1	1979	AK	60 13 52.38	140 27 24.03
22	Cascade 2	1979	AK	60 13 47.96	140 12 43.62
23	Cascade 3	1979	AK	60 06 03.67	140 21 01.20
24	Mount Meager	1986	BC	50 38 04.37	123 30 00.15
25	North Creek	1986	BC	50 39 33.74	123 14 04.16
26	Frobisher Glacier 1	1990	BC	59 46 23.12	137 45 55.72
27	Frobisher Glacier 2	1991	BC	59 46 23.12	137 45 55.72
28	Kshwan Glacier	1991	BC	55 45 35.96	129 43 43.64
29	Salal Creek	1992	BC	50 38 25.29	123 18 59.01
30	Iliamna 94	1994	AK	60 01 31.54	153 02 20.92
31	Mount Munday	1997	BC	51 19 12.27	125 13 21.54
32	Iliamna 97	1997	AK	60 01 31.54	153 02 20.92
33	Howson Range	1999	BC	54 31 24.92	127 47 17.00
34	McGinnis Peak N	2002	AK	63 34 04.71	146 15 11.10
35	McGinnis Peak S	2002	AK	63 32 29.57	146 14 35.80
36	Black Rapids E	2002	AK	63 27 40.01	146 09 52.23
37	Black Rapids M	2002	AK	63 28 26.28	146 15 19.70
38	Black Rapids W	2002	AK	63 28 26.28	146 19 13.74
39	West Fork Glacier N	2002	AK	63 26 28.06	147 29 44.70
40	West Fork Glacier S	2002	AK	63 26 57.41	147 29 37.21
41	Mount Steller	2005	AK	60 31 13.52	143 05 27.85
42	Mount Steele	2007	YK	61 05 33.19	140 17 59.08
43	Mount Miller	2008	AK	60 28 40.45	142 14 23.94
44	Mount Steller 1	2008	AK	60 31 13.52	143 05 27.85
45	Mount Steller 2	2008	AK	61 31 13.52	144 05 27.85
46	Capricorn Creek	2010	BC	50 37 15.45	123 30 00.38
47	Lituya Mountain	2012	AK	58 47 42.72	137 25 44.42
48	La Perouse	2013	AK	58 33 40.86	137 03 48.27

We consider this list to be a complete inventory of observed rock avalanche events in the study region of northwest North America which were greater than 1 Mm³. However, we recognize the possibility that events which occurred between 1899 and 1965 may not have been observed by any researcher, nor visible in the satellite data archive, and therefore unintentionally omitted from the inventory.
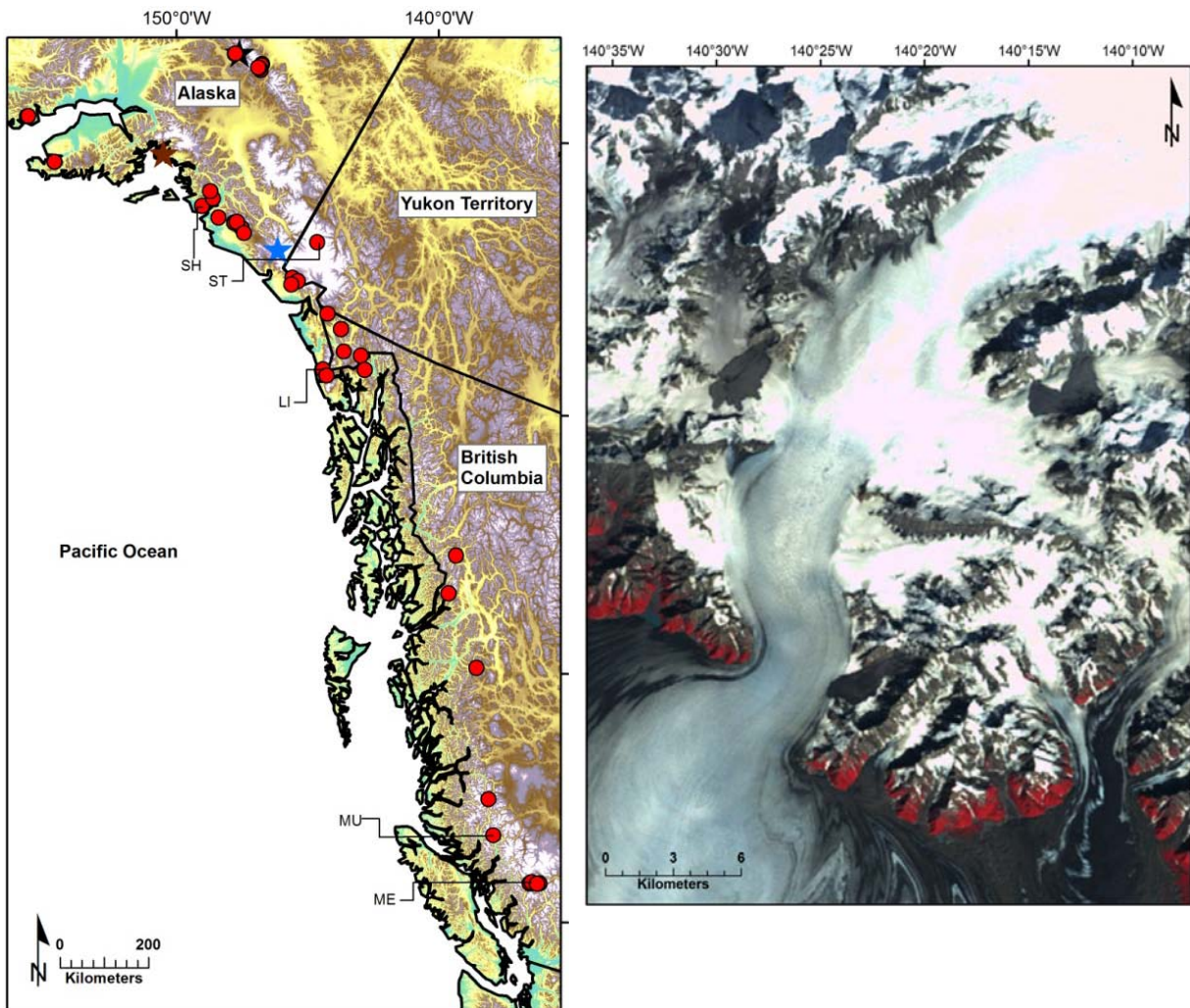
Figure 1.2: *LEFT* - Inventory of 48 rock avalanches on glaciers in northwest North America (*red circles*). Highlighted events: SH: Sherman Glacier (1964); ST: Mount Steele (2007); LI: Lituya Mountain (2012); MU: Mount Munday (1997); and ME: Mount Meager (2010). The three major earthquakes are marked with coloured stars: Brown - 1964 (M9.2); Blue - 1979 (M7.5); Black - 2002 (M7.9). *RIGHT* - LANDSAT3 image taken August 1979 of three Cascadia rock avalanches within a 10 km radius, all triggered by the 1979 Alaska earthquake (M7.5).

One of the current research themes involving rock avalanches includes the anomalous mobility of large events, which can travel hundreds or thousands of meters further downslope than would be expected, dealing with a high frictional material, such as rock (e.g. Hungr, 1995; Dade and Huppert, 1998; Davies and McSaveney, 1999; Legros, 2002; Schneider et al, 2011; Sosio et al, 2012; Pudassaini and Miller, 2013; De Blasio, 2014; Sosio et al,. 2014). With advances in computer technology, the modeling of mass wasting events has become

5

more evident in the scientific literature, attempting to replicate various physical parameters such as: 1) the mobility of a rock mass over various slope types, geologic surfaces, or topographic impediments; 2) the entrainment of additional earth materials along their path, and; 3) the depths of deposits which may form at the valley floors (e.g. McDougall and Hungr, 2004; McDougall and Hungr, 2005; Sosio et al., 2008; Evans et al., 2009a, 2009b; Hungr and McDougall, 2009; Bowman et al., 2012; Sosio et al,. 2014).

One of the most recent advances in the landslide literature is the use of digital datasets including both digital topographic models (e.g. SRTM-3, ASTER GDEM2, state/province datasets, and LiDAR data) (e.g. Chen et al., 2006; Evans et al, 2009a, 2009b; Lipovsky et al., 2008; Jaboyedoff et al., 2012), as well as high resolution digital satellite imagery (e.g. LANDSAT1-8, ASTER, EO-1, Pleiades, and SPOT) (e.g. Wang and Lu, 2002; Evans et al., 2009a, 2009b; Kargel et al., 2010; Harp et al., 2011) . These digital topographic datasets allow scientists to calculate values for the magnitudes and geometrics of large events (e.g. elevations, width and length of path, slope orientations, and slope angles; landslide dammed lake areas, extents, and volumes), and their temporal occurrence can be obtained through satellite imaging (e.g. Wang and Lu, 2002; Evans et al., 2009a, 2009b; Kargel et al., 2010; Evans et al., 2011). There has also been extensive validation and inter-comparisons of digital topographic datasets to real world elevations, with promising results (e.g. Farr et al., 2007; Becek, 2008; Huggel et al., 2008; Li et al., 2012; Suwandana et al., 2012; Jing et al., 2013; Mashimbye et al., 2014).

The collation and analysis of these above factors can allow for the creation of magnitude and frequency relations of mass wasting events regionally, or globally (e.g. Corominas and Moya, 2010; Florsheim and Nichols, 2013; Hurst et al., 2013; Regmi et al., 2013). In our inventory of rock avalanches in northwest North America, magnitudes (e.g. volume) were gathered on 28 events, resulting in the relationship shown in Figure 1.3. However, the graphed data also highlights the lower counts of events between 1 Mm³ and 10 Mm³, where

the graph no longer follows the power law. This is assumed to be from the smaller events missing in the inventory.
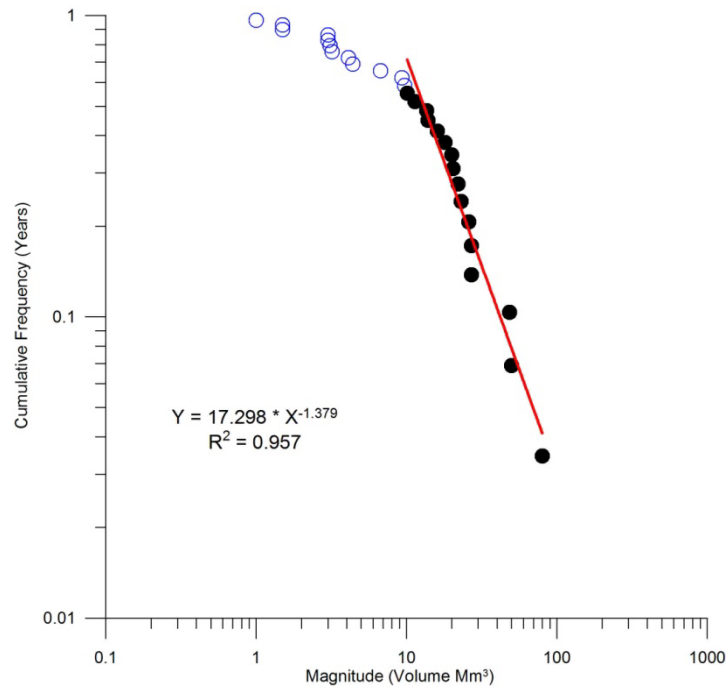
Figure 1.3: Magnitude and frequency relationship curve for 28 northwestern North America rock avalanches on glaciers in the inventory.

This magnitude and frequency relationship suggests that an event of 1 Mm³ could occur approximately once every 17 years, a 10 Mm³ event could occur once every 413 years in the study region, and that the maximum volume shown above, an event of ca. 80 Mm³ could occur approximately once every 7,283 years. Korup and Clague (2009) completed a similar magnitude and frequency analysis for three other regions, the New Zealand Alps, the European Alps, and China. For the New Zealand Alps, Korup and Clague (2009) calculated a return period of approximately 1 in 1000 years for an event only 1 Mm³, however, they believe this number is exaggerated due to a poor dating history and incomplete inventory. For the European Alps, they calculated a return interval of approximately 1 in 350 years for an event 1 Mm³ in volume. Finally, for the mountains in China, Korup and Clague (2009) calculated a very short return period of 1 in 4 years for events of 1 Mm³ in volume.

Many secondary effects from slope failures in mountainous terrain can also prove challenging and often costly to overcome, such as the growth and failure of landslide dammed lakes (e.g. Costa and Schuster, 1988; Hewitt, 1998, 2006c, 2011; Evans et al., 2006, 2011; Dortch et al., 2009). These reservoirs can grow to many cubic kilometers in volume, creating hazards to both upstream and downstream communities, through the flooding and loss of large tracts of land up-valley, or the possibility of catastrophic outburst floods down-valley, triggered through overtopping of the natural debris dam (Schroder et al., 1991; Chen et al., 2004; Evans et al., 2011; Butt et al., 2013; Yang et al., 2013). Although many rock avalanche dammed lakes have been historically created, few last as permanent features on the landscape, with many events failing prior to two years in existence (Costa and Schuster, 1988; Evans et al., 2011). These natural dam failures and outburst floods have been observed to be some of the largest outburst discharges recorded in history, creating a hazardous situation for downstream communities (Evans, 1986; Costa and Schuster, 1988; Evans et al., 2011). Digital elevation models are now more frequently being to be used in the calculation of volumes and areas for naturally dammed reservoirs (e.g. Evans et al., 2011), improving our knowledge of the magnitude that past and present impoundments can reach, and also acting as input data to flood outburst scenarios for downstream hazard simulations (e.g. Mergili et al., 2011; Wang et al., 2012; Aggarwal et al., 2013; Butt et al., 2013; Schneider et al., 2014; Westoby et al., 2014).

1.2 **Thesis Objectives**

This thesis is an attempt to analyze and explain the behavior and distribution of rock avalanches in mountainous terrain; including their emplacement dynamics (e.g. length, width, velocities), deposit morphologies (e.g. areas, volumes, depths, rock mass fragmentation, flow lines), energetics (e.g. total potential (J) and specific energy (J/t)), and their secondary impacts regarding the creation and failure of landslide-dammed reservoirs (e.g. volumes, areas, growth rates, extents), and associated outburst floods. This thesis covers two broad regions globally, the northwestern Cordillera of North America (British

Columbia, Yukon Territory, and Alaska), and the Pamir and Himalayan Mountain chain of southern Asia (Pakistan, Afghanistan, Tajikistan, and Tibet).

To accomplish the above, the use of geographic information systems (GIS) and remotely sensed data (e.g. digital elevation models, aerial photography, and satellite imagery) will be heavily relied upon. Field work to these regions was not possible, therefore simulation models for some of the past and present rock avalanches was completed and discussed, in both a 2D (DAN-W) and 3D (DAN 3D) framework, as well as outburst events from selected natural dam impoundments (FLO2D). Finally, an attempt to quantify the inherent errors involved in using digital datasets will be addressed at length, to determine the real world utility of using remotely sensed datasets. Some questions which will be addressed: Are these datasets accurate? Are they acceptable for use in large scale catastrophic disasters such as rock avalanches and landslide-dammed lakes? What is the error of digital datasets? Are the model outputs really representative of reality?

1.1 **Chapter Overviews**

Each chapter is written as a stand-alone paper which addresses one or more of the themes and questions put forth above. This format results in chapters that can be read and understood on their own, with individual results and conclusions. However, this modular format does result in the unavoidable repetition of some ideas, themes, concepts, and data analysis. Each chapter is outlined here:

- Chapter 2 focuses on the Pamir and Himalayan Mountains of southern Asia (Pakistan, Afghanistan, Tajikistan). An extensive review of many rock avalanche deposits and natural dammed reservoirs (stable and breached) is presented. A historical perspective of some of the largest known natural dam impoundments and outburst floods are analyzed in detail using digital topographic models, and verified by firsthand accounts from scientific observers of the time. The ability to test these

individual accounts of the events from the mid-19th century, and recreate past scenarios using current techniques and technology is shown.

- Following the extensive review of rock avalanches and landslide-dammed lakes in the Pamir and Himalayas, a case history from the Pamir Mountains is presented in Chapter 3, focusing on the recent 2010 Attabad rock avalanche in northern Pakistan. An analysis of the geology, the rock avalanche event and the growth and shrinkage of the naturally impounded Lake Gojal is presented, with a focus on the use of remotely sensed data (digital topographic and satellite datasets). A new statistical approach is presented for determining the pool elevations for an impounded reservoir (Lake Gojal), from SRTM DEM data. This event is also compared to historical events from 1841 and 1858, which were studied in detail in Chapter 2.

- Chapter 4 analyses another case study: the large Yigong rock avalanche and impounded landslide-dammed reservoir the Himalayan Mountains (Tibet). This event occurred in 2000, and the landslide, growth in lake area and volume, as well as the catastrophic outburst flood were all recorded in various forms of digital remotely sensed data (digital topographic data and satellite imagery). A 2D (DAN-W) and 3D (DAN3D) model of the landslide was able to successfully simulate the entire event, including the velocities of the rock mass emplacement, entrainment of additional earth materials along the path, and the general size and shape of the resulting landslide dam. An outburst simulation (FLO2D) was able to model a comparable floodwave downvalley to that which was observed at the time of the event.

- Chapter 5 brings the study back to North America; with a third case history, this time of the 1997 Mount Munday rock avalanche. This chapter outlines the processes involved for a complete analysis of a rock avalanche on a glacier surface, from the source rock mass, morphology of the emplacement, flow paths, and final deposit. The rock avalanche is also successfully modeled in both 2D (DAN-W) and 3D (DAN 3D) frameworks, highlighting the utility of back-analysis. A comparison of energetics, and the relationships between volume and runout is discussed for a number of rock avalanches. Finally, this chapter also introduces a brand new remote

sensing technique which attempts to quantify the larger block fragmentation of a rock avalanche on a glacier solely through remotely sensed data.

- Chapter 6 provides an overview of the processes and data analysis involved in the study of a large catastrophic rock avalanche on a glacier, in the form of a case study on the 2007 Mt Steele rock and ice avalanche. A discussion on the geology, emplacement, and deposit morphology is presented. High resolution satellite and digital elevation data were utilized (LiDAR), and a successful 2D simulation (DAN-W) is performed. This event has been determined to be one of the largest mass wasting events in recent Canadian history.

- Finally, Chapter 7 will attempt to summarize and place into global context all of the above chapters, drawing on the analysis, discussions, and conclusions, presented therein. It will summarize such topics as the magnitude and frequency relationships, the modeling of mass wasting flows and outburst floods, the utility of the remotely sensed data (DEMs and satellite imagery) in the Earth science discipline, and the possible introduction of errors from those digital datasets. It will conclude with a final overall assessment of this work in context with the recent scientific literature.

Chapter 2

Rockslide Dams in the Northwest Himalaya (Pakistan, India) and the Adjacent Pamir Mountains (Afghanistan, Tajikistan) Central Asia

Delaney, K.B. and Evans, S.G.

Introduction

The remains of rockslide dams are widespread in the northwest Himalayas (Hewitt, 1998, 1999, 2006a, 2006c, 2011) and the adjacent Pamir Mountains (Ischuk, 2006) of Afghanistan and Tajikistan, Central Asia. The region contains in excess of three hundred known rockslide deposits of, as yet, unknown age that have interrupted surface drainage and previously dammed major rivers in the region in prehistoric time. Most of these dams have been breached and only remnant debris, and in some cases lacustrine deposits from formerly impounded lakes, are visible today in the deep valleys of the region.

In addition, the region contains: (1) the highest rockslide dam (Usoi rockslide) in the world that dams the largest rockslide-dammed lake (Lake Sarez) on Earth; (2) the largest documented outburst flood associated with a historical rockslide dam outburst (the 1841 Indus Flood); and (3) the world's most recent (2010) rockslide dammed lake emergency, the Attabad rockslide dam on the Hunza River (Kargel et al., 2010), in the Upper Indus basin of northern Pakistan (Fig. 2.1). The outburst flood hazard presented by Lake Sarez has attracted global scientific attention (Stone, 2009).

The spatial distribution of rockslide dam deposits, the rate and frequency of rockslide dam formation, the subsequent behaviour of the rockslide dam and outburst flood potential are important elements in landslide hazard assessment in the region. To some extent the accuracy

of the hazard assessment is conditioned by the interpretation of rubbly valley fill deposits as representing rockslide debris as opposed to glacial deposits, a debate that continues to simmer today (e.g. Malik et al., 2008), and the conceptualizing and analysis of various breaching scenarios. In addition, a consideration of rockslide dam hazard is important for the assessment of hydroelectric potential in the region and in some cases, as noted below, the suitability of natural dam debris for foundations of constructed dams.
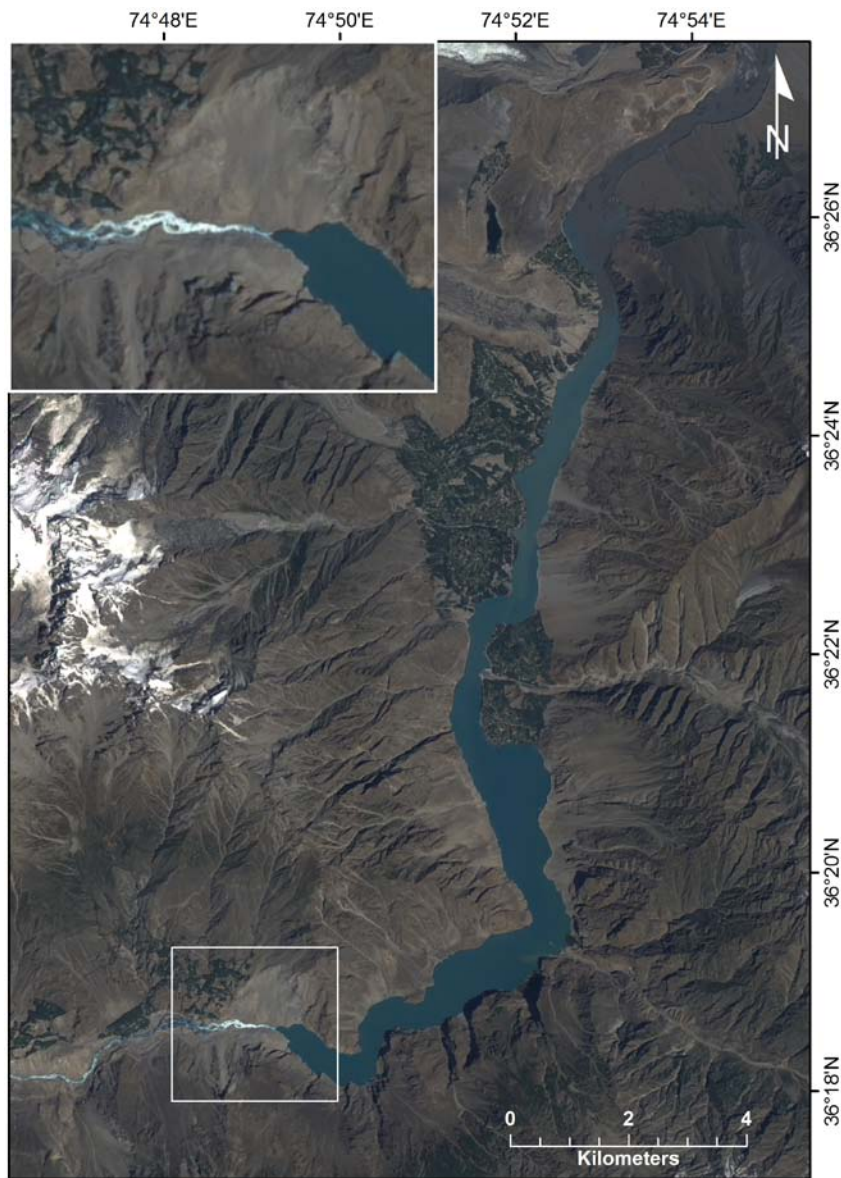
Figure 2.1: Lake Gojal, Hunza Valley, northern Pakistan, the rockslide-dammed lake impounded by the Attabad rockslide that occurred on January 4, 2010. Extent shown on EO-1 satellite image obtained on August 04, 2011.

13

White rectangle is enlarged in inset, which shows Attabad rockslide and heavy flow in spillway over rockslide dam debris.

In this paper we: (1) review previous work carried out on the presence of rockslide debris that formed prehistoric rockslide dams in the region; (2) report new data on previously unknown rockslide dams; and (3) using remote sensing imagery and SRTM-3 digital terrain data (Farr et al., 2007), we determine and analyse the geometry, geomorphology and behaviour of four rockslide dams that have formed in historical time, i.e., in 1841 (Indus), 1858 (Hunza), 1911 (Murgab/Bartang), and 2010 (Hunza).

2.1 **Methodology**

We carried out a review of the literature on rockslides and rock avalanches in the northwest Himalayas and the adjacent Pamirs (Fig. 2.2). This has included a review of a number of original contemporary accounts of rockslide dam events including those on the Indus (e.g. Falconer, 1841), Hunza (e.g. Henderson, 1859), and the Murgab (Bartang) Rivers (e.g. Prebrajensky, 1920).
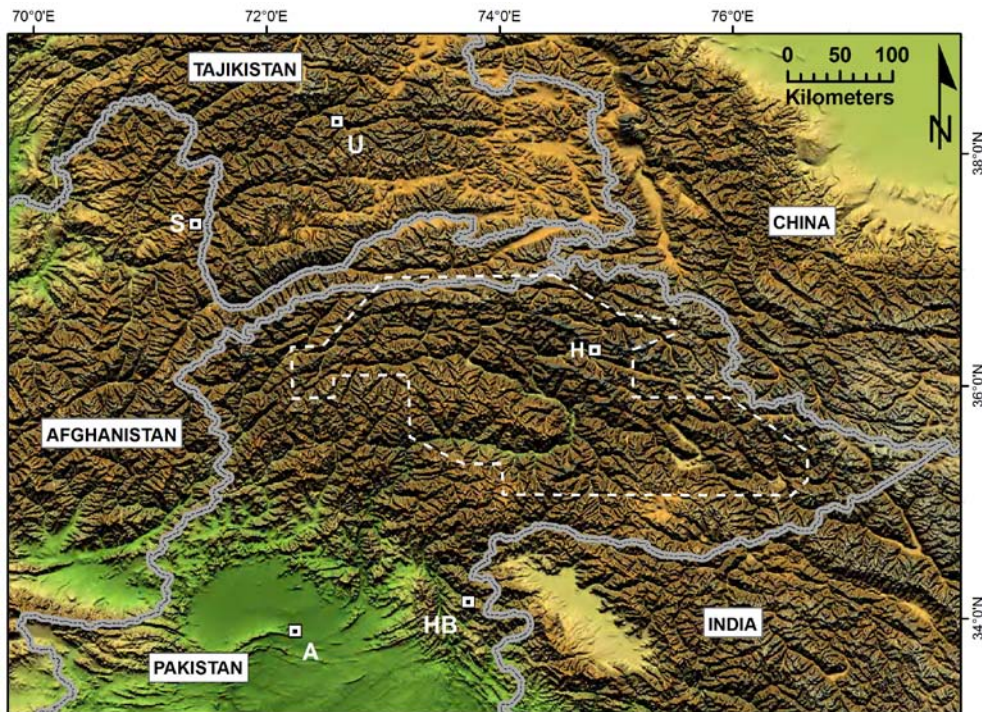
Figure 2.2: Map of northwest Himalayas (India and Pakistan) and adjacent Pamir mountains (Tajikistan and Afghanistan). Key to locations discussed in text is as follows; A-Attock on the Lower Indus River, H – 2010

14

Hunza River rockslide dam, HB – 2005 Haittan Bala rockslide dam, *S* – Shiwa Lake rockslide dam, and U – 1911 Usoi rockslide dam and Lake Sarez. *Dashed white line* outlines area mapped by K. Hewitt in a series of papers since 1998 (see text for references and Fig. 4.3 for further details).

For topographic data we utilised the SRTM-3 (3 arc second) data set obtained during the Shuttle Radar Topography Mission in February 2000 (Farr et al., 2007) to develop digital elevation models (DEMs) for the rockslide-dammed lakes discussed in both the northwest Himalayas and the Pamirs. To assess the accuracy of the SRTM data in the region of interest, we compared the elevation of three runways at Gilgit and Skardu obtained from the SRTM digital terrain models to the official air navigation elevations of both ends of the three runways (cf. Becek, 2008). The mean error of six SRTM elevations was less than 3 m, suggestive of high vertical accuracy.

SRTM-3 data has been used in conjunction with Google Earth and LANDSAT-7 satellite imagery to illustrate geomorphic features of rockslide dam deposits and to determine the extent and volume of historic and prehistoric rockslide-dammed lakes.

2.2 **Rockslide Dams in the Northwest Himalayas**

2.2.1 Previous Work

Our knowledge of rockslide dams in the northwest Himalayas is largely due to the work of K. Hewitt. In a series of papers beginning in 1998, Hewitt has reported on the occurrence of rockslide and rock avalanche deposits in the Karakoram Himalaya, Pakistan. His work has: (1) successively mapped the distribution of rockslide and rock avalanche deposits (Fig. 2.3); (2) developed diagnostic criteria for the identification of rockslide dam deposits thus correcting the apparent misinterpretation of the genesis of bouldery debris in Karakoram valleys that had previously been mapped as moraines; (3) described the field geomorphology and inferred landslide behaviour of selected rockslides and rock avalanches; (4) outlined the impact of rockslides on river systems, specifically river damming; and (5) developed a conceptual model of fragmented/interrupted river systems in which landslide damming impacts on the geomorphic evolution of mountain river systems and mountain relief.

15
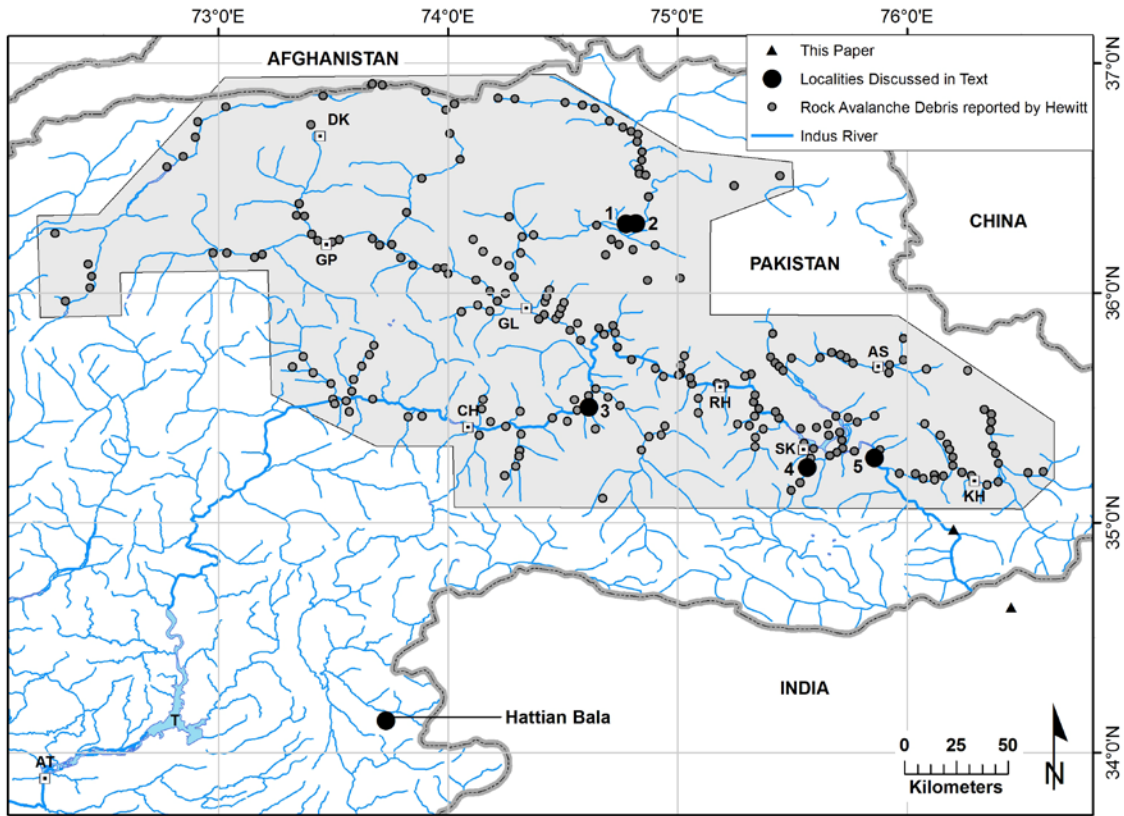
Figure 2.3: Map showing distribution of 233 rockslide deposits (*grey dots*) extracted from maps published by K. Hewitt between 1998 and 2009 (see text for references) and imported into GIS. *Shaded area* approximates area mapped by Hewitt (see Fig. 2.2 for location). Also shown are two additional large scale rockslide deposits in the upper Indus (*black triangles*) mapped in this study. Key to towns and villages; AS-Askole, AT-Attock, CH-Chilas, DK-Darkot, GL-Gilgit, GP-Gupis, KH-Khapalu, RH-Rhondu, SK-Skardu. The Tarbela Reservoir is labelled T. Location of historic landslide dams and prehistoric rockslide deposits discussed in text (*black dots*) are *1*: Hunza 1858, *2*-Hunza-2010, *3*-Indus 1841, *4*-Satpara Lake, and *5*-the Gol Ghone rockslides. The location of the earthquake-triggered 2005 Hattian Bala rock avalanche and rockslide-dammed lake (Fig. 2.4) is also shown.

We note that with respect to (1) no formal inventory, involving a complete listing of rockslide sites, has been published by Hewitt. Each successive published map shows an incremental increase in the number of identified rockslide/rock avalanche deposits; 104 events in 1998 and 1999 (Hewitt, 1998, 1999), and 143 in 2002 and 2006 (Hewitt, 2002a, 2006a, 2006b), and 90 in 2009 (Hewitt, 2009a, 2009b). Over 80% of these rock avalanches/rockslides formed valley-blocking rockslide dams (Hewitt, 2006c) that impounded the Indus, its tributaries, or other major rivers in the region.

16

We collated the Hewitt maps and imported the location of rockslides shown on them into a GIS referenced framework (Fig. 2.3) in an attempt to quantify his mapping in a regional and global context. By our count, there are total of 233 rock avalanches identified on Hewitt's maps (This should be considered a minimum as Hewitt (2011), reports a new total of 322 within his study area). With the addition of the 2010 Hunza rockslide, this makes a total of 234; three of these events have taken place in the period of 1841–2010, a frequency of occurrence of 1 in 56 years. For the area mapped by Hewitt, estimated in Fig. 2.3 as 49,783 km², this is equivalent to roughly 50 major rockslides (interpreted from their deposits) per 10,000 km². In Fig. 2.3, two previously undocumented rock avalanches that once blocked the Upper Indus are shown as is the location of the 2005 Hattian Bala rockslide dam and the 2010 blockage of the Hunza River.

Other work has been carried out on the geomorphology of rockslides of the northwest Himalaya by Shroder (1989, 1998), Shroder et al. (1989), Owen (1996), and more recently by Seong et al. (2009) and Dortch et al. (2009). In addition, investigations of lacustrine deposits formed in rockslide-dammed lakes have been reported by Burgisser et al. (1982) in the Skardu area of Pakistan, and Fort et al. (1989) and Phartiyal et al. (2009) in the Ladakh Himalayas of northwest India.

We also note the occurrence of the Hattian Bala rock avalanche (34°08'24"N, 73°43'46"E), located in Fig. 2.3 and illustrated in Fig. 2.4. The landslide (est. volume 85 Mm³ Dunning et al., 2007) was triggered by the M7.6 October 2005 Pakistan Earthquake (Dunning et al., 2007; Owen et al., 2008; Schneider, 2009) and dammed surface drainage to form significant impoundments in a tributary watershed to the Jhelum River (Fig. 2.3).
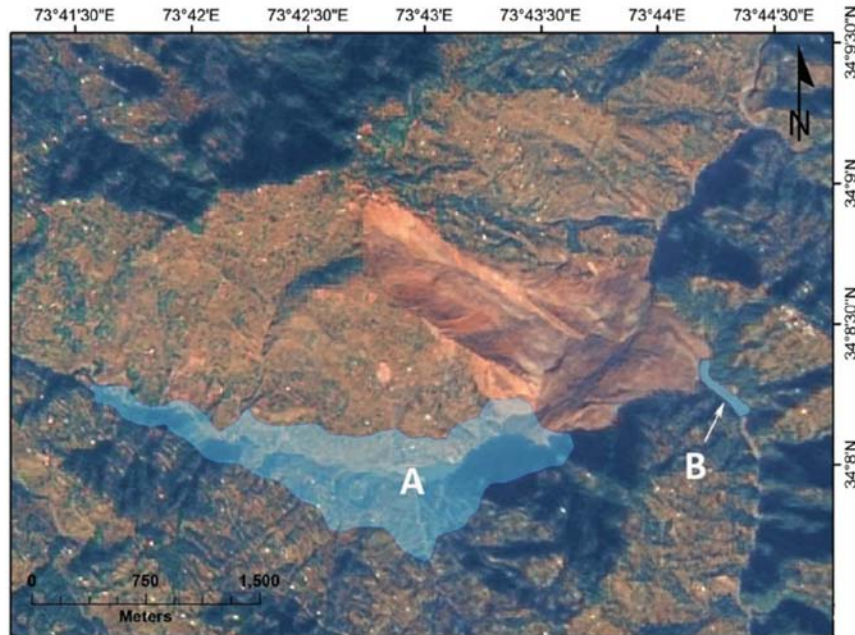
Figure 2.4: The Hattian Bala rock avalanche (est. vol. 85 Mm³) triggered by the 2005 M7.6 Kashmir earthquake at 34°08'24"N, 73°43'46"E. The rock avalanche debris blocked two streams forming two rockslide-dammed lakes, A (Karli Lake) and B (Tang Lake). The maximum volume of Karli Lake was estimated at 65 Mm³. EO-1 image obtained on November 4, 2005. Lake outlines based on SRTM-3 DEM. Karli Lake drained, after heavy rains, in February 2010.

The larger lake (Karli Lake) reached a volume of about 65 Mm³ (Dunning et al., 2007; Schneider, 2009) before overtopping through a 425 m long excavated spillway in April 2007 (Dunning et al., 2007). Following overtopping the lake level was more or less stable as overflow passed through the spillway. The smaller lake (Tang Lake) reached a volume of about 3.5 Mm³ before overtopping through a second excavated spillway, 130 m in length, over the debris (Schneider, 2009).

2.2.2 Prehistoric Rockslide Dams and Deposits: Two Examples in the Skardu Region (Upper Indus)

The deep valleys of the northwestern Himalayas and the adjacent Pamirs frequently contain complex valley fills characterised by chaotic rubbly debris (Fig. 2.5) as well as stratified silts (e.g. Burgisser et al., 1982). The interpretation of these deposits as remnant rockslide debris and lacustrine sediments deposited in rockslide-dammed lakes only became established after work by M. Fort and co-workers (Fort and Peulvast, 1995; Fort et al., 1989) and K. Hewitt

18

between 1989 and 1999 (Hewitt, 1998, 1999). Previously, beginning with the earliest scientific observations (e.g. Drew, 1873), they had generally been interpreted as moraine deposits and lake sediments deposited in glacial lakes, respectively (see full discussion in Hewitt, 1999). A notable exception to this was a discussion contributed to Drew's paper (1873, p. 471) by W.T. Blanford who, in disagreeing with Drew, argued that the rubbly deposits in the Upper Indus were rockslide deposits and that the origin of the laminated fine-grained sediments was in rockslide-dammed lakes.

Figure 2.5: Typical example of complex valley fill deposits in the Upper Indus basin, northern Pakistan. Previously unmapped deposits include (1) older rockslide deposits at A and B that both dammed the Indus River, (2) younger rockslide deposts (C) that have dammed a tributary forming a rockslide-dammed lake at D and ran up the opposite valley slide to a limit indicated by *vertical arrow*. This rockslide also dammed the Indus. Length of Indus (flowing from top *right* to bottom *left*) seen in image is 13 km. *Google Earth* image at 34°58'09"N, 76°11'19"E, 65 km SW of Skardu. Locality is indicated in Fig. 2.3.

The re-interpretation of the origin of these deposits was significant in four ways: (1) the occurrence of major rockslides was established as a relatively common phenomenon over a large area of mountainous terrain and thus a critical geomorphic process; (2) that in the past, the Indus and other major rivers in the region had been dammed by large volumes of

rockslide debris, and, in some cases had formed very large, persistent rockslide-dammed lakes; (3) the geometry of some rubbly deposits indicated that they had formed massive rockslide dams that impounded gigantic rockslide-dammed lakes; and (4) the rubbly deposits (and associated lacustrine sediments) were Holocene rather than Pleistocene (Late Glacial) in age (i.e. were much younger than previously thought). Together these implications have led to a new interpretation of the mountain landscape in the region in which rockslides and their effects are both critical geomorphic processes in landscape evolution (e.g. Korup et al., 2010), and also pose significant hazards to communities and infrastructure with a spatial and temporal frequency that had not been recognised hitherto (Hewitt, 2010). The presence of remnant rockslide deposits is also a major factor in the high sediment yield in river basins of the region (e.g. Ali and de Boer, 2007; Ali and de Boer, 2008).

These implications will be examined with reference to two examples from the Skardu region (Fig. 2.3).

2.2.2.1 Gol Ghone Rockslides

The Gol Ghone rockslides (35°17'12"N, 75°51'34"E) were first identified by Hewitt (1998). They consist of two massive rock avalanches that occurred on the west side of the Indus River, 28 km upstream of Skardu, and 9 km downstream from the confluence of the Indus and Shyok rivers (Fig. 2.3); their deposits overlap and the older larger deposit is designated Gol Ghone A, the younger (southern) deposit is designated Gol Ghone B (Hewitt, 1998). The deposits of the two rock avalanches, which as Hewitt (1998, p. 63) notes were previously interpreted as moraines, filled the Indus River for a distance of 5 km along the thalweg.

The geomorphology of the deposits was examined on satellite imagery and in the SRTM-3 DEM. This examination indicates that the younger Gol Ghone rockslide dam had a minimum dam height of 2,565 m a.s.l., 300 m above the Indus at this point. This is taken as a minimum pool level for the impoundment formed by the rockslide damming of the Indus. At this pool

elevation, a massive rockslide dammed lake would have formed in the Indus and Shyok Rivers (Fig. 2.6) that was 219 km² in area and 25.7 Gm³ in volume.
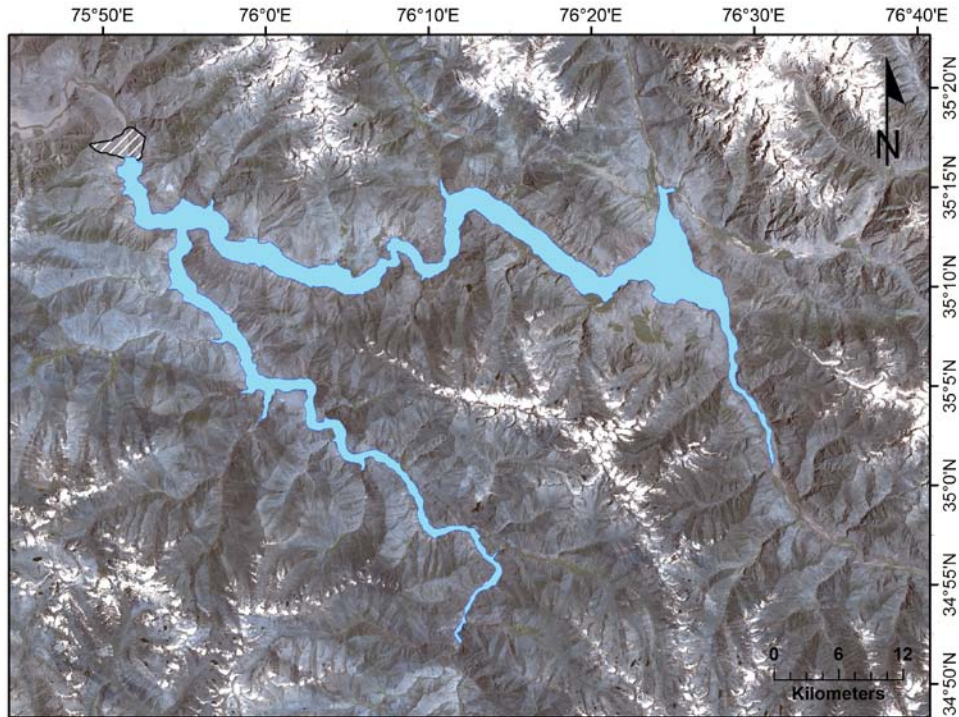
Figure 2.6: LANDSAT-7 satellite image showing extent of rockslide-dammed lake (*white fill*) that would have formed in the Indus and Shyok Valleys as a result of damming by the Gol Ghone B rockslide (*black stippled* pattern) at a spillway elevation of 2,565 m a.s.l. Extent of lake based on SRTM-3 DEM. The Gol Ghone rockslides (Hewitt, 1998) are located in Fig. 2.3.

The Gol Ghone example exemplifies the massive impoundment volumes implied by the presence of very large remnant rockslide dams in the Indus and other valleys of the Karakoram Himalaya (cf. Hewitt, 2011).

2.2.2.2 Satpara Rockslide – Dammed Lake and Satpara Dam

Satpara Lake (35°14'17''N, 75°37'51''E), located 6 km south of Skardu (Fig. 2.3), is impounded by a natural debris dam (Fig. 2.7). The natural dam is utilised as the foundation for the Satpara Dam which (as of 2010) is under construction; the 40 m high earth-core rockfill dam will augment the storage capacity of Satpara Lake and will have a gross capacity of 115 Mm³.

When completed the Satpara Project will generate 17.36 MW of hydropower, irrigate 6,287 ha of lands and supply 14 million litres daily of drinking water to Skardu (Malik et al., 2008).

Satpara Lake was identified as a rockslide-dammed lake by Hewitt (1998) in interpreting the debris forming the dam as a rockslide deposit. He also identified a clear source area for the debris on the east side of Satpara Valley (Fig. 7 in Hewitt (1998); Fig. 2.7). As reviewed by Hewitt (1999), a succession of workers dating back to 1906 had previously identified the Satpara debris dam as being morainic in origin. The lines of evidence that support the interpretation of the Satpara debris as rock avalanche in origin include: (a) a clear source scar on the mountain slope above the debris; (b) run-up of debris on the opposite valley side; (c) the rim-like boundary of the upper limit of debris run-up; and (d) the nature of the debris as described from surface exposures by Hewitt (1999). These features strongly suggest a rock avalanche origin for the Satpara debris.
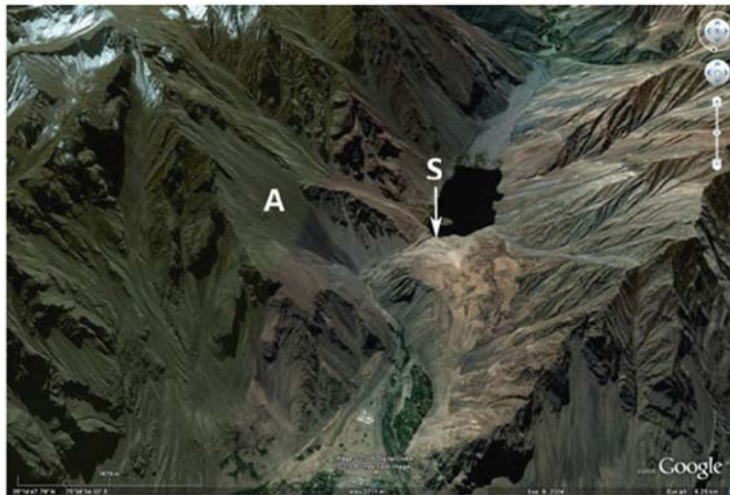
Figure 2.7: *Google Earth* image of the site of Satpara Dam (*S*), northern Pakistan, currently under construction (2010). The structure will utilise a prehistoric rockslide dam deposit that impounded Satpara Lake. Source of rockslide is at A. Satpara Lake is located in Fig. 2.3. See text for further discussion.

Despite this evidence, other workers have more recently at least partially disputed this interpretation suggesting that the identification of major rockslide deposits in the valleys of the northwest Himalayas is still not a routine geomorphological exercise. The dispute is discussed by Malik et al. (2008). These authors prefer the interpretation of Kuhle (2004) who

suggests that the debris dam is hybrid in origin, consisting of a mixture of late-glacial moraine deposits and rock avalanche debris.

The characteristics of the debris reported by Malik et al. (2008), based on a detailed sub-surface investigation of the natural dam, indicate: (1) that the materials are a mixture of large angular boulders in a finer matrix that consist of sand, silt and clay; (2) that bedrock is over 100 m deep in the middle of the valley; (3) the presence of high permeability zones along the sides and the base of the rock avalanche deposit; (4) that within the debris dam, permeability generally increases towards the surface where it approaches 10^{-3} m/s; and (5) that during permeability testing some zones of excessive water losses were encountered indicating the presence of open-work zones within the debris.

These characteristics appear consistent with a geomorphological setting in which rock avalanche debris overlies a valley fill consisting of morainic and alluvial materials which were probably partially incorporated into the landslide debris during emplacement by entrainment.

2.2.3 Historical Rockslide Dam Blockages of the Indus and the Hunza Rivers 1840, 1858, and 2010

2.2.3.1 Historical Rockslide Dams I – 1841-1841 Indus

The cataclysm on the Indus resulting from the breach of a rockslide dam in 1841 was first reported by Falconer (1841). Early reports, including Falconer's, describing the circumstances and effects of the formation and failure of the 1840–1841 Indus rockslide dam were summarised in the benchmark paper on great floods of the Indus by Mason (1929).

In describing what Mason termed "*The Great Indus Flood* " the following facts emerge: (1) In December 1840 or 1841 a rockslide dammed and blocked the Indus completely; (2) the rockslide, apparently triggered by an earthquake, originated in the Lechar Spur of Nanga Parbat; (3) a rockslide-dammed lake formed and filled; in April 1841 local leaders issued

warnings of an impending breach to downstream locations; (4) most probably at the beginning of June 1841, the 300 m high dam was "liberated" and the impounded waters, nearly 65 km in length, were catastrophically released in a period of about 24 h; (5) the outburst flood devastated the Indus valley downstream of the blockage, sweeping away many villages, with "thousands of human beings and cattle"; at Chach, near Attock, a Sikh Army was overwhelmed by the waters of the Indus that suddenly rose 24 m; (6) during the blockage the Indus at Attock was easily fordable; in spite of this, and the warnings received, no notice was taken; and (7) the height of the flood wave at Attock is believed to have been approximately 13 m above the "normal high flood of summer".

We reviewed the original sources used by Mason (1929), and other earlier reports, to obtain further details as follows:

a)   *The timing of the blockage*: some uncertainty surrounds the precise timing of the blockage. However, Abbott (1848), Montgomerie (1860) and Drew (1875) remark upon the fact the Indus had been observed from December 1840 to be unusually low at Attock. Drew (1875) also reports an interview with a local man that put the date of the blockage in the late autumn of 1840.

b)   *The location and geometry of the 1840–1841 rockslide dam*: as Mason (1929) notes, there was much contemporary discussion on the location of the rockslide blockage (e.g. Falconer, 1841; Henderson, 1859). Based on reports by Becher (1859), Montgomerie (1860) and Drew (1875), Mason (1929) concluded that there is "not the slightest doubt that the dam was directly caused by a great fall of rock from the western spurs of Nanga Parbat" (p. 17).

c)   *The rockslide-dammed lake*: Mason (1929) reports that at its maximum extent the lake was 65 km in length. Drew (1875) reports that the lake extended far up valley and rose up to the level of Bawanji (Bunji) Fort, ca. 100 m above the level of adjacent Indus river level. This indicates a pool elevation of 1,335 m a.s.l. Drew (1875) also notes that the lake extended up the Gilgit valley to "where the Hunza

24

stream falls in". The elevation of this confluence is approximately 1,415 m a.s.l. We suggest that these historical observations bracket the actual maximum pool elevation of the 1841 rockslide dammed lake.

d)   *Timing of the breach*: Drew (1875) reports the breach as occurring in the beginning of June, "as near as I can make out". We take this estimate as being the most credible estimate of the timing of the breach suggesting that the rockslide dam may have existed for roughly 170 days.

e)   *Characteristics and effects of outburst flood*: the massive outburst flood devastated communities in the Indus valley (Becher, 1859). The flood suddenly appeared at Attock, 406 km downstream as an "overwhelming irrestible wall (a "bore") of discoloured waters" (Becher, 1859) and swept away at least 500 soldiers of a Sikh army encamped on the flood plain (Abbott, 1848). Witnesses describe a distant sound, similar to that of cannons or thunder before the river appeared as an "absolute wall of mud" (Abbot, 1848; p. 231). Vast agricultural areas of the Indus Plain were covered with sand deposited by the flood.

f)   *Extent of flood downstream of Attock*: Henderson (1859) reports that the 1841 flood was observable at least as far as Kalabagh (157 km downstream of Attock), a settlement on the Indus about 563 km downstream of the 1841 rockslide dam.

With respect to point b) above, even given this knowledge from earlier work, there has been disagreement in more recent literature on the precise location of the rockslide dam (cf Butler and Prior, 1988; Butler et al., 1988; Owen, 1989; Shroder, 1989; Shroder et al., 1989). However, a consensus appears to have emerged (e.g., Hewitt, 2009a) on the location of 1840–1841 rockslide dam, as being that initially suggested by Code and Sirhindi (1986) and Butler et al. (1988). Shroder (1998) describes the rockslide location in detail and we locate it at 35°30'36"N, 74°37' 22"E on the left bank of the Indus (Fig. 2.8).

As suggested above, historical observations bracket the maximum credible pool elevation as being between 1,335 and 1,415 m a.s.l. We also note that Code and Sirhindi (1986) in describing the effects of the Bunji slide give the approximate elevation of the town of Bunji as 1,387 m a.s.l.; this suggests an alternative credible minimum elevation and a range of 1,387 - 1,415 m a.s.l.

We examined satellite imagery of the site in conjunction with a SRTM-3 DEM, and together with the results of the review of the literature summarised above, we estimate the maximum pool elevation of the 1840–1841 Indus landslide-dammed lake to be a minimum of 1,390 m a.s.l. and a maximum of 1,400 m a.s.l. (cf. Code and Sirhindi, 1986). For a first approximation in this paper we take the most probable maximum pool elevation of the 1841 rockslide-dammed lake as 1,390 m a.s.l.

From the SRTM-3 DEM we calculate that an impoundment to the minimum pool elevation (1,390 m a.s.l.) formed a lake (Fig. 2.8) a maximum of 57 km in length, 88 km² in area with a volume of 6.5 Gm³. Our volume estimate is compared to that of Code and Sirhindi (1986) who obtained a volume of 4.6 Gm³ for a maximum pool elevation of 1,387 m a.s.l. and to that of 1.2 Gm³ estimated by Shroder et al. (1991).
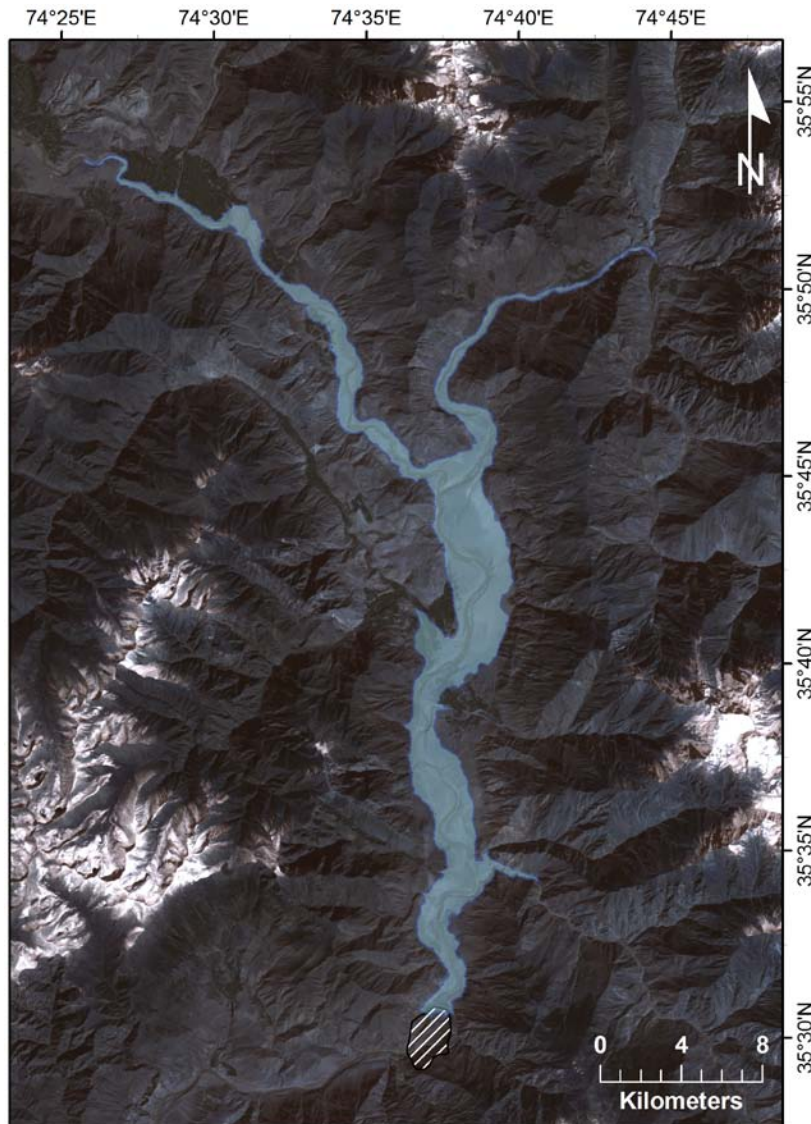
Figure 2.8: LANDSAT-7 image showing extent of rockslide-dammed lake (*light-blue fill*) that formed in 1841 in the Indus River, northern Pakistan as a result of a rockslide (*white hatched* pattern), 9 km upstream of Gor. The extent of the rockslide dammed lake (88 km² in area) is based on a SRTM-3 DEM and assumes a pool elevation of 1,390 m a.s.l. At this elevation the rockslide dammed lake has a calculated volume of 6.5 Gm³. The dam breached in June 1841 and the full impounded volume was catastrophically released causing a massive flood downstream (*The First Great Indus Flood* of Mason (1929)). The 1841 event was the largest documented outburst from a rockslide-dammed lake in historical time.

If our estimates of lake volume and duration are correct, the mean discharge of the Indus River into the lake over the 170 days of impoundment was 442 m^3/s for the most probable maximum pool elevation estimated above. This discharge is far below the mean streamflow estimates for the Indus for the months inferred for the blockage in the vicinity of the

27

rockslide dam reported by Code and Sirhindi (1986, p. 101). In addition, using the monthly mean instantaneous discharge data from Code and Sirhindi (1986) we calculate that for the 170 days of impoundment suggested by historical accounts, assuming that the Indus was totally blocked, that a lake of 9.7 Gm³ in volume would have been formed. This clearly is not the case given the geometry of the blocking landslide, the topography of the Indus valley in the area where it is known that the lake existed, and the fact that it is certain that the rockslide-dammed lake did not reach Gilgit and therefore did not exceed 1,415 m a.s.l. in water surface elevation. Both these discrepancies suggest a shorter duration for the existence of the 1841 rockslide dammed lake.

If we assume that Drew's account (Drew, 1873) of the date of the outburst flood at Attock is more or less correct, say June 5, then working back, and again using the mean streamflow data from Code and Sirhindi (1986) for the preceding months, we obtain a lifetime of about 65 days for the lake and the date of the damming event as around the end of March under conditions of comparatively low flow in the Indus. A hypothetical filling curve for this scenario is illustrated in Fig. 2.9 suggesting that failure took place after a sharp rise in lake level as a result of a summer-related increase in discharge. We note that the first warnings were sent downstream in April of 1841 by local leaders who had observed the filling landslide-dammed lake (e.g. Drew, 1875; Mason, 1929) and that Falconer's original letter, dated 6 July, stated that the rockslide dammed lake had existed for 4 months prior to its writing, suggesting a lake being formed in the previous March. For a lake volume of 6.5 Gm³, and a lifetime of about 65 days, the average discharge into the lake would be about 1,150 m³/s.
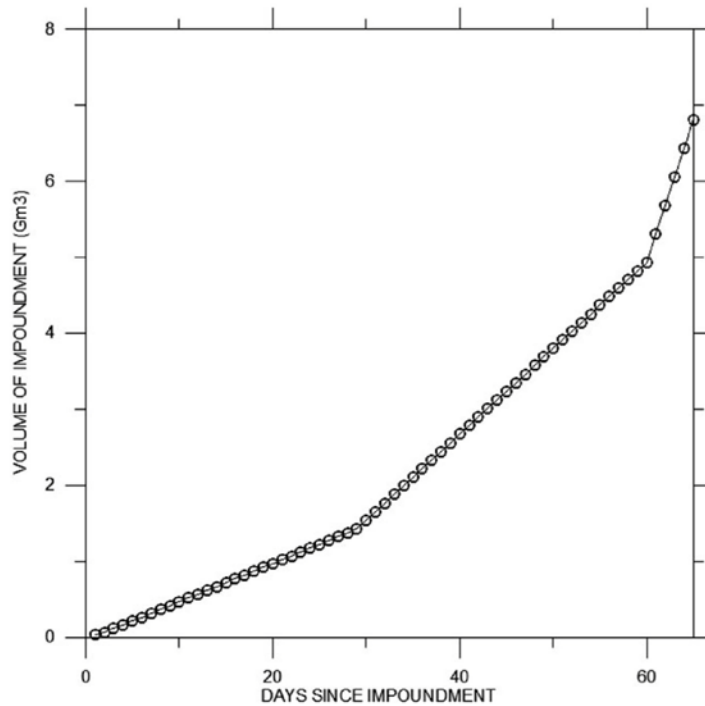
Figure 2.9: Hypothetical filling curve for 1841 rockslide-dammed lake on the Indus River, northern Pakistan. The rockslide dam is assumed to have breached on June 5 (based on Drew (1875)) with a volume of 6.5 Gm³ at a maximum pool elevation of 1,390 m a.s.l. The filling curve was derived by working backwards from that date using the discharge data of the Indus for a reach just downstream from the rockslide blockage (see Table 1 in Code and Sirhindi (1986)). It is assumed that the Indus was totally blocked by the rockslide.

Using the relationship developed by Evans (1986) a peak discharge of 114,334 m³/s is calculated for an outburst volume of 6.5 km³. Further, if we assume that the entire impoundment drained off in 24 h, an average breach discharge of 75,230 m³/s is obtained.

Hewitt (1968) has estimated the discharge of the 1841 outburst flood at Attock as 56,640 m³/s. The Indus River has been gauged at Attock since 1868 (Khan, 1969). Prior to the construction of the Tarbela Dam, the highest rainfall floods measured at Attock were in 1882 (22,087 m³/s) and 1929 (24,352 m³/s) whilst the highest snowmelt floods measured were in 1878 (21,634 m³/s) and 1924 (19,538 m³/s). These discharges compare to those of glacial outburst floods, originating in the Shyok River in 1926 and 1929 (19,482 m³/s). The volume of the 1929 flood obtained from the Attock hydrograph was 1.2 Gm³, corresponding to a maximum increase in stage of 8.7 m (Khan, 1969). If we assume that the base June discharge at Attock before the Tarbela Dam was built was around 6,000 m³/s, from the descriptions of

the flood stage in 1841we estimate the discharge of the flood at Attock to be roughly 38,000 m^3/s.

2.2.3.2 Historical Rockslide Dams II – 1858 Upper Hunza

The documentation of the outburst flood, that was observed at Attock on August 10, 1858 as a result of the breaching of a rockslide dam on the Hunza River is considerable, largely because the experience of the 1841 flood described above was very much on the mind of local people and officers of the British colonial forces present in Pakistan at the time. These early reports are summarised in the paper by Mason (1929) noted above.

In describing what he termed the "*Second Great Indus Flood* ", the following facts emerge from Mason's review, largely based on Henderson (1859) but augmented with important detail on the location of the blockage supplied by a Mr. H. Todd, the Political Agent at Gilgit: (1) the flood resulted from the secondary effect of a rockslide that dammed the Hunza River, a tributary of the Gilgit River, which in turn runs into the Indus at 450 km above Attock; (2) the rockslide (reported as the Ghammesar landslide) originated on the left (south) bank of the Hunza, 11 km above Altit and 1.6 km below Attabad (scene of the 2010 rockslide dam described below). The landslide reportedly resulted from the action of snow and rain in the winter of 1858; (3) a rockslide-dammed lake formed and filled and stretched back as far as Pasu, roughly 30 km upstream and where, according to the local Mir, a line of silt observed on the valley side marked the maximum lake level; local leaders issued warnings of an impending breach to downstream locations; (4) in August, the rockslide dam was breached and the impounded waters were catastrophically released; (5) the outburst flood caused damage in the Hunza and Indus, including the destruction of Nomal Fort, located about 23 km upstream of the Hunza/Gilgit confluence; (6) during the blockage no significant variation of the Indus stage at Attock was observed; (7) the rising of the flood wave at Attock was witnessed by Henderson (1859), who was in a rowboat on the river during the period of rising waters; the river began to rise at 6:00 a.m. on August 10, 1858 and eventually rose to a maximum level at 1:30 p.m. that day; and (8) as in 1841 the rising Indus waters flowed into

30

the Kabul River reversing its flow and flooding areas up to 48 km upstream from the confluence.

We reviewed the original sources used by Mason (1929), other earlier reports, and more recent literature to clarify details related to these points:

(a)   *The timing of the blockage*: as in 1841, some uncertainty surrounds the precise timing of the blockage. However, Henderson (1859) relates that the first news of the blockage reached Attock about the middle of July 1858. He refers to a July report that indicates the Hunza had been closed for 3 months, inferring that the blockage took place at the beginning of April, 1858. Dismissing this estimate, Henderson (1859) argues for the blockage to have taken place in the middle of May. Becher (1859) on the other hand suggests that the rockslide "dammed up the narrow bed of the river for 6 months", indicating a rockslide damming event in early February.

(b)   *The location and geometry of the 1858 rockslide dam*: as in 1841 there was much contemporary discussion on the location of the rockslide blockage (e.g. Drew, 1875; Henderson, 1859; Montgomerie, 1860). The report by Mr. Todd quoted in Mason (1929) above gives almost a precise location, which we estimate as 36°18' 16"N, 74°46'54"E (see also Shroder, 1989). At this location the bed of the Hunza is approximately 2,250 m a.s.l.

(c)   *The rockslide-dammed lake*: Reports that the lake reached Pasu are noted by Mason (1929). Thus the rockslide dam would have had a spillway elevation, and a maximum pool elevation, of at least 2,450 m a.s.l., 200 m above the bed of the Hunza at the site of damming rockslide. At this pool elevation the lake would extend roughly 30 km upstream. Based on the observations of Shroder (1998), an examination of satellite imagery and the SRTM-3 DEM, we estimate the maximum pool elevation of the 1858 Hunza landslide-dammed lake to be 2,450 m a.s.l. From the SRTM-3 DEM we calculate that this pool elevation formed a

lake 28 km long, 15.6 km² in area with a volume of approximately 805 Mm³ (Fig. 2.10).

(d)   *Timing of the breach and characteristics and effects of outburst flood*: the outburst flood reached Attock at around 6:00 a.m. on August 10, 1858. Montgomerie (1860) suggests that the flood passed Bunji, 118 km downstream of the rockslide dam, on August 9, at 9:00 or 10:00 a.m. This indicates an average velocity to Attock, 426 km downstream of roughly 5–6 m/s and the time of the breach as being early on August 9, 1858. The 1858 outburst flood destroyed many forts and villages and extensive areas of agricultural lands in the Hunza and Indus valley (Becher, 1859) but no major loss of life occurred. This was due to warnings given and the fact that the events of 1841 were still fresh in the memory of the local people (Becher, 1859; Henderson, 1859).

(e)   *Observations at Attock*: several writers published observations on the 1858 flood at Attock in the Journal of the Asiatic Society of Bengal. The behavior of the rising water was quite different than in 1841; instead of the arriving flood waters approximating a bore or a wall of mud and water (as in 1841) the 1858 flood was more like a rising wave that rose, peaked and passed. When the flood wave arrived the river was lower than normal; Henderson (1859) notes that "at first it came welling up quite rapidly, not less than 1 ft/min". Beginning at 6 am it rose to its peak of 17 m above the ordinary July-August flood level (Henderson, 1859). Henderson (1859) mentions substantial deposition of sediment in the bed of the Indus as reported by boatmen.

(f)   *Damage downstream of Attock*: Henderson (1859) reports 100 houses were demolished by the flood at Mokkad (Makhad), about 130 km downstream of Attock, where the river reached 3.5 m above annual flood level. Damage was also recorded at Marree (Mari) (154 km downstream; river level 2.5 m above the annual flood level) and at Kalabagh (157 km downstream of Attock), a settlement about 700 km downstream from the 1858 rockslide dam. According to Henderson (1859)

32

Kalabagh was also the limit of the 1841 flood, ca. 563 km downstream of the 1841 rockslide dam.

As noted above, we estimate the volume of the 1858 lake (Fig. 2.10) to be in the order of 805 Mm³. If we assume the Hunza was blocked completely during the impoundment, for blockages of 6, 4, and 3 months this impounded volume would be created by average discharges in the Hunza of 52, 78, and 106 m^3/s respectively. These discharges are significantly less than the values of the mean monthly instantaneous discharge of the Hunza for the possible months of the blockage reported by Archer (2003) at the Dainyor Bridge, 98 km downstream from the 1858 rockslide dam.
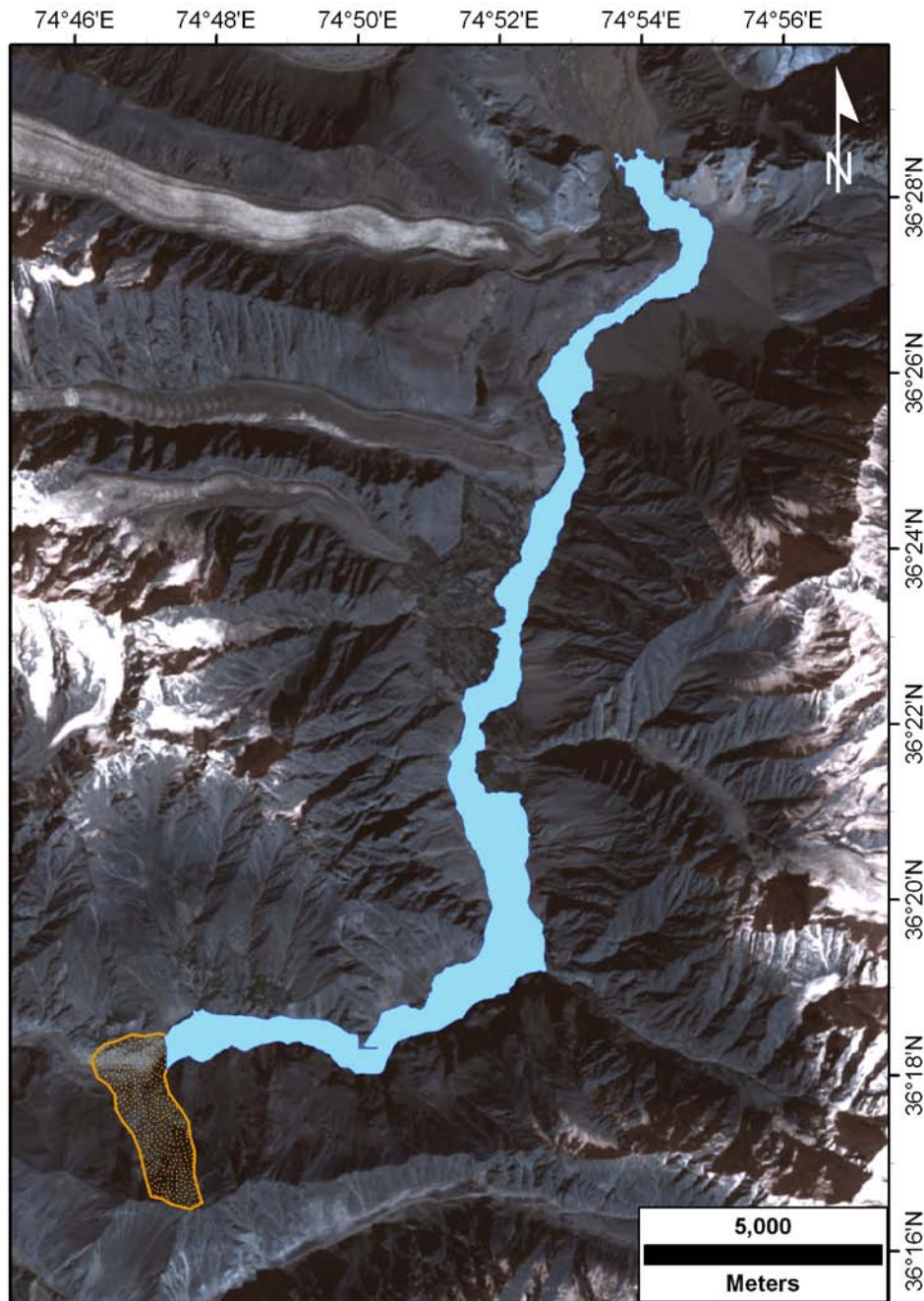
Figure 2.10: LANDSAT-7 image showing extent of 1858 Hunza rockslide-dammed lake (*light-blue fill*) impounded behind rockslide (*yellow stipple*). Lake extent is based on a maximum pool elevation of 2,450 m a.s.l. which was established in a SRTM-3 DEM. Volume of lake at this maximum pool elevation is calculated to be 805 Mm³.

Using the relationship developed by Evans (1986) a peak breach discharge of 37,792 m³/s is calculated for an outburst volume of 805 Mm³ in the 1858 Hunza event.

2.2.3.3 Historical Rockslide Dams III – 2010 Upper Hunza at Attabad

A second major rockslide (the Attabad rockslide) blocked the Hunza River (Kargel et al., 2010) at about 13:00 h on January 4, 2010 at a location (34°18'24"N, 74°49'17"E) (Figs. 2.1 and 2.11) only 2.5 km upstream of the 1858 blockage described above. In 2010 the rockslide originated on the north side of the Hunza valley and the volume of the debris is estimated to be in the order of 55 Mm³. The rockslide mobilised valley fill sediments from the valley floor of the Hunza that liquefied and travelled as a rapid mudflow over the valley floor up to a distance of 2.7 km downstream. Part of the mudflow debris swept up the valley side overwhelming part of a village downstream of Attabad, killing about 20 people (Fig. 2.1 & Fig 2.11). The rockslide blocked the Hunza River and a rockslide-dammed lake (Lake Gojal) immediately began to form upstream. The elevation of the Hunza River at the blockage site is estimated from our SRTM-3 DEM at 2,325 m a.s.l. The minimum height of the dam is estimated as ca. 125 m for an overflow crest elevation of about 2,450 m.a.s.l.

Figure 2.11: Aerial view of Attabad rockslide (est. vol. 55 Mm³) that blocked the Hunza River, northern Pakistan on January 4, 2010. Rockslide slid from right. Rockslide-dammed lake is filling behind the debris on January 17 (Day 13 of impoundment). View is downstream. [*Pamir Times* photograph].

As the waters of the lake rose they flooded several villages, large tracts of agricultural land adjacent to the Hunza, and 22 km of the Karakoram Highway linking Pakistan and China, disrupting road travel and commercial transport between the two countries (Fig. 2.12).

Figure 2.12: Aerial view of 2010 Hunza rockslide-dammed lake in northern Pakistan. At the time of the photograph (May 13, 2010; day 127 of impoundment) lake waters are still rising (pool el. 2,423 m a.s.l.), filling the Hunza Valley. View is upstream. Lake would rise another 12 m before overtopping on May 29, 2010 [*Pamir Times* photograph].

To achieve an eventual controlled overflow, Pakistani authorities began the excavation of a spillway over the debris on 29 January (day 25 of impoundment) completing it around May 15 (day 128). The excavation of the spillway lowered the effective crest of the dam by around 15 m, equivalent to a maximum possible pool height of 2,435 m a.s.l.

We remotely tracked and quantified the filling of the 2010 Hunza rockslide dammed lake by utilizing: (1) SRTM-3 digital terrain data; (2) multi-temporal satellite imagery; and (3) data published on the websites of the *Pamir Times* (http://pamirtimes.net/) and the National Disaster Management Authority (NDMA - http://www.ndma.gov.pk/) of Pakistan. As noted above, from the SRTM data we took the elevation of the valley floor at the site of the rockslide to be 2,325 m a.s.l. Taking this elevation as the local datum, i.e., a lake depth of 0.0

m, a filling curve for Lake Gojal was plotted (Fig. 2.13) based on the depth of the lake reported by the NDMA on their website from January 31 (day 27). To obtain the pool elevation in metres above sea level (Fig. 2.13) we added the reported depth of the lake to the elevation of the local datum as given above. We also tracked the development of the lake through multi-temporal satellite imagery obtained on 16 March (EO-1), 5, 22, and 25 May and 1 June (All ASTER images) (e.g. Fig. 2.14) as summarised in Kargel et al. (2010).
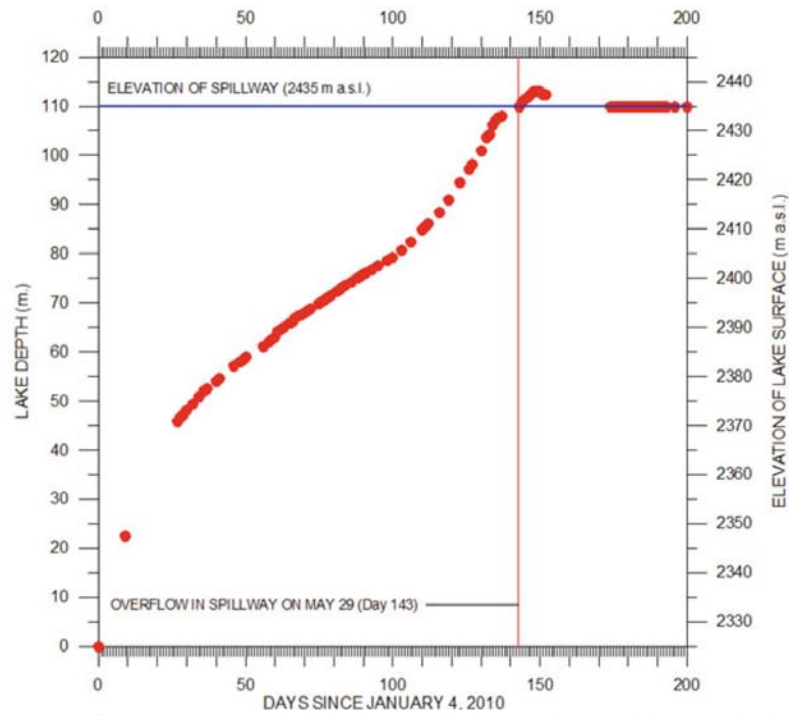
Figure 2.13: Filling curve of 2010 Hunza rockslide-dammed lake, northern Pakistan. Lake began to form on January 4, 2010 as a result of the river blocking Attabad rockslide and overtopped through an excavated spillway on May 29 (day 143). As of July 20, 2010, stable overflow continues as Pakistan authorties consider other drainage/partial drainage strategies (Data derived from the National Disaster Management Authority (NDMA) Pakistan).
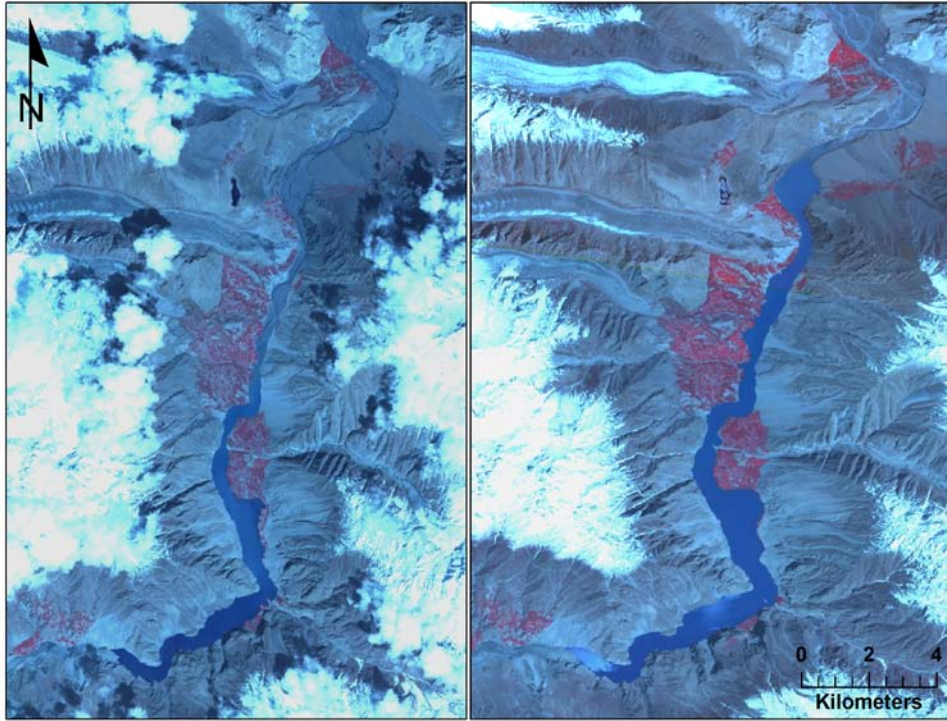
Figure 2.14: ASTER satellite images showing filling of 2010 Hunza rockslide-dammed lake between May 5 (*left*) and May 25 (*right*). Lake level on May 5 is 2,416 m a.s.l. and May 25 is 2,433 m a.s.l. The lake overtopped the rockslide dam on May 29 at a spillway elevation of 2,435 m a.s.l.

No large scale topographic maps were available to us. In addition to the calibration of the SRTM-3 DEM based on runway elevations mentioned in Section 2 above, we further checked the accuracy of the DEM by referring to news reports that indicated that the waters of the landslide dammed lake reached the piers of the Karakoram Highway Bridge across the Hunza River located at Gulmit, 10.5 km upstream of the rockslide dam on February 10 (day 37). The elevation of the bridge piers is estimated at 2,375 m a.s.l. which is within 1 m of the estimate of the lake level on that day from the NDMA data; the SRTM-3 DEM indicates that the lake volume on day 37 was 66.55 Mm³ at the pool elevation of 2,375 m a.s.l.

During filling, seepage began to appear in the downstream face on approximately March 5 (day 60) at a pool elevation of ca. 2,387 m a.s.l. Initial estimates of seepage were made on March 9 (day 64) and approximated 18,348 m^3/day. This seepage had increased to 40,367 m^3/day by March 17 (day 72). Seepage then appeared at various locations in the downstream face and discharge through the debris had notably increased. This resulted in the occurrence

38

of internal erosion within the rockslide debris and the formation of sink holes on the surface of the debris. Despite this evidence of substantial seepage forces the integrity of the rockslide remained intact and the lake level continued to rise until overtopping on May 29, through the excavated spillway.

The elevation at overtopping on 29 May (day 143) was estimated from the SRTM DEM to be 2,435 m a.s.l. At this maximum pool elevation the lake area was 9.74 km² and its volume was 430 Mm³. To verify our maximum pool elevation we superimposed the 2,435 m contour from the SRTM DEM on the ASTER June 1 image; the contour and the lake outline corresponded almost exactly.

After overtopping the lake level continued to rise a further 3 m (an equivalent additional volume of ca. 30 Mm³) in the five days up to June 3, since lake inflow exceeded lake outflow (Fig. 2.13). By 5 June, however, the lake level had stabilized (Fig. 2.13) as discharge in the spillway increased, and stable overtopping continued (Fig. 2.15). Photographs published by the *Pamir Times* after overtopping show the enlargement of the spillway, first by deepening through head-ward erosion from the lowest part of the spillway and then by widening through lateral undercutting and seepage erosion of the spillway walls.

Figure 2.15: View of overflow of 2010 Attabad rockslide dam and the Hunza rockslide-dammed lake in the background. Date of photograph is June 10, 2010 12 days after overtopping on May 29 (143 days after impoundment). Volume of lake is ca. 430 Mm³. Note limited erosion of spillway. Photograph by Focus Humanitarian Assistance, Pakistan.

Pakistani authorities have been active in mitigating the hazard at the rockslide dam and the risk to downstream communities. In addition to excavating the spillway over the debris to effect a controlled overtopping and to reduce the maximum volume of the lake, they have also been diligent in monitoring the lake, delimiting possible flood zones downstream, evacuating threatened areas, and installing a siren-based warning system in the event of a catastrophic breach being initiated.

As of July 25, 2010 (day 200 of impoundment) the Hunza rockslide-dammed lake continued its stable overflow of the spillway over the debris. Lake level has been more or less maintained at around 2,435 m a.s.l. as Pakistani authorities consider engineering strategies to lower the level of the lake thus alleviating the upstream flooding of large tracts of the Hunza Valley and the Karakoram Highway.

2.3 **Rockslide Dams in the Pamir Mountains (Tajikistan and Afghanistan)**

Rockslide-dammed lakes are widespread throughout the Pamirs of Tajikistan and Afghanistan (e.g. Ischuk, 2006). They include Yashilkul Lake, Lake Sarez, and Shiwa Lake. In addition the remnants of large rockslide debris masses that previously blocked surface drainage, comparable in geomorphic character and scale to those examples noted in the Himalayas of India and Pakistan, are evident on satellite imagery at many locations in the Pamir Mountains of Tajikistan and Afghanistan. These include the gigantic Pasor rock avalanche, Tajikistan (38°23'50"N, 73°34'33"E) that has previously blocked the upper Bartang River (Fig. 2.16), only 12 km north of the 1911 Usoi rockslide described below. However, no detailed field survey has been performed in the region.

Figure 2.16: *Google Earth* image of the gigantic Pasor rockslide (*A*) that has blocked the Bartang River (flowing from *right* to *left*) in the Pamirs of Tajikistan at 38°23'03"N, 72°34'49"E. The rockslide debris extends 2.72 km across the valley floor and has a volume in excess of 500 Mm³.

2.3.1 Rockslide Dams in the Gunt River Basin, Tajikistan

The Gunt River Basin drains the south west portion of Tajikistan and joins the Panj River at Khorog, just east of the Afghanistan border. A number of rockslide dams are noted in the Gunt River Basin including the giant Bedurth rockslide (37°31'27"N, 71°36'00"E) that blocked the Gunt River in prehistoric time before being breached. The deposits of the

rockslide are visible on satellite imagery, 7 km upstream from the city of Khorog. In addition several present-day lakes are dammed by substantial rockslide deposits within the Gunt River basin, for example Lake Rivakul (37°36'59"N, 72°03'48"E).

The largest rockslide-dammed lake in the Gunt River basin is Lake Yashilkul, located at 37°47'07"N, 72°44'47"E in southwestern Tajikistan; the lake was formed when a rock avalanche from the steep southern slope of the Gunt River valley blocked surface drainage to form the 20 km long rockslide dammed lake (Fig. 2.17).
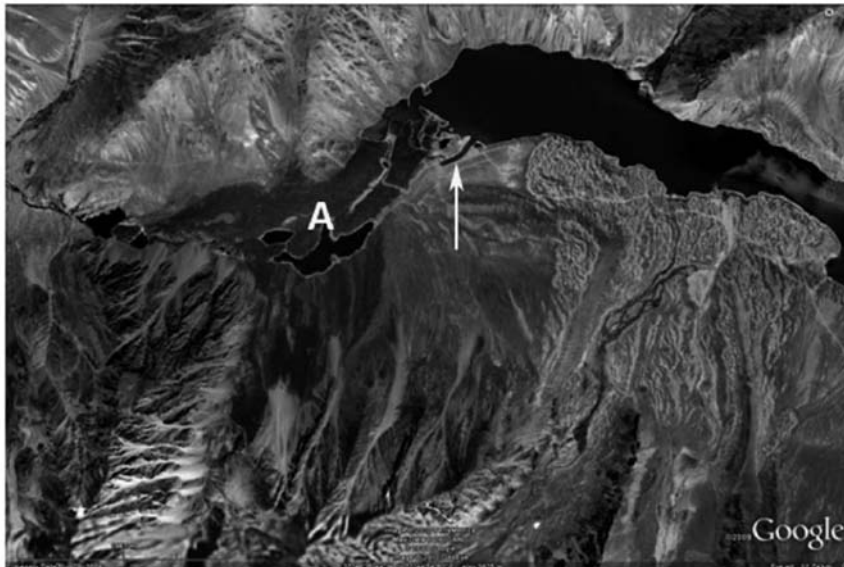
Figure 2.17: *Google Earth* image of Lake Yahilkul in the Pamir Mountains of Tajikistan (37°47'37"N, 72°45'06"E). The lake is formed by rock avalanche debris (A) which has been dated to ca. 4,400 yr. (Zech et al., 2005). Note spillway (*white arrow*) that forms part of civil engineering works to regulate lake level and outflow in Lake Yashilkul.

The rock avalanche has been studied by Zech et al. (2005) who used cosmogenic surface age dating to determine that the landslide occurred ca. 4,400 yr. In recent years an engineered retention structure and spillway have been constructed over the rockslide debris to regulate the lake level and winter outflow of Yashilkul Lake to, in turn, regulate flow in the Gunt River for downstream power generation at the 28 MW run-of-the-river Pamir 1 plant, at Khorog (ca. 130 km downstream), during periods of high winter electricity demand.

2.3.2 Shiwa Lake (Afghanistan)

In this study we identified Shiwa Lake, located in the Pamirs of northeast Afghanistan (37°23'37"N, 71°22'42"E), 20 km southwest of Khorog, as a rockslide-dammed lake (Fig. 2.18). The lake has a maximum length of 9.75 km and is 14 km² in area.
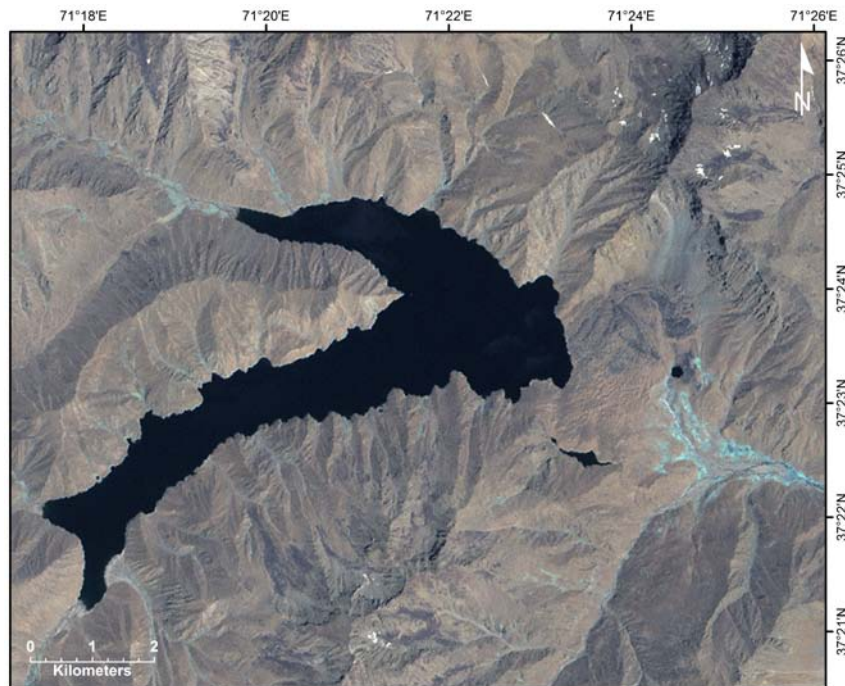
Figure 2.18: LANDSAT-7 image of Lake Shiwa, western Pamir Mountains, northeastern Afghanistan (37°23'37"N, 71°22'42"E). The valley blocking rockslide, of unknown age, is approximately 800 Mm³ in volume and the impounded Lake Shiwa has a surface area of 14 km².

The damming rockslide has an estimated volume of 800 Mm³ and is of unknown age. Shiwa Lake existed as early as 1921 since its presence was recorded by maps produced by the Surveyor-General of India. The rockslide dam is ca. 400 m high at its mid point (Fig. 2.19) and has a freeboard of about 80 m above the current pool height (ca. 3,142 m a.s.l.). Lake Shiwa (Shewa) was recently described by Shroder and Weihs (2010).
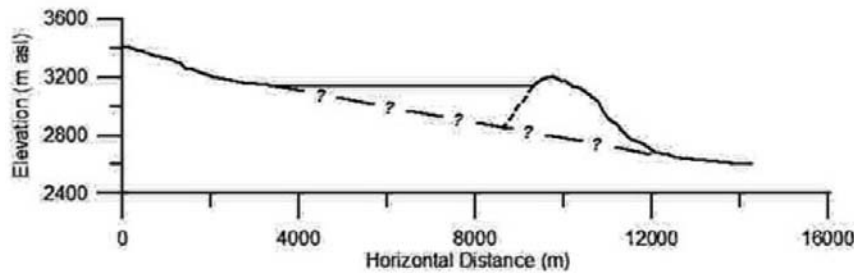
Figure 2.19: Longitudinal profile (vertical exaggeration = 4H) of rockslide-dammed Shiwa Lake, Afghanistan, based on SRTM-3 topographic data. Pool elevation of lake is 3,142 m a.s.l. Profile is through the southern arm of the lake (see Fig. 4.18).

2.3.3 1911 Usoi Rockslide and Lake Sarez (Tajikistan)

Lake Sarez was formed when the Bartang (Murgab) River was blocked by the gigantic Usoi rockslide (est. vol. 2 Gm³) triggered by the 18 February 1911 Pamir Earthquake (Preobrajensky, 1920; Shpilko, 1914; Stein, 1916; Stein, 1928). Although much has been published on the rockslide and rockslide-dammed Lake Sarez in the Russian language (see Stucky (2001)), only summary reports have been published in English (e.g. Gaziev, 1984; Schuster and Alford, 2004). The stability of the Usoi Dam and the potential outburst hazard that it represents has become of global scientific interest (Stone, 2009).

2.3.3.1 18 February 1911 Pamir Earthquake

Despite the fact that the Pamir Earthquake was recorded by seismographs around the world, some uncertainty still surrounds the location and magnitude of the earthquake. As discussed by Oldham (1923), Richter (1958) and Weichert et al. (1994) some initial reports tried to demonstrate that the enormous rockslide had generated the Pamir earthquake (Galitzin, 1915; Jeffreys, 1923; Klotz, 1915). An analysis of seismograms by Galitzin (1915) and Klotz (1915) showed the epicentre of the 1911 earthquake to be in close proximity to the landslide and it was thus argued that the gigantic landslide had generated the Pamir earthquake. In this argument, the epicentre of the earthquake was considered to be coincident with the location of the rockslide given by Shpilko (1914) as 38°16'N, 72°34'E. The idea that the Pamir earthquake had in fact been caused by the Usoi rockslide was first challenged by Oldham

44

(1923) followed by Macelwane (1926). By 1937, Jeffreys (1923) had reversed his opinion on the landslide origin of the February 1911 Pamir Earthquake.

Figure 2.20: LANDSAT-7 ETM+ image of Lake Sarez formed behind the blocking Usoi rockslide (diagonal pattern) emplaced during the 1911 Pamir earthquake. Epicentre (taken from Rautian and Leith (2002)), of the earthquake shown as black dot.

In a summary of Soviet earthquake catalogues, Rautian and Leith (2002) give the epicentre of the 1911 Pamir earthquake as 38.2°N, 72.8°E, at a distance of 19 km southeast from the rockslide dam (Fig. 2.20), in the vicinity of the former village of Sarez (Oldham, 1923). The focal depth is given as 26 ±5.2 km. Also in the Soviet catalogues (Rautian and Leith, 2002), the magnitude of the Pamir Earthquake (Ms) is given as 7.0 ±0.3; this compares to recalculated values of M7.3 by Abe and Noguchi (1983) and M7.2 by Pacheco and Sykes (1992). We note that the epicentre reported in Gutenberg and Richter (1954), Abe and Noguchi (1983) and Pacheco and Sykes (1992) is incorrect since the epicentre reported in these publications (40.0°N, 73.0°E) is 195 km north of Usoi in Kyrgyzstan.

The 1911 earthquake shook a large area of the Pamirs and other landslides occurred in the epicentral region (Oldham, 1923; Stein, 1916; Stein, 1928).

2.3.3.2 Usoi Rockslide

The geology of the source area is complex involving NNW steeply-dipping structurally-disturbed Paleozoic (Sarez Formation) and Mesozoic sediments cut by two major geological structures, the Usoi Thrust that steeply dips to the SE, and a second shear zone steeply dipping to the NW (Evans et al., 2006; Ischuk, 2006; Ischuk, 2011). Although the relationship between the geological structure of the source rock mass and the movement mechanism involved in the Usoi rockslide has not been ascertained in detail, the direction and morphology of movement is suggestive of a large scale-wedge failure. The wedge-failure generated a giant rockslide (Fig. 2.21) in which the debris underwent a limited vertical displacement (750 m – Preobrajensky, 1920) and in which large masses of the source rock mass remained intact during movement (Evans et al., 2006).
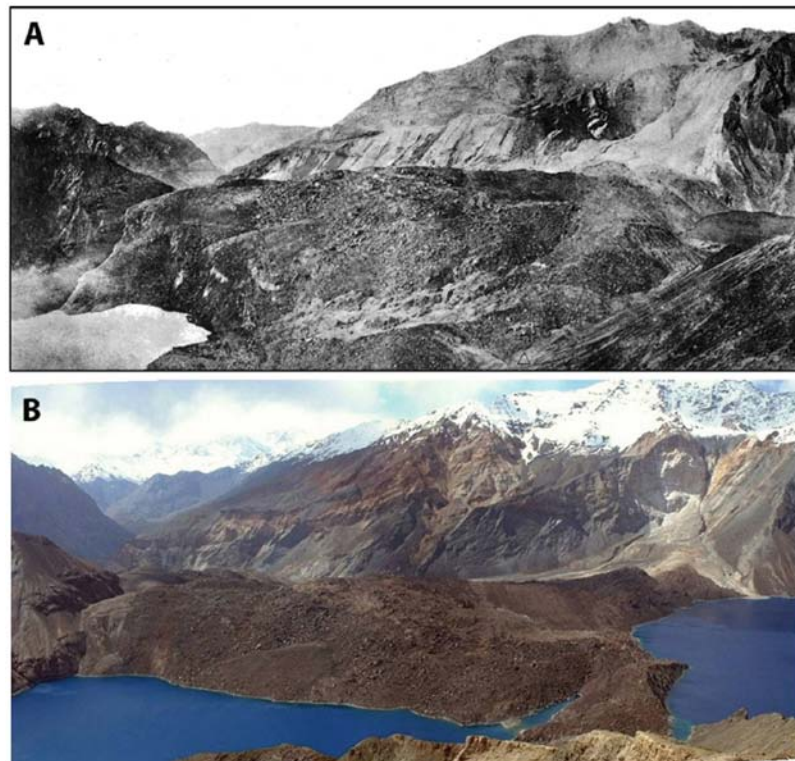
Figure 2.21: Views of 1911 Usoi rockslide dam. A – View of Usoi rockslide debris filling the Murgab (Bartang) valley damming the flow of the river. Note the waters of Lake Sarez filling the impoundment at lower right of photograph, and Lake Shadau filling at lower left. The photograph is reproduced from Preobrajensky (1920) and was taken in August 1915 when lake levels were ca. 3,100 m a.s.l. B – Photograph by A. Ischuk taken from a similar location in 2002 when lake levels were ca. 3,260 m a.s.l. In both photographs the source scar of the Usoi rockslide is seen at right.

The topography of the rockslide was instrumentally surveyed in August 1915 by Preobrajensky (1920) who also reconstructed the pre-rockslide topography of the site with the help of local Tajiks familiar with the pre-rockslide terrain. Using this topographic data he estimated the source volume of the rockslide as 2 Gm³ and the debris volume as 2.2 Gm³, which as discussed by Preobrajensky (1920), is equivalent to a 20% bulking factor due to fragmentation.

The rockslide debris fills the Murgab (Bartang) valley, covers an area of ca. 16 km² and forms the Usoi rockslide dam (Figs. 2.20, 2.21). The dam has a length along the thalweg of 7 km (Biedermann and Attewill, 2002), a maximum height of 740 m (3,490 m a.s.l.) above the Bartang river bed and a lowest crest elevation of 3,310 m a.s.l. (Raetzo, 2006; Stucky, 2001), 560 m above the base of the dam (2,750 m a.s.l.) at its upstream limit.

2.3.3.3 The Filling of Lake Sarez

Preobrajensky (1920) summarises the filling of Lake Sarez up to August 1915 when he carried out his survey of the rockslide debris (Fig. 4.21A). He reports the relative lake level elevations in sazhens, an old Russian unit of length equivalent to 7 ft or 2.1336 m (Gordin, 2003). We converted his measurements to metres to generate the initial part of the filling curve in Fig. 2.22 based on a datum elevation of 2,750 m a.s.l. The datum elevation is an estimate of the intersection of the rockslide debris surface with the pre-slide thalweg of the Bartang River based on a comparison of Preobranjenky's (1920) maps, information contained in Stucky (2001) and the Tajikistan 1:50,000 scale topographic map of Usoi/Lake Sarez.

The filling curve (Fig. 2.22) indicates rapid initial filling up to ca. 3,102 m a.s.l. in August 1915 (Gladkov et al., 1990). According to Shpilko (1914) and Preobrajensky (1920) it appears that the Usoi rockslide initially blocked the Bartang River completely. Seepage began to appear in the downstream face of the rockslide dam only in the Spring of 1914

(Preobrajensky, 1920) when the lake level reached el. 3,050 m a.s.l. (Fig. 2.22), taken as the maximum lake level with zero seepage (cf. Gladkov et al., 1990). In the autumn of 1914 water appeared in the Murgab River again, downstream of the rockslide dam (Ischuk, 2011). This corresponded to a lake elevation of about 3,080 m a.s.l. The village of Sarez, located ca. 20 km upstream of the dam, was inundated in the summer-fall of 1912.
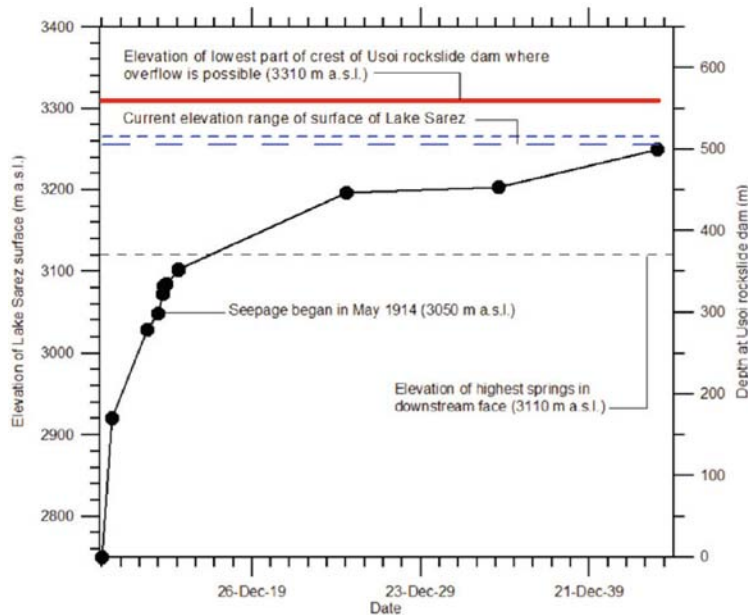
Figure 2.22: Filling curve for Lake Sarez from February 1911 to early 1944. Current elevation range of the lake surface is ca. 3,255 to 3,265 m.a.s.l. resulting in 55–45 m freeboard at the Usoi rockslide dam. Data summarised from Preobrajensky (1920) and Stucky (2001).

After the lake reached 3,102 m a.s.l. in August 1915, the filling rate decreased dramatically as outflow, through seepage through the dam, began to increase and approach inflow. For the period 1940–1991, the average inflow into Lake Sarez was ca. 45 m^3/s (Biedermann and Attewill, 2002); if we assume that this was the case in the early filling period, 6.55 Gm³ of water had accumulated behind the Usoi rockslide dam before steady seepage developed after August 1915. This is about 38% of the estimated current volume of Lake Sarez. The remainder of the volume (62%) of the lake accumulated under conditions of a decreasing rate of surface rise conditioned by increasing seepage as the more permeable upper parts of the Usoi rockslide dam were encountered.

48

Thus the filling curve (Fig. 2.22) indicates that Lake Sarez filled to its present level in three stages: (1) 1911–1914 – under conditions of total blockage up to about el. 3,050 m a.s.l.; (2) 1914 to 1944 in a decreasing rate of increase to its pre-present level (ca. 3,250 m a.s.l.) conditioned by increasing seepage through the Usoi dam to the point where outflow by seepage approached inflow; and (3) 1944 to the present where very gradual increase in lake level to a mean surface elevation of 3,260 m a.s.l. Today outflow roughly balances inflow (Biedermann and Attewill, 2002) and the level of Lake Sarez varies between 3,255 and 3,265 m a.s.l. (Fig. 2.22), resulting in a freeboard ranging between 45 and 55 m. One of the highest lake levels (3,270 m a.s.l.) was reached in 1994 with a minimum freeboard of 40 m, but according to Stone (2009) this was superseded in 2008 when the freeboard reached 38 m due to unprecedentedly high lake levels (3,272 m a.s.l.). The area of Lake Sarez as determined from Fig. 2.20 is 87 km² at a lake level of 3,264 m a.s.l.

The long term filling and the present change in the level of Lake Sarez is a function of the water balance of the lake, broadly inflow and outflow. Since there is no surface outflow over the debris dam all outflow occurs through the debris in subsurface pathways as seepage. Seepage is dependent on the permeability of the rockslide debris which may vary: (1) with time (e.g., consolidation of debris, filling of voids through sedimentation, enlarging of voids by seepage erosion); and (2) in the vertical direction from the base of the debris to its surface reflecting the structure of the rockslide debris. With respect to (1) it has been suggested that consolidation of the Usoi debris has resulted in a decrease in permeability, and thus a decrease in seepage over time (e.g. Gladkov et al., 1990). With respect to (2) the filling of the lake to the elevation without observed seepage (3,050 m a.s.l.) is an indication of an impermeable zone within the rockslide dam up to that point. Calculations by Gladkov et al. (1990), using the observed filling rate of Lake Sarez, indicate a marked increase in permeability above 3,140 m a.s.l. to a maximum in the surface carapace of the rockslide dam. It is noted that the highest spring in the downstream face of the Usoi dam is at 3,110 m a.s.l. (Fig. 2.22).

Data indicates that between 1949 and 1999 the level of Lake Sarez rose at about 18.5 cm/year, a rate which continues today. The small difference between outflow and inflow in which 98.7% of the inflow is converted into outflow apparently contributes to the increase in lake level (Stucky, 2001). The role of a possible long term increase in inflow (e.g., by melting glaciers in the Sarez watershed) or a long term decrease in the permeability of the Usoi barrier (e.g., consolidation or so-called "mud-clogging" of voids in the debris due to redistribution of finer material) remains uncertain (Stucky, 2001).

2.3.3.4 Lake Sarez Hazard Assessment

As summarised in Stucky (2001), there has been substantial and lengthy investigation of the possible outburst hazard at Lake Sarez and the effects of an outburst flood in the Murgab River downstream. This dates back to the original Russian scientific expeditions of Shpilko in 1913 and Preobrajensky in 1915. Concern has centred on the possibility of some form of catastrophic breaching resulting in the release of all or part of the impounded lake waters.

The hazard assessment has examined the possible modes of failure of the Usoi rockslide dam in five scenarios (Shuster and Alford, 2004; Stucky, 2001; Ischuk, 2011). These consist of: (1) slope instability in the downstream and upstream faces under static and/or dynamic conditions; (2) the potential of rockslide dam failure by piping (internal erosion); (3) breach induced by retrogression of present surface erosion in the downstream face into the body of the dam; (4) breaching caused by overtopping involving retrogressive erosion of an overflow channel when the lake level exceeds 3,310 m a.s.l.; and (5) breaching initiated by dynamic overtopping by a displacement wave generated by a landside into Lake Sarez from its shoreline with the lake at its approximate current level.

With respect to (1) a number of studies have shown that the stability of the upstream and downstream faces is high, due in part to their gentle slopes and the high shear strength of the debris. In (2) the analysis of piping potential indicates that the high hydraulic gradients necessary for piping do not exist in the Usoi Dam. In (3), the retrogression of surface erosion

at the head of the so-called "canyon" controlled by springs at about 3,110 m a.s.l. in the downstream face is also considered unlikely since the head-ward progression of the canyon would have to penetrate the blocky carapace of the debris on a low geomorphic gradient (Stucky, 2001). With respect to (4) it is considered to be very unlikely that Lake Sarez will overflow at 3,310 m a.s.l., since this would require an additional 3.2 Gm³ of water to be added to the lake without outflow taking place (Stucky, 2001). In the fifth scenario, the possible breaching initiated by an overtopping displacement wave generated by a large rapid rockslide from the shoreline of Lake Sarez has been investigated in detail. In particular, the stability of the Right Bank Landslide has been analysed and the slopes have been monitored (Droz et al., 2008; Droz and Spaasic-Gril, 2006; Risley et al., 2006). At this site (circle in Fig. 2.23), rocks of the Sarez Formation dip into the steep slope and evidence of slope movement observed is probably due to toppling with an unknown catastrophic potential.
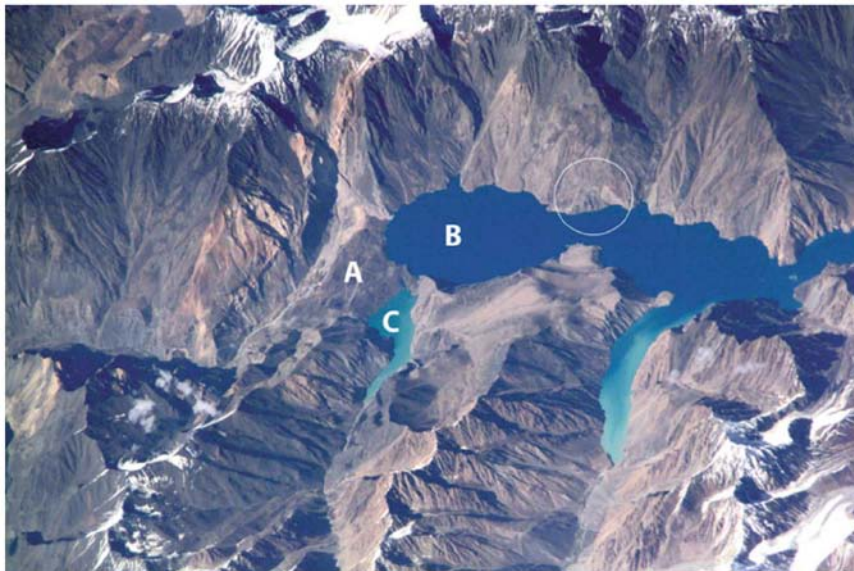
Figure 2.23: Usoi rockslide dam (A), Lake Sarez (B), and Lake Shadau (C) in an oblique photograph taken from the International Space Station in September 2001. The Right Bank landslide discussed in text is circled (NASA Photograph ISS002-E-7771).

The hazard assessment has led to the establishment of a monitoring and early warning system for Lake Sarez which became operational in 2004 (Droz et al., 2008; Droz and Spaasic-Gril, 2006). The early warning system would provide lead-time for evacuation of downstream

communities in the event of a flood wave being produced by a breach of the Usoi rockslide dam.

Finally, recent reports indicate a developing focus on the possibility of reducing the hazard at Lake Sarez by drawing down the lake level (Stone, 2009) by the excavation of a drainage tunnel in the left abutment of the Usoi rockslide dam. This drawdown could be up to 100 m (Stucky, 2001), which would have the effect of increasing the freeboard of the rockslide dam to as much as 140 m, and reducing the possible outburst volume.

2.4 **Conclusion**

The remains of rockslide dams are widespread in the river valleys of the northwest Himalayas (Pakistan and India) and the adjacent Pamir Mountains of Afghanistan and Tajikistan, Central Asia. The region contains in excess of two hundred known rockslide deposits of, as yet, unknown age that have interrupted surface drainage and previously dammed major rivers in the region in prehistoric time. Most of these dams have been breached and only remnant debris, and in some cases lacustrine deposits from formerly impounded lakes, are visible today in the deep valleys of the region. In addition, the region contains: (1) the highest rockslide dam (the 1911 Usoi rockslide, Tajikistan) in the world that dams the largest rockslide-dammed lake (Lake Sarez) on Earth (est. volume 17 Gm³); (2) the largest documented outburst flood (6.5 Gm³) associated with a historical rockslide dam outburst (the 1841 Indus Flood, Pakistan); and (3) the world's most recent (2010) rockslide-dammed lake emergency, the Attabad rockslide dam on the Hunza River, in the Upper Indus basin of northern Pakistan. In the Karakoram Himalaya, mapping of remnant rockslide deposits by K. Hewitt indicates a density of rockslides of about 50/10,000 km². This density is approximately 5 times that of the Alps (data in Abele, 1974). A critical step forward in the understanding of these mountain landscapes was the re-interpretation of rubbly debris and lacustrine deposits as, respectively, remnant rock avalanche debris and sediments deposited in rockslide-dammed lakes by M. Fort and coworkers and K. Hewitt between 1989 and 1999.

However, recent discussion of the genesis of the Satpara rockslide deposit indicates that the interpretation of rubbly valley fill deposits remains far from routine. We show that some prehistoric rockslide dams in the northwest Himalayas impounded massive lakes with volumes in excess of 20 Gm³, significantly larger than present-day Lake Sarez. Data on rockslide dams in the Pamir Mountains of Afghanistan and Tajikistan is also summarised from primary sources but further detailed mapping is necessary to define the regional landslide dam signature for the Pamirs.

We used SRTM-3 digital terrain data and satellite imagery to analyse four major historical rockslide damming events as follows: (1) our analysis of the 1841 Indus rockslide-damming event indicates that the volume of the impoundment and subsequent outburst was a minimum of 6.5 Gm³, the largest outburst from a rockslide-dammed lake in historical time; (2) the 1858 Hunza Valley rockslide dam impounded about 805 Mm³ before catastrophic outburst in August 1858; (3) the development of the 2010 Hunza rockslide-dammed lake is described in detail. It reached a maximum volume of 430 Mm³ before stable overflow of the rockslide debris began on May 29, 2010. This remains the situation as of July 25, 2010 (200 days after impoundment) as Pakistani authorities consider alternative mitigation strategies to lower the waters of the lake; and (4) the filling curve of Lake Sarez was developed from primary sources; it was conditioned by excessive outflow seepage through the debris to the extent that a freeboard of ca. 50 m is still naturally maintained without engineering intervention.

The emplacement of rockslide dams and the behaviour of their impounded lakes are critical hazards to communities and the development of infrastructure, including hydroelectric facilities, in the northwest Himalayas (India and Pakistan) and adjacent Pamir Mountains (Afghanistan and Tajikistan).

Chapter 3

A Remote Sensing Analysis of the 2010 Attabad Rockslide and its River Damming Effects, Karakoram Himalayas, Pakistan

Delaney, K.B. and Evans, S.G, for submission to Remote Sensing of the Environment

OVERVIEW: The remnants of rockslide dams are widespread in the incised river valleys of the northwest Himalayas (Pakistan and India) and the adjacent Pamir Mountains of Afghanistan and Tajikistan. In January 2010 a major rockslide (est. vol. 55 Mm^3) dammed the Hunza River and a rockslide-dammed lake (Lake Gojal) immediately began to form. The lake overtopped the rockslide dam 143 days later after the excavation of a spillway over the debris by Pakistan authorities; the lake has successively reduced in volume through the deepening and widening of the spillway, until on June 30, 2014 a remnant lake remains. Using SRTM-3 digital terrain data and seven high resolution satellite images from the period 2010-2014 we document the Attabad rockslide, track and quantify the development of rockslide-dammed Lake Gojal and calculate lake volumes at various stages of filling, stable overtopping, and partial draining. We introduce a method of delimiting lake shorelines by a pixel-by-pixel method and find that this technique results in very accurate estimates of shoreline elevation and corresponding lake volumes. We estimate the maximum volume reached by Lake Gojal shortly after overtopping to have been 432 ± 29.2 Mm^3. Using this data we evaluate the mitigation works carried out by Pakistan authorities and find that 1) they achieved a reduction of 33% in the maximum possible volume of Lake Gojal (without engineering intervention) and 2) that up to April 03, 2014 had achieved a 71% reduction in the volume at overtopping without catastrophic release taking place. Finally, we place the Attabad rockslide-dammed lake in the context of other natural dam impoundments in the Upper Indus and worldwide. The emplacement of rockslide dams and the behaviour of their impounded lakes are critical hazards to communities and the development of infrastructure, including hydroelectric facilities, in this region of Central Asia. We show that a combination of high-resolution optical satellite imagery and digital topographic data is very effective in producing key data on rockslide-dammed lakes for geomorphic and hydrological analysis and engineering mitigation.

3.1 Introduction

3.1.1 Background

Rockslide dams are created when debris generated by a mass movement of rock, in the form of a rockslide or a rock avalanche, blocks surface drainage (Evans et al., 2011; Fan et al., 2012). As a result of this blockage a rockslide-dammed lake may form, flooding valley floors

upstream from the dam; the rockslide-dammed lake may persist as a permanent element of the landscape, undergo stable draining over a period of time, fill up with sediment, or undergo catastrophic failure at some point in its lifetime generating a destructive outburst flood downstream (e.g. Evans, 1986; Costa and Schuster, 1988; Korup et al., 2010; Evans et al., 2011, Delaney and Evans, 2011; Fan et al., 2012). The formation and possible failure of rockslide dams is thus an important component of landslide hazard in mountainous terrain and plays an important role in mountain landscape evolution.

On January 4th 2010, without an apparent trigger, a massive rock slope failure (estimated volume 55 Mm³) at Attabad in northern Pakistan (36.31N / 74.81E) slid into the narrow valley of the Hunza River completely blocking its flow (Delaney and Evans, 2011). A rockslide dammed lake immediately began to form, flooding the Karakoram Highway (linking China and Pakistan) and villages and agricultural land in the Hunza valley (Fig. 3.1). We have applied the informal name of Lake Gojal to the rockslide-dammed lake (Fig. 3.1; Kargel et al., 2010; Delaney and Evans, 2011).

Figure 3.1: EO-1 satellite image obtained March 16th 2010 showing the Attabad rockslide and debris dam (inset) and the extent of rockslide-dammed Lake Gojal 72 days after impoundment.

In this paper we utilize geographical information systems (GIS) and remotely-sensed data to 1) quantify the geometrics of the 2010 Attabad rockslide and subsequent natural debris dam, 2) measure the filling and partial drainage of Lake Gojal (viz. water surface elevation, lake area and volume), 3) evaluate the utility of remote sensing data and techniques in characterising the development and behaviour of a rockslide-dammed lake, 4) quantify the impact of Pakistan's rockslide-dammed lake mitigation attempts, and 5) examine comparative historical rockslide-dammed impoundments in the Upper Indus and worldwide.

56

3.1.2 Rockslide Dams in the northwest Himalayas and Adjacent Areas

Previous studies have identified large numbers of rockslide deposits in the Pamir and Himalaya mountain regions of Central Asia (Fig. 3.2), some of which have impounded surface waters forming significant rockslide-dammed lakes in both prehistorical and more recent historical time (Hewitt, 1968; 1982; 1998; 1999; 2001; 2006a; 2006c; 2008; 2009a; 2011; Korup et al., 2010; Delaney and Evans, 2011). Factors involved in this high frequency of rockslide dams include deep narrow valleys resulting from the incision of high mountain topography that provide a valley geometry favourable for damming, a high incidence of massive rock slope failure, and active collisional tectonics resulting in frequent major earthquakes and high rates of uplift (cf. Ouimet et al., 2007).

The massive Usoi rockslide dam in the Pamirs of Tajikistan (Fig. 3.2), which impounds the largest rockslide-dammed lake on Earth, Lake Sarez (87 km², ca. 17 Gm³) (Ischuk, 2006; Evans et al., 2011; Delaney and Evans, 2011) is also located in the region (Fig. 3.2). Further, as noted below, the largest documented outburst flood from a natural dam failure occurred in the Indus basin in 1841 (Mason, 1929; Delaney and Evans, 2011; Fig. 3.2) as a result of the catastrophic breach of a rockslide dam.
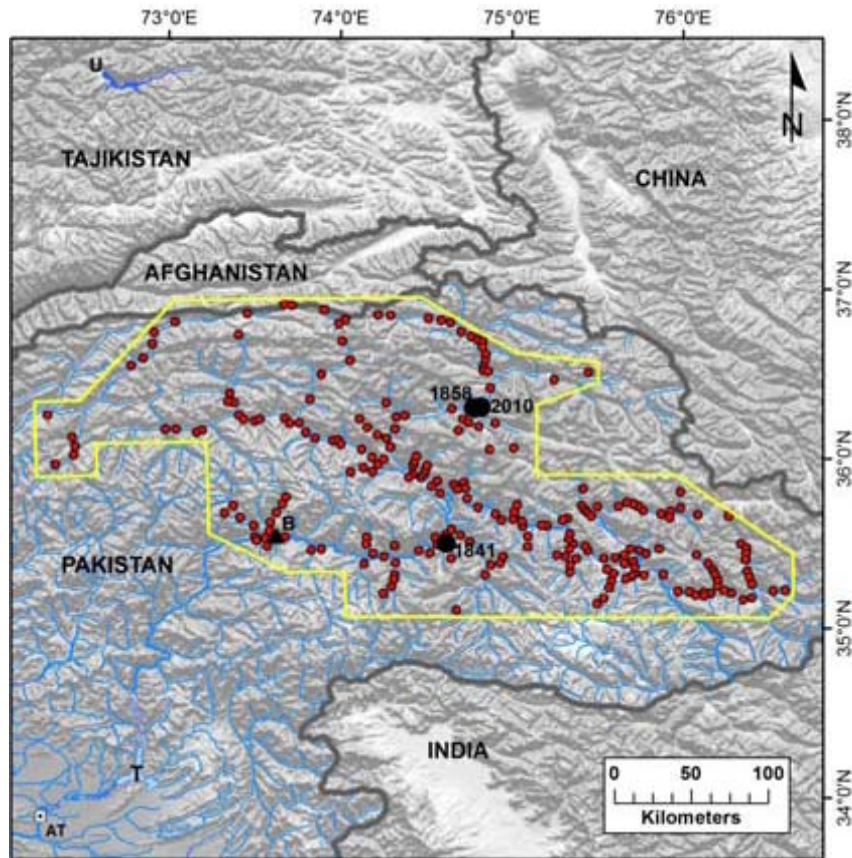
Figure 3.2: Map of northwest Himalayas and adjacent Pamir Mountains showing location of Attabad rockslide (black circle 2010), other rockslides mapped by Hewitt and others (red circles within yellow line; see text for references), rockslide dams on the Indus and Hunza discussed in text (black circles with dates) and other locations discussed in text (AT - Attock; B - Daimer-Basha Dam; T - Tarbela Reservoir), U - Usoi rockslide dam).

3.2 **Digital Topography**

3.2.1 Digital Topographic Datasets

The use of digital elevation models (DEMs) to quantify the geometrics of catastrophic landslides, landslide-dammed lakes, other types of lakes formed by natural dams, and artificial reservoirs has emerged as a vital tool in the study of earth surface and hydrological processes (e.g. Wang et al., 2005; Fujita et al., 2008; Evans et al., 2007, 2009a, 2009b, 2009c; Smith and Pavelsky, 2009; Delaney and Evans, 2011; Fan et al., 2012; Suwandana et al., 2012; Duan and Bastiaanssen, 2013; Pan et al., 2013; Wang et al., 2013). These data can

be used to define topographic surfaces, water surface elevations, and to calculate 2D (area) and 3D (volume) values of geomorphic and hydrologic events.

As of June 2014, there are two sources of global scale GIS-compatible digital topographic data: the NASA funded Shuttle Radar Topographic Mission (SRTM) DEM, and the Advanced Spacebourne Thermal Emission and Reflection Radiometer (ASTER) GDEM2, created by the Japanese Ministry of Economy Trade and Industry.

The SRTM DEM was completed on an 11-day Shuttle mission during Feburary 2000, creating two distinct datasets: SRTM-1 (1 arc second), a 30 m horizontal resolution dataset covering the continental United States; and the SRTM-3 (3 arc second), a 90 m horizontal resolution dataset representing the global land surface between 60°N and 56°S (Farr et al, 2007). The SRTM-3 v.4 dataset for this study was obtained from the CGIAR Consortium for Spatial Information (http://srtm.csi.cgiar.org/).

The ASTER GDEM1 was originally released in June 2009; however it was shown to have a global bias of -5 m, and many unexplained elevation artifacts (i.e. drastic unaccountable variations in elevation over short distances) (e.g. Fujita et al., 2008; Bolten and Waldoff, 2010; Wang et al., 2011; Suwandana et al., 2012). A later release in October 2011 (ASTER GDEM2) removed the -5 m bias, as well as adding an improved water mask, higher horizontal accuracy, and a reduction (but not total elimination) of most of the unexplained artifacts. This newer version (hereafter referred to as GDEM2) also improved the global vertical accuracy by 3 m from approximately 20 m to 17 m (Meyer et al., 2011). The GDEM2 dataset was created from over 1.3 million ASTER VNIR stereo-pairs, covering the global surface from 83°N to 83°S, in the form of 1° x 1° DEM tiles with a 30 m horizontal resolution (Meyer et al., 2011). If cloud-free stereo-pairs were not available, the voids were manually filled with alternate datasets, such as SRTM, national elevation datasets, or provincial/state datasets (Meyer et al., 2011). The ASTER GDEM2 dataset was obtained from the Japan Space Systems website (http://gdem.ersdac.jspacesystems.or.jp/).

3.2.2 Assessment of Error in Digital Topographic Data I – Vertical Elevation of Topography

Farr and Kobrick (2000) estimated the maximum vertical error of the SRTM dataset to be approximately 15 m globally, but expect variations of the elevation error dependant on the exact location, topography, and the combination of slope angle and aspect. Rodriguez et al. (2006) calculated a global error between 5 m and 14 m, and Becek (2008) in his analysis of international airport runway elevations, calculated an error between -5 m and 4 m. Farr et al. (2007) also analyzed vertical errors for specific regions of the Earth; for Eurasia, they determined an average error between 6 m and 8m, and in mountainous regions of northern Pakistan, they assert that the average vertical error in elevation varies between 10 m and 15 m.

Bolton and Waldoff (2011) analyzed the ASTER GDEM2 dataset and calculated a RMSE value of 8.02 m. Wang et al. (2011) found a RMSE value of 12.5 m, and the ASTER GDEM2 validation team calculated and RMSE of 8.68 m (Meyer et al., 2011). Meyer et al. (2011) also categorized errors from individual regions using ICESat elevation data as their baseline. They found that the average RMSE over Eurasia to be between 10.38 m and 11.87 m. Meyer et al. (2011) also calculated a general error for mountainous regions in Japan as 15.1 m.

To assess the vertical accuracy of SRTM and GDEM2 elevation data, we followed the methodology of Becek (2008) by comparing the elevation of both ends of three runways in the Upper Indus with the official aeronautical data for civil aviation (Table 3-1). The runways are at Gilgit (62 km to the southwest of Attabad (35°55"07'N, 74°20"02'E)) and Skardu (125 km to the southeast (35°20"14'N, 75°32"01'E)); runway elevation data is listed in the World Aeronautical Database (http://worldaerodata.com/). For the SRTM dataset the vertical difference is ± 3 m over all the runways, with a RMSE of 0.0 m for Gilgit, and 1.0 m and 2.2 m for Skardu (Table 3-1). The GDEM2 had a much higher absolute vertical

difference of ± 19 m for all the runways, with a RMSE of 4.5 m for Gilgit, and 17.5 m and 15.9 m for Skardu (Table 3-1).

Table 3-1: Actual vertical elevation of runways in the Attabad region (data from World Aeronautical Database (http://worldaerodata.com/) compared to vertical elevation as measured in SRTM and GDEM2 DEMs. RMSE for both DEMs is also reported.

Airport	Runway #	Elev. (m a.s.l.)	SRTM (m a.s.l.)	RMSE (m a.s.l.)	GDEM2 (m a.s.l.)	RMSE (m a.s.l.)
Gilgit	07	1461	1461	0.0	1457	4.5
	25	1462	1462		1467	
Skardu #1	15	2227	2226	1.0	2210	17.5
	33	2230	2229		2212	
Skardu #2	14	2212	2209	2.2	2200	15.9
	32	2225	2226		2206	

3.2.3 Assessment of Error in Digital Topography Data II – Area and Volume of River Impoundments

To assess the accuracy of the two DEMs for estimating the volumes of rockslide-dammed lakes in the Upper Indus, we compared the engineered volume of the proposed Diamer-Basha dam reservoir (Fig. 3.2) as calculated by the Water and Power Development Authority of Pakistan (WAPDA), with the volume of the reservoir calculated from the SRTM and GDEM2 digital topographic data. The 272 m-high Diamer-Basha dam will be constructed on the Indus River (Site A of Code and Sirhindi, 1986) about 95 km downstream from the 1841 Indus-damming rockslide (Delaney and Evans, 2011; Fig. 3.2) described below, and 245 km downstream from Attabad. The dam will form an artificial reservoir to a maximum pool elevation of 1,160 m a.s.l., with a maximum storage capacity of 10 Gm³ and an area of 110 km² (data obtained from http://www.wapda.gov.pk).

Taking the maximum pool elevation to be 1,160 m a.s.l. and using the SRTM digital topography as the ground surface of the flooded upstream region of the Indus valley, we calculated the total volume of the reservoir to be 10.7 Gm³ with an area of 109.5 km², a difference of +6.5% and -0.5%, respectively. Using the ASTER GDEM2 topography at the maximum pool elevation, we calculated a total volume of the reservoir to be 11.3 Gm³ with an area of 120.5 km², a difference of +13% and +9.5%, respectively, from the engineered design specifications.

The results of this assessment leads us to conclude that 1) SRTM 3-arcsecond (90m x 90m) digital data can provide satisfactory first-order topographic characterisation of valley terrain in the Upper Indus, 2) SRTM digital terrain data is far more accurate than the GDEM2 data in determining elevation of topographic surfaces in the Upper Indus; this is despite the fact that GDEM-2 has a higher horizontal resolution, and 3) the SRTM data is superior in providing accurate first-order areas and volumes of impounded water bodies in the region.

3.3 The 2010 Attabad Rockslide and River Damming Event

3.3.1 The January 2010 Rockslide

On January 4th 2010 a massive rock slope failure occurred at Attabad (36.31N / 74.81E) and slid into the Hunza River valley (Figs. 3.1 and 3.3). The volume of the debris is estimated to be in the order of 55 Mm³ (Delaney and Evans, 2011; Ekström and Stark, 2013); Petley et al. (2010) and Schneider et al., (2013) give a slightly lower volume (45 Mm³). Some eyewitness accounts noted that the total rock mass volume consisted of one large, and several additional smaller mass movements (Petley, 2011; Iqbal et al., 2014). The 2010 rockslide took place only 2.5 km upstream of the 1858 valley-blocking rockslide described below (Figs 3.1, 3.2, 3.3).

Figure 3.3: Aerial view of the Attabad rockslide (looking downstream) on January 17 2010 (day 13). Note characteristics of natural debris dam that blocked the Hunza River forming Lake Gojal, filling in lower foreground [photograph from *The Pamir Times*].

The rock mass impacted the valley floor and liquefied fluvial and lake sediments in the valley bottom generating destructive mudflows that travelled both upstream and downstream. Liquefied valley bottom sediments rose up the opposite valley side and flowed backwards across the deposit surface, covering the fragmented rock debris with a fine-grained muddy slurry. A second mud flow ran almost 3 kilometres downstream to Sarat, where it resulted in the deaths of 19 people (Petley et al., 2010; Petley, 2011; Schneider et al., 2013; Iqbal et al., 2014).

The highest elevation of the sliding mass on the source slope was 3,004 m a.s.l., and the total horizontal travel distance in a SSW direction was 1,390 m. The horizontal movement was constrained by the opposite valley wall, which resulted in a thicker rockslide deposit, and therefore a larger dam, than an otherwise unconstrained flow (Fig. 3.4). Using the SRTM DEM, we calculated the height of the drop as 679 m (H), which gives a H/L = 0.488 and a *fahrböschung* ($\tan^{-1}$ H/L) of 26°.

The geology of the source region of the Attabad rockslide consists of two lithologic units separated by a major (NW-SE) thrust fault associated within the Main Karakoram Thrust zone (Searle, 1991). The younger unit (Red fill in Fig. 3.4), at the northern limit (upper part) of the rockslide source area, is the Hunza pluton. This rock type consists mainly of granodiorites, containing plagioclase, quartz, biotitie, hornblende, and potassium feldspar, in concentrations ranging from granite to diorite (Searle, 1991). Le Fort et al. (1983) estimated the age of this rock formation as 95 ± 5 Ma.
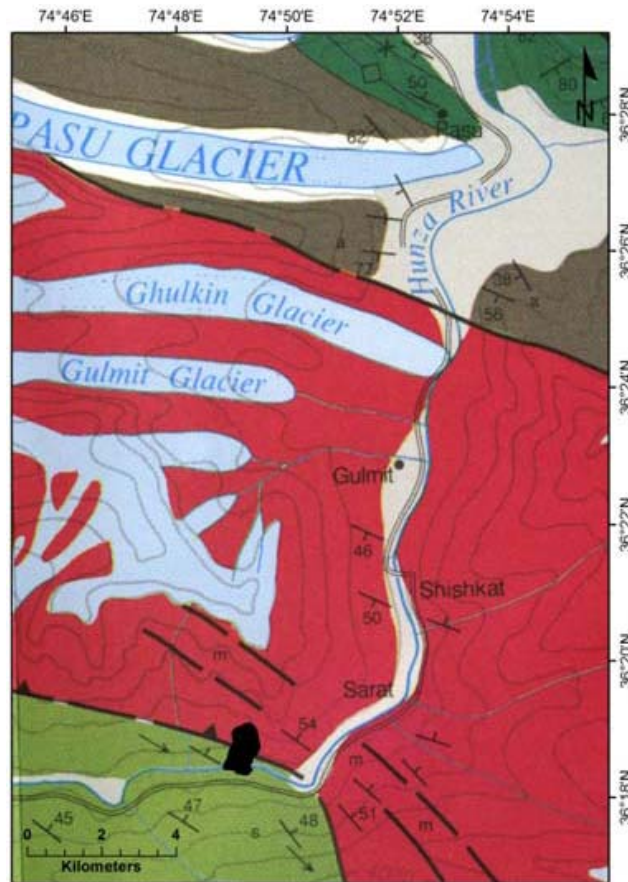
Figure 3.4: Geology of the Attabad region, northern Pakistan. The rockslide is shown (black polygon) overlapping the 2 main geologic formations (Red: Hunza Plutonic Unit; Light Green: Dumordu Unit) and a thrust fault (*modified* from Searle, 1991).

The older rock formation, which underlies the lower part of the rockslide source zone is the Dumordu Metasedimentary Unit (Light Green fill in Fig. 3.4). This unit consists mainly of meta-sedimentary marble, with minor amounts of interbedded amphibolities, pelites, orthoquartzites, and conglomerates (Searle, 1991). Notably, the foliations in the Dumordu meta-sedimentary marbles are dipping 45° to 50° to the NNE, almost directly opposite to the movement direction of the Attabad rockslide (Fig. 3.4). However, the site and sliding direction of the rockslide (SW) coincides with the presence and dip of a collision-related thrust fault (Fig. 3.4) that places the older Dumordu meta-sedimentary unit above the Hunza Pluton.

64

According to eye-witnesses, several large cracks had appeared in the rockslope that underwent failure in 2010 at elevations just above the village of Attabad following seismic activity in 2002 (Petley, 2011; Iqbal et al., 2014). These cracks became larger (both laterally along the slope and by depth) and more widespread between their initial discovery in 2002 and the failure of the rock slope in 2010 (Petley, 2011; Iqbal et al., 2014).

3.3.2 The Attabad Rockslide Dam

As noted above, the rockslide blocked the Hunza River completely (Fig. 3.3; Delaney and Evans, 2011) and a rockslide-dammed lake immediately began to form upstream (Figs. 3.1, 3.3, 3.5). The elevation of the Hunza River at the blockage site is estimated from our SRTM-3 DEM at 2,325 m a.s.l. The minimum height of the dam was estimated as ca. 125 m (e.g. Schneider et al., 2013) for a maximum overflow crest elevation, prior to excavation of the spillway over the debris, of about 2,450 m a.s.l.

Survey work by National Engineering Services of Pakistan (NESPAK) (2014) determined that the elevation of the river valley at the upstream margin of the rockslide dam at the Hunza River is 2,322 m a.s.l. This elevation is based on the Survey of Pakistan benchmark surveyed in from Sikandrabad, 40 km downstream from the Attabad rockslide, and corresponds to a local datum with a lake depth of zero (Khali Ahmad Ghauri (WAPDA) personal communication, June, 24, 2014). It is noted that this local datum is only 3 metres lower than that we obtained from the SRTM DEM (2,325 m a.s.l.) as discussed above. We also note that the former datum used by the Frontier Works Organisation (FWO) and reported in earlier work on the rockslide dam and impoundment (e.g., Iqbal et al., 2014) was 31.014 m lower than the Survey of Pakistan value, i.e., 2,291 m a.s.l. (Khali Ahmad Ghauri (WAPDA) personal communication, June, 24, 2014). For our work summarised below we retained the SRTM-3 determined datum for consistency within the SRTM DEM.

As the waters of the lake rose they flooded several villages, large tracts of agricultural land

adjacent to the Hunza River, and about 22 km of the Karakoram Highway linking Pakistan and China disrupting road travel and commercial transport between the two countries (Figures 3.1, 3.2, 3.5, 3.11; Petley et al., 2010; Cook and Butz, 2013; Shah et al., 2013; Schneider et al., 2013).

Pakistan authorities were immediately active in mitigating the hazard at the rockslide dam and the risk to up and downstream communities. In addition to excavating a spillway over the debris both to effect a controlled overtopping and to reduce the maximum volume of the lake, they actively monitored the lake, delimited possible flood zones downstream, evacuated threatened areas, and installed a siren-based warning system for use in the event of a catastrophic breach being initiated.
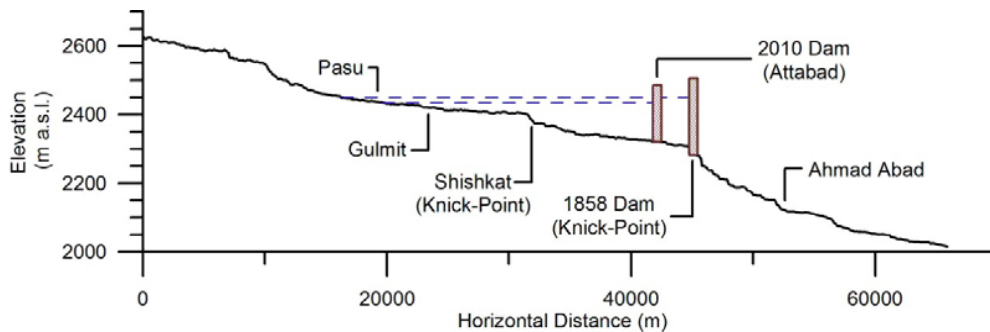
Figure 3.5: Topographic profile generated from the SRTM dataset. Both the 2010 and 1858 debris dams and resulting reservoirs are shown for comparison. Note that several knick-points are visible in the profile, suggesting similar historic events have occurred in the Hunza valley.

3.3.3 The 1858 Rockslide Dam on the Hunza River

The 2010 rockslide occurred just upstream from a previous rockslide dam on the Hunza River that blocked the river in the winter-spring of 1858 (Mason, 1929; Fig. 3.5, 3.17). The breaching and outburst of this impoundment in August 1858 created the "*Second Great Indus Flood*" of Mason (1929). The rockslide (reported as the Ghammesar landslide) originated on the left (southern) bank of the Hunza, 11 km above Altit and about 2.5 km below the 2010 Attabad rockslide dam. A rockslide-dammed lake formed and filled, and stretched roughly 30 km upstream as far as Pasu. In August 1858, as discussed in more detail below, the rockslide

66

dam was breached and the impounded waters were catastrophically released (see detailed summary in Delaney and Evans, 2011).

3.4 **The Development of Lake Gojal – Remote Sensing Methodology**

3.4.1 Data Utilised

In order to quantify the filling, overtopping, and subsequent partial draining of Lake Gojal, we utilised: 1) SRTM and GDEM2 digital terrain data described above; 2) multi-temporal satellite imagery of the Hunza valley - seven images from 2010-2104 as detailed below; 3) lake filling information and data published on three internet websites as follows: a Pakistani news website *The Pamir Times* (http://pamirtimes.net/) - mainly qualitative descriptions and photographs of the filling and partial draining of Lake Gojal; the National Disaster Management Authority (NDMA; http://www.ndma.gov.pk/) - measurements of lake depth as filling proceeded to overtopping (no data was published after July 30, 2010 once overtopping was stabilised); 4) reports from the National Engineering Services of Pakistan (NESPAK; http://www.nespak.com.pk/) - bathymetric survey data on lake surface elevation and valley bottom topography in July 2011; and 5) and data directly supplied by WAPDA (Khalil Ahmad Ghauri, personal communication, June 24, 2014).

No large scale (>1:250,000) topographic maps were available for the study region, and no fieldwork was undertaken at Attabad.

3.4.2 Optical Satellite Imagery

We utilized seven images from three satellite platforms for optical data: LANDSAT8 OLI, EO-1 ALI, and ASTER. These satellite platforms all have sufficient temporal resolution and archived data to accurately show the growth and shrinkage of Lake Gojal from the initial rockslide in 2010 to its status in 2014. The seven images were accessed from the United States Geological Survey (USGS) Earth Resources Observation and Science Center (EROS) Global Visualization Viewer (GloVis: http://glovis.usgs.gov/).

The LANDSAT8 OLI imagery (May 18, 2013 and April 3, 2014) has a panchromatic horizontal resolution of 15 m, covering an area of 183 km x 190 km, and utilizing a possible 11 spectral bands (USGS, 2013). The ASTER imagery (May 2, May 25, and June 1, 2010) has a (non-panchromatic) spatial resolution of 15 m, covering an area of 60 km x 60 km, and gathers data across 14 spectral bands (NASA, 2004). The EO-1 imagery (March 16, 2010 and August 4, 2011) has the highest panchromatic horizontal resolution of 10m, with an elongated image area of 36 km x 82 km, and 8 spectral bands for analysis (USGS, 2011).

The DEMs and optical images were processed and analyzed in ESRI ArcGIS 10.2. This includes mosaics of DEM tiles, combining various spectral bands for optical analysis and exporting of digital topographic data for process analysis.

3.4.3 Lake Gojal I – The Filling of the Rockslide Dammed Lake (First-Order DEM Analysis)

A first approximation to the geometrics of the landslide-dammed lake involved the use of the contour interpolation method with digital topographic data. This method uses the contour function within the 3D Analyst module in ArcGIS 10.2, in conjunction with the SRTM and GDEM2 datasets. The interpolation creates contours based on a comparison between the surrounding DEM elevations, estimating the heights between the individual grid cells centre point. We assumed a local datum of 2,325 m a.s.l. for the river valley floor at the site of the rockslide, i.e., a lake depth of 0 m (see below), and a maximum pool height elevation of 2,435 m a.s.l. Within these elevation limits eleven 10 m-interval contours were interpolated from the DEMs and used as a proxy for the lake shorelines during the filling of the reservoir (Table 3-2). For each interpolated contour level, area and volume values for the lake were calculated from both digital data sets (Table 3-2).

68

To obtain the pool elevation in metres above sea level we added the depths of the lake reported by NDMA, beginning on January 31, 2010 (day 27), to the elevation of our SRTM-based local datum (2,325 m a.s.l.) and a filling curve was plotted (Fig. 3.6).
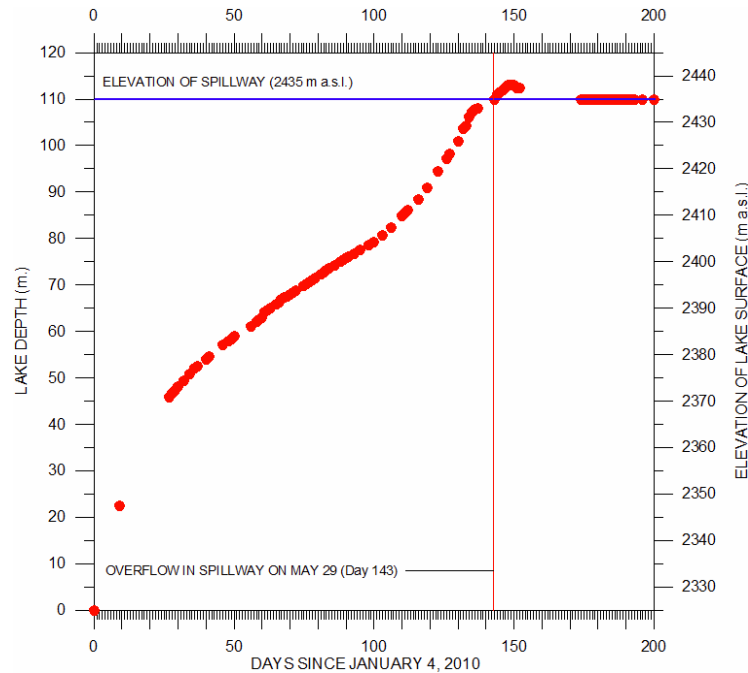
Figure 3.6: Filling curve of lake depths and water surface elevations of Lake Gojal during rockslide-dammed lake development. As of April 03, 2014, the lake elevation had dropped to 2,398.0 m a.s.l. (± 4.13 m at CL(95%)), and as of June 30, 2014 controlled overtopping continues (after Delaney and Evans, 2011).

We were also able to check the vertical accuracy of the SRTM DEM by referring to local news reports and the NDMA lake depth data; for example, on February 10 2010 (day 37) Lake Gojal had reportedly reached the piers of the Karakoram Highway bridge located at Gulmit, upstream of the impoundment. The elevation of the SRTM grid cell under the bridge piers at this location is recorded as 2,375 m a.s.l., which is within 2 m of the elevation (2,377 m a.s.l.) indicated by the NDMA lake depth (ca. 52 m) reported on that day.

We also calculated areas and volumes for a range of lake surface elevations during the filling and partial draining of Lake Gojal using the SRTM and GDEM2 DEMs (Table 3-2; Fig. 3.7) in the contour interpolation method in ArcGIS as described above.

69

Table 3-2: Data for the filling of Lake Gojal, including first-order estimations of lake lengths, areas, and volumes from contour interpolation of SRTM-3 and ASTER GDEM2 digital topography data. Maximum pool elevation reached by Lake Gojal was 2,435 m a.s.l. (highlighted).

Pool Height (m asl)	Height Above River (m)	SRTM-3			GDEM2		
		Length (km)	Area (km²)	Volume (Mm³)	Length (km)	Area (km²)	Volume (Mm³)
2375	50	9.2	2.3	64.2	9.8	3.3	86.9
2385	60	9.5	2.9	98.91	10.3	3.9	125.3
2395	70	9.9	3.6	140.2	10.5	4.5	165.8
2405	80	10.2	4.4	185.7	10.5	5.2	214.8
2415	90	15.3	5.9	250.7	13.0	6.6	282.7
2425	100	18.7	8.1	333.9	16.4	8.4	364.4
2435	110	22.1	9.8	430.7	21.2	11.0	491.9
2440	115	22.6	13.6	494.9	21.4	11.7	548.6
2445	120	23.8	15.1	562.6	26.9	17.5	674.8
2450	125	24.6	16.7	650.0	27.2	18.8	764.4

NESPAK conducted bathymetric surveys at Lake Gojal during July 2011 and reported elevations based on a newly established benchmark surveyed in by the Survey of Pakistan. NESPAK (2014) determined the elevation of the river valley at the upstream margin of the rockslide dam to be 2,322 m a.s.l., which as noted above corresponds to a local datum with a lake depth of zero (Khali Ahmad Ghauri (WAPDA) personal communication, June, 24, 2014). In addition, NESPAK (2014) determined a maximum lake elevation of 2,434 m a.s.l., only 1 metre below the elevation calculated from the SRTM DEM.

In evaluating these three sets of data (Table 3-2; Fig. 3.7) the GDEM2 values are consistently larger than the SRTM values in both area and volume (Table 3-2) for a given lake surface elevation; this difference grows larger with increasing water surface elevation and lake volume.

We also compared the calculated volume of Lake Gojal from the first-order DEM contour assessment using SRTM and GDEM2 data with the NESPAK results based on the bathymetric survey in July 2011 (NESPAK, 2014; Fig. 3.7). It is noted (Fig. 3.7) that the

NESPAK data underestimates the lake volume for a given water surface elevation. The differences in the volume estimates becomes significant in hazard assessment (e.g., use in outburst flood modeling) at the full pool elevation reached by Lake Gojal (~ 2,435 m a.s.l.) when the maximum volume suggested by the three data sets are as follows; NESPAK (337.4 Mm^3), SRTM-3 (430.7 Mm^3) and GDEM2 (491.9 Mm^3), a range of 154.5 Mm^3.

The slope of the rating curve shows a significant change between 2,405 m a.s.l. and 2,415 m a.s.l. in both DEMs and the NESPAK (2014) data (Table 3-2, Fig. 3.7). This reflects the effect of the knick-point (Fig. 3.5) in the Hunza River valley adjacent to Shishkat at ca. 2,405 m a.s.l., caused by deposition from the alluvial fan complex on the western shoreline.
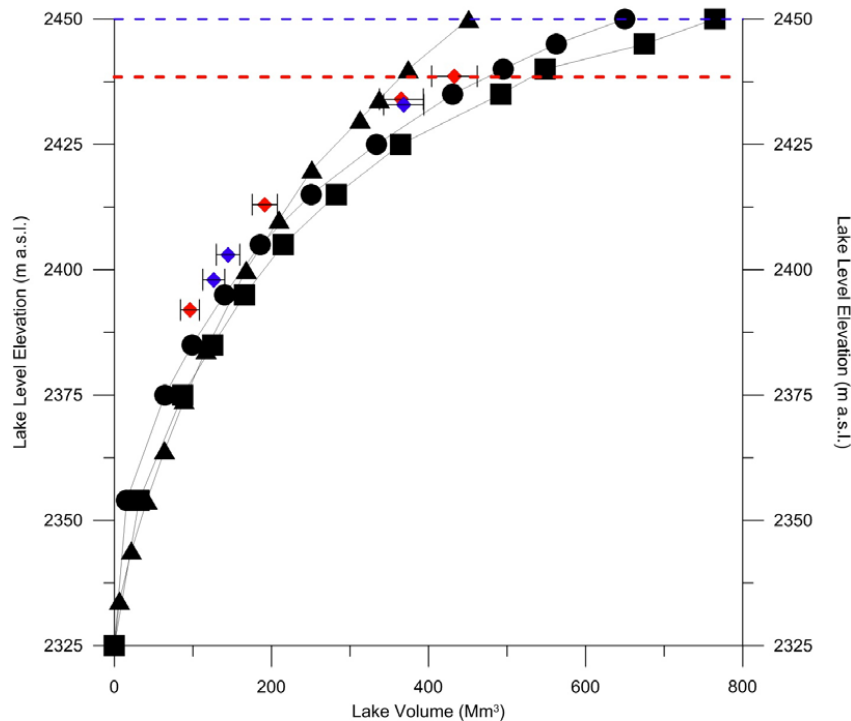
Figure 3.7: Plot of lake level elevations (m a.s.l) and associated volumes for the SRTM (circles) and GDEM2 (squares) DEMs (both calculated by the contour-interpolation method), and the NESPAK data based on field survey (NESPAK, 2014; Table 6) (triangles). Diamonds illustrate pixel-by-pixel shoreline methodology results for filling (red) and draining (blue), with error bars for 95% CL Datum is taken as 2,325 m.a.s.l. Red horizontal dashed line denotes estimated maximum pool elevation reached by Lake Gojal after stable overtopping began (2,435 m a.s.l.). Blue horizontal dashed line marks the estimated maximum pool elevation (2,450 m a.s.l.) that Lake Gojal would have reached without engineering intervention, i.e., the excavation of the spillway.

The discrepancy between the NESPAK (2014) data and the digital datasets used in this study most likely results from the very limited number of cross-sections obtained by NESPAK in the upper reaches of Lake Gojal, north of Shishkat. According to NESPAK (2014; their Figure 8 and Table 5) 29 cross-sections were taken along the entire ca. 22 km length of Lake Gojal; however, only 4 of these cross-sections were measured in the upper 9.5 km of the lake, whereas 25 cross-sections were taken in the lower 12.5 km.

3.4.4 Lake Gojal II – Analysis of Pixel-by-Pixel Shoreline Polygons (Filling and Partial Draining)

We attempted a more precise estimate of the area and volume of Lake Gojal based on a more rigorous delimitation of the elevation of the lake shoreline during filling, overtopping, and partial draining. We developed a pixel-by-pixel method to obtain a mean pool height of Lake Gojal using a combination of satellite imagery and digital topographic data. The method, similar to that used by Dong et al. (2014), involves the following steps: for each of the 7 satellite images, the reservoir shoreline was visually traced out forming a polyline in GIS. Once the shoreline was created, the elevation of each SRTM 90 m x 90 m grid cell directly under this polyline was recorded for the entire perimeter of the lake. The number of SRTM counted grid cells varied from 289 to 634 for the lake shorelines analysed. We then took the mean value of these measurements as an estimate of the true lake elevation, and compared it where possible, to field observed values. The range in shoreline elevations is seen in the associated histogram for each lake.

March 16, 2010: the first high-resolution satellite image of Lake Gojal was taken March 16th, 2010, with the EO-1 ALI satellite (Fig. 3.8).
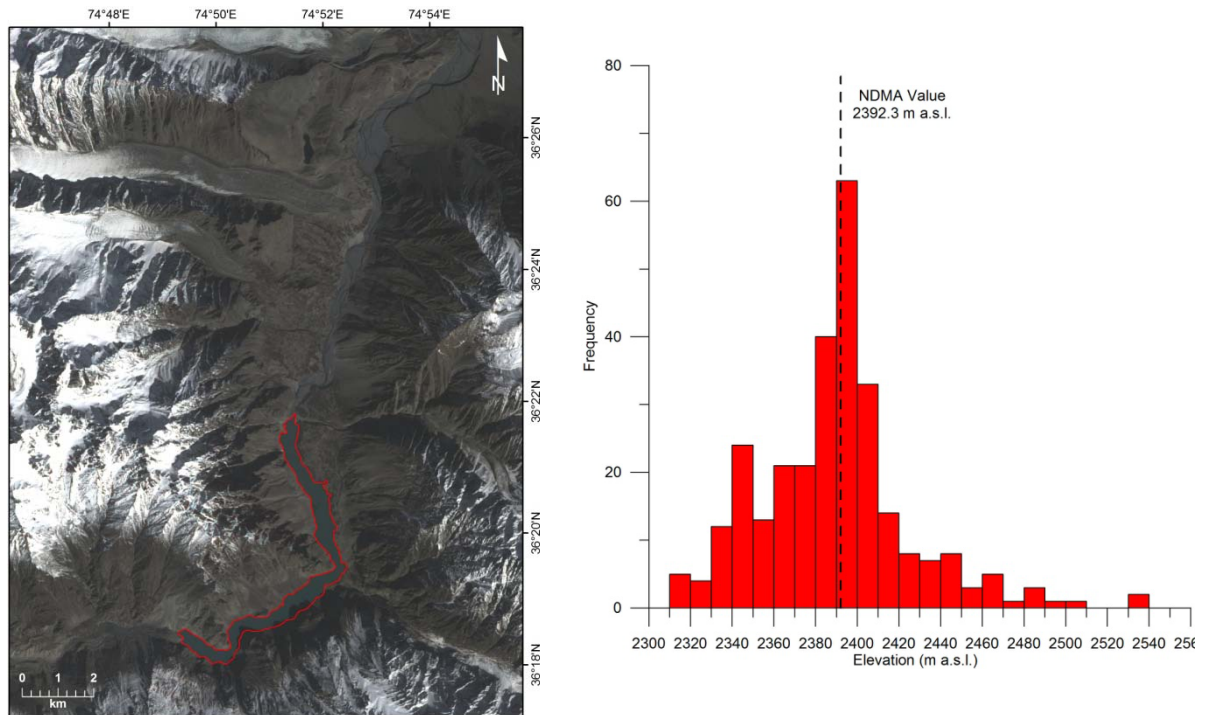
Figure 3.8: A: EO-1 ALI satellite image from March 16th, 2010, with shoreline in red determined by the pixel-by-pixel method to be 2389.74 m a.s.l. At this time, SRTM DEM contour interpolation of the same lake shoreline elevation resulted in a volume of 115.5 Mm³. B: histogram of 289 values of shoreline elevation measurement by the pixel-by-pixel method. The water surface elevation given by NDMA measurement of lake depth (datum assumed = 2,325 m a.s.l.) is indicated.

A mean pool height elevation on March 16th of 2,389.74 m a.s.l. (± 4.13 m at CL (95%)), was obtained from 289 SRTM grid cells around the perimeter of the reservoir. The NDMA recorded a lake depth of 67.3 m on this date indicating an elevation of 2,392.3 m a.s.l., a difference of only +2.56 m. At this elevation, and using the traced shoreline pixel by pixel method, the volume of Lake Gojal is ca. 96.2 Mm³ (± 11.5 Mm³).

May 02, 2010: Lake Gojal was imaged by the ASTER satellite on May 02 2010 in false-colour (Fig. 3.9).
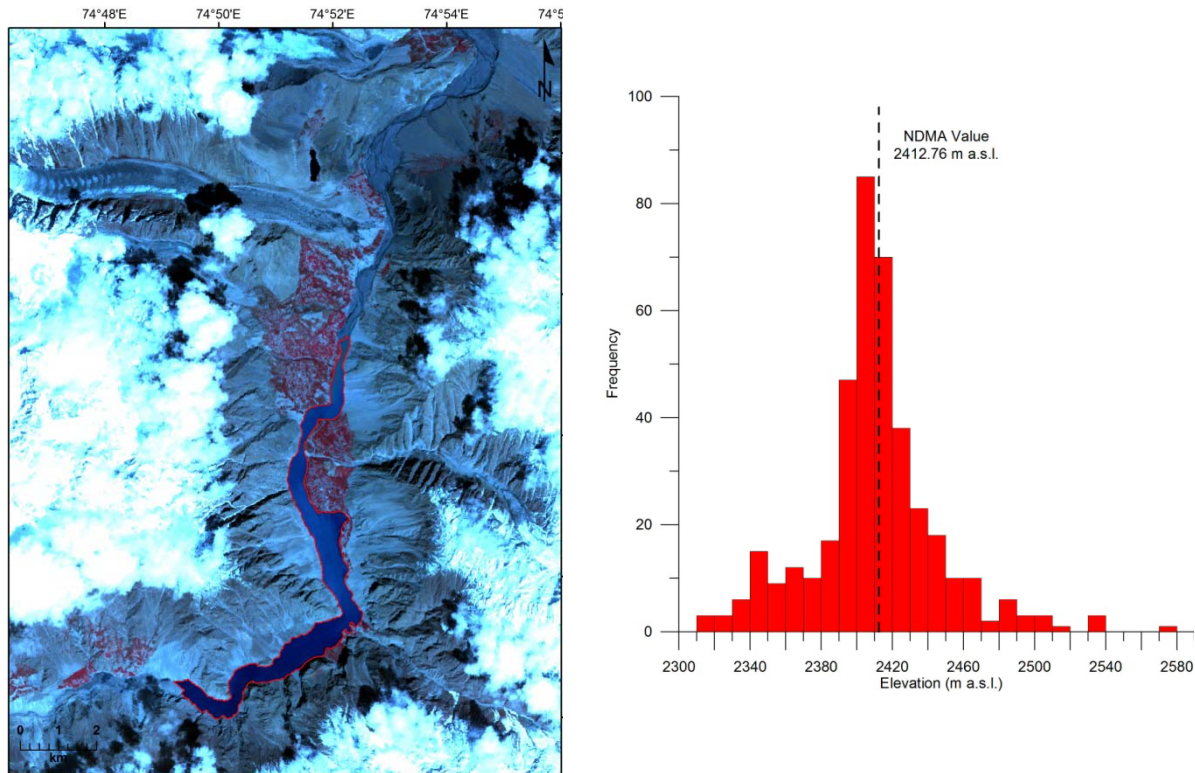
Figure 3.9: A: Lake Gojal filling imaged on May 02nd 2010, by the ASTER satellite, shoreline outlined in red. B: histogram of 395 values of shoreline elevation measurement by the pixel-by-pixel method. The water surface elevation given by NDMA measurement of lake depth (datum assumed = 2,325 m a.s.l.) is indicated.

The average pool height elevation on May 02nd from the SRTM DEM is 2410.48 m a.s.l. ($\pm$ 3.52 m at CL(95%)), calculated from 395 grid cells around the perimeter of the lake at this time. The NDMA lake depth reported on May 03rd was recorded as 88.4 m indicating a lake elevation of 2413.4 m a.s.l., a vertical difference of 3.9 m (there was no NDMA report published on May 02nd). At this elevation, and using the shoreline trace pixel-by-pixel method as the area, the volume of Lake Gojal is ca. 191.5 Mm³ ($\pm$ 15.8 Mm³).

May 25, 2010: The lake was imaged again by the ASTER satellite during the filling process on May 25th 2010, however, this time two images taken concurrently were required, and the mosaic 'stitch' line can be clearly seen running across the image set (Fig. 3.10).

74
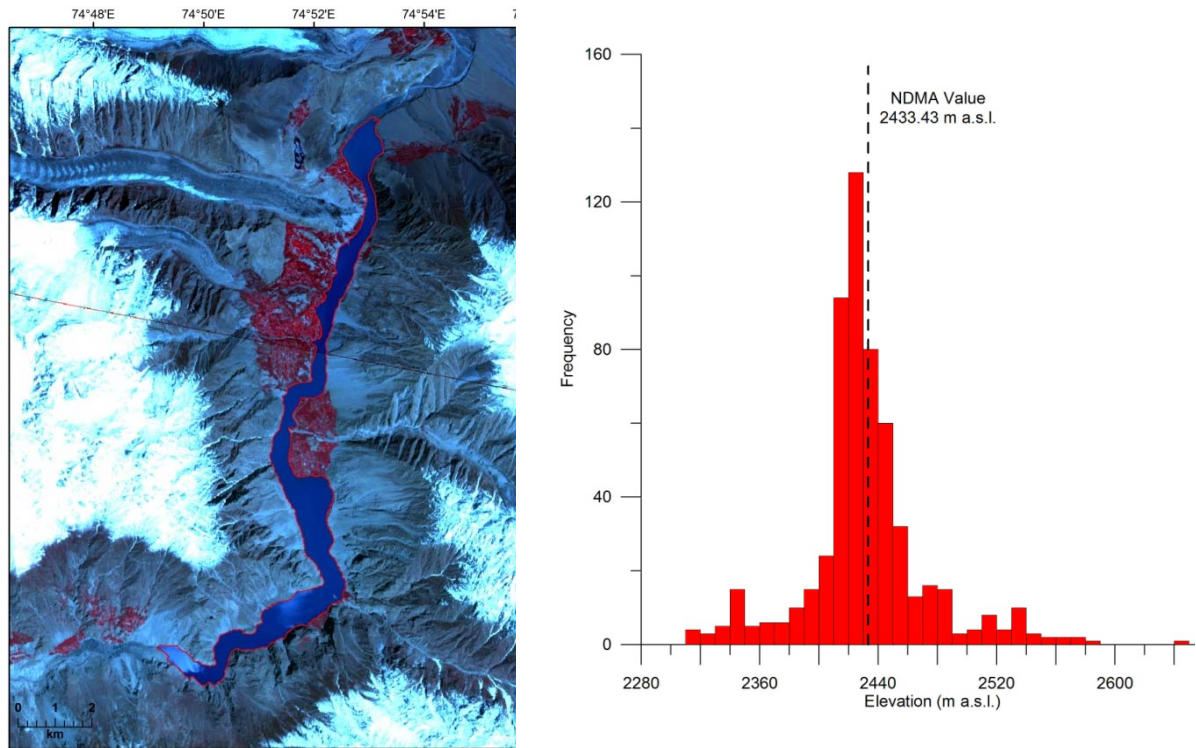
Figure 3.10: A: Mosaic of two ASTER satellite images taken May 25th 2010 of Lake Gojal; shoreline in red. B: histogram of 571 values of shoreline elevation measurement by the pixel-by-pixel method. The water surface elevation given by NDMA measurement of lake depth (datum assumed = 2,325 m a.s.l.) is indicated.

The average pool height elevation from the SRTM DEM on May 25th is 2432.42 m as.l. ($\pm$ 3.39 m at CL(95%)), calculated from 571 SRTM grid cells. The NDMA lake depth was recorded as 108.4 m indicating a lake elevation of 2433.4 m a.s.l., a vertical difference of only 1.01 m. At this elevation, and using the shoreline trace pixel by pixel method as the area, the volume of Lake Gojal is ca. 365.4 Mm³ ($\pm$ 27.6 Mm³).

June 01, 2010: Two days after overtopping had commenced through the spillway, Lake Gojal was imaged again by the ASTER satellite on June 01st 2010, and the furthest extent of the lake observed by satellites can be seen (Fig. 3.11). During this time, the NDMA reports the lake increased in depth by 1.62 m to 111.6 m above the overtopping elevation of 2,435 m a.s.l., to an elevation of 2,436.6 m a.s.l. on June 01st, 2010. NDMA notes that the lake does increase in depth an additional ca. 4 m from May 29th 2010, until July 02nd 2010, when the lake level begins to fall.
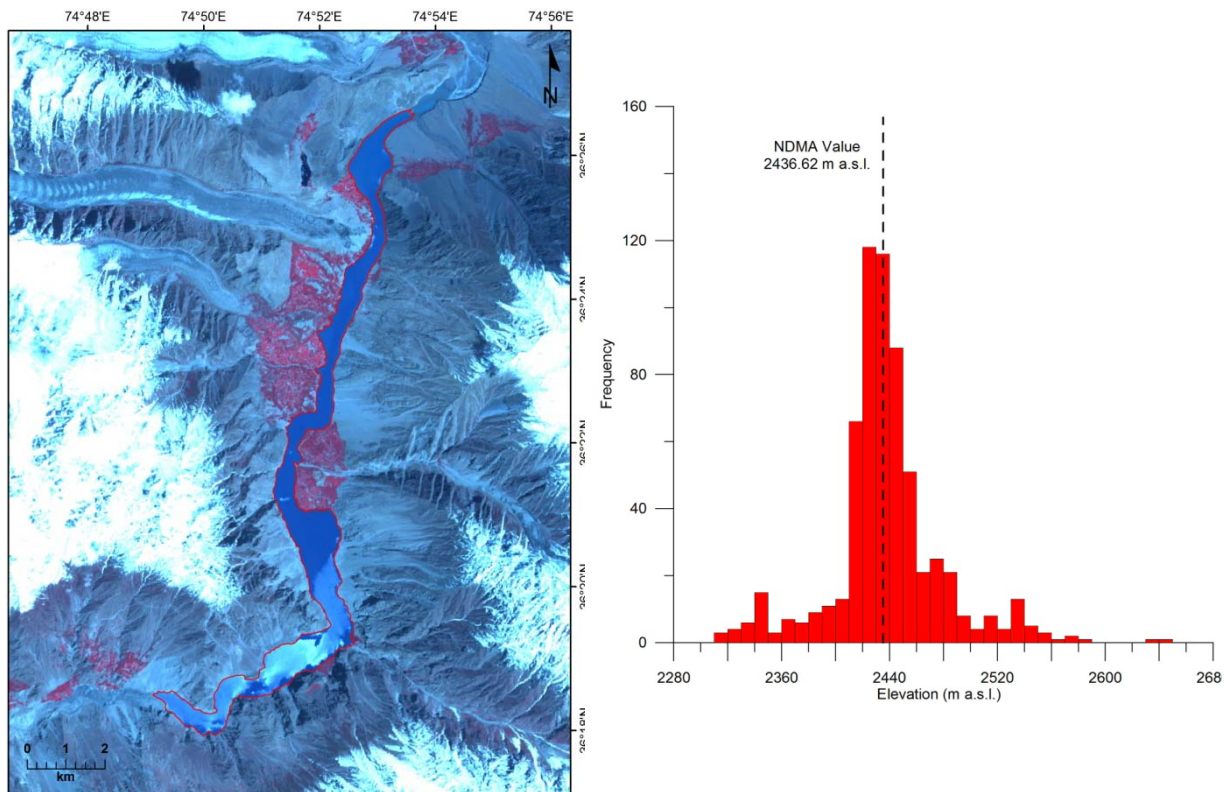
Figure 3.11: A: June 01st 2010 ASTER image of Lake Gojal, 2 days after overtopping the rock avalanche; shoreline shown in red. B: histogram of 634 values of shoreline elevation measurement by the pixel-by-pixel method. The water surface elevation given by NDMA measurement of lake depth (datum assumed = 2,325 m a.s.l.) is indicated.

The average pool height elevation from the SRTM DEM on June 01st is 2438.56 m a.s.l. (± 3.25 m at CL(95%)), calculated from 634 SRTM grid cells. The NDMA recorded a lake depth of ca 112.2 m indicating an elevation of 2434.2 m a.s.l., a vertical difference of -4.36 m. At this elevation, and using the shoreline traced by the pixel-by-pixel method as the area, the volume of Lake Gojal is ca. 432.8 Mm³ (± 29.2 Mm³), which we take as the maximum lake volume reached. This is quite comparable to the first-order DEM contour interpolation calculation of 430.7 Mm³ (Table 3-2) for the maximum volume of the lake at 2,435 m a.s.l.

The NDMA did not continue to report lake depth from Lake Gojal after July 30th 2010. However, the pixel-by-pixel methodology described above was highly satisfactory in estimating the lake elevations from a fusion of satellite and DEM data. Calculated mean lake

surface elevation values differ from lake elevations calculated from the field observed
NDMA lake depth data (assuming a datum of 2,325 m a.s.l.) in a range from -4.36 m to
+3.90 m. The errors in the mean elevation data range from ± 3.25 m to ± 4.13 m at the 95%
confidence level.

The International Sedimentation Research Institute of Pakistan, Pakistan Water and Power
Development Authority (ISRIP-WAPDA) determined that the pool elevation of the lake on
July 31st, 2011, was 2,434.57 m a.s.l. Unfortunately, no other field data was obtained during
the draining of Lake Gojal. Therefore, in an attempt to obtain pool height measurements for
Lake Gojal during this post-overtopping period when partial draining took place, the above
pixel-by-pixel methodology was repeated on three additional satellite images; the EO-1 ALI
image from August 2011, and LANDSAT8 OLI images from May 2013 and April 2014.

August 4, 2011: On August 04th 2011, the EO-1 ALI satellite acquired an image of Lake
Gojal (Fig. 3.12) within 4 days of the survey carried out by ISRIP-WAPDA. After one year
of controlled overtopping, combined with the excavation and further erosion of the
engineered spillway, the lake depth, surface area, and volume has reduced slightly from its
maximum size obtained in July 2010.
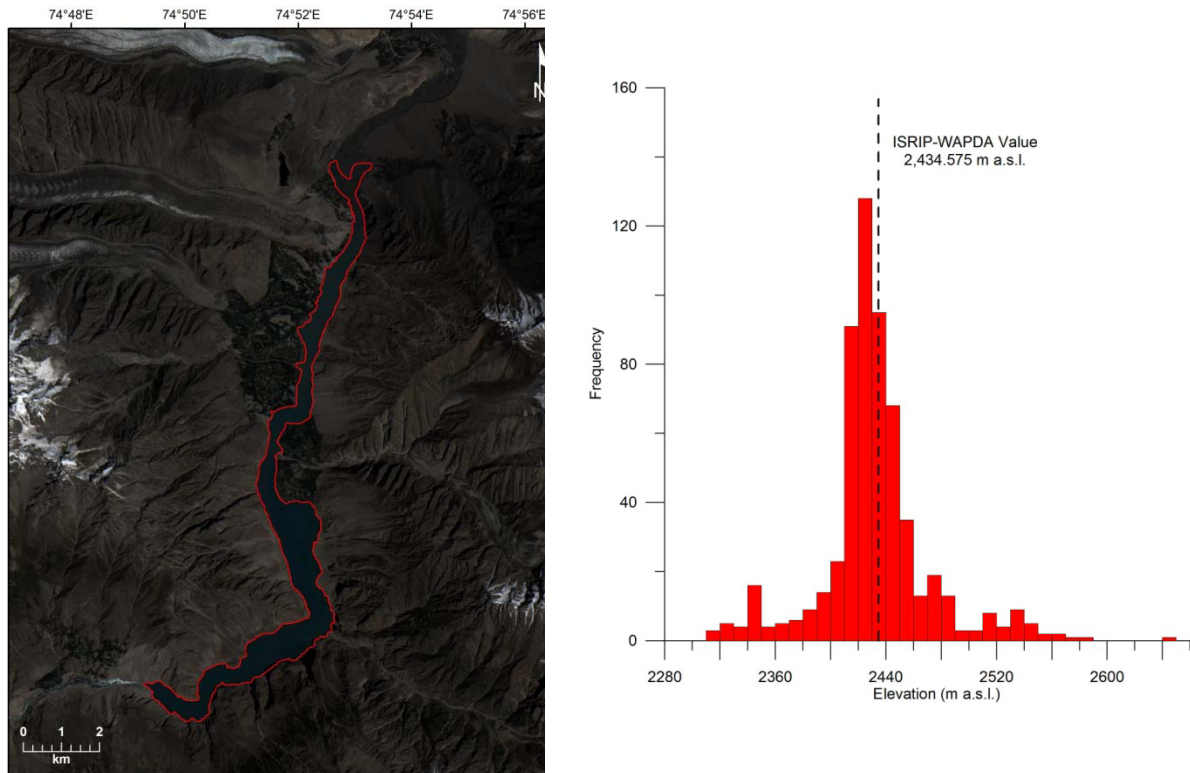
Figure 3.12: A: EO-1 ALI image taken August 04th 2011 of Lake Gojal, post-overtopping. Shoreline shown in red. B: histogram of 590 values of shoreline elevation measurement by the pixel-by-pixel method. The water surface elevation measured by ISRIP-WAPDA (Khali Ahmad Ghauri (WAPDA) personal communication, June 24th 2014; datum assumed = 2,322 m a.s.l.) on July 31st, 2011 is indicated.

The average pool height from the SRTM DEM on August 04th 2011 was 2,432.9 m a.s.l. (± 3.25 m at CL(95%)), calculated from 590 SRTM grid cells. At this elevation, the volume of Lake Gojal, calculated by the pixel by pixel method, is ca. 368.4 Mm³ (± 25.6 Mm³), a successful reduction of about 62 Mm³ from the maximum volume subsequent to overtopping in July 2010 (see above). On July 31st 2011, just 4 days prior to the EO-1 ALI image above (Fig. 3.12), NESPAK tasked the International Sedimentation Research Institute of Pakistan, Pakistan Water and Power Development Authority (ISRIP-WAPDA), to carry out field bathymetric measurements of Lake Gojal. They determined that the pool elevation of the lake at this time was 2,434.6 m a.s.l., a difference of only +1.7 m.

May 18, 2013: On May 18th, 2013, the LANDSAT8 satellite acquired this image of Lake Gojal (Fig. 3.13). After excavation and further erosion increased discharge through the

78

spillway, the lake surface area and lake volume had reduced significantly from its maximum in July 2010.
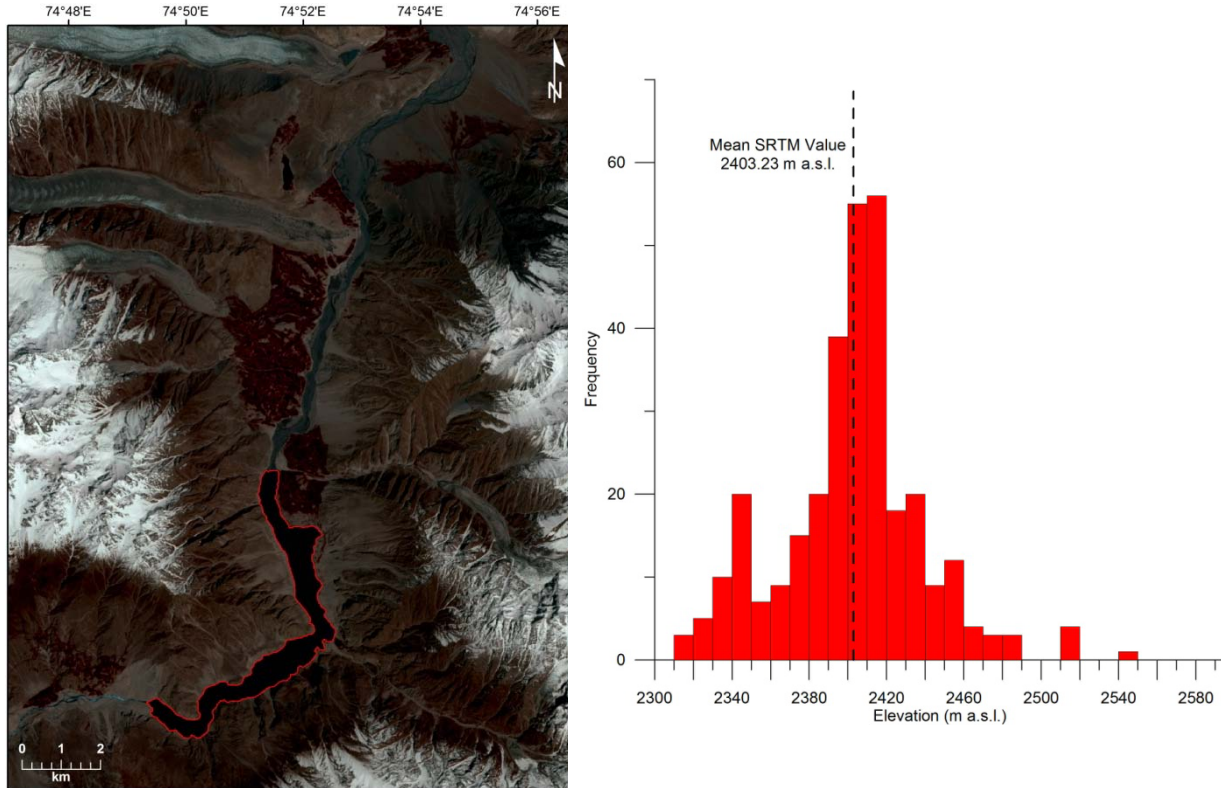
Figure 3.13: A: LANDSAT8 image taken May 18th, 2013 of Lake Gojal. Shoreline shown in red. B: histogram of 313 values of shoreline elevation measurement by the pixel-by-pixel method. Mean value is indicated.

The average pool height from the SRTM DEM on May 18th 2013 was 2403.23 m a.s.l. ($\pm$ 4.09 m at CL(95%)), calculated from 313 SRTM grid cells. At this elevation, the volume of Lake Gojal calculated by the pixel-by-pixel method is ca. 144.7 Mm³ ($\pm$ 15.2 Mm³), a successful reduction of about 282 Mm³ (~66%) from its maximum volume subsequent to overtopping in 2010.

April 03, 2014: The final and most recent image used in this study was taken by the LANDSAT8 OLI satellite on April 03 2014 (Fig. 3.14). Although this image has a high percentage of cloud cover, the lake is still clearly visible.
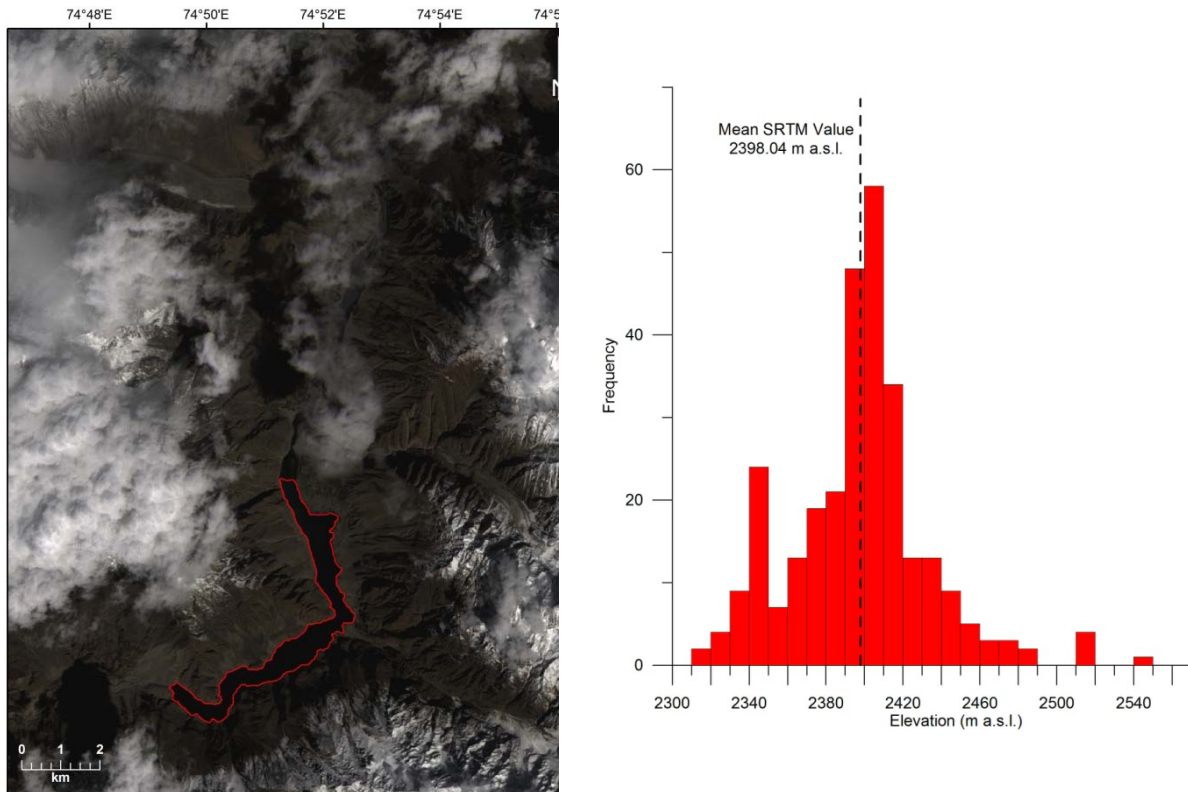
Figure 3.14: A: April 03rd 2014 LANDSAT8 image of Lake Gojal, shoreline in red. B: histogram of 292 values of shoreline elevation measurement by the pixel-by-pixel method. The mean value is indicated.

The average pool height from the SRTM DEM was 2398.0 m a.s.l. (± 4.13 m at CL(95%)), calculated from 292 SRTM grid cells. At this elevation, the volume of Lake Gojal is ca. 126.5 Mm³ (± 13.5 Mm³) calculated by the pixel by pixel method, a total reduction of about 303.5 Mm³ from the maximum overtopping volume (~71%).

3.4.5 Comparison of SRTM DEM Analysis and Pixel-by-Pixel Method

The shoreline pixel-by-pixel statistical methodology results in lake volumes which are lower than the first-order values determined from the interpolated SRTM DEM contours for a given shoreline elevation (Fig. 3.7, 3.15). We suggest that this is mainly due to the fact that the true shoreline is more accurately delimited in the pixel-by-pixel method, resulting in a smaller area than the lake area created through the interpolation of SRTM DEM heights into contour data for a given shoreline. Thus, in the presence of an extensive high-resolution temporal satellite image archive, together with accurately observed field measurements of lake depth

or absolute lake surface elevation, the pixel-by-pixel method can be used to obtain very accurate estimates of impoundment areas and volumes.
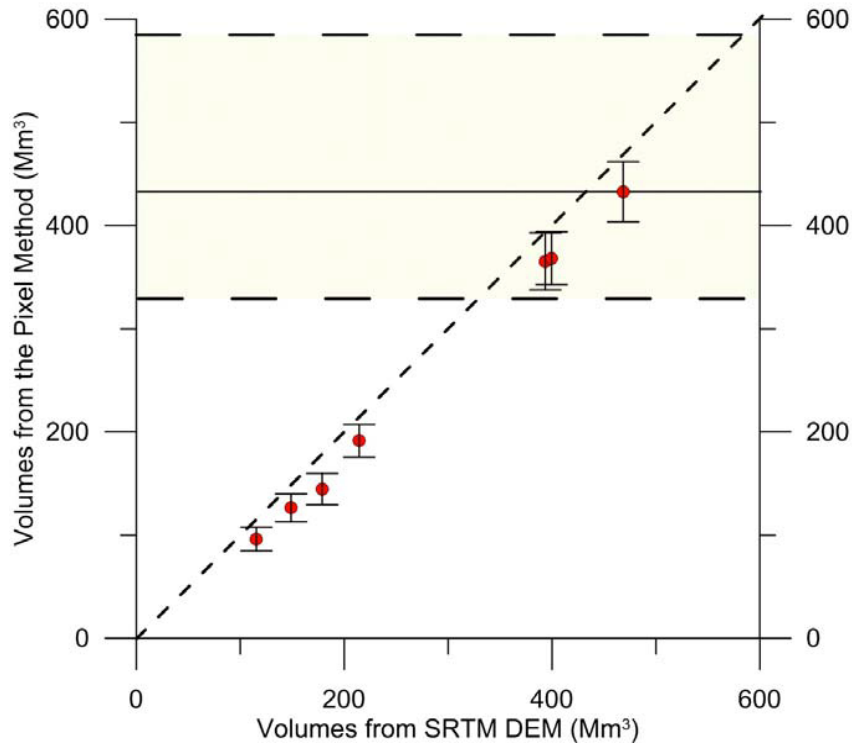
Figure 3.15: Plot of volumes of rockslide-dammed Lake Gojal calculated by the pixel-by-pixel method for seven shorelines compared to the lake volumes calculated for the same shorelines by the contour interpolation method. It is noted that the pixel method calculates lower mean values for a given shoreline; however, the SRTM contour interpolation value lies within the error defined by the 95% confidence limit of the pixel derived data. Also shown (horizontal dash lined with fill) is the range of values of the maximum volume of Lake Gojal reported in the literature (see text) and the volume of Lake Gojal (horizontal solid line) calculated by the mean value of the pixel by pixel method (432 Mm³).

The first-order interpolated values from the SRTM dataset appear to over-estimate the areas and thus the volumes of Lake Gojal for the range of pool heights considered here (Fig. 3.7; Table 3-2, 3-3).

We note that the original 430.7 Mm³ volume calculation from the first-order SRTM DEM interpolated contours (Table 3-2) falls within the 95% confidence interval of the volume estimated by the pixel-by-pixel analysis (Table 3-3; 432.8 Mm³ ($\pm$ 29.2 Mm³)) for the maximum pool elevation reached by Lake Gojal. This value may be compared (Fig. 3.15)

with the estimates of Kargel et al. (2010): 585 Mm³ ± 40 Mm³, Petley (2011): 450 – 500 Mm³, Schneider et al. (2013): 450 Mm³, Iqbal et al., (2014): 408 Mm³, Butt et al. (2013): 334 Mm³, NESPAK (2014): 329 Mm³.

Table 3-3: Comparison of shoreline elevation data (observed and pixel-by-pixel method) and associated lake volume calculations using the pixel and SRTM contour interpolation methods (see plot of data in Fig. 3.15).

Imagery Date	Satellite Platform	Elevations Based on NDMA Depths (m a.s.l.)	ISRIP-WAPDA Observed Elevations (m a.s.l.)	Pixel Method Elevations (m a.s.l.)	SRTM Volumes (Mm³)	Pixel Method Volumes (Mm³)
March 16 2010	EO-1	2392.3	-	2389.7 ±4.13	115.5	96.2 ±11.5
May 02 2010	ASTER	2412.8	-	2410.5 ±3.52	214.4	191.5 ±15.8
May 25 2010	ASTER	2433.4	-	2432.4 ±3.39	393.5	365.4 ±27.6
June 01 2010	ASTER	2436.6	-	2438.6 ±3.25	468.4	432.8 ±29.2
August 04 2011	EO-1	-	2434.6	2432.9 ±3.25	399.6	368.4 ±25.6
May 18 2013	LANDSAT8	-	-	2403.2 ±4.09	178.8	144.7 ±15.2
April 03 2014	LANDSAT8	-	-	2398.0 ±4.13	148.9	126.5 ±13.5

3.5 **Evaluation of Mitigation**

The detailed analysis presented above of the change in lake volumes in the 52 month period January 4, 2010 to April 3, 2014 also provides important data for the evaluation of the mitigation measures undertaken by Pakistan authorities in firstly, controlling the maximum height (and therefore volume) of Lake Gojal, and secondly, by successively reducing the volume of the Lake by the enlargement (widening and deepening) of the spillway.

Without engineering intervention, in the form of the excavation of the spillway, we estimate the pool elevation would have reached 2,450 m a.s.l. and Lake Gojal would have had a volume of ca. 650 Mm³ before natural overtopping and possible breaching (Table 3-2). This lake volume would have thus approached the volume of the 1967 Tanggudong rockslide-dammed lake in Sichuan, China (Wang et al., 2012). As a result of the spillway excavation, the initial overflow elevation was reduced to 2,435 m a.s.l., and the volume (the maximum volume reached by Lake Gojal) was 432 Mm^3, an initial reduction in volume of 33%. By April 3, 2014, a period of 1,400 days after overtopping, the rockslide-dammed lake had been drawn down approximately 37 m and the overtopping volume reduced by 303.5 Mm (71%) to 126.5 Mm^3. With reference to the maximum possible pool elevation and lake volume these values are 52 m and 523.5 Mm³ (80%) respectively. This substantial reduction in lake

volume, and thus outburst hazard, was achieved without any catastrophic release of the impoundment. As such, the partial draining of Lake Gojal by engineering measures should be viewed as one of the most successful rockslide dammed lake mitigation projects in recent history (cf. Evans et al., 2011; Schuster and Evans, 2011).

3.6 **Comparative Rockslide Dammed Lakes 1841 – 2014**

3.6.1 Rockslide Dammed Lakes in the Upper Indus

The Upper Indus has a well-documented history of natural dam formation by both glaciers and rockslides and massive outburst floods resulting from their catastrophic failure (Mason, 1929; Gunn, 1930; Kahn, 1969; Hewitt, 1982; Hewitt and Liu, 2010; Delaney and Evans, 2011). The greatest of these was the 1841 flood resulting from the breaching of a rockslide dam (Fig. 3.16), the *Great Indus Flood* of Mason (1929, p. 15-17).

Delaney and Evans (2011) examined satellite imagery of the 1841 rockslide-dam site in conjunction with a SRTM-3 DEM, and together with the results of their review of the literature, they estimated the maximum pool elevation of the 1841 Indus landslide-dammed lake to be 1,390 m a.s.l. From the SRTM-3 DEM Delaney and Evans (2011) calculated that an impoundment to this pool elevation formed a lake (Fig. 3.16) a maximum of 57 km in length, 88 km² in area with an impounded volume of 6.5 Gm³. The outburst of this rockslide dam in June 1841 is thought to have occurred directly as a result of initial overtopping (Delaney and Evans, 2011).

Figure 3.16: LANDSAT7 image with showing the 1841 rockslide debris dam on the Indus River and impoundment of the large reservoir downstream of Gilgit. The maximum pool elevation of the lake is estimated at 1,390 m a.s.l. Based on SRTM-3 data the 1841 rockslide-dammed lake had a maximum area of 88 km² and a volume of 6.5 Gm³ (see Delaney and Evans, 2011).

Fifteen years later in the nineteenth century, a second major rockslide dam formed in the Upper Indus in 1858, 2.5 km downstream of the 2010 Attabad rockslide dam on the Hunza River (Fig. 3.17; Mason, 1929; Shroder, 1998; Delaney and Evans, 2011). The rockslide-dammed lake formed and filled in the winter-spring of 1858 and reached roughly 30 km upstream. In August 1858, the rockslide dam was breached and the impounded waters were catastrophically released creating a destructive outburst flood. Henderson (1859, p. 199) relates that the first news of the blockage reached Attock about the middle of July, 1858. He refers to a July report that indicates the Hunza had been closed for three months (p. 203),

84

inferring that the blockage took place at the beginning of April, 1858. Dismissing this estimate, Henderson (1859) argues for the blockage to have taken place in the middle of May. Becher (1859, p. 203) on the other hand suggests that the rockslide "*dammed up the narrow bed of the river for 6 months*", indicating a rockslide damming event in early February, 1858.
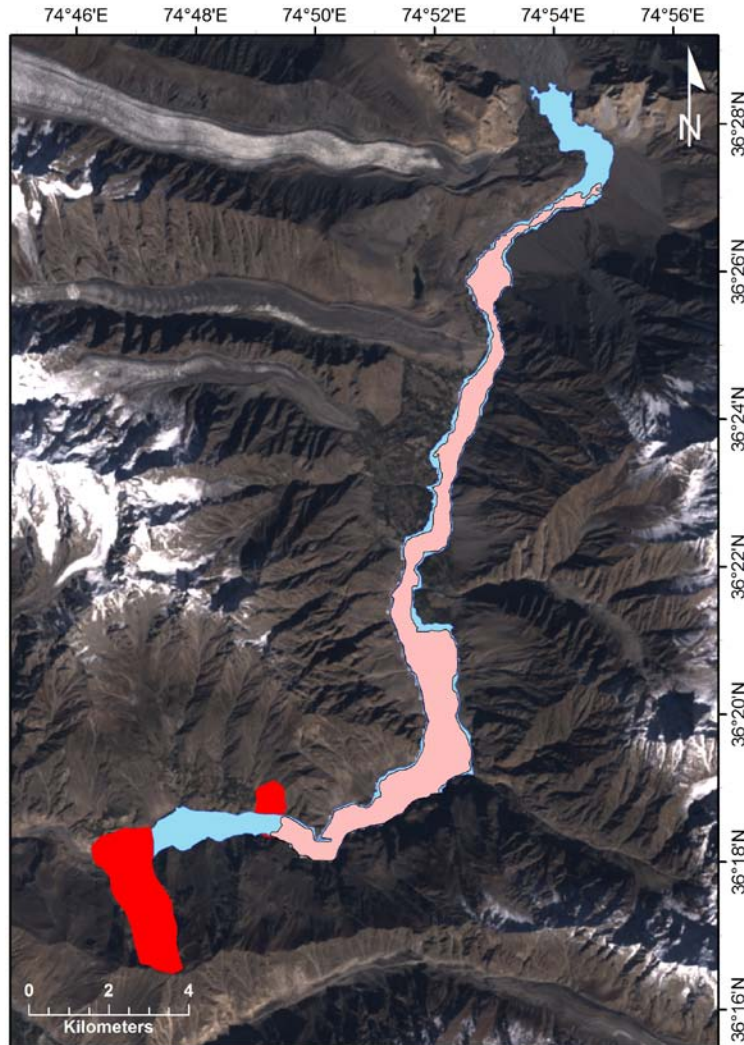
Figure 3.17: LANDSAT7 image with the 1858 rockslide and reservoir (blue) shown with the 2010 rockslide and reservoir (pink) created from SRTM-3 data. The 1858 reservoir had a pool elevation of 2,450 m a.s.l. and a volume of ca. 805 Mm³, while the 2010 reservoir has a pool elevation of 2,435 m a.s.l. and a volume of ca. 430 Mm³.

There was much contemporary discussion on the location of the rockslide blockage (e.g. Drew, 1875; Montgomerie, 1860; Henderson 1859). The report by Mr. Todd quoted in

Mason (1929) above gives almost a precise location, which we estimate as being 36.304N/74.781E (Shroder, 1998). At this location the bed of the Hunza is approximately 2,250 m a.s.l. Reports that the lake reached Pasu are noted by Mason (1929). Thus the rockslide dam would have had a spillway elevation, corresponding to a maximum pool elevation, of at least 2,450 m a.s.l., 200 m above the bed of the Hunza at the site of damming rockslide. At this pool elevation the lake would extend roughly 30 km upstream. Based on the observations of Shroder (1998), an examination of satellite imagery and the SRTM-3 DEM, we estimate the maximum pool elevation of the 1858 Hunza landslide-dammed lake to be 2,450 m a.s.l. From the SRTM-3 DEM we calculate that this pool elevation formed a lake 28 km long, 15.6 km² in area, and with an impounded volume of approximately 805 Mm³ (Fig. 3.17). The outburst flood (the Ghammesar Flood of Gunn (1930)) reached Attock (544 km downstream from the 1858 rockslide dam) at around 6 a.m. on August 10, 1858.

Delaney and Evans (2011) argue that the 1858 Hunza rockslide-dammed lake filled to overflow some time before breaching and suggest that the rockslide dam formed on approximately May 15, that filling of the lake occurred very roughly around June 18 (maximum volume ca. 805 Mm³), and that overflow of the rockslide debris through a natural spillway took place from that date to catastrophic breaching on August 9, a period of some 62 days.

These outburst volumes may be compared with the volume of some of the largest glacier dammed lake outbursts documented in the Upper Indus of 1.35 Gm³ (Gunn, 1930) resulting from the outburst of a glacial lake dammed by the Chong Khumdan Glacier in the Upper Shyok valley at 35°10'40"N / 77°41'50"E (Mason, 1935; Gunn, 1930; Gunn et al., 1930). The 1929 Chong Khumdan glacier dam outburst volume, however, exceeds both impoundments of the 1858 and 2010 Hunza rockslide dams (805 Mm³ and 430 Mm³, respectively).

3.6.2 Global Comparisons

The 2010 Attabad rockslide-dammed impoundment and the nineteenth century rockslide

dammed lakes (1841 and 1858) in the Upper Indus are some of the largest rockslide-dammed lakes formed in recent history (Table 3-4). In the historical record, the volume of the 1841 Indus lake is second only to the volume of Lake Sarez (ca. 17 Gm³) impounded by the 1911 Usoi rockslide, Murgab valley, Tajikistan (Ischuk, 2006; Delaney and Evans, 2011).

Table 3-4: Comparative data on impounded volumes in rockslide-dammed lakes that formed in the period 1841-2011 (Data from Evans et al., 2011; see this reference for details on sources for data in Table 3). The 3 events discussed in this text are highlighted.

Rank	Location	Date of Impoundment	Impounded Volume (Mm³)	Date of Outburst	Outburst Volume (Mm³)
1	Lake Sarez, Tajikistan	1911	17,000	n/a	-
2	Indus River, Pakistan	1841	6,500	1841	6,500
3	Yigong Zangbo, Tibet	2000	2,015	2000	2,015
4	Rio Barrancas, Argentina	Prehistoric	1,550	1914	1,550
5	Hunza River, Pakistan	1858	805	1858	805
6	Tanggudong, China	1967	680	1967	640
7	Condor-Sencca, Peru	1945	721	1945	664
8	Hunza River, Pakistan	2010	430	n/a	-
9	Mayunmarca, Peru	1974	352	1974	350

3.7 **Summary and Conclusions**

The remnants of rockslide dams are widespread in the incised river valleys of the northwest Himalayas (Pakistan and India) and the adjacent Pamir Mountains of Afghanistan and Tajikistan. The region has a rich history of lake formation and catastrophic natural dam outbursts; it hosts the largest rockslide dammed lake on Earth (Lake Sarez, Tajikistan) and the largest documented outburst flood from a rockslide dammed lake (the 1841 flood on the Indus River, Pakistan).

In January 2010, a major rockslide (est. vol. 55 Mm^3) dammed the Hunza River and a rockslide-dammed lake (Lake Gojal) immediately began to form. The lake overtopped the rockslide dam 143 days later after the excavation of a spillway over the debris by Pakistan authorities; the lake has successively reduced in volume through the deepening and widening of the spillway, and by June 30th, 2014 only a remnant lake remains (126 Mm^3).

Using SRTM-3 digital terrain data and seven high-resolution satellite images from the period 2010-2014 we document the Attabad rockslide, track and quantify the development of rockslide-dammed Lake Gojal, and calculate lake volumes at various stages of filling, stable overtopping, and partial draining. We use two methods to achieve this objective. First, we used a first-order method using interpolated contours from the SRTM-3 DEM. Second, we introduced a more rigorous method of delimiting lake shorelines using a pixel-by-pixel method and find that this technique results in very accurate estimates of shoreline elevation and corresponding lake volumes. We estimate the maximum volume reached by Lake Gojal shortly after overtopping to have been 432 ± 29.2 Mm^3. Although both methods returned reasonable estimates of shoreline elevation and lake volumes, the pixel method was deemed more accurate because of the more precise delimitation of the shoreline and the comparable elevations to field observations. Using this data, we evaluated the mitigation works carried out by Pakistan authorities and find that: 1) through spillway excavation, they achieved a reduction of 33% in the maximum possible volume of Lake Gojal (without engineering intervention); and, 2) that up to April 03rd, 2014 had achieved a 71% reduction in the volume at overtopping without catastrophic release of the rockslide-dammed lake taking place. Their mitigation effort should be viewed as one of the most successful treatments of rockslide-dammed lakes in recent times.

Finally, we place the Attabad rockslide-dammed lake in the context of other natural dam impoundments in the Upper Indus and worldwide. The emplacement of rockslide dams and the behaviour of their impounded lakes are critical hazards to communities and the development of infrastructure, including hydroelectric facilities, in this region of Central Asia. A combination of high-resolution optical satellite imagery and digital topographic data is very effective in producing key data on rockslide-dammed lakes for geomorphic and hydrological analysis and engineering mitigation.

Chapter 4

The 2000 Yigong Rock Avalanche, Landslide Dam, and Outburst Flood (Tibetan Plateau): Remote Sensing Analysis and Process Modelling

Delaney, K.B. and Evans, S.G., for submission to the Journal of Asian Earth Sciences

OVERVIEW: In April 2000 a large-scale rock avalanche dammed the Yigong Zangpo River, forming an extensive rockslide-dammed lake. The impoundment lasted for 62 days before a catastrophic breaching caused a massive outburst flood in the Yarlung Zangpo (Tibet) and the Dihang Rivers (India) that travelled downstream to the floodplain of the Brahmaputra in northeastern India. In response to discrepancies in the published literature on the event, we present a review and re-evaluation of the characteristics of the rock avalanche and associated landslide-dammed lake. We use digital topographical data (SRTM-3) and dynamic landslide modeling (DAN-W/DAN3D) to determine the salient characteristics of the damming landslide; our analysis indicates that the volume of the damming rockslide was ca. 90 Mm^3, one of the largest to have occcured worldwide since 1900. The debris travelled 10.1 km down Zhamulong Gully into the Yigong river with a average velocity of approximately 15-18 m/s, resulting in a landslide dam with a minimum height of about 55 m. Using LANDSAT-7 imagery (obtained before, during and after impoundment) in conjunction with our SRTM DEM, we traced the filling of the lake. We determine that the landslide dam formed an extensive reservoir with an impounded volume of 2.015 Gm^3 and a maximum possible lake level of 2264 m.a.s.l (rounded to 2265 m a.s.l.). Our figures differ from those previously published but are believed to be well-constrained credible estimates of the volumes of the 2000 Yigong events. The outburst occurred after an attempt by army personnel to manually dig a spillway over the landslide debris and resulted in the entire volume of the lake draining in about 12 hours. The outburst flood travelled over 500 km south into India, with a recorded rise of 5.5 m at the Pasighat gauging station, 462 km downstream. In terms of historical outburst volumes from rockslide-dammed lakes, the volume of the 2000 Yigong event is only exceeded by that of the 1841 outburst flood from the Indus River rockslide-dammed lake, northern Pakistan.

4.1 Introduction

4.1.1 Landslides, River Damming, and Remote Sensing

The damming of major rivers by catastrophic landslides is an important geological hazard and a significant geomorphic process in high relief mountainous regions (Evans et al., 2011).

Often the river damming results from massive natural impoundments that approach and, in some historical cases, exceed the volume of the largest artificial reservoirs dammed by conventional dams (Evans, 2006). Landslide dams can sometimes fail and generate destructive outburst floods, although not all landslide dams are unstable or have failure potential (Evans, 1986; Evans, 2006; Evans et al., 2011). Indeed the majority of rockslide dams that form do not fail. Some landslide dams impound lakes that persist in the landscape for millennia and become permanent features of the landscape whilst other rockslide dam sites have been utilized as foundations of dams constructed for water supply or hydroelectric power generation. Evans et al. (2011) estimated that roughly 20% of major rockslide dams fail within 75 days of formation; the temporary nature of many landslide-dammed lakes, often occurring in remote regions, thus presents a challenge to the earth scientist and remote sensing specialist in accurately characterising the damming landslide, the filling behaviour of a landslide-dammed lake and its possible subsequent drainage.

Remote sensing, utilising digital terrain data in combination with archived optical imagery, has emerged as a vital tool in the rapid characterisation of catastrophic landslides (e.g., Evans et al., 2007; Roberts and Evans, 2013) and their process modelling (Evans et al. 2009a, 2009b), establishing landslide dam geometry and the evolution of the landslide-dammed impoundment to filling and possible emptying (Evans and Delaney, 2011; Delaney and Evans, 2011; Kargel et al. 2010, Schneider et al., 2013, Fan et al. 2012). This use has been in parallel with the development of current interest in the application of remote sensing in quantifying the geometry and volumetric storage of natural and artificial lakes in the landscape (e.g., Fujita et al., 2008; Evans et al., 2011; Delaney and Evans, 2011; Pan et al., 2013; Wang et al., 2013) and in first-order outburst process modelling (e.g., Wang et al., 2012; Schneider et al., 2014).

4.1.2 River Damming in the Tibetan Plateau and the 2000 Yigong Event

The deeply incised valleys of the Tibetan Plateau are particularly prone to landslide damming (Ouimet et al., 2007; Fan et al., 2012) through a process feedback system in which uplift-generated incision results in steep slopes that in turn generate damming landslides in narrow

deep valleys. In this active geomorphic environment, earthquakes are a major landslide trigger. Further, megafloods generated by the breaching of landslide dams may have made a major contribution to the geomorpholgy of the region (e.g., Lang et al., 2013). Since the mid-eighteenth century at least five major impoundments (three of which were triggered by earthquakes), involving impoundment volumes of greater than 100 Mm^3, have occurred on major rivers draining the Tibetan Plateau (Fig. 4.1). In this paper we present a first order remote sensing analysis of the largest of these events, the 2000 damming of the Yigong Zangpo River by the Yigong rock avalanche which occurred in the mountains of Tibet at 30° 10' 39"N, 94° 56' 25"E (Figure 1) on April 9, 2000 (Shang et al. 2003; Wen et al. 2004; Xu et al., 2012).
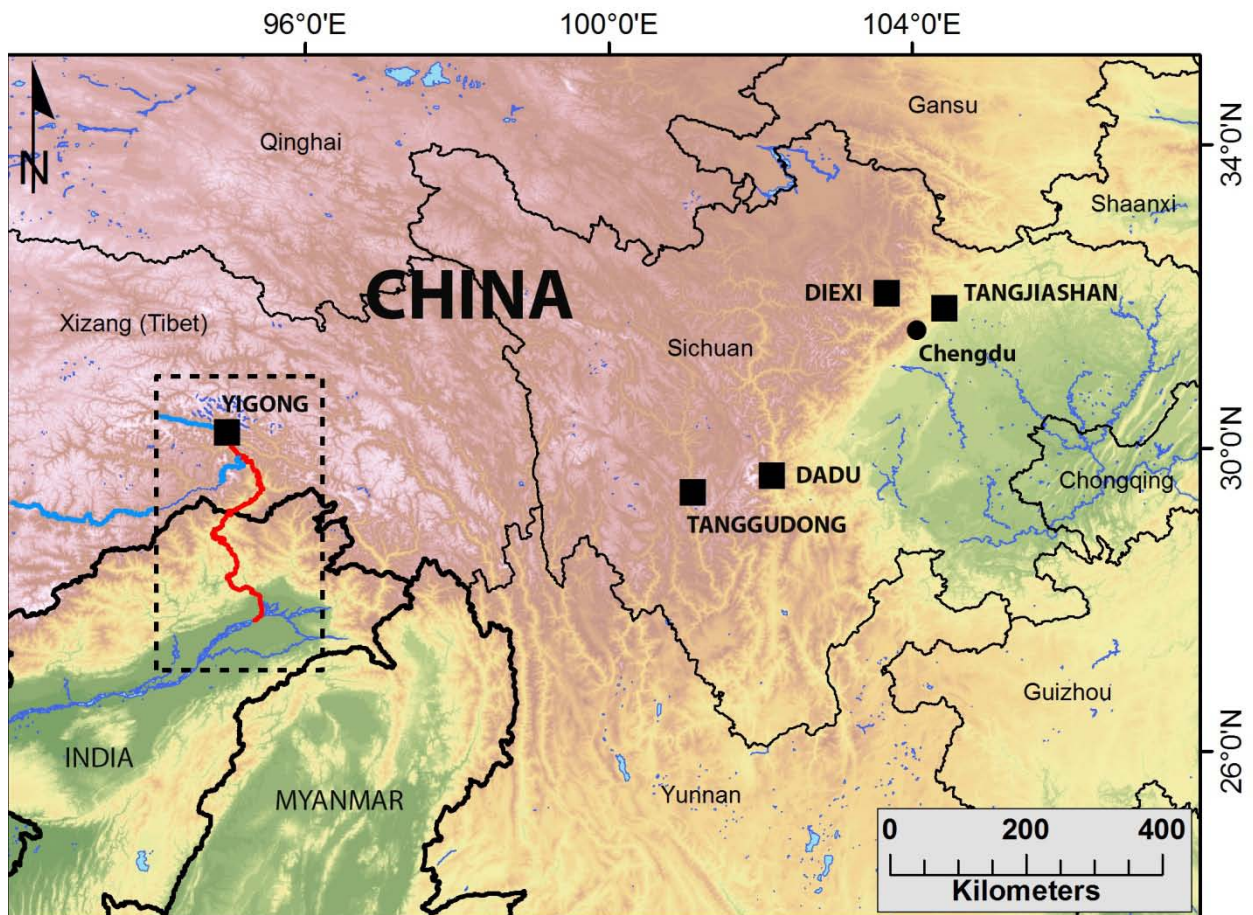
Figure 4.1: Shaded relief map created from SRTM-3 data showing major historical landslide dams in Tibetan Plateau. The 2000 Yigong landslide and rockslide dammed lake is black square within dashed rectangle. Within rectangle, red line traces path of outburst flood. Rectangle outline corresponds to area of Fig. 14A.

Other black squares denote major landslide-dammed impoundments (impounded volume > 100 m[3]) on rivers draining the eastern part of the Tibet Plateau - Dadu River (1786) , Diexi (Min River - 1933), Tanggudong (Yalung River, 1967), and Tangjiashan (2008).

The landslide debris completely blocked the Yigong Zangpo River (Fig. 4.2), a major tributary of the Yarlung Zangpo, which in turn is a major tributary of the Brahmaputra River (Figs. 4.1, 4. 2). The dam failed 62 days later on June 10, 2000 when the debris dam breached following overtopping through an excavated spillway, generating a major outburst flood downstream in the Yarlung Zangpo (Tibet), Dihang, and Bramaputra (India) Rivers.

The Yigong landslide/landslide-dammed lake case history is of global significance because, if the volumes of both landslide and impoundment reported in the literature are correct then: a) the landslide is one of the largest to have occurred worldwide since 1900 and is deserving of the hyperbolic adjectives "monster", "super-large", and "gigantic" that have been variously used to describe it in the literature; b) it formed one of the largest landslide-dammed impoundments documented in history; c) the reported volume (3.0 Gm[3]) of the outburst in the most detailed reports on the event (Shang et al., 2003; Xu et al., 2012) is the largest outburst flood from a landslide-dammed lake ever documented; and, d) discharges of the outburst flood reported 18 km downstream approach the highest reported for an outburst flood (120,000 m[3]/s; Shang et al., 2003).

It is further noted that the 2000 event occurred at the same location as an even larger landslide dam and landslide-dammed lake which formed and failed in 1900, resulting in a massive outburst flood in the Yalung Tsangpo (e.g., Shang et al., 2003). Finally, from a landslide dam engineering standpoint, it is an example of a successful management and mitigation of a major landslide dam emergency (Evans and Delaney, 2011).
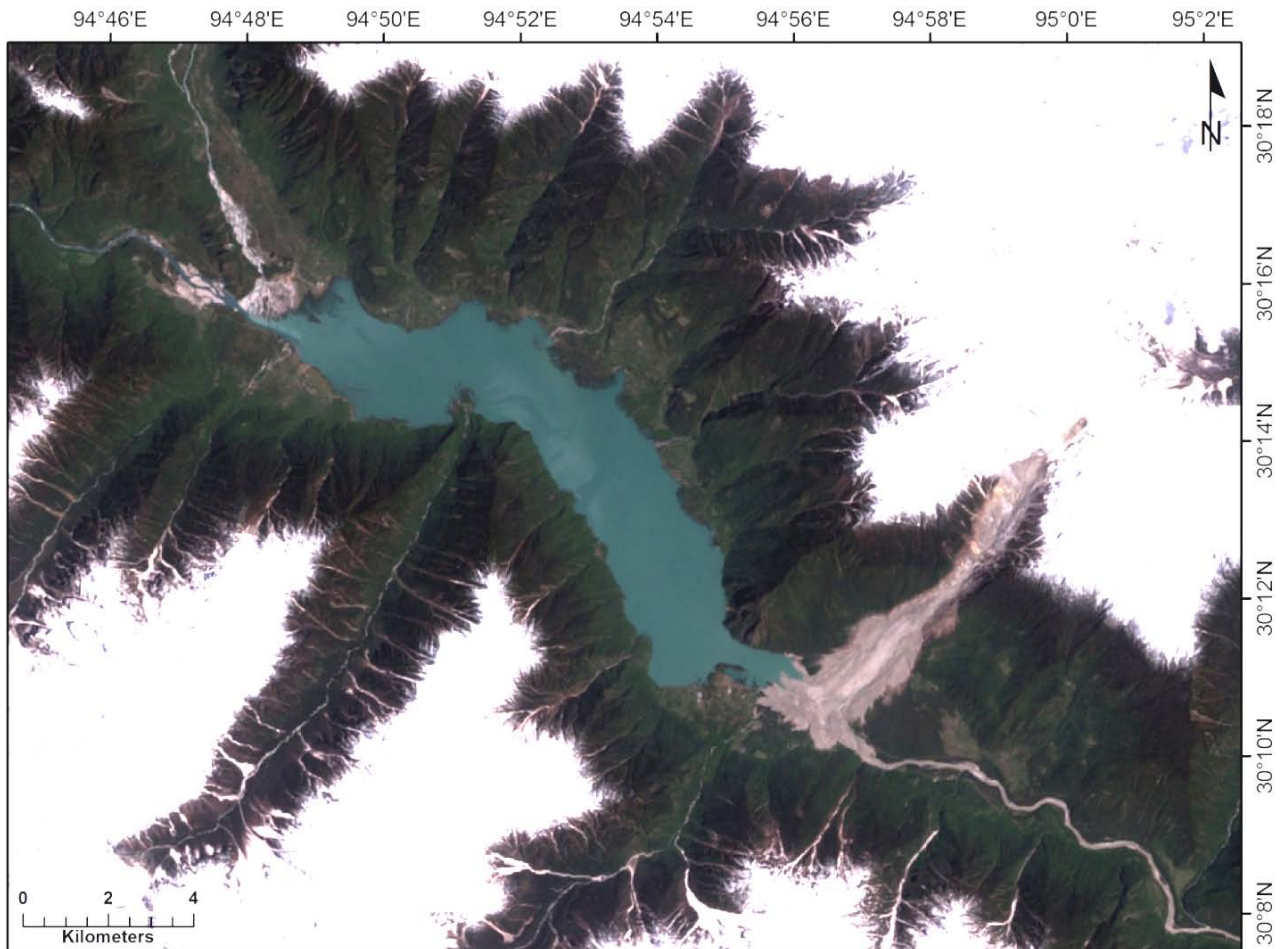
Figure 4.2: LANDSAT-7 image obtained on May 4, 2000 (Day 25 of impoundment) showing Yigong landslide and landslide-dammed Yigong lake forming upstream. Lake pool elevation is estimated at 2,225 m a.s.l. and on this date the lake had a volume of approximately 313 Mm^3.

4.1.3 Motiviation and Objectives of Present Paper

The motivation for the present paper is the existence of notable inconsistencies in the considerable body of published literature (2000-2013) on the 2000 Yigong landslide and the resulting landslide-dammed Yigong Lake. Broadly, these inconsistencies concern the geometry and volume of the damming landslide (including the volume of entrainment (Hungr and Evans, 2004)), the filling behaviour and maximum volume of the impounded Yigong Lake, and the outburst discharge up to 18 km downstream (at the Tongmai bridge) during the breach event on June 10, 2000.

Further, important discrepancies were noted in the most-cited paper on the event by Shang et al. (2003) which have persisted in the most recent paper published on the Yigong events (Xu et al., 2012). These discrepancies concern such key data as the geometry of the damming landslide path, the volume of the source rock mass, the volume of material entrained by the landslide, the final volume of the landslide debris and the geometry of the dam itself, the rate of filling of the landslide-dammed lake, and the final pool geometry and volume of the impoundment which breached on June 10, 2000.

The objectives of this paper are to attempt to resolve these issues through the analysis of remote sensing data (digital topographic data and satellite imagery) available for the Yigong Zangpo region, evaluate the accuracy of the remote sensing data analysis, and to carry out retrospective remote sensing-based modelling of the Yigong rock avalanche and outburst flood.

The landslide dam was emplaced in the evening of April 9, 2000. Our review and analysis uses an event chronology beginning on April 10 (Day 1) and ending on Day 62 (June 10), the date of overtopping and breach. For consistency we refer to the watershed in which the damming landslide occurred as the Zhamulong Gully.

The present paper expands on, and makes corrections to, an earlier paper by Evans and Delaney (2011) which focussed on the filling and geometry of landslide-dammed Yigong Lake.

4.2 **Remote Sensing Methods – Digital Topographic Data and Satellite Imagery**

4.2.1 Digital Topographic Data

We utilise digital topographic data (SRTM-3 v.4.0 (3 arc-second) downloaded from http://srtm.csi.cgiar.org/) acquired during the Shuttle Radar Topography Mission (SRTM) in February 2000 (Farr et al., 2007), only months before the river-damming Yigong landslide occurred. This data has a spatial resolution of 90 m x 90 m and an estimated vertical error of

approximately 10 m in the general region of the Yigong rockslide dam (Fig. 14 in Farr et al., 2007).

To assess more precisely the vertical accuracy of the digital elevation data we followed the method of Becek (2008) which in our case involves the comparison of known airport runway elevations in the World Aeronautical Database (http://worldaerodata.com/), with SRTM-3 data. We examined data for two Tibetan airports located in similar terrain to the Yigong rock avalanche; Qamdo Bangda Airport (30° 33' 13"N; 97° 06' 31"E - 215 km to the east of Yigong) and Gonggar Airport (29 17 52N, 90 54 43E - 400 km to the west of Yigong). The newly constructed Nyinchi Aiport (29° 18' 10"N; 94° 20' 02"E – 113 km to the south-south west) did not exist at the time of the SRTM mission. Gongarr and Qamdo Bangda have registered elevations of 3,570 m a.s.l. and 4,334 m.a.s.l., respectively.

For Qamdo Banga, the SRTM-3 DEM averaged an elevation of 4,336 m.a.s.l. (2 m above). For Gonggar, the SRTM-3 DEM averaged an elevation of 3,575 m.a.s.l. (5 m above). This data suggests that SRTM-3 elevations in the mountainous valleys in Tibet are well within the error range specified for the region in Farr et al. (2007), and superior to the vertical resolution suggested by the contour interval, of a 1:100,000 scale topographic map.

The elevation of the Yigong River at the upstream margin of the landslide dam prior to the event is given as 2,210 m a.s.l. by Wang and Lu (2001) and Zhou et al. (2001). SRTM-3 data also gives an elevation of 2,210 m a.s.l. for the same location; this is the datum used in this analysis.

Using this datum to determine shoreline elevation for each lake level, the lake volume at these levels was calculated using ArcGIS 3D Analyst. The lake bottom bathymetry was taken from the pre-event SRTM-3 DEM of the Yigong valley, and the lake surface elevations were estimated from the optical imagery and reported lake depths at the debris dam.

4.2.2 Optical Satellite Imagery

We analysed LANDSAT-7 imagery obtained on September 23, 1999 (before the landslide dam was emplaced), May 04 and May 20, 2000 (during the filling of the landslide-dammed lake) and August 08, 2000 and December 14, 2000 (after the June 10, 2000 breach and outburst flood). The May images allowed us to delimit the extent of Yigong Lake at two time intervals as it was filling.

Chinese topographic maps of greater scale than 1:1,000,000 of the Yigong area were not available to us and field work in Tibet was not carried out.

4.3 The Yigong Rock Avalanche; Source, Geometry of Initial Failure Mass, Entrainment and Volume of Debris

The Yigong landslide originated at the head of the Zhamulong Gully (30.178N/94.940E) on April 09 2000. The source area is made up of granitoid rocks, which have been partially metamorphosed into granitic gneiss (Shang et al., 2003). Colluvial debris, and debris from previous rock avalanches, fills much of Zhamulong Gully and makes up the debris fan at its mouth. At the mouth of Zhamulong Gully, the Yigong river valley (WNW – ESE) follows the Jiali strike-slip fault (Shang et al., 2005), one of the major active faults of the Tibetan Plateau (Lee et al., 2003).

4.3.1 Volume and Characteristics of the Damming Landslide – Review of Literature 2000-2013

Ren et al. (2001), Zhou et al. (2001), Wang & Lu (2002), and Xu et al. (2008, 2012) report that the landslide occurred at about 20:00 h on April 09, 2000. It had its source in a rock slope high in the head of Zhamulong Gully (Fig. 4.3). Ren et al (2001) and Xu et al. (2008)

are precise about the time of initial failure (19:59h) based on landslide-generated seismogram traces at nearby seismic stations. The landslide was also reported by the USGS National Earthquake Information Centre (http://neic.usgs.gov) as two shallow earthquakes (M3.5 and M4.6) approximately 12 seconds apart (19:59:58 and 20:00:10 local time) with estimated epicentres 5.5 km and 2.5 km, respectively, east of the source area.

Zhou et al. (2001), and Wang & Lu (2002) both report the landslide deposit volume as 300 Mm^3. Ren et al. (2001) present an account based on GPS-controlled traverses of the landslide debris and estimate the total volume of the 2000 deposit to be more than 380 Mm^3.

Other authors distinguish initial and final volume of debris but differ in their estimates of initial and deposit/entrained volumes. Both Han (2003) and Xu et al. (2008) suggest that the landslide initiated as a 30 Mm^3 rockfall from the source area, with the final deposit of 300 Mm^3 apparently due to the entrainment of 270 Mm^3 of material along its path. In the most-cited paper on the 2000 Yigong event, Shang et al. (2003) estimate that the damming landslide had a volume of 300 Mm^3 and report that the initial wedge failure involved a rock mass of about 100 Mm^3 that increased its volume by entrainment to 300 Mm^3 in its ca. 10 km of travel. Wen et al. (2004) report that the initial failure was 200 Mm^3 in volume which entrained 100 Mm^3 more material in its travel down Zhamulong Gully for a final total volume of 300 Mm^3.
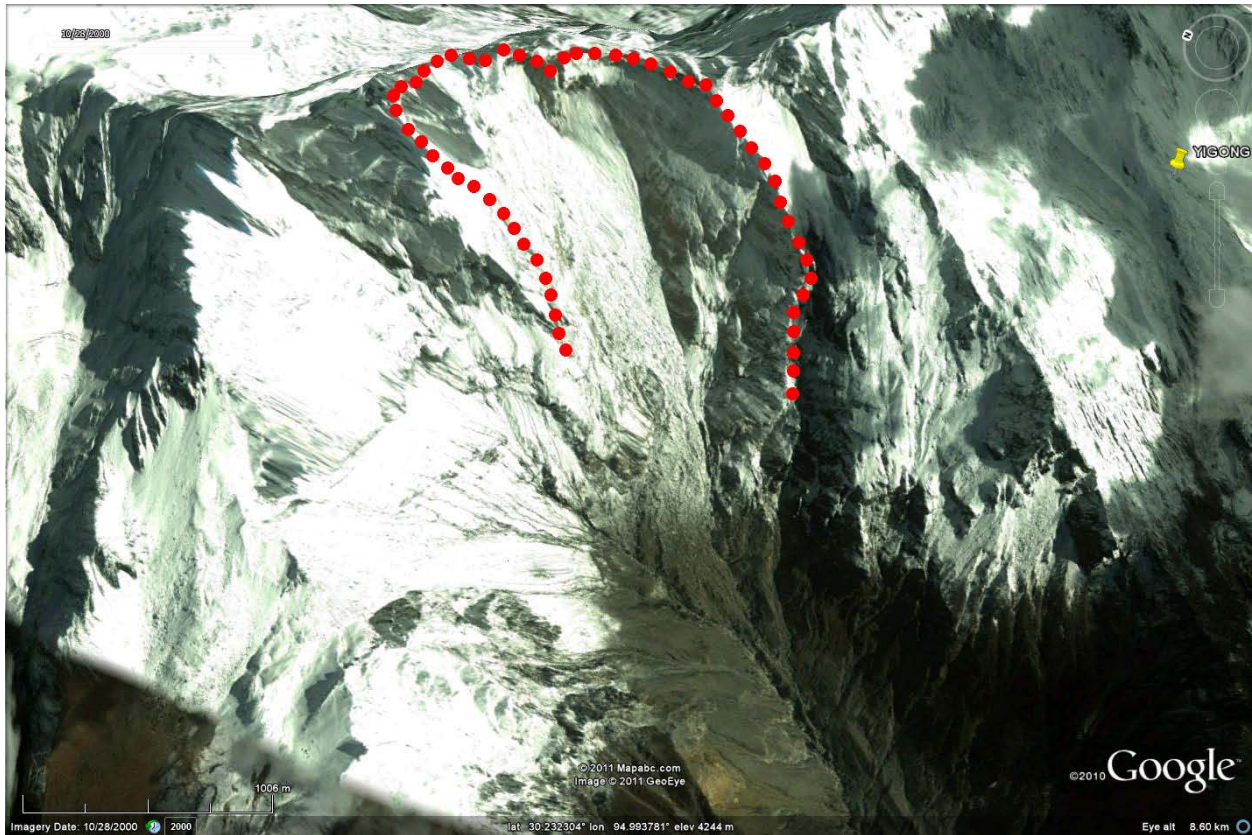
Figure 4.3: Oblique view from Google Earth of source area of 200 Yigong rock avalanche (outlined by *red dotted line*). Note steeply dipping basal sliding surface and left lateral scarp forming a massive wedge failure.

Wang (2008) and Xu et al. (2012) report detailed remote sensing and topographic analyses of the Yigong landslide. With respect to the source volume Wang (2008) estimates that 91.18 Mm^3 of rock was involved in the initial failure, whilst Xu et al. (2012) give a comparable estimate of 90 Mm^3. However, Wang (2008) also calculates the volume of the deposit to be 95.5 Mm^3, roughly the same as the source volume, an estimate apparently not reflecting either bulking of the source rock mass due to fragmentation; and/or entrainment in Zhamulong Gully (which, based on published photographs and satellite imagery of the debris was obviously considerable (see figures in Xu et al., 2012)).

In recognising that previous work overestimated the volume of the landslide (ca. 300 Mm^3), Wang (2008) mentions that this may have been due to the inclusion of the older and dissected remains of the 1900 landslide debris in estimates of the newer 2000 landslide debris volume

(see below). However, Xu et al. (2012), give a final volume estimate of 300 Mm^3 for the 2000 damming landslide, implying a volumetric bulking of 210 Mm^3 due to dilation of the initial failure mass and entrainment of material along its path. If we assume dilation bulking of 20% in the initial failure mass, this suggests entrainment of 182 Mm^3, equivalent to 61% of the final volume.

Most recently, Ekstrom and Stark (2013) presented a novel analysis of seismograms generated by 29 rock avalanches that occurred worldwide between 1980 and 2012; for the Yigong rock avalanche they calculated a total mass of 4.4x10^{11} kg. Assuming a density of 2.68 g/cc for the rock debris this estimate of mass is equivalent to a total mobilised volume of ca. 165 Mm^3.

Thus, in the published works reviewed above: 1) the reported initial failure volume of the Yigong landslide varies by an order of magnitude from 30 to 300 Mm^3; 2) the final debris volume of the landslide reported varies from 91 to 300 Mm^3; and, 3) the volume of entrainment reported varies from 0 to 270 Mm^3.

4.3.2 Path Geometry, Volume and Characteristics of the Damming Landslide – Remote Sensing Analysis

To determine the geometry of the Yigong rock avalanche path and to estimate the extent and volume of the source rock mass and the deposition area of the rock avalanche we: 1) examined pre- and post-event LANDSAT-7 imagery; 2) analysed digital terrain data from the pre-event SRTM-3 dataset obtained just months prior to the landslide; and, 3) re-constructed in GIS, the isopleths of the depletion zone reported by Wang (2008, Fig. 8) and Xu et al. (2012, Fig. 24), and the deposit zone given by Wang (2008, Fig. 13).

The SRTM-3 DEM indicates that the highest point of failed rock in the source area is 5,132 m a.s.l. and the distal tip of the debris is at 2,163 m a.s.l. (H = 2,969 m; Table 2). The total horizontal length of the landslide path (L) is 10,675 m; thus the *fahrböschung* (tan^{-1}H/L) is 15.5º (Fig. 4.4; Table 4-1). The total area of the landslide footprint is 12.3 km^2.
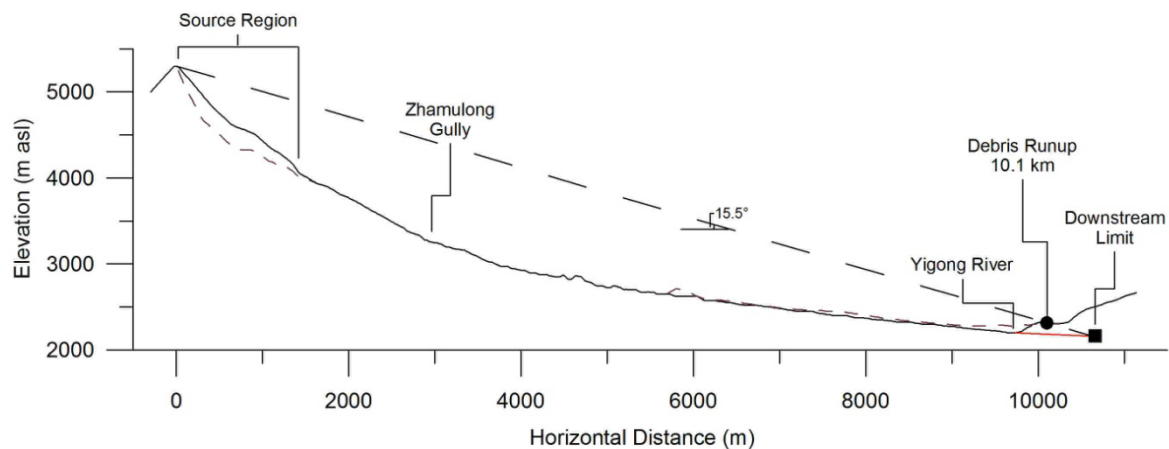
Figure 4.4: Topographic profile of the Yigong rock avalanche based on SRTM-3 digital terrain data. For this profile H = 2,969 m, L = 10,675 m, and fahrböschung ($\tan^{-1}$ H/L) is 15.5°.

By comparing the SRTM-3 DEM and LANDSAT-7 imagery with previously published source and debris isopleth maps (Wang, 2008; Xu et al., 2012) digitised in GIS, Wang's (2008) estimate of the initial failure volume (91 Mm^3) appears plausible.

In estimating the final volume of the debris we digitised the isopleths of debris thickness (Fig. 4.5) from Figure 13 in Wang (2008), which was created from GPS-controlled field mapping. Measured in ArcGIS (Fig. 4.5), the debris isopleths represent a debris volume of only 95 Mm^3, a volume slightly smaller than the bulked initial failure volume estimated above, but a volume that does not reflect any entrainment from Zhamulong Gully. We also compared the SRTM-3 data and LANDSAT-7 imagery with published dam height values, to obtain a rough estimate of debris volume of 115 Mm^3.

Entrainment by the rock avalanche during its travel down Zhamulong Gully is evident on post-event satellite imagery (Fig. 4.2 and 4.5) and is remarked on by several authors (e.g., Wen et al., 2004; Xu et al., 2012). The volume of entrainment is estimated by subtracting the bulked initial failure volume (109 Mm^3) from our estimate of the total volume of the debris (115 Mm^3); this yields ca. 6 Mm^3 of material entrained from Zhamulong Gully.

Thus despite increases in the volume of the initial failure mass due to bulking and entrainment, the estimated total volume of the landslide (115 Mm^3) is slightly over one third of the maximum estimate of 300 Mm^3, the most widely reported volume for the Yigong rock-debris avalanche (e.g. Shang et al., 2003; Xu et al., 2012).
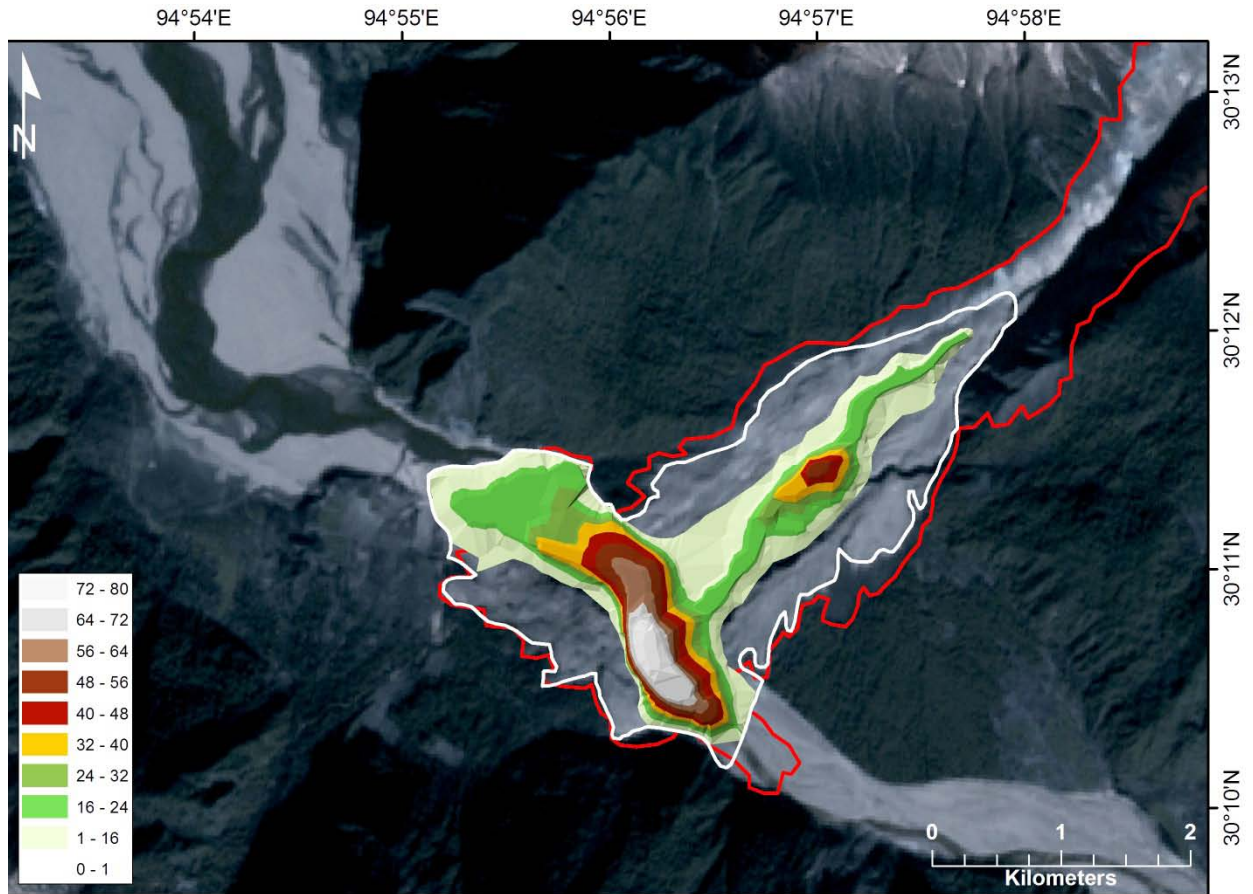
Figure 4.5: A TIN surface of the Yigong rock avalanche debris created by importing debris isopleths from Wang (2008, Figure 13) into ArcGIS to calculate the debris volume (95 Mm^3). Wang (2008), reporting field observations, considered the area between the TIN and the white line (that outlines the debris area) to be thin debris between 0 and 1 m in thickness. Legend gives depth of debris (metres), red outline is total area affected by the rock avalanche. Background image is LANDSAT-7 obtained on December 14, 2000.

Table 4-1: Summary parameters for 2000 Yigong rock avalanche.

Date and time of occurrence	2000-04-09 (20:00 h)
Elevation of top of source rock mass (H1)	5,132 m a.s.l.
Elevation of base of source rock mass (H2)	4,350 m a.s.l.
Area of source rock mass	0.776 km^2
Volume of source rock mass (V)	91 Mm^3
Volume of fragmented source rock mass (V*1.2)	109 Mm^3
Area of debris	6.2 km^2
Volume of debris	115 Mm^3
Volume of entrainment	6 Mm^3
Elevation of distal limit of debris (H3)	2,163 m a.s.l.
Horizontal distance between H1 and H3 (L)	10,675 m
Vertical height of path (H = H1-H3)	2,969 m
H/L	0.278
Fahrboschung (tan^{-1}H/L)	15.5°

4.3.3 The 1900 Landslide Dam

The measurement of the 2000 landslide dam geometry is complicated by the presence of the dissected remnants of the 1900 landslide dam mentioned above. This is evident in the longitudinal profile of the Yigong River in the vicinity of the 2000 landslide dam (Fig. 4.6) which shows aggradation and knick-point development (cf. Korup, 2006; Walsh et al., 2012) associated with the 1900 blockage. The 1900 landslide (the Jazhong landslide) originated in Zhamulong Gully in July 1900 and Zhou et al. (2001) estimates the volume to be 1.0 Gm^3. Zhu et al. (2003) also give details of the 1900 landslide dam (reported as being emplaced in 1902). According to Shang et al. (2003) the 1900 landslide was about 500 Mm^3 in volume and impounded a lake with an area of 51.9 km^2. After one month the 1900 landslide dam breached releasing a reported 2.7 Gm^3 of water (Zhu et al., 2003). The 1900 damming and the development of debris flow fans from the south had resulted in a constriction in the

Yigong valley, aggradation upstream and the development of a braided channel which during high river flows formed a lake (Lake Yigong). Shang et al. (2003) estimates the volume of the 1900 event to be approximately 500 Mm^3, or almost twice the size of their estimation of the 2000 event. This older large rock avalanche would also have created a large impoundment, and been a factor in the creation of the low-gradient braided stream system.
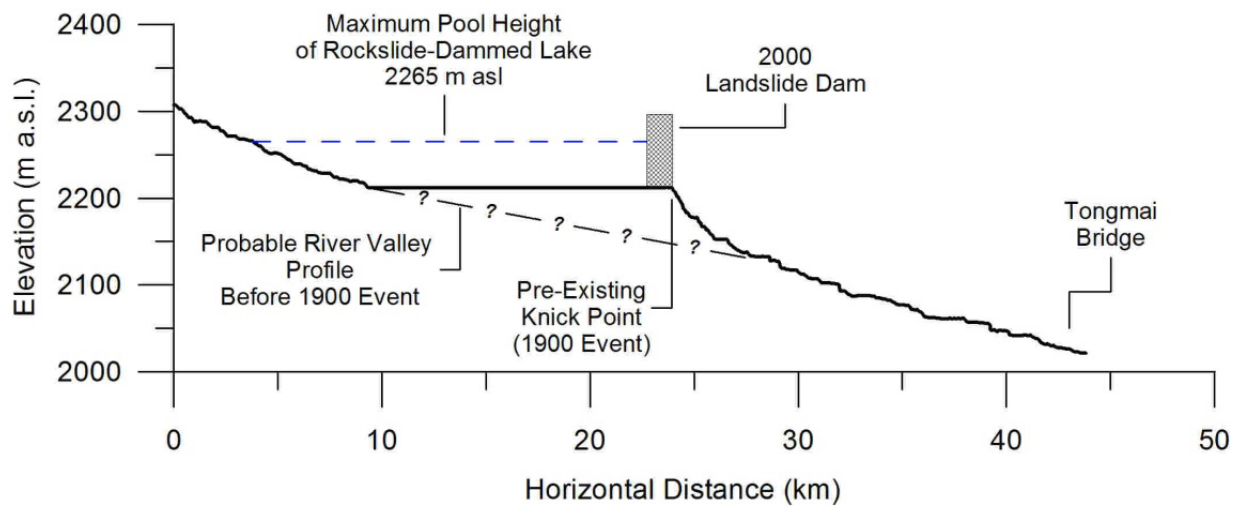
Figure 4.6: Profile (Vertical exaggeration = 41.7 x horizontal) of Yigong River at the site of the 2000 Yigong rock avalanche dam derived from SRTM-3 data. Note location of 1900 rockslide dam forming pre-existing knick point, upstream aggradation behind this dam, the location of the 2000 landslide dam and the maximum elevation of the 2000 rockslide-dammed lake. Note also location of Tongmai Bridge (mentioned in text), 17 km downstream from 2000 dam.

4.4 Dynamic Analysis of the Yigong Rock Avalanche (DAN-W & DAN3D)

A first-order dynamic back analysis of the Yigong landslide was carried out using the two-dimensional numerical simulation model DAN-W (Hungr 1995; Hungr and Evans, 1996; Hungr and McDougall, 2009) and the three-dimensional simulation model DAN3D (Hungr and McDougall, 2009; Sosio et al., 2012). DAN-W and DAN3D have been used to simulate the behavior (i.e. run-out distance, velocity along path, and deposit depths) of a number of catastrophic landslides including rock avalanches, debris avalanches, and debris flows (e.g. Hungr and Evans 1996; Evans et al. 2001, 2007; Hungr and Evans 2004; Sosio et al. 2008, 2012; Delaney and Evans, 2014).

For both 2D and 3D simulations, the Voellmy rheology (Hungr 1995) was selected to model the basal resistance of the moving mass. The Voellmy basal resistance model consists of frictional (f) and turbulence (ξ) parameters, which are estimated on the basis of empirical field observations to produce a simulation that best fits the observed landslide behavior from failure, through transport, and deposition. For non-glacial rock avalanches, Hungr and Evans (1996) found that frictional parameters (f) ranging from 0.03 to 0.24, and turbulence parameters (ξ) ranging from 100 to 1000 m/s^2 have been successfully used to simulate similar mass movements.

4.4.1 Two-Dimensional Simulation Using DAN-W

The DAN-W simulation requires that the path widths along the entire length of the profile be input as an initial parameter. These path widths were measured from a 15m panchromatic LANDSAT-7 ETM image obtained on May 04, 2000 (Fig. 4.2). Given the source volume determined above, path widths from LANDSAT-7 satellite imagery and topography from the SRTM-3 DEM, the runout, velocity, and depth of deposition can be simulated using appropriate Voellmy model parameters (f and ξ) (Fig. 7).

Three surface materials, corresponding to source (A in Fig. 4.7), entrainment (B in Fig. 4.7), and depsotion (C in Fig. 4.7) were defined for the path of the landslide. The values of the friction (f) and turbulence (ξ) parameters for each of these segments that best simulated the emplacement behavior are listed in the caption of Fig. 4.7.
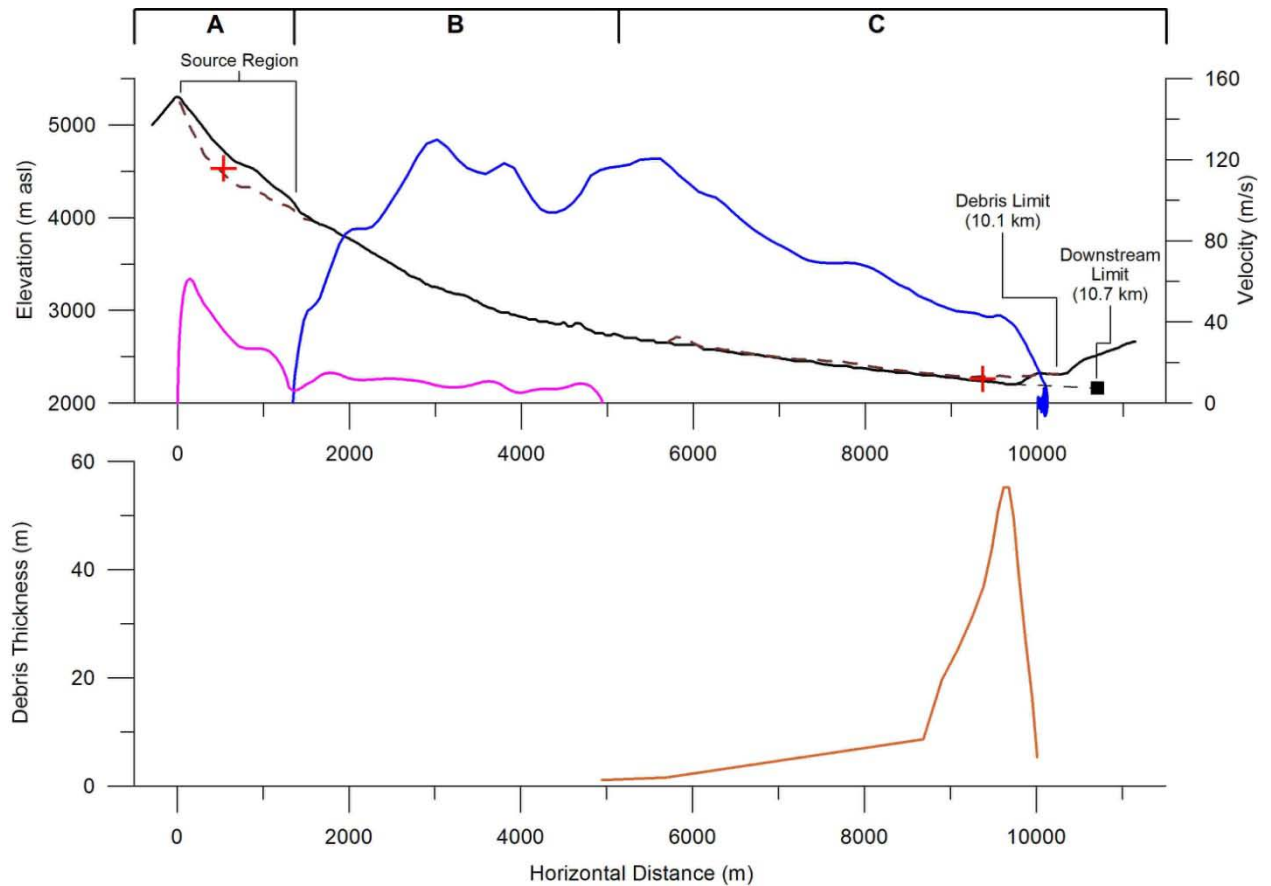
Figure 4.7: The upper plot shows the results from the 2D DAN-W simulation showing the velocity of the moving mass (*blue* = front velocity, *purple* = rear velocity), the displacement of the centre of gravity (*red crosses*), and the topographic profile of the rock avalanche from Fig.4 (based on SRTM-3 data). Path segments are delimited at the top of the plot - A (source), B (entrainment), and C (deposition). Voellmy parameters used for path segments were as follows; A, f=0.10 and ξ = 750 m/s^2; B, f=0,08 and ξ = 800 m/s^2, and C, f=0.05 and ξ=900 m/s^2. In segment B an entrainment depth of 3 m was assumed. The lower plot shows the DAN-W simulated debris thickness.

Note that the values of the Voellmy parameters assigned to the surface materials in the three path segments fall (Fig. 4.7) within the range used in previous successful simulations of similar landslides (e.g. Hungr and Evans 1996; Ayotte and Hungr 2000; Evans et al. 2009; Guthrie et al. 2012). The change in the Voellmy parameters along the rock avalanche path (Fig. 4.7) generally reflect the transformation of an initial fragmenting rock avalanche into a more complex rock-debris flow characterised by increasing fluidity and increasing mass by the addition of materials through entrainment.

For a DAN-W determined source volume of 92.8 Mm^3, the Voellmy rheology simulated a runout distance of 10,012 m and a depth of the debris deposit of 55.3 m at the confluence of Zhamulong Creek and the main channel of the Yigong river (Fig. 4.7). The source volume is slightly larger than the change detection estimation, due to the coarse topographic data points inputted into the simulation model. DAN-W also simulated the total duration of the flow as 575 seconds, However, this time includes some of the internal debris 'sloshing' back and forth at the end of the simulation (runup and fall-back of the debris on the opposite bank, shown as negative velocities in Fig. 4.7) where the general deposit geometry remained unchanged. The simulated DAN-W rock avalanche reached a maximum velocity of 129.9 m/s 3.02 km from the source, and resulted in an average velocity of 17.6 m/s for the entire event.

From the post-event LANDSAT-7 imagery (cf. Fig 4.2), it is clear that some amount of entrainment occurred. In DAN-W we specified a 3 m depth of entrainment in path segment B (horizontal path length = 3,750 m) in Fig. 4.7. As a result of entrainment, the original simulated source volume (92.8 Mm^3) resulted in a final deposit volume of 101.4 Mm^3, an increase of 8.6 Mm^3. These values can be compared to the original change detection volumes of 91 Mm^3 for the source mass, 109 Mm^3 for the bulked fragmented source material, and 115 Mm^3 of the final deposit volume, from the GIS analysis.

DAN-W estimated that the centre of gravity of the rock avalanche originated at a height of 4,532 m a.s.l., and dropped vertically 2,271 m, to an elevation of 2,261 m a.s.l., while travelling a horizontal distance of 8,833 m (Fig. 4.7). The travel angle, the angle of the line joining the two centres of gravity, is equivalent to the true angle of friction (φ) of a rock avalanche (cf. Delaney and Evans, 2014); for the Yigong rock avalanche, the true angle of friction is 14.4°, representing a coefficient of friction of 0.25. This represents a reduction in friction of 36% for granitic gneiss due to transport effects.

The final deposit forming the rockslide dam was simulated by DAN-W to be a maximum of 55.3 m in depth (Fig. 4.7) equivalent to an elevation of 2,265.3 m a.s.l. This corresponds to the observed maximum elevation (2,265 m a.s.l.) reached by the rockslide-dammed lake before overtopping and breaching (see discussion below) and the final lake depth (55 m) given by Zhou et al. (2001), Shang et al. (2003), and Xu et al. (2012).

4.4.2 Three-Dimensional Simulation Using DAN3D

The Voellmy parameters that resulted in the best-fit DAN-W simulation obtained above were then used in a 3-dimensional DAN3D simulation. DAN3D differs from DAN-W in that it does not require an input of path widths that constrain the movement. Instead, the debris is free to interact dynamically with the topographic surface, which in this case is determined by the SRTM-3 DEM. Due to the unconstrained topography used in DAN3D, the Voellmy parameters were modified slightly to best simulate the event, and the number of materials was reduced to two for computational reasons (Fig. 4.8).

The DAN3D analysis was reasonably successful in simulating the geometry and emplacement dynamics of the Yigong rock avalanche (Fig. 8). DAN3D estimated a total source volume of 91.7 Mm^3, a runout distance of 9,940 m, a total duration of 639 seconds, and a *fahrboschung* of 16.3°. This implies an average velocity of 15.6 m/s, comparable to the 17.6 m/s simulated from DAN-W. An increase in the turbulence parameters in the 3D model was required to reflect the behaviour of the channelized flow in Zhamulong Gully. The DAN-W simulation has path widths which cannot be exceeded, forcing the total flow through the narrow Zhamulong Gully, whereas the DAN-3D simulation allowed the mass to expand slightly beyond these path width limits, decreasing its turbulence and resulting velocity.
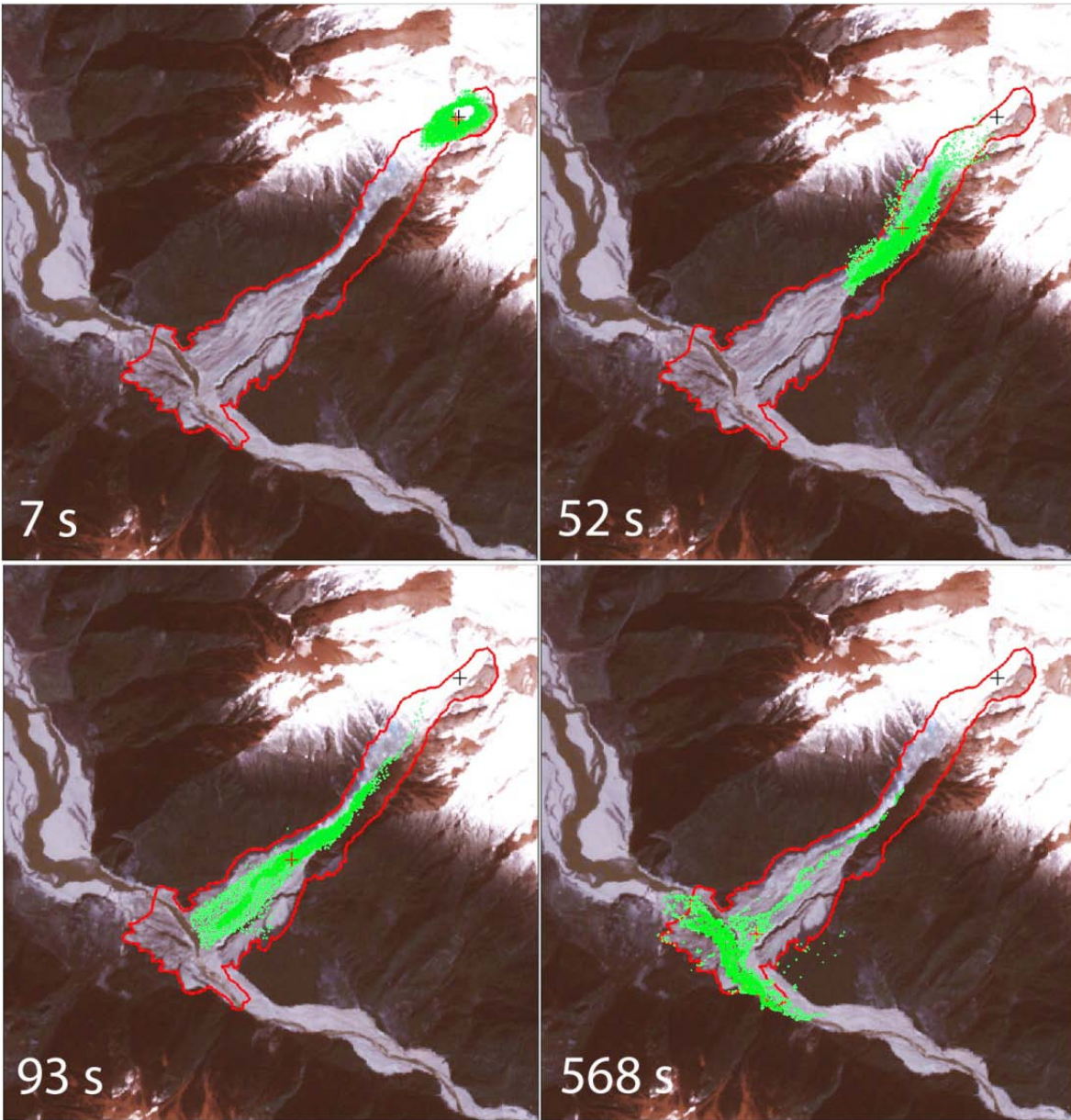
Figure 4.8: Outputs from the DAN3D simulation (*green dots*) at 4 successive time steps using a Voellmy rheology for basal resistance approximation. Green dots are the 4,000 particles that DAN3D uses to simulate the fragmenting rock mass in its travel downslope. Voellmy parameters used for simulation are as follows: source region, $f = 0.05$, $\xi = 1,1250$ m/s^2; path, $f=0.08$, $\xi = 1,250$ m/s^2. *Red line* is outline of rock avalanche path from post-event satellite imagery (Fig. 2). Background image is LANDSAT-7 obtained on December 14, 2000.

Figure 4.8 shows a temporal sequence of rock avalanche motion, as simulated by DAN3D. The 4000 green dots created by DAN3D represent the total volume of the material divided by the total number of particles, and is the maximum number allowable in the model; there is no

108

further fragmentation of the particles during movement or addition to the total number through entrainment as the simulation progresses.

The DAN3D simulation probably under-estimates the total extent (runout distance and area) of the deposit, while possibly overestimating its depth. The flow-lines of the particles (Fig. 4.8) appear to visually match the observed field characteristics of the deposit surface, and the debris is deepest at the confluence of Zhamulong Gully and the Yigong River as indicated by Wang (2008) and Fig. 4.5 above. Although the number of modelled particles cannot change during the simulation (see above), DAN3D is able to incorporate entrainment of debris along its path by adding to the mass of the particles through the specification of an entrainment rate. Thus, the original source volume (91.7 Mm^3) was increased downslope through entrainment to a final deposit volume of 102.6 Mm^3, an increase of 10.9 Mm^3 of additional material in the DAN3D simulation. These values are compared to the original change detection volumes of 91 Mm^3 for the source region, 109 Mm^3 of the bulked source mass, and 115 Mm^3 of the final deposit volume.

4.4.3 Evaluation of 2D and 3D Simulations

Overall, the two simulations had similar results. The runout of the rock avalanche was simulated almost precisely by both DAN-W and DAN3D. The 2D and 3D simulations produced rockslide dam volumes with a difference of only 1.2 Mm^3, and which were similar to the volumes calculated by Wang (2008) on the basis of a field survey. The DAN3D simulation did continue on past 639 seconds to a total of 779 seconds; however as with the DAN-W simulation, this included only small internal movements of the debris. Both simulations were able to incorporated some entrainment (DAN-W: 8.6 Mm^3; DAN3D: 10.9 Mm^3) which made important contributions to the final debris volume.
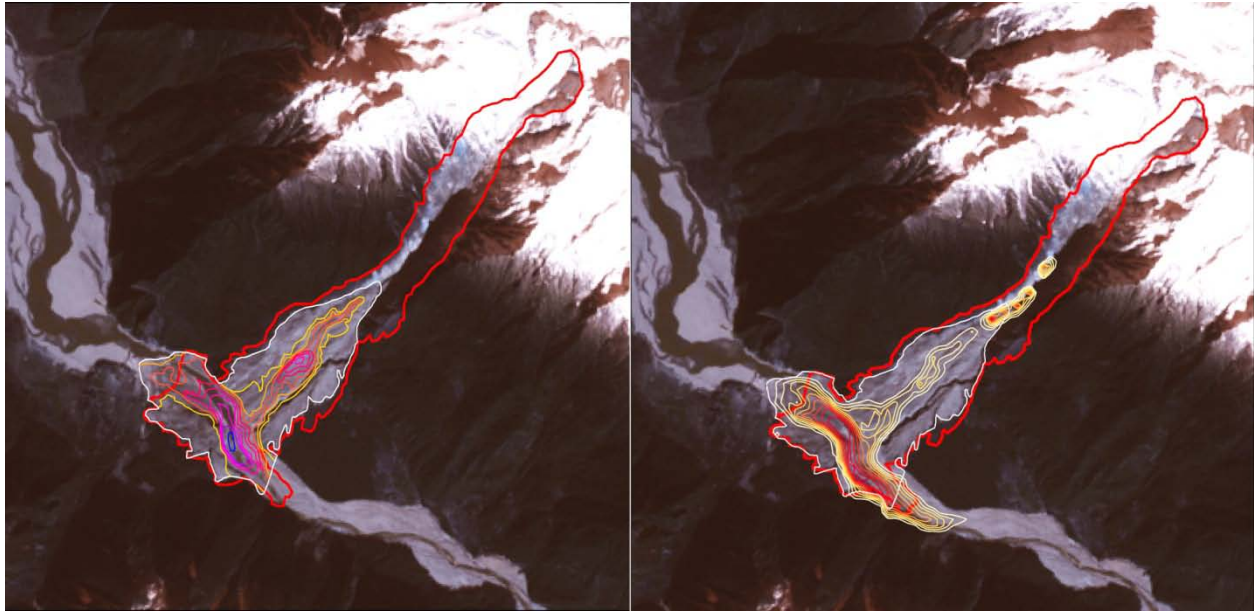
Figure 4.9: Comparison of debris distribution and depth between digitized contours of debris depth in Wang (2008; Fig. 13) (*left*) based on a field survey and the simulated deposition of the Yigong rock avalanche by DAN3D (*right*). Wang (2008) measured a maximum depth of ca. 80 m (*blue contour*), while DAN3D simulated a maximum depth of 55 m (*dark red contour*). DAN-W also simulated a maximum debris depth of 55 metres at this location. Background image is LANDSAT-7 obtained on December 14, 2000.

We compared the digitized field-determined deposit isopleths from Wang (2008, Figure 13) with our DAN3D simulation (Fig. 9). We note that that Wang (2008) defined regions in Fig. 4.5 where the debris was less than 1 metre in depth, and "*approaches zero where the ground surface is basically unchanged*" (Wang, 2008, p. 2116). It is noted that DAN3D also simulates the outline of this region of very thin (or none) deposition (Fig. 4.9). In addition, the overall bulk shape of the mass is shown to be very similar to the field mapped outline following the thalweg of Zhamulong Gully, the overall shape of the alluvial fan, and the Yigong River valley (Fig. 4.9).

During their field investigation, Wang (2008) also identified an isolated mass of debris (455 x 10^4 m^3) which remained at the mouth of the Zhamulong Gully, approximately 5 km along the landslide path (polygon 'G' in Fig. 13 in Wang (2008)). It is of interest to note that DAN3D also simulated this mass (Fig. 4.9), which was not transported the entire length of the path, and stopped where Zhamulong Gully widens onto the main alluvial fan in the lower reaches of the valley (Fig. 4.9).

110

If we assume that the original Yigong River valley is located at a height of 2,210 m a.s.l. (see discussion of SRTM-3 data above), the DAN-W and DAN3D simulated depths of 55 metres would imply a maximum dam elevation of 2,265 m a.s.l. This corresponds very well to the maximum lake depth (55 m) and equivalent elevation of the actual overtopping (2,265 m a.s.l.) and breach suggested by Shang et al. (2003) and others.

In summary, the DAN-W and DAN3D simulations appear to have successfully replicated the landslide dam volume, the depth distribution, areal extent, and overall bulk shape of the debris forming the dam, and its overtopping elevation.

4.4.4 Energetics of Landslide Movement

Assuming an average density of 2,600 kg/m^3 for the source rock and a volume of 91 Mm^3, results in an estimated source mass of 2.37×10^{11} kg, before entrainment along the rock avalanche path. Using the equation for potential energy ($PE = zg\gamma V$; where z is the vertical distance between the centres of gravity from the initial to final position estimated from the DAN-W simulation (Fig. 4.7), g is the gravitational constant, γ is the unit weight of the material, and V is the failed source volume; Erismann and Abele (2001)), we estimate that the Yigong rock avalanche had a minimum potential energy of 5.27×10^{15} J. Ekström and Stark (2013) attempted to calculate the potential energy of the Yigong event by integrating the vertical component of the landslide force history from seismograms, resulting in a comparable value of 4.12×10^{15} J. In terms of specific energy (defined as energy per unit mass) the rock avalanche expended a total of 2.23×10^4 J/kg; the specific energy can be taken as a measure of the potential energy stored per unit mass in the source rock mass. The value for the Yigong event is typical of rock avalanches (Delaney and Evans, 2014). These calculations, however, do not consider the energetic implications of the entrainment of additional material during emplacement.

4.5 **The Filling of Yigong Lake and Estimate of Maximum Lake Volume I –
Review of Literature 2000-2013**

4.5.1 The Filling of the Landslide-Dammed Lake

The landslide debris blocked the Yigong River forming a landslide-dammed lake (Yigong Lake) which is reported to have flooded several villages and the Yigong tea plantation (Xu and Wang, 2008; Xu et al., 2012). As detailed by Evans and Delaney (2011), Zhou et al (2001) and Han (2003) report a satellite image analysis of the filling of Yigong Lake, expressed as an increase in lake surface area.

In a more complete report Wang and Lu (2002) also outline a satellite image analysis of the Yigong events and they provide key data in the most detailed and systematic study of lake filling (Table 1 in Wang and Lu, 2002). These datasets are plotted in Figure 4.10. Topographic control was provided by: 1) measurement of post-event ground control points by GPS on the surface of the landslide deposit; and, 2) selection of pre-event ground control points from a 1:100,000 scale topographic map. As seen in Table 2, Wang and Lu (2002) examined 5 sets of satellite imagery obtained during the impoundment; the last satellite image examined is dated May 20 (Day 41), 21 days before the breach. Pre-event contour data was apparently derived from the 1:100,000 scale topographic map.
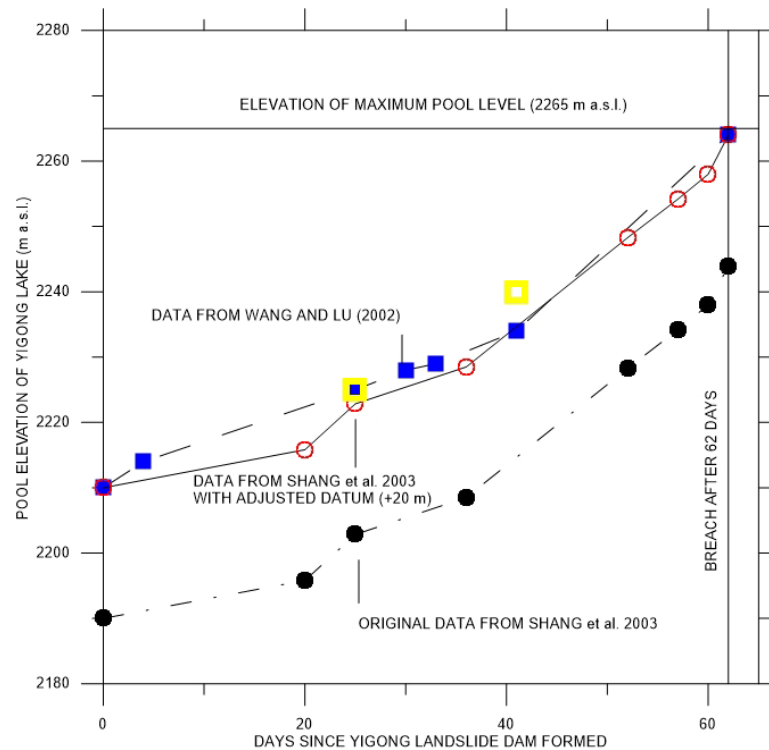
Figure 4.10: Filling curves for rockslide-dammed Yigong lake based on data of Wang and Lu (2002) in Table 2 and data derived from Fig. 8 in Shang et al. (2003). The original data of Shang et al. (2003) was plotted with a datum at 2,190 m a.s.l. When using the same datum as Wang and Lu (2002) (2,210 m a.s.l. - 20 m higher) the filling curves are very close. *Yellow squares* are the pool elevations determined on Days 25 and 41 from LANDSAT-7 imagery and SRTM-3 DEM.

Shang et al. (2003) report that the landslide dam was 2,500 m in length along the thalweg of the Yigong River. No elevations of the water level during lake filling are provided by Shang et al (2003) but, noting that the lake was 15 km^2 in area on April 14 (Day 5; cf. Zhou et al 2001), Shang et al (2003) report the lake volume as 70 Mm^3 on that day. No additional volume estimates are given during filling, and lake areas given by Shang et al. (2003) are reproduced from Zhou et al (2001) up to May 9 (Day 30), 32 days before the breach.

Shang et al. (2003) note that during the 62 days of impoundment the water rose by about 54.0 m in the landslide-dammed lake. Pre-event elevations in the paper are apparently taken from a report on the area completed in the mid-1980s (see Fig. 3 in Shang et al. 2003) and the elevation of the Yigong River channel directly upstream of the landslide is given as 2,190 m a.s.l. (see Fig. 6 in Shang et al. 2003), 20 m below the elevations reported by Zhou et al.

113

(2001) and Wang and Lu (2001) (Fig. 10), as well as the values we obtained from the SRTM-3 DEM. Data given by Shang et al. (2003) thus suggest a final pool elevation of only 2,244 m a.s.l (i.e., 2190 + 54m).

However, if we assume that the pre-landslide river bed had an elevation of 2,210 m a.s.l. as given in Zhou et al. (2001), Wang and Lu (2001), and the SRTM-3 DEM, then the depth (54.0 m) reported by Shang et al. (2003) and others is equivalent to a full pool elevation of 2,264 m a.s.l. (Fig. 10). Xu et al. (2012) also calculated a final lake depth of 55.0 m, a similar value to the elevations given in Shang et al. (2003) and Zhou et al. (2001). Shang et al. (2003) also present a time-line diagram (Fig. 8 in Shang et al. (2001)) which indicates that the lake level increased by 45.0 m in the 37 days between May 4 (Day 25) and June 10 (Day 62), the day of the breach. This data does not correspond with that in Table 3 which tabulates the data of Wang and Lu (2002).

Table 4-2: The filling of Yigong rockslide-dammed lake reported by Wang and Lu (2002) (Data reproduced from Table 2 in Wang and Lu (2002)). Pre-lake datum is given by Wang and Lu (2002) as 2210 m a.s.l.

Date	Day of Impoundment	Elevation of rockslide-dammed lake (m a.s.l.)	Lake area (km^2)	Lake volume (Mm^3)
2000-4-13	4	2,214	18.909	85.4
2000-5-4	25	2,225	33.659	514.3
2000-5-9	30	2,228	36.32	706.2
2000-5-12	33	2,229	37.979	770.7
2000-5-20	41	2,234	43.121	1,234.5
2000-6-10	62	2,264[1]	52.855	2,259.0

---

[1] Elevation given in original Table is 2,244 m a.s.l. which was a typographical error. The correct value is 2,264 m a.s.l. (Z. Wang, personal communication to the authors, 2009).

4.5.2 The Maximum Pool Elevation and Pre-Breach Volume of Yigong Lake

Zhou et al. (2001) do not report the maximum lake level before breaching nor estimate the pre-breach/outburst volume. However, they estimate the lowest height of the landslide dam above the river channel at 55.0 m (p. 328 and p. 331). Xu et al. (2012, p. 603) report a similar observation, i.e., that the lake water level rose to a maximum depth of 55.36 m. Since the elevation of the river channel directly upstream of the dam is given as 2,210 m (Fig. 5 in Zhou et al. 2001; SRTM-3 data) this suggests a maximum possible pool elevation before overtopping of the landslide dammed lake of ca. 2,265 m a.s.l. We note that the lowest point on the crest of the upstream face is in the order of 2,282 m a.s.l. and the highest point of the dam is 2,306 m a.s.l The spillway reported to have been dug was 18 m deep at the dam crest (Yang et al., 2010) which effectively constrains a maximum pool elevation at about 2,265 m a.s.l.

Wang and Lu (2002; Table 1) report the immediate pre-breach volume as 2.259 Gm^3 for a landslide dammed lake 52.855 km^2 in area and a maximum water level elevation of 2,264 m a.s.l. (Table 4-2). The sources of this final estimate are not given.

Zhu et al. (2003), Shang et al. (2003), and Xu et al. (2012) all estimate the outburst volume as 3.0 Gm^3. Wang (2008) estimates that 2.4 Gm^3 of water outburst from Yigong Lake after reaching a maximum pool elevation of 2,280 m a.s.l., the highest of the maximum published pool elevation estimates.

4.5.3 The Excavated Spillway and the Timing of the Breach

The timing of the breach was linked to the excavation of a spillway over the debris by Chinese soldiers using heavy machinery (Han 2003; Xu and Wang, 2008; also see time-line diagram in Fig. 8 in Shang et al. (2003). According to Shang et al. (2003) excavation of the spillway began on May 3 (Day 24) and was completed as designed on June 3 (Day 55), after the excavation of 1.36 Mm^3 of rock and soil. The spillway had a maximum depth of 24.1 m but was only 18 m deep at the dam crest (Yang et al., 2010). No elevation is reported for the

spillway. Han (2003) reports that water began to flow in this channel at 06:00 on June 8 (Day 60) and that the dam failed catastrophically on June 10 (Day 62).

Wang and Lu (2002) give the time and date of the breach as 21:30 on June 10, 2000 (Day 62). Xu et al. (2008) note that following the excavation of a man-made spillway the lake drained catastrophically earlier on June 10 (Day 62) at 21:00.

Thus in reviewing published works, with respect to the landslide-impounded Yigong Lake: 1) the maximum pool elevations reported vary from 2,244 to 2,280 m a.s.l.; and, 2) reported impounded volumes varied from 2.259 to 3.0 Gm^3, estimates that also correspond to the range in reported outburst volumes.

4.6 The Filling of Yigong Lake and Estimate of Maximum Lake Volume II – Remote Sensing Analysis

4.6.1 The Filling of the Landslide-Dammed Lake

In order to track the filling of Yigong Lake and to estimate its maximum volume before it breached on June 10, 2000 (Day 62) we constructed a digital elevation model (DEM) of the topography forming the Yigong Lake basin using SRTM-3 digital terrain data obtained in February 2000.

As noted above, SRTM-3 data and elevations given by Wang and Lu (2001) and Zhou et al. (2001) establish that the elevation of the Yigong River valley at the upstream face of the landslide dam is 2210 m a.s.l. This is also taken as the pre-event datum by Wang and Lu (2002) and assumed as the datum in our calculations for relative water level measurements reported in Shang et al. (2003; Fig. 8). These data are compared to those derived from our analysis of the SRTM-3 DEM.

LANDSAT-7 images from May 4 (Day 25) and May 20 (Day 41) showing the extent of Yigong Lake on those dates were imported into the SRTM-3 DEM and the lake levels were visually matched at 2,225 m a.s.l. and 2,240 m a.s.l. respectively on these dates (Fig. 4.11). Data obtained from Table 2 in Wang and Lu (2002) (reproduced above in Table 4-2 in this paper) and derived from Fig. 8 in Shang et al. (2003) give lake elevations for May 4 (Day 25) of 2,225 and 2,220 m a.s.l. respectively, assuming the datum at 2,210 m a.s.l., and for May 20 (Day 41) of 2,234 and 2,233 m a.s.l. respectively (Fig. 4.10). For May 4, the elevation of Wang and Lu (2002) corresponds precisely with the SRTM-3 data. The estimate derived from Shang et al. (2003) is 5 m below the lake level given by SRTM-3 data based on the extent of Yigong Lake obtained from LANDSAT-7 images; for May 20 the differences are 6 m and 7 m below the SRTM-3 surface obtained from a visual match of lake outlines visible on LANDSAT-7 imagery (Fig. 4.10). The difference reflects the difference in the resolution of the data sets.

We have noted that Shang et al. (2003) report a final lake depth of 54 m and that this roughly corresponds to that reported by Zhou et al. (2001) and Xu et al., (2012). This maximum depth is thus equivalent to a maximum water elevation of 2,264 m a.s.l. and, rounding to 2,265 m a.s.l., we take this as a credible estimate of the maximum water level reached by Yigong Lake on Day 62, the day of the breach, based on reported maximum lake depths.
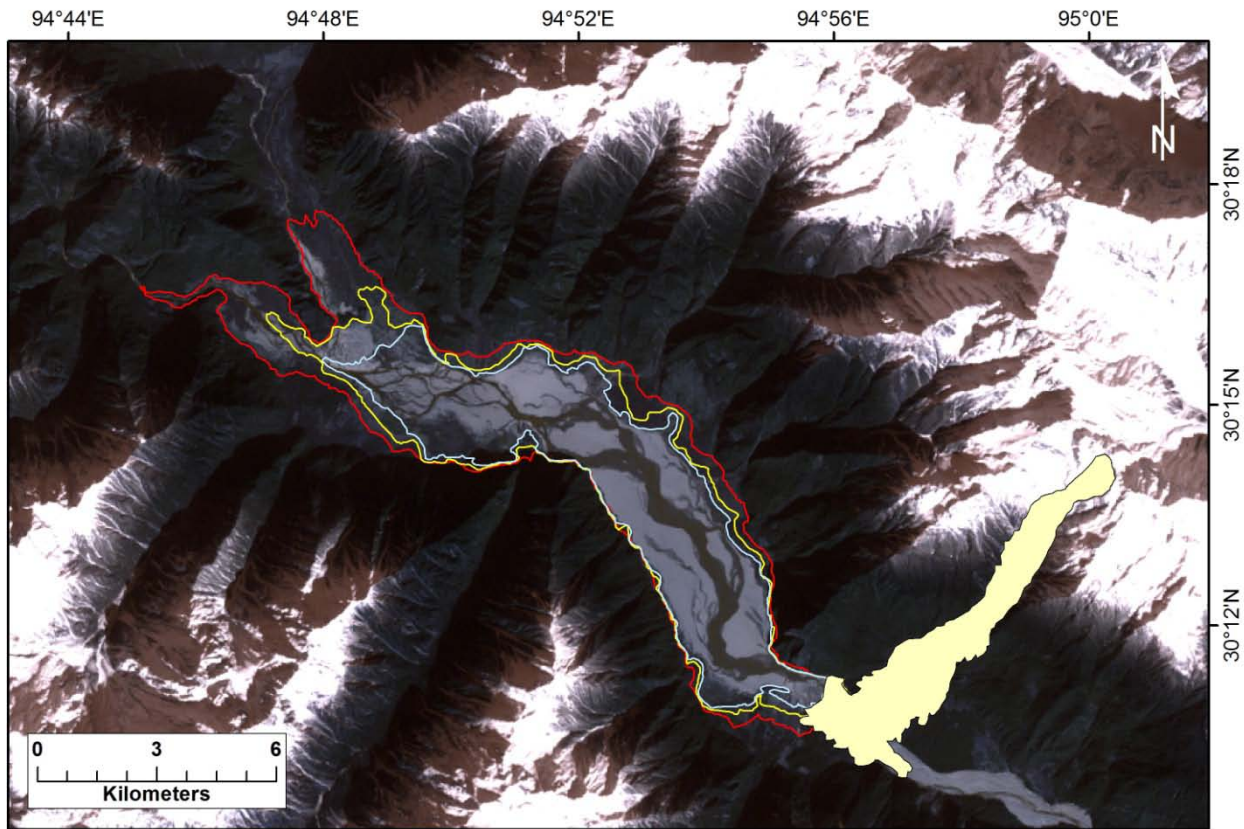
Figure 4.11: LANDSAT-7 image obtained on December 2000 with outline of Yigong rock avalanche (*yellow fill*) and outline of rockslide-dammed lake at lake levels on May 4 2000 (2,225 m a.s.l. - *blue*), May 24, 2000 (2,240 m a.s.l.- *yellow*) and June 10, 2000 (2,2265 m a.s.l. full pool elevation before overtopping and breaching - *red*). SRTM DEM assumes datum for lake depth of zero is 2,210 m a.s.l. (see text for discussion).

4.6.2 Maximum Volume of Landslide-Dammed Lake

Using 3D Analyst in ArcGIS we then calculated the area of Yigong Lake and the volume of water impounded at ten lake levels from 2,220 m a.s.l. to 2,280 m a.s.l. (Table 4-3) using the SRTM-3 topography to approximate the ground surface of the lake basin (Fig. 4.12). The data of Wang and Lu (2002) in Table 4-2 closely follows the power law best fit line with the exception of their final data point which seems to be anomalous (Fig. 4.12).

118
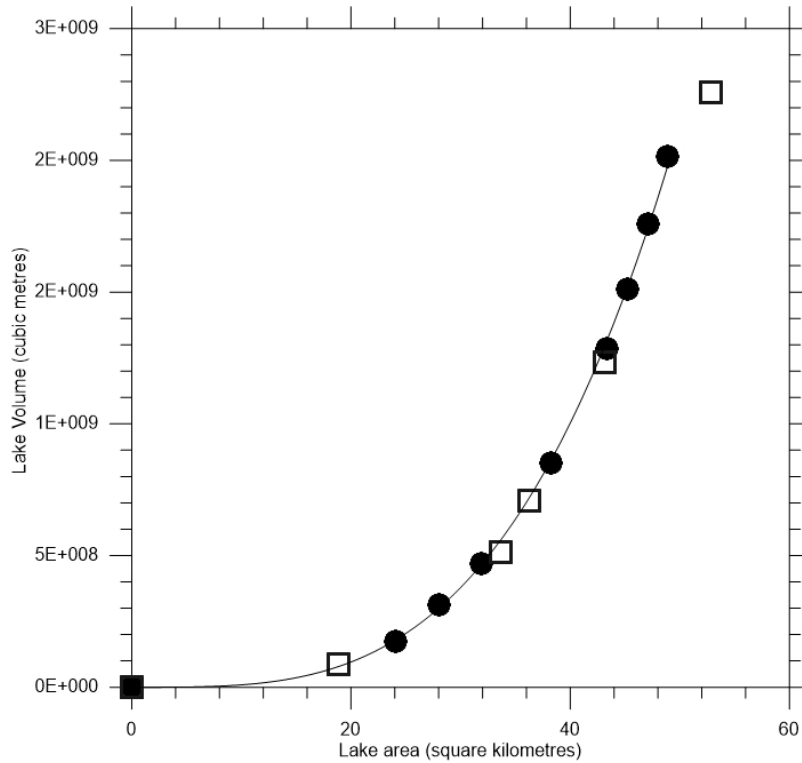
Figure 4.12: Plot of rockslide-dammed lake volume v area. *Black dots* are from SRTM-3 DEM in this work (Table 3) and *open black squares* are data from Wang and Lu (2002) in Table 4-2. Best fit line is a power law where lake volume (V) = Area$^{3.385}$ * 3778.05.

Table 4-3: Area and volume of rockslide-dammed Yigong Lake at ten successive pool elevations based on DEM generated by SRTM-3 data. Maximum pool elevation attained was ca. 2265 m a.s.l (highlighted).

Elevation of lake surface (m a.s.l.)	Lake area (km^3)	Lake volume (Mm^3)
2220	24.072	175.404
2225	28.010	312.615
2230	31.939	469.282
2240	38.241	850.688
2250	43.371	1286.914
2255	45.251	1511.389
2260	47.064	1759.248
2265	48.926	2014.946
2270	50.578	2280.128
2280	53.272	2828.906

119

We also carried out calculations in GIS for two further hypothetical lake levels of 2,270 and 2,280 m a.s.l., elevations higher than our credible maximum levels. From the results in Table 4-3 we see that on May 4 (Day 25) the lake had an area of 28.01 km^2 and a volume of 312.6 Mm^3 at a water level of 2,225 m a.s.l. This area compares to 34.7 km^2 reported by Zhou et al. (2001) and Shang et al. (2003), and 33.659 km^2 reported by Wang and Lu (2001) on May 4, whereas the volume reported by Wang and Lu (2002) was a much larger 514 Mm^3. On May 20 (Day 41), our analysis shows that the lake had increased to an area of 38.2 km^2, with a volume of 850.7 Mm^3, at a water level of 2,240 m a.s.l. This area compares to 43.121 km^2 reported by Wang and Lu (2001) on May 20, who also report a volume of 1.23 Gm^3. On June 10 (Day 62) on the day of the breach we estimate the lake had an area of 48.9 km^2, compared to 52.855 km^2 reported by Wang and Lu (2001).

In measuring the maximum volume of Yigong Lake, we established a maximum lake level at 2,265 m a.s.l. in the SRTM-3 DEM (Figs. 4.11, 4.13). At this elevation a lake volume 2.015 Gm^3 is calculated (Table 4-3). Given the vertical error in the SRTM data approximated above, volumes were estimated at ± 5 m of the maximum lake elevation. At the limits of this error term (2,260 and 2,270 m a.s.l.) lake volumes of 1.759 Gm^3 and 2.280 Gm^3 were calculated from the SRTM data. We suggest that these data represent a minimum and maximum credible maximum volume of Yigong Lake at the time of breaching. We note that the estimate (2.26 Gm^3) of Wang and Lu (2001, p.37) reported without an error term falls within this range.
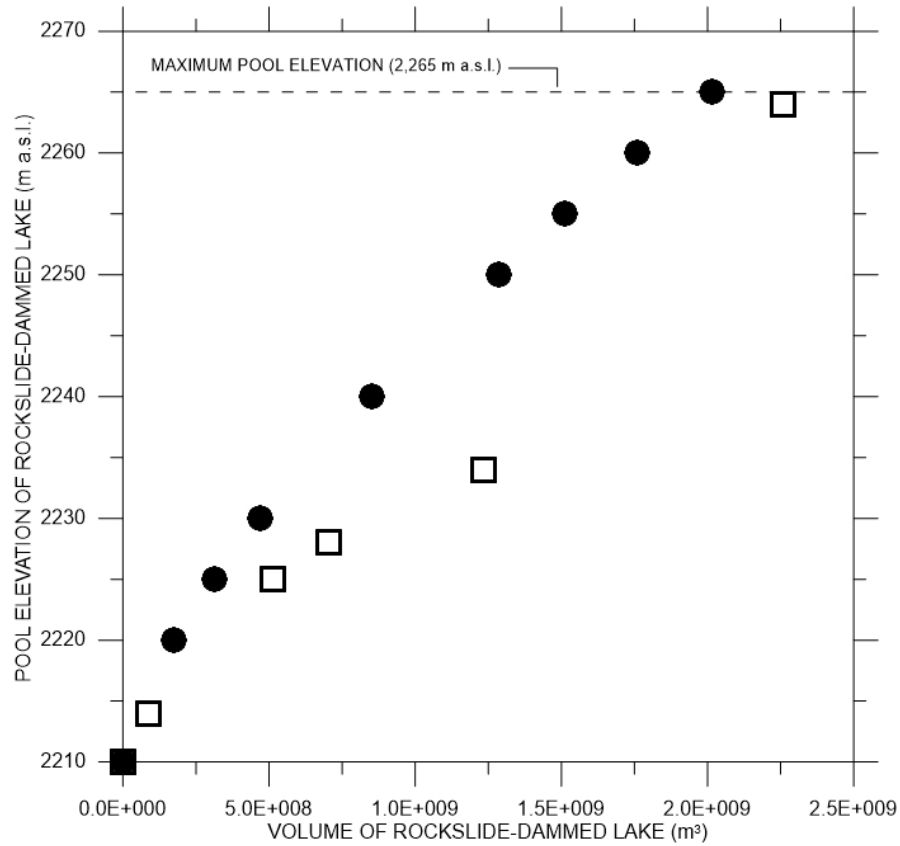
Figure 4.13: Comparison in pool elevation -volume relationships for the filling of Yigong rockslide-dammed lake. Data are from Wang and Lu (2002-*open squares*) in Table 4-2 and SRTM-3 DEM generated for this study (*solid circles*) in Table 4-3. Data assumes an original base datum of 2210 m a.s.l. and a final pool elevation of 2264 m a.s.l., rounded to 2265 m a.s.l.

Our best estimate volume of 2.015 Gm^3 is equivalent to a minimum average inflow of 376 m^3/s over the 62 days of river damming. For a rockslide-dammed lake of 3.0 Gm^3 (e.g., Shang et al. 2003; Xu et al. 2012), an equivalent minimum average inflow of 560 m^3/s is indicated. These inflow data may be compared to the average monthly discharge in the Yigong reach of 88.5 m^3/s (April), 261 m^3/s (May) and 761 m^3/s (June) (Shang et al., 2003); averaging these discharges over the length of the impoundment we obtain an average inflow of 283 m^3/s, half the average minimum inflow suggested by an impoundment volume of 3.0 Gm^3.

Our analysis shows that it is very unlikely that the area of the lake reached 70 km^2 or that the maximum pool elevation reached 2,280 m a.s.l. (e.g., Wang, 2008). However, as noted

above, the excavated spillway reduced the maximum pool elevation of Yigong Lake by ca. 18 m (Yang et al., 2010) to 2,265 m a.s.l. Without this mitigation effort, the minimum natural spillway elevation would have been at about 2,283 m a.s.l. Thus despite being ineffective in preventing a catastrophic outburst, our DEM analysis (Table 4-3) shows that the excavation of the spillway reduced the maximum volume of the rockslide-dammed lake by almost 1.0 Gm^3, a reduction in outburst volume of almost one third, and was therefore effective in reducing the outburst hazard.

4.7 **Outburst Volume, Peak Discharge, and Downstream Flood Characteristics**

Zhu et al. (2003) estimate the outburst involved a volume of 3.0 Gm^3 of water and lasted only 6 hours. This is equivalent to an average discharge of 138,888 m^3/s; they also estimate the maximum breach discharge as 30,250 m^3/s. Discharge calculated at an unspecified point downstream (probably the Tongmai Bridge) was 126,400 m^3/s, 36 times greater than the normal river flood (Zhu et al., 2003). Shang et al. (2003) also report a maximum instantaneous discharge of about 120,000 m^3/s at the Tongmai Bridge, 17 km downstream from the dam (T in Figure 4.14) and they note that the outburst volume totalled 3.0 Gm^3 of impounded water. Xu et al. (2012) report that the flood peak passed the Tongmai Bridge, 17 km downstream of the dam, at 02:50 on June 11 (this suggests a flood wave velocity of 1.1 m/s which appears to be very unlikely); the river rose 41.77 m, 32.0 m above the deck of the bridge, and the maximum discharge was 12,000 m/s (an order of magnitude lower than estimates of Zhu et al. (2003) and Shang et al. (2003); noted above, possibly a typographical error); 26 times the normal river flood. We approximated the cross-sectional area of the Tongmai Bridge reach (ca. 7,500 m^2) and for this discharge a flow velocity of 16 m/s is obtained.

122
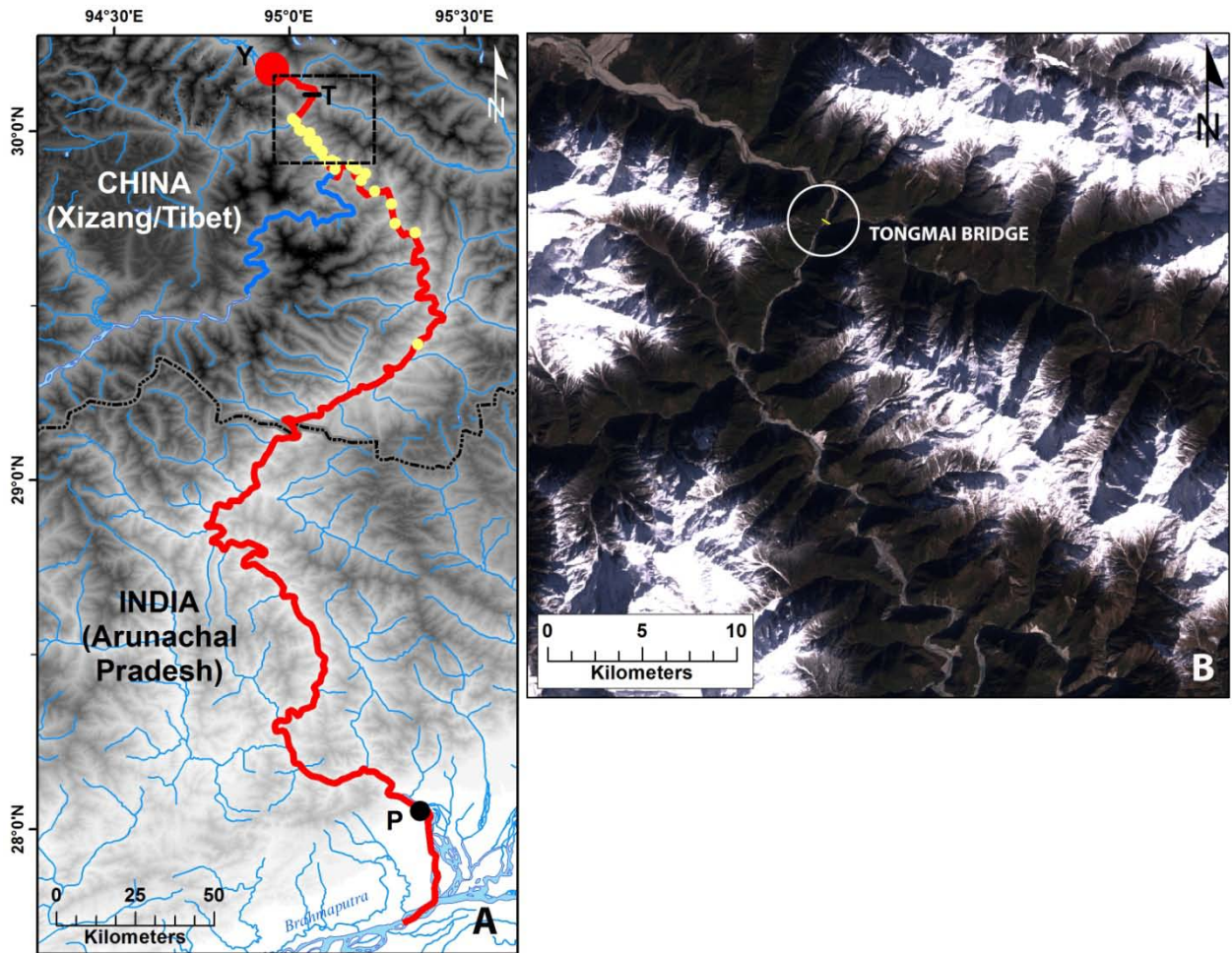
Figure 4.14: A: Location of 2000 Yigong landslide dam (Y), path of outburst flood (*red line*) resulting from the breach of the dam 62 days after emplacement, and small secondary landslides triggered by the passing floodwave (*yellow triangles*). The flood followed the Yarlung Zangbo (Xizang/Tibet) and Dihang (India) Rivers, and entered the main Brahmaputra below Pasighat (P) which is located 462 km downstream from the landslide dam. Tongmai Bridge (T) is a locality discussed in text. Rectangle outlined in black is area in B. B: LANDSAT-7 image obtained on December 14, 2000 showing extensive erosion by the outburst flood along the Yarlung Zangbo, downstream of breached landslide dam (*visible top left*). Tongmai Bridge is circled.
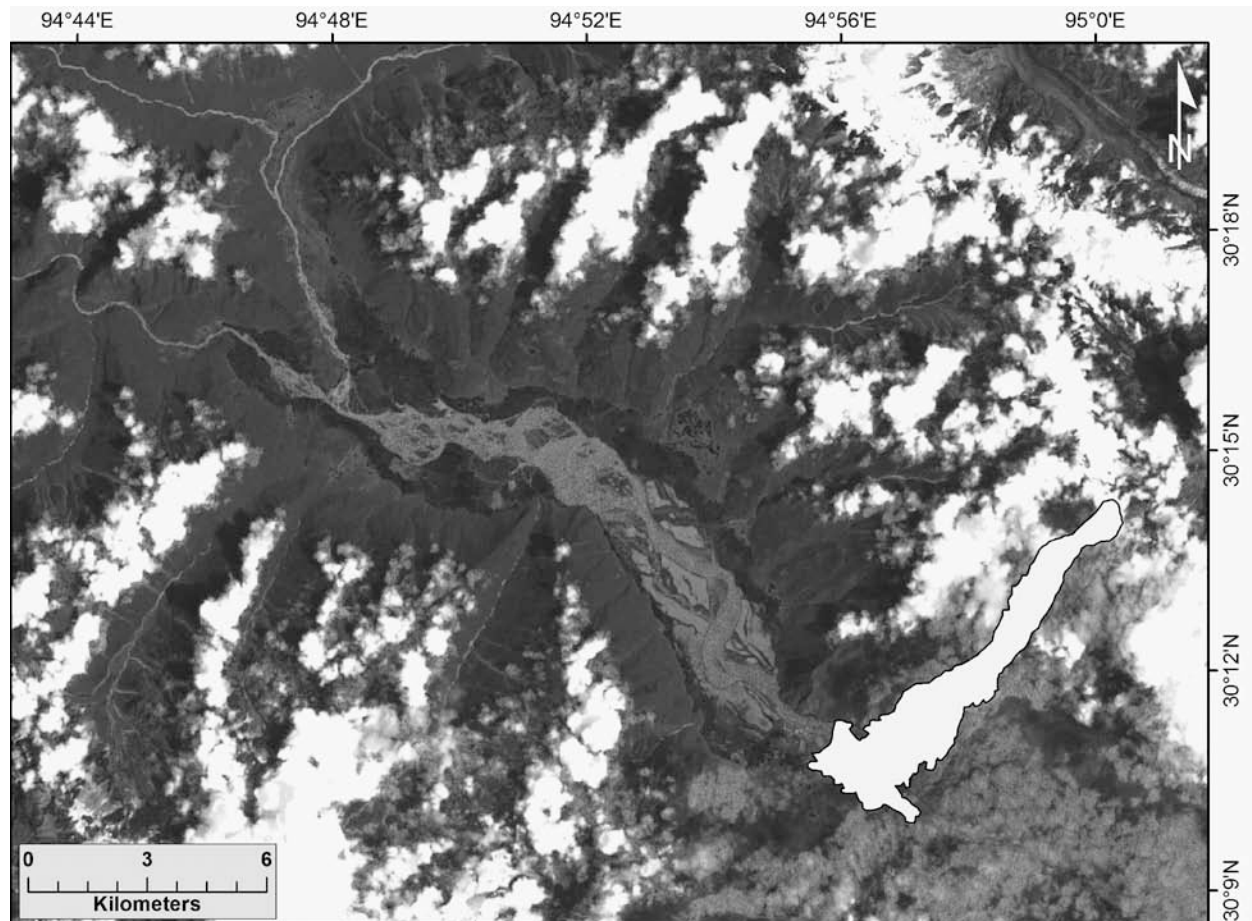
Figure 4.15: LANDSAT-7 image obtained on August 08, 2000, 59 days after the breach of the Yigong rockslide dam. Note the rockslide-dammed lake basin is completely empty, and the lake shoreline is still visible.

Satellite imagery obtained on August 8, 2000 shows that the basin of the rockslide-dammed lake is empty (Figure 4.15) and that the impounded water discharged completely during the breach. In the absence of a residual lake, we therefore assume that the outburst volume is 2.015 Gm^3, the credible volume of Yigong Lake determined above from the GIS analysis. With this outburst volume we may calculate the peak breach discharge using the empirical formula of Evans (1986). This yields a maximum breach discharge of 61,461 m^3/s.

Inputting this peak discharge into FLO-2D along with the 12 hour drainage hydrograph and the SRTM-3 digital elevation model as the topographic surface, an outburst simulation shown in Fig. 16 was produced.

124
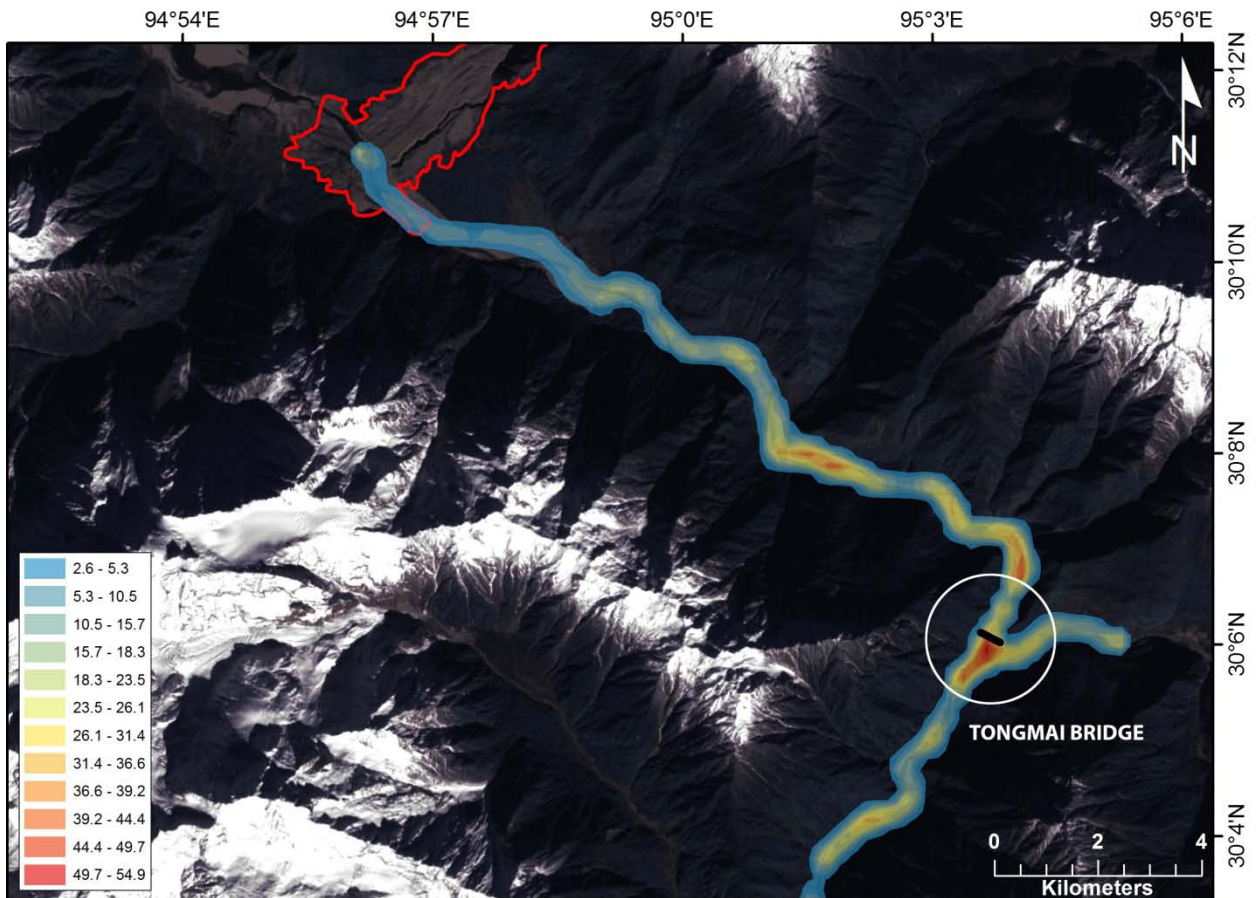
Figure 4.16: FLO-2D analysis of the Yigong outburst flood to the Tongmai Bridge (*circled*) 17 km downstream from the landslide dam (see *red outline*). The colours represent depths in metres from 2 m (light blue) to 55 m (*dark red*) - see legend. Background image is LANDSAT-7 image obtained on December 14, 2000.

The FLO-2D analysis indicates a flow that follows the general path of the trim-lines seen on the LANDSAT-7 imagery, including the upstream flows in the tributary (Parlung River) in the vicinity of Tongmai bridge (Fig. 4.16). The greatest depths in the first 50 km of the flood occur at the confluence of the Yigong and Parlung rivers, just below the Tongmai bridge. At this location, the flow depths reached a simulated maximum depth of 54.9 metres, and a velocity of 14.57 m/s.

As noted above, Shang et al. (2003) calculated a maximum discharge of 120,000 m^3/s at Tongmai, which is very similar to the discharge of ca. 110,000 m^3/s simulated in the FLO-2D model. The discharge value noted by Xu et al. (2012) of only 12,000 m^3/s is assumed to be a

typographical error; as such a low discharge is not probable from a breach event with this magnitude.
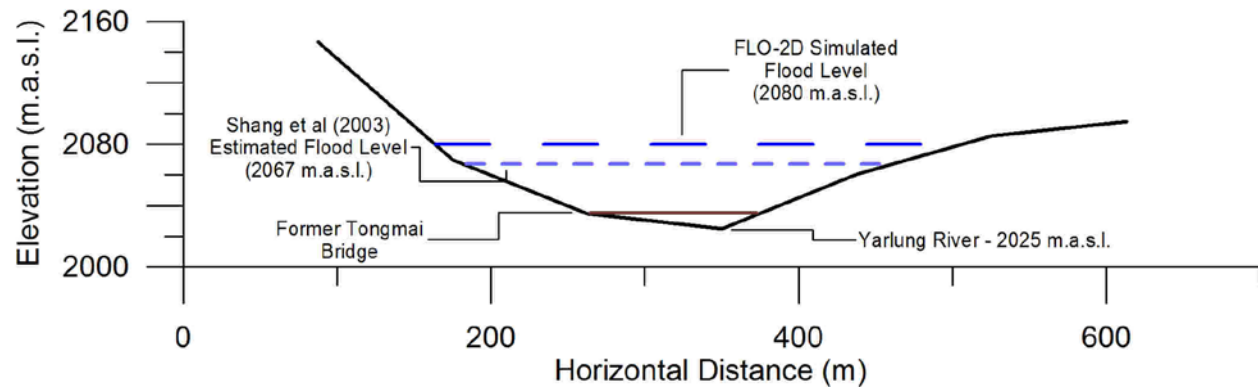
Figure 4.17: Cross section of Yigong River at Tongmai Bridge, 17 km downstream from the breached Yigong landslide dam. Note estimated flood level from Shang et al. (2003) and flood level simulated by FLO-2D. Topography based on SRTM-3 DEM.

A flood discharge of 120,000 m^3/s was directly estimated (Shang et al., 2003) at Tongmai Bridge, located 17 km downstream from the rockslide dam (Fig. 4.14), at 02:50 on June 11, 5 hours and 50 minutes after the initiation of the breach.

The outburst flood resulting from the breaching of Yigong Lake has not been documented in detail and only summary details have been published (e.g., Shang et al., 2003; Tewari, 2004; Zhu and Li, 2000/2001). In China, the downstream flood resulted in dramatic erosion immediately downstream of the rockslide dam (Fig. 4.14), and caused a significant number of small slope failures (Fig. 4.14). The flood destroyed an additional 5 highway bridges downstream from Tongmai and substantial channel erosion destroyed a number of sections of the Sichuan-Tibet highway in China.

Floodwaters travelled through the mountains of China in the Zangpo River system and into the Dihang River system of India, a tributary of the Brahmaputra (Figures 4.1, 4.14). In India, the flood reached the floodplain of the Brahmaputra at a distance of about 500 km.

126

The rising waters were measured from a water level gauge at Pasighat (Arunachal Pradesh) (Tewari, 2004) at a distance of 462 km from the breached landslide dam (Figure 4.14, 4.18). The water level began to rise at 12:00pm on June 11, 17 hours and 50 minutes after the breach, indicating a downstream flood wave velocity of about 7 m/s. Peak discharge of 44,200 m^3/s (Tewari, 2004) was measured at Pasighat at 18:00, 22 hours and 50 minutes after the breach. The maximum rise measured at the Pasighat stage was 5.54 m (Tewari, 2004).
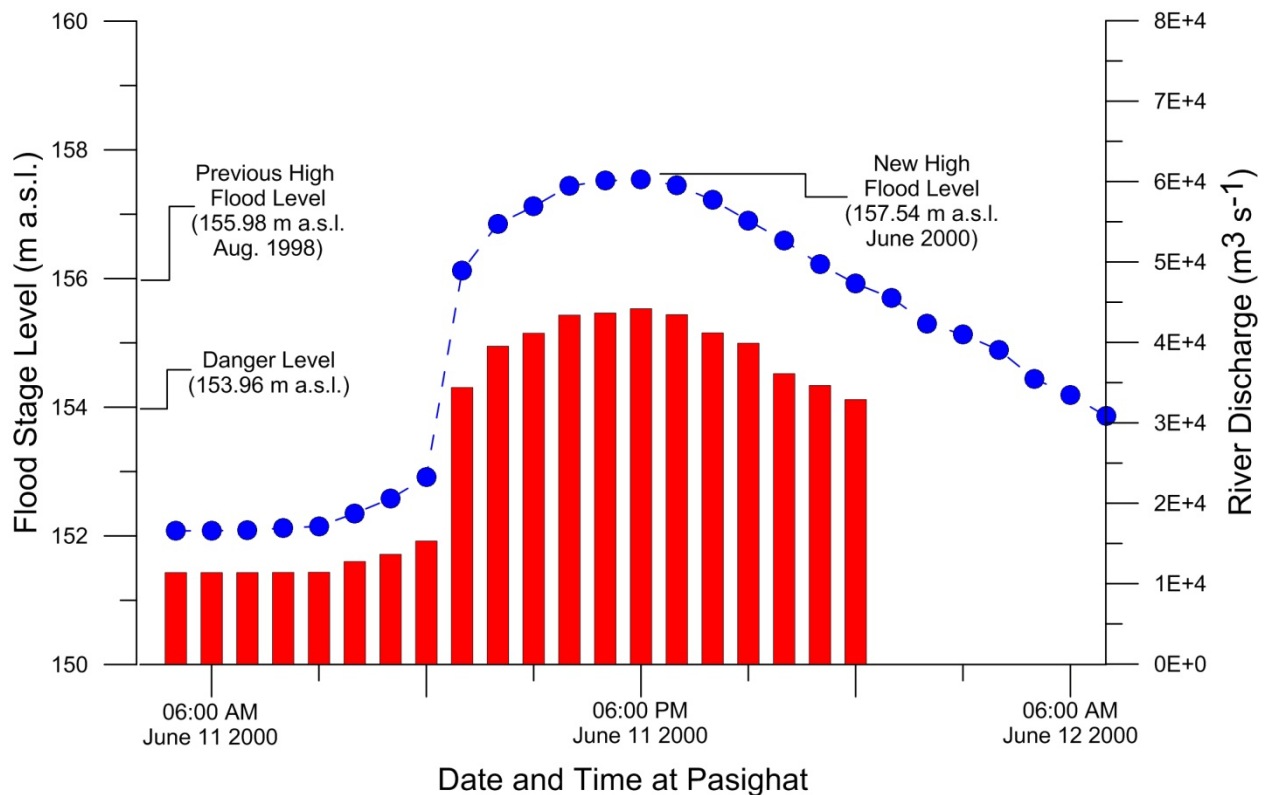
Figure 4.18: Elevation of river (*blue line*) and river discharge (*red bars*) measured at Pasighat, India, during the passing of the Yigong floodwave from 05:00 June 11 to 07:00 June 12, 2000. The floodwave peaked at 157.54 m a.s.l., 1.56 m higher than the previous highest stage (August 1998), and 3.58 m above the bankfull level. Pasighat is 462 km downstream from the Yigong landslide dam (Data from Tewari, 2004).

4.8 **Conclusions**

This paper attempts to reconcile inconsistencies in the published literature on the 2000 Yigong landslide and its associated landslide dammed lake, with specific reference to the characteristics and volume of the rock avalanche, the nature of the landslide dam, and the

127

temporal evolution of (areas and volumes) of the landslide-dammed lake. The impoundment had a lifetime of 62 days.

We reviewed the extensive literature on the Yigong events and, using digital topographic data (SRTM-3) in conjunction with LANDSAT -7 imagery, we have presented credible and verifiable values for the original landslide source volume (91 Mm^3), the total deposit volume of 115 Mm^3, (including entrainment and bulking), and the final and outburst volume of Yigong lake (2.0 Gm^3). These volumes are considerably lower than in the previously published literature.

Our analysis shows that the volume of the Yigong rock avalanche was not exceptional when compared to similar events worldwide since 1900. However, the Yigong lake volume of ca. 2.0 Gm^3 is the second largest outburst volume ever recorded, exceeded only by the First Great Indus Flood (Pakistan) of 1841, which had an estimated volume of 6.5 Gm^3 (Delaney and Evans, 2011). We note that while the excavated spillway did not prevent a catastrophic release of lake water, it did significantly reduce the maximum outburst volume by almost 1.0 Gm^3.

We conclude that freely available remotely sensed data, including digital topographic data and satellite imagery, can be reliably used to 1) characterise the geometry of large-scale rock avalanches, 2) calculate areas and volumes of large landslide-dammed lakes as they fill and empty, and 3) provide data to model their emplacement and outburst dynamics.

Chapter 5

The 1997 Mount Munday Landslide (British Columbia) and the Behaviour of Rock Avalanches on Glacier Surfaces

Delaney, K.B. and Evans, S.G.

OVERVIEW: Rock avalanches onto glacier surfaces, involving volumes 1Mm³ or more, are common in the glacier environments of NW North America. We analyse the Mount Munday rock avalanche (British Columbia) which occurred in July 1997. It involved the initial movement of 3.2Mm³ of granitic gneiss that underwent a high degree of fragmentation as it was emplaced on Ice Valley Glacier as a thin 2.6 km² debris sheet. The total height of the path was 850m, and its length was 4,163 m, yielding a fahrböschung of 10°, suggestive of a long runout in relation to volume. Potential energy expended in the movement was calculated as 4.33×10^{13}J and its specific energy was estimated at 5,204J/kg. A simulation of the movement using 2D DAN-W and DAN 3D strongly supports the idea that debris sheet geometry (runout and thickness) and behaviour (velocity profile) resulted from movement on a low friction surface (glacier ice). Our analysis of the debris sheet geometry of 23 unconstrained rock avalanches on glacier surfaces in NW North America indicated that the debris sheets are distinct from those in non-glacial environments in that they are (a) longer in relation to volume and (b) more extensive in area in relation to volume. These two effects result in a very thin supra-glacial debris sheet. Using image analysis software, we found that ca. 85% of the initial source rock volume was fragmented to fragment sizes less than 4.7 m³ in volume during emplacement, and that within the debris sheet, the highest degree of fragmentation is associated with the thinnest debris. In the emplacement of rock avalanche debris sheets on glacier surfaces, the low friction glacier surface drives debris sheet thinning through spreading, which in turn results in the fragmentation of its entire thickness. We thus propose low friction surface-driven fragmentation as a process that contributes to long runout of rock avalanches on glacier surfaces and explains their distinctive debris sheet geometry.

5.1 Introduction

Rock avalanches onto glaciers are a common occurrence in the mountains of northwest North America (Fig. 5.1; Shreve, 1966; Post, 1967; Marangunić and Bull, 1968; McSaveney, 1978; Evans and Clague, 1988, 1994, 1999; Evans et al., 1989; O'Connor and Costa, 1993; Jibson

et al., 2006; Lipovsky et al., 2008; Huggel, 2009; Schneider et al., 2011; Guthrie et al., 2012; Sosio et al., 2012; Ekström and Stark, 2013; Uhlmann et al., 2013; Gorum et al., 2014). At least 46 rock avalanches, with volumes in excess of 1 Mm³, have occurred in the glacial environments of the region since 1945 (Fig. 5.1; Evans, unpublished data), the most recent being the June 2012 Lituya Mountain rock avalanche, St. Elias Mountains, Alaska (Fig. 5.1). They are of interest in landslide research since, when the rock avalanche runout is contained within the extent of the glacier surface, the events afford an opportunity to examine rock avalanche emplacement mechanisms (including source rock fragmentation) from initial failure to deposition, without the influence of complex topography in runout travel or other earth materials being entrained in the debris (Hungr and Evans, 2004).
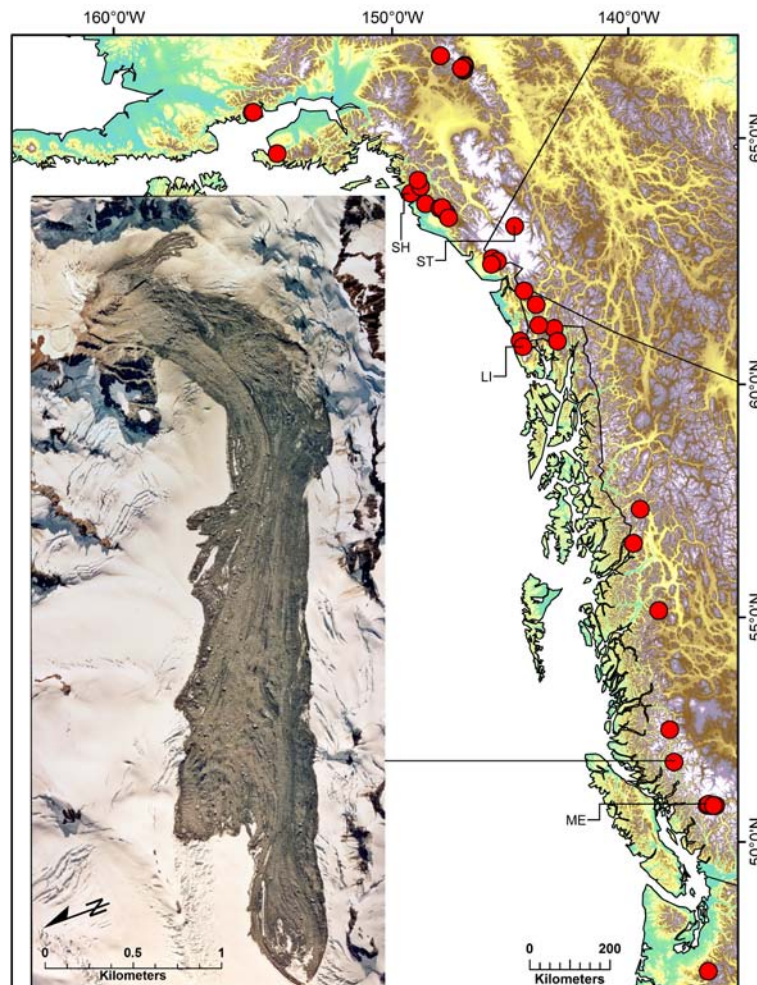
Figure 5.1: Rock avalanches in glacier environments of NW North America. Map shows locations of 46 known rock avalanches with volumes in excess of 1 Mm³ (*red dots*) that ran out on to glacier surfaces in the period 1945 to 2012 (Evans, unpublished data). Locations of rock avalanches discussed in text are LI: 2012 Lituya Mountain rock avalanche, ME: 2010 Mount Meager rock avalanche, SH: 1964 Sherman Glacier rock avalanche and ST: 2007 Mount Steele rock avalanche. Inset photo is vertical ortho-rectified aerial photograph of the path of 1997 Mount Munday rock avalanche (Coast Mountains, British Columbia) from source area to debris limit on Ice Valley Glacier (image obtained on August 20, 1997).

Sometime in late July 1997, a large rock avalanche occurred on the southern flank of Mount Munday (elevation (el.) 3,367 m a.s.l.; 51.321°N, 125.221°W) in the Waddington Range of British Columbia's Coast Mountains, approximately 280 km northwest of Vancouver (Fig. 5.1). The rock avalanche is one of a recent number that have involved failure of rock slopes adjacent to glaciers, with debris travelling over the glacier surface, in the Coast Mountains of British Columbia (Fig. 5.1; Evans and Clague, 1988, 1999; Guthrie et al., 2012). The rock avalanche took place 6.5 km southeast of Mount Waddington (4,019 m), British Columbia's highest peak, and involved highly resistant gneissic rocks of the Coast Plutonic Complex which form a number of jagged peaks in the Waddington Range. The debris flowed across and down Ice Valley Glacier, forming a spectacular tongue-shaped deposit on the snow-covered glacier surface (Figs 5.1, 5.2).
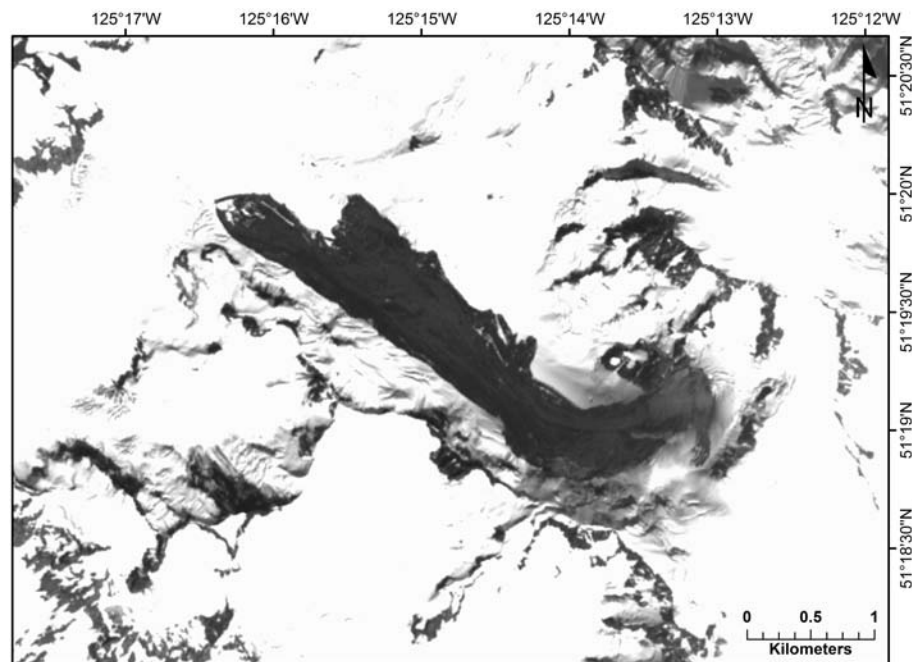
Figure 5.2: SPOT image of 1997 Mount Munday rock avalanche obtained on August 11, 1997. Note the absence of snow cover on the debris and dust still visible on the snow surface adjacent to the rock avalanche.

The rock avalanche is not evident on LandSat5 imagery on July 12, 1997 and is first evident in LandSat5 imagery obtained on July 28, 1997.

This paper builds on three previous reports on the Mount Munday rock avalanche (Evans and Clague, 1998, 1999; Delaney and Evans, 2008). Here, we report: (1) a comprehensive characterization of the rock avalanche based on observations from a field inspection of the rock avalanche on August 30, 1997, an analysis of large-scale aerial photographs taken on August 20, 1997, satellite imagery obtained since June 26, 1997 and digital terrain data derived from a photogrammetric analysis of the aerial photographs; (2) the results of a dynamic 2D (DAN/W) and 3D (DAN 3D) simulation of the runout of the rock avalanche on the surface of Ice Valley Glacier; (3) an analysis of rock avalanche fragmentation and debris generation in the Mount Munday event; and (4) a general consideration of debris sheet geometry and fragmentation characteristics of rock avalanches on glacier surfaces.

5.2 **1997 Mount Munday Rock Avalanche I – Occurrence and Trigger**

5.2.1 Date of Occurrence

The rock avalanche was not witnessed. However, we were able to establish the date of the event to within a 16-day window by examining satellite images obtained during July and August 1997. The rock avalanche is first visible on a LANDSAT5 image taken on July 28, 1997, followed by a SPOT image obtained on August 6 and again on August 11, (Fig. 5.2) 1997. LANDSAT5 images obtained on June 26 and July 12, 1997 do not show the rock avalanche deposit. Thus, the rock avalanche occurred sometime between July 12 and July 28, 1997; this date range refines the time of occurrence first reported by Evans and Clague (1998) who estimated that the event occurred between May 25 and July 10, 1997.

5.2.2 Trigger

Geological Survey of Canada (2008) data indicates that no significant earthquakes that could have triggered the rock avalanche occurred in or near the Waddington Range during the 16-day event window. We attempted to identify a rock avalanche seismic signal in seismograph

records from the Canadian Seismic Network, but were unsuccessful. It is likely that the smooth sliding surface of the glacier and low fall height of the rock avalanche mass sufficiently damped the seismic signal, making it difficult to distinguish from the background data on seismographs.

Environment Canada climate data (Environment Canada, 2012) from Tatlayoko Lake (el. 865 m a.s.l.), approximately 70 km to the northeast, shows no exceptional climatic conditions likely to have been a trigger (Fig. 5.3). However, within the event window, it is noted that: (a) a freeze–thaw cycle occurs between July 18 and 28, 1997; and (b) maximum, minimum and average daily temperatures show spikes above temperature normals for 1971–2000 (Fig. 5.3). The location experienced measureable precipitation (Fig. 5.3) prior to and during the event window (Fig. 3.3); any precipitation falling at the high elevation of the source area on Mount Munday would have been in the form of snow.
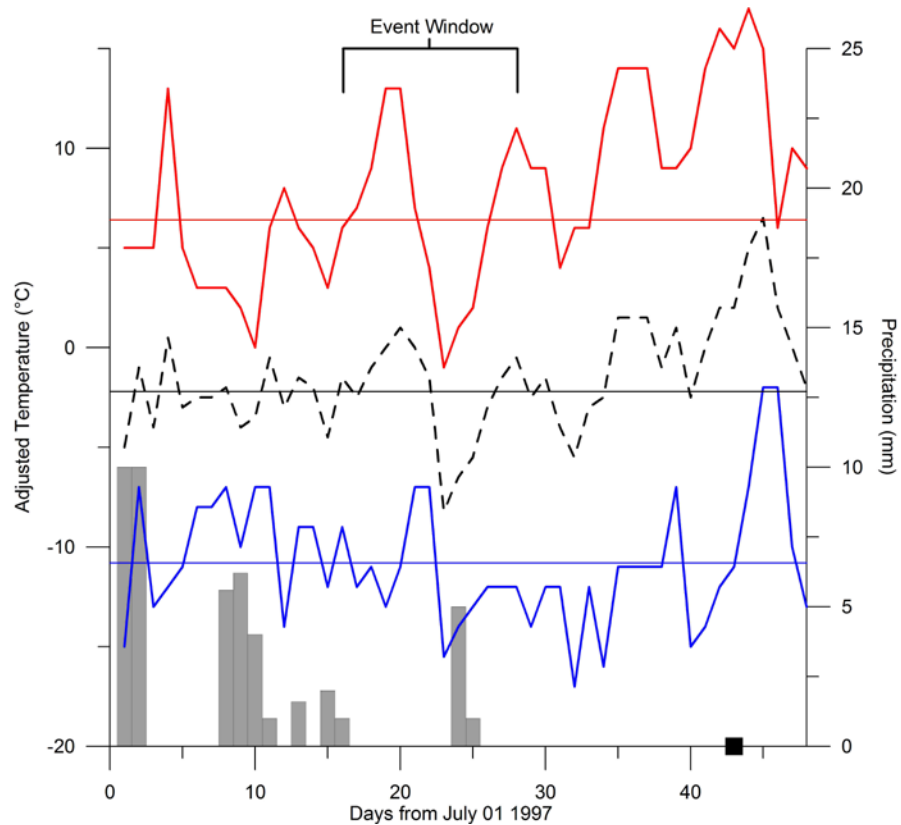
Figure 5.3: Climate conditions in the event window of the Mount Munday rock avalanche. Estimated temperature in the source area of the Mount Munday rock avalanche (daily minimum—*blue*; daily average—*black*; daily maximum—*red*). These estimates were based on temperature data from the Tatlayoko Lake climate station (51.66N, 124.40 W, WMO ID#71028) for 48 days from July 1 to August 17, 1997. Tatlayoko Lake climate station is at el. 865 m a.s.l., 1,935 m below the base of the Mount Munday rock avalanche source area (2,830 m a.s.l.), 70 km distant to the southwest. In order to roughly estimate the temperature in the Mount Munday source area, we used a dry atmospheric lapse rate (−6.5 °C/1,000 m) applied to the elevation difference between the station and the source area. This results in a temperature reduction of ca. 16 °C for each data point recorded at the weather station. The horizontal lines are the average minimum (*blue*), average mean (*black*) and average maximum (*red*) temperatures obtained by the adiabatic adjustment as above for the Mount Munday source area. These values were calculated from the 1971 to 2000 climate normals for the Tatlayoko Lake climate station (Environment Canada 2012; Canadian Climate Normals or Averages 1971–2000 http://www.climate.weatheroffice.gc.ca/climate_normals/index_e.html). Black square on horizontal axis marks the date (August 12, 1997) of the Queen Bess glacier avalanche and associated moraine-dammed lake outburst at el. 1700 m a.s.l., 45 km to the SSW of the Tatlayoko Climate Station (Kershaw et al. 2005) and 54 km east of Mount Munday. Precipitation measured at Tatlayoko Lake, British Columbia, July 1–August 6, 1997 (Environment Canada 2012) is also shown (grey histogram bars).

It is of interest to note that a second glacier-related catastrophic event, the glacier–avalanche induced outburst of moraine-dammed Queen Bess Lake, took place on August 12, 1997 (Fig. 5.3; Kershaw et al., 2005) at Queen Bess Lake (51.253°N, 124.516°W), located only 48 km ESE of Mount Munday. The event occurred during a similar spike in temperature data (Fig. 5.3).

5.3 **1997 Mount Munday Rock Avalanche II – Path, Source and Debris Characteristics**

5.3.1 Path Geometry

The highest point of failed rock in the source area was 2,950 m a.s.l. and the distal tip of the debris was at 2,100 m a.s.l. (H=850 m). The total horizontal distance of travel (L) was 4,613 m; thus, the fahrböschung ($\tan^{-1}$(H/L)) for the Mount Munday rock avalanche is 10° (Fig. 5.4) (Table 5-1).
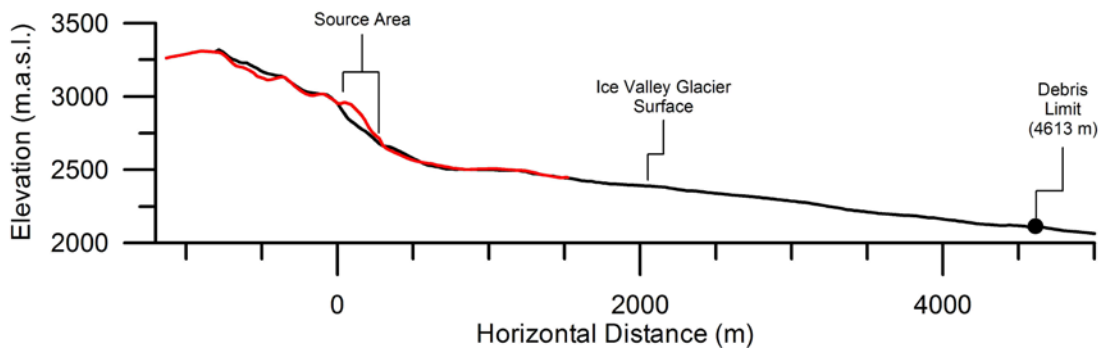
Figure 5.4: Topographic profile of the pre-landslide (1981—*red line*) and post-event (*black line*) 1997 Mount Munday rock avalanche path. Summary of path geometry—H=850 m, L=4,613 m, fahrböschung $(\tan^{-1} H/L) = 10°$.

Table 5-1: Summary parameters for 1997 Mount Munday rock avalanche.

Rock avalanche parameter	Value	Unit
Source rock mass volume	3.2	Mm^3
Mass of source rock mass	8.32×10^9	kg
Deposit volume (obtained by assuming 20 % bulking during emplacement), (DV)	3.8	Mm^3
Area of debris on Ice Valley Glacier (A)	2.6	km^2
Average depth of debris sheet (DV/A)	1.5	m
Length of rock avalanche path (L)	4,613	m
Height of rock avalanche path (H)	850	m
(H/L)	0.185	
Fahrböschung $(\tan^{-1}(H/L))$	10	°
Maximum velocity from best-fit DAN-W 2D simulation	63.6	m/s
Total runout time from best-fit DAN-W 2D simulation	419	s
Average velocity from best-fit DAN-W 2D simulation	11	m/s
Centre of gravity vertical displacement (V)	521	m
Centre of gravity horizontal displacement (HD)	2,620	m
Travel angle $(\tan^{-1}(V/HD))$	11	°
Potential energy expended during movement	4.33×10^{13}	J
Specific energy	5,204	J/kg

5.3.2 Initial Rock Slope Failure

The rock avalanche originated on a shoulder that forms the lower southwest flank of Mount Munday and rises steeply from the surface of Ice Valley Glacier (Figs. 5.4 and 5.5). The initial failure mass consisted of hornblende-rich dioritic granitoid gneiss of the Central Gneiss Complex of the Coast Mountains pluton, coarsely foliated (Fig. 5.5), with foliation dipping steeply (70–82°) to the SW–SSW (Roddick, 1985).

135

Figure 5.5: Oblique aerial view (to the northwest), taken on August 30, 1997, of the source area (*right*) and path (*left*) of the Mount Munday rock avalanche. Note steeply dipping foliation cut by a more southerly striking and more gently dipping fault surface. The tip of the debris is visible in the distant centre background.

The highest elevation of the source area was 2,950 m a.s.l. The base of the detachment runs from 2,600 to 2,650 m a.s.l. located at the boundary of the rock slope and the surface of Ice Valley Glacier (Fig. 5.5). Failure involved a rock slope ca. 350 m in height with an average slope of 46° and an orientation of 220° SSW (Fig. 5.6). Comparison of photogrammetry-derived digital elevation models (DEMs) obtained from pre-slide (1981) and post-slide (1997) aerial photography indicates that the volume of rock which detached from Mount Munday was 3.2 Mm³ (Fig. 5.6).
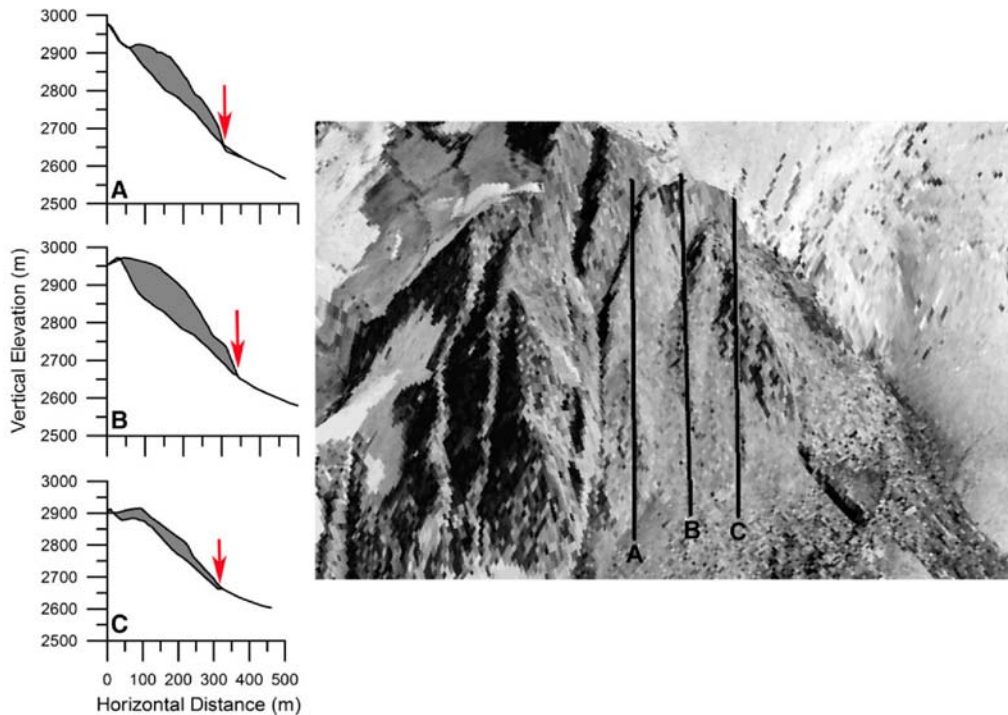
Figure 5.6: Cross sections of source area of Mount Munday rock avalanche. Three profiles (A–C, located on right) illustrate the change in pre- (1981) and post-landslide (1997) topography in the source area. Rock mass involved in initial failure is infilled grey. Vertical red arrow denotes the rock slope–glacier surface transition. Note position of glacier surface is unchanged between 1981 and 1997.

The initial movement direction of the detached mass was 237°. The mechanics of the initial sliding appear to have been complex but controlled by a steeply dipping planar fault surface that has a more southerly dip direction than the foliation and cuts across it a lower dip angle (Fig. 5.5). This discontinuity geometry gives rise to multiple wedges some of which detached completely, whilst others slid a limited distance. In the centre of the source area, a portion of the disturbed rock remains on the failed slope (Fig. 5.5), and although this mass slid a short distance, it did not completely detach from the mountain side.

As indicated in Fig. 5.6, the base of the initial failure coincided with the transition between the surface of Ice Valley Glacier and the adjacent rock slope. Evans and Clague (1994) suggested that recent glacier down-wasting is an important process in debutressing rock slopes adjacent to glacier surfaces in glacierised mountain regions. It is known that glaciers in the Coast Mountains have undergone extensive thinning as a result of twentieth century

climate change (e.g. Holm et al., 2004; Schiefer et al., 2007; Moore et al., 2009). However, no change is noted in the position of the glacier surface between 1981 and 1997 (Fig. 5.6); also, it is noted that the initial failure occurred above the equilibrium line altitude of Ice Valley Glacier. Thus, although the precise relation between possible glacier surface down-wasting and initial failure is not known, it appears that the elevation of the Ice Valley Glacier surface at the base of the source rock slope was unchanged in the 16 years prior to the landslide.

5.3.3 Rock Avalanche Debris and Emplacement Mechanism

The failed mass slid onto the surface of Ice Valley Glacier and, deflected by the opposite glacier slope, turned 70° towards the NW (Figs. 5.1, 5.2 and 5.7). The debris travelled ca. 4 km over the smooth snow-covered surface of Ice Valley Glacier on a slope of only 6° (Figs. 5.5 and 5.7). The rock mass pushed up large pressure ridges of snow at the frontal and lateral margins of the debris as it travelled down glacier (Fig. 5.8).

Figure 5.7: Perspective view to the southeast of the Mount Munday rock avalanche on Ice Valley Glacier, Waddington Range, southern Coast Mountains. Image prepared from orthorectified aerial photographs flown on August 20, 1997 draped over DEM prepared by photogrammetry from the same photographs. Note flow lines in debris.

The rock avalanche debris ranged from fine dust to large boulder-sized blocks (Figs. 5.8 and 5.9). Silt- to sand-sized fragments of hornblende and mica were noted and wet black dust covered many large boulders and some areas of the adjacent glacial surface (cf. Fig. 5.2). Huge blocks of bedrock were present (Fig. 5.9), and clearly defined overlapping flow lines were evident in the debris sheet (see discussion below).

Figure 5.8: Distal Distal margin of rock avalanche (in A and B August 30, 1997). A: Note snow pressure ridges and debris limit. B: Limit of debris. Person is standing on remnant of pressure ridge, consisting of winter snow cover, pushed up ahead of the sliding debris. Note the very sharp boundary of the debris and size variation of boulders. C: Large block at distal limit of debris (at left; note person at right for scale) slid to present position bulldozing the snow-creating pressure ridges and train of finer debris behind the block. (Photograph courtesy of Robin Mounsey).

Aerial photographs of the rock avalanche debris taken on August 20, 1997, a maximum of 39 days after the landslide took place, allowed us to examine primary directional features and flow structures on the surface of the debris formed during emplacement (Fig. 5.10). These features are assumed not to have been modified by glacier motion in the short interval between rock avalanche emplacement and aerial photography. The flow lines illustrate the movement of the largest blocks and, since the glacier surface is visible in many flow line segments, also indicate the overall shallow depth of the debris.

140
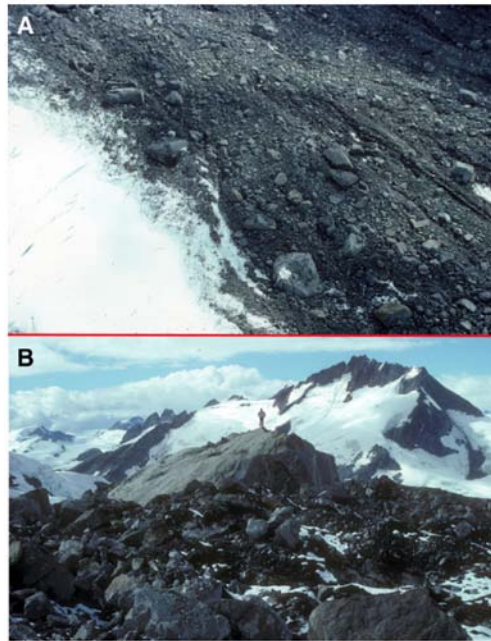
Figure 5.9: Debris of rock avalanche. A: aerial view of debris and flow lines. B: Ground view (to south) across debris. The person is standing on a gneissic block approximately 25 m in longest dimension.

Examination of flow lines and their cross-cutting relationships indicate two distinct zones (B and C in Fig. 5.10) in the debris down glacier of the sharp turn, suggesting two separate streams in the debris emplacement, resulting from the micro-topography of the glacier surface. Stream B preceded stream C since the flow lines of C cross cut those of B. The first of the two main flows (B in Fig. 5.10) of disintegrated rock turned downslope on Ice Valley Glacier after being deflected by the opposing slope and continued in a more northerly direction before stopping 1.5 km from the source zone. The second (and later), larger debris mass (C in Fig. 5.10) continued in a northwesterly direction and traveled 3.1 km further on the glacial surface, to the final runout distance of 4.61 km.
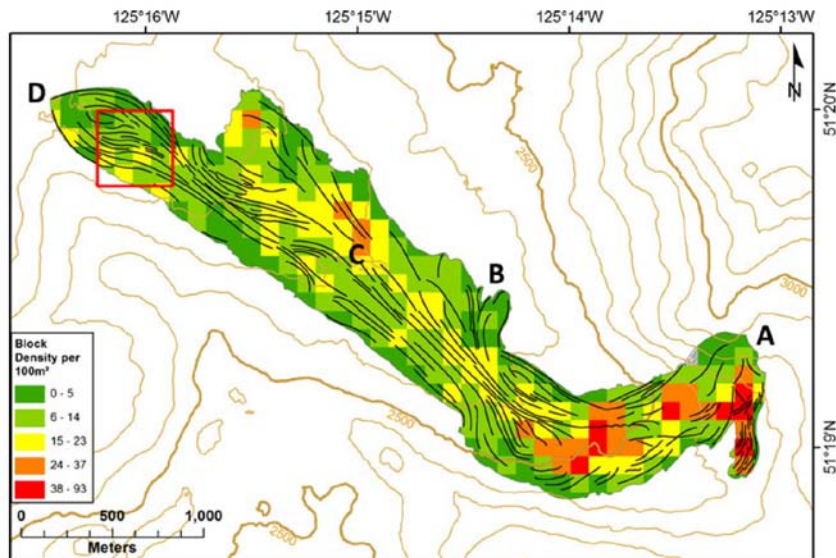
Figure 5.10: Outline of Mount Munday rock avalanche with main flow paths (*black lines*) traced on aerial photographs and block density obtained from image analysis (see text for technique and methodology). Source area is at A. The first debris stream (B) pushed upslope to the north. The second stream (C) overlapped stream B (note crosscutting flow lines) and continued downslope to terminate in distal tongue (D). Red square outlines area in Fig. 17.

The geomorphology of the debris is characterised by distinctive tracks of overlapping 'trains' of debris headed by a large boulder (Figs. 5.10, 5.11 and 5.12). These trains are several metres wide and are roughly parallel to the directions of the major flow streams within the debris. They are most visible in the lateral margin, central region and in the distal limit of the debris (Figs. 5.1b, 5.10, 5.11 and 5.12).
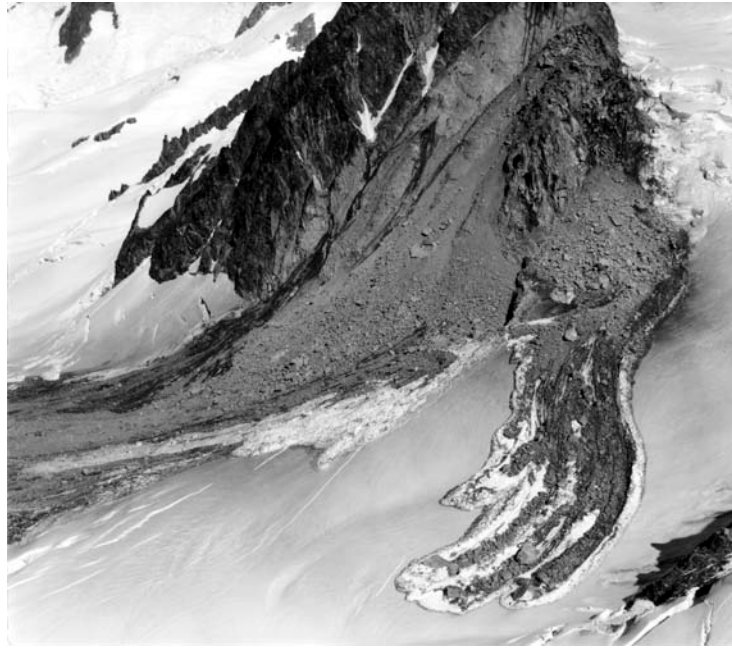
Figure 5.11: Interpretation of debris movement I. Debris resembling a hand extends down from the source area. This image illustrates the 'lead bulldozing' of individual boulders and 'train' features of finer debris formed behind. (Photograph courtesy of Robin Mounsey).
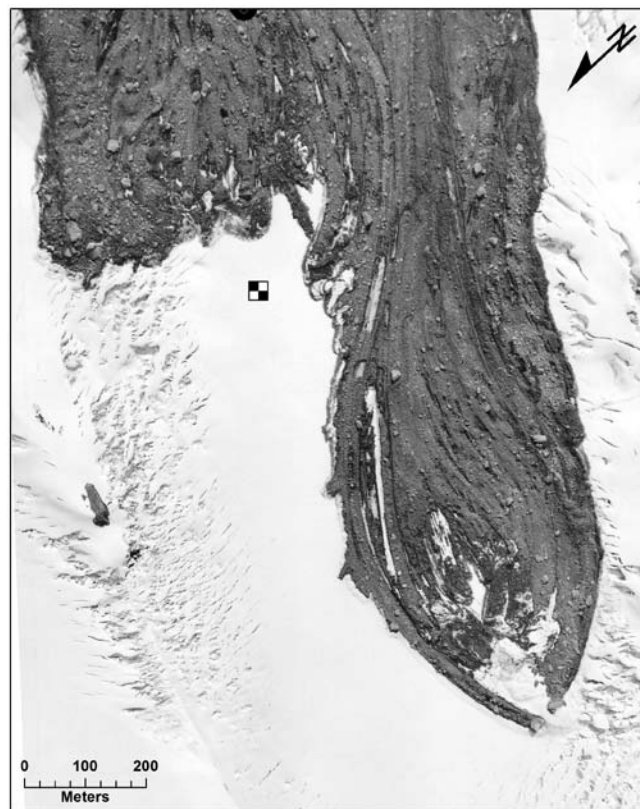
Figure 5.12: Interpretation of debris movement II. Aerial photograph (taken on August 20, 1997) of distal

143

tongue showing flow and sub-flow paths and boulders followed by debris trains (see text for discussion). Chequered square is scaled 30 m square from source area (see Fig. 5.19).

Similar observations were made in the debris of the 1964 Sherman Glacier landslide (Shreve, 1966; McSaveney, 1978), the 1975 Lyell Glacier rock avalanche, South Georgia (Gordon et al., 1978) and 2002 Black Rapids Glacier rock avalanches (Shugar and Clague, 2011). The morphology of the trains is strongly suggestive of a furrowed path being 'snow ploughed' by the leading boulder(s) with the finer material following behind on the exposed glacial ice and constrained by the micro-channels in the snow. This boulder ploughing behaviour suggests that the underlying exposed glacier ice surface has a lower frictional resistance than the snow covered surface. Trains and flow lines indicate differential mobility of debris within the debris sheet. Multi-directional flow lines in the debris indicate spreading of the debris sheet towards the distal and lateral margins of the debris (Figs. 5.10 and 5.12). The rock avalanche was partially halted at its northern limit by a rough glacier surface and micro-topographic anomalies as it neared the end of its path (Figs. 5.10 and 5.12). The southerly stream forming the distal tongue traveled 930 m further downslope, taking advantage of an elongate lower area (topographic depression) of the glacier surface which formed a shallow channel for the debris; the streamlines in this area are almost unidirectional in the direction of the distal tip (Figs. 5.10 and 5.12).

5.3.4 Initial Source and Debris Volume

Quantitative comparison of DEMs obtained from photogrammetric analysis of pre-slide (1981) and post-slide (1997) aerial photographs indicates that the volume of rock that detached from Mount Munday was 3.2 Mm³. Based on data from vertical aerial photographs taken on August 20, 1997 and satellite imagery from August 11, 1997, the debris covers an area of ca. 2.6 km². If we assume that the bulking of the rock mass during fragmentation and transport is 20 %, as in the case of the Sherman Glacier rock avalanche (Marangunić and Bull, 1968; McSaveney, 1978), then the deposited volume becomes 3.8 Mm³ and the calculated average thickness of the debris sheet is thus only 1.5 m. Field estimates by Evans and Clague (1998) suggest a debris depth of between 2 and 5 m. In comparison, the average thickness of the Sherman Glacier rock avalanche debris sheet was 1.65 m (McSaveney,

1978). The low values for debris thickness result from the combination of an unconstrained path and a low frictional surface, which led to increased lateral and downslope debris spreading.

The field estimates of the debris depth were higher due to the presence of large unfragmented blocks (cf. discussion in McSaveney, 1978, pp. 213–215). However, it was noted that the debris sheet was approximately one block deep in most areas and did not consist of multiple layers of superimposed rock fragments.

5.4 **Analysis of Runout on the Surface of Ice Valley Glacier**

5.4.1 Runout Behaviour

The mobility of a rock avalanche is defined from the geometry of its path and can be expressed as the ratio of the path height (H) to the horizontal length (L) of the path between the top of the source area and the distal tip of the debris. H/L is found to vary inversely with source volume (e.g. Hungr, 1990; Legros, 2002). Evans and Clague (1988, 1999) first suggested that rock avalanches that travel on a glacier surface exhibit higher mobility than non-glacial events due to the fact that for a given volume, travel distances over glacier surfaces are enhanced due to the low friction at the debris-glacier interface. As noted above, the fahrböschung ($\tan^{-1}$(H/L)) of the Mount Munday rock avalanche is 10° for a source volume of 3.2 Mm³. This is less than the fahrböschung that would be expected for non-glacial rock avalanches of similar volume (see Fig. 3.6 in Evans and Clague (1988)) indicative of enhanced mobility.

Below the sharp bend in its path, the debris traveled an additional 4 km on a slope of only 6°, suggesting a coefficient of kinetic friction of approximately 0.11. This compares to the direct estimate of kinetic friction of rock debris sliding on ice noted by McSaveney (1978) at the 1964 Sherman Glacier rock avalanche, Alaska (0.10) and McSaveney (2002) at the 1991 Mount Cook rock avalanche in the New Zealand Alps (0.11).

5.4.2 Runout Simulation (DAN-W and DAN 3D)

First-order 2D and 3D dynamic analyses were carried out using the simulation models DAN-W and DAN 3D (Hungr, 1995; Hungr and Evans, 1996; Hungr and McDougall, 2009; Sosio et al., 2008, 2012). With respect to rock avalanches running out on glacier surfaces, Hungr and Evans (1996) found that the runout behaviour was best simulated with a Voellmy basal resistance model using frictional parameter (f) values ranging from 0.03 to 0.15 and turbulence parameter (ξ) values from 250 to 1,500 m/s^2 (cf. Sosio et al., 2008). Rock avalanches running out over non-glacier surfaces have been successfully simulated with similar turbulence parameter values, but higher frictional parameter values due to rock-rock basal contact (Hungr and Evans, 1996).

A 2D simulation of the 1997 Mount Munday rock avalanche was carried out using DAN-W (Fig. 5.13). Using the Voellmy rheology, we successfully simulated the runout distance of theMount Munday rock avalanche (4,611 m) with values of f=0.085 and ξ=850 m/s^2 (Fig. 5.13). Values of ξ between 250 and 1,500 m/s^2 have previously led to successful 2D simulations of rock avalanches on glacier surfaces (Hungr and Evans, 1996; Sosio et al., 2008). DAN-W simulated a shallow average deposit thickness (2.3 m) (Fig. 5.13) that compares very well to field observations of thickness reported above (Fig. 5.9). The simulation suggests that the rock avalanche had a duration of 419 s for a maximum travel distance of 4,611 m, yielding an average velocity of 11 m/s and a peak velocity of 64 m/s recorded at a path distance of only 1,116 m, shortly after the rock mass reached the glacier surface (Fig. 5.13).
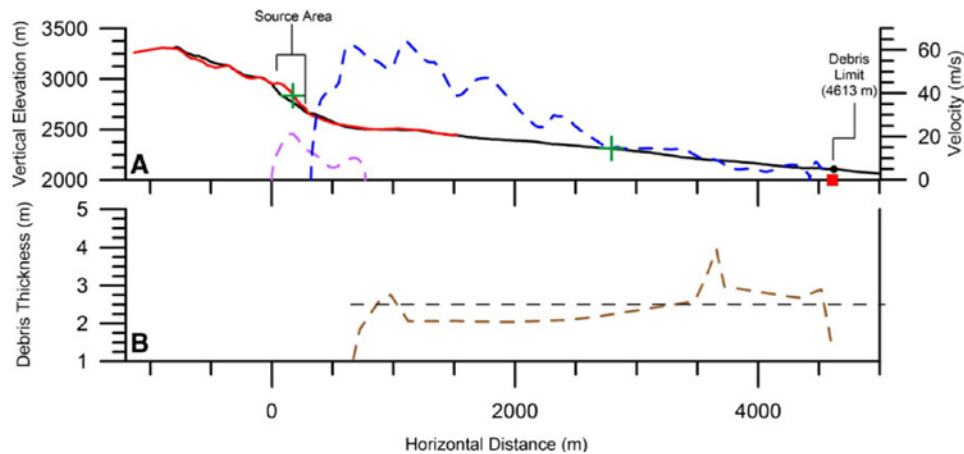
Figure 5.13: Results of 2D DAN-W analysis. A: Simulation used a Voellmy basal resistance model in which *f*=0.085 and ξ=850 m/s2. Data shown are pre-landslide 1981topographic profile (*red*), post-1997 landslide topographic profile (*black*), simulated velocity of front of slide (*dashed blue*) and velocity of rear of slide (*dashed purple*). Green crosses denote centre of gravity of initial rock mass (*left*) and debris sheet (*right*) of rock avalanche. Simulated runout distance of 4,611 m (*red square* on X-axis) closely corresponds to actual runout distance of 4,613 m. B: Simulated debris depth along path. Horizontal dashed line is average simulated depth (2.3 m).

Figure 5.14 plots the simulated velocity of the Mount Munday rock avalanche with reference to time (seconds) in the 2D DAN-W analysis. The velocity profile has three distinctive phases: (1) a very rapid acceleration in the first 20 s of movement to a maximum velocity of 64m/s; (2) a very rapid deceleration in the next 50 s to a velocity of less than 20 m/s; and (3) a period (ca. 350 s) of gradually decaying velocity around 10 m/s. Within this latter phase, the velocity shows a pulsating pattern of deceleration and acceleration as debris from the rear pushes the debris in front of it before finally stopping. The velocity troughs correlate with a distended flow front during which time the debris thins and slows. The debris then accelerates when the front thickens as a result of faster moving debris catching up with the front and imparting a pushing force to the debris in front, initiating another thinning and slowing phase.

147
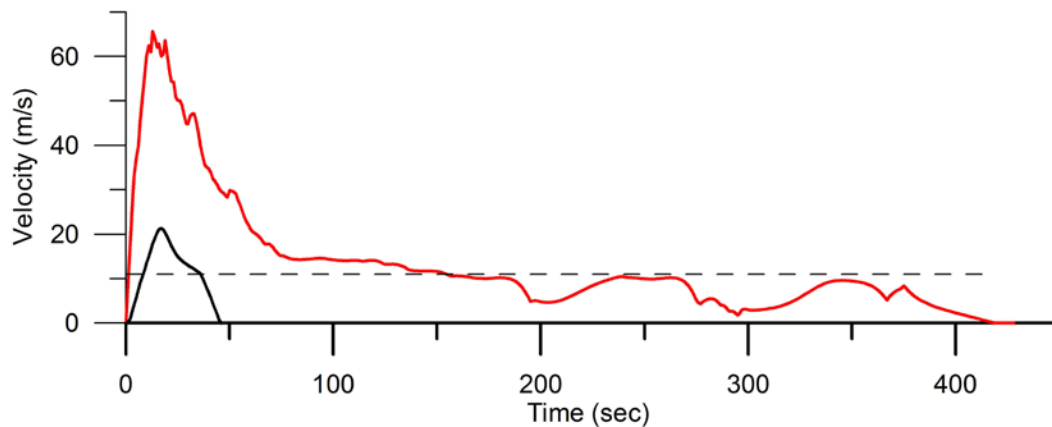
Figure 5.14: Velocity–time plot calculated by DAN-W for the Mount Munday rock avalanche. Red indicates velocity at front and black at the rear of the rock avalanche. Horizontal dashed line is simulated mean velocity (11 m/s).

DAN-W indicates a mean velocity in the rock avalanche simulation of 11 m/s (Fig. 5.14). This is slow compared to rock avalanches of similar size in non-glacial environments and results from the extended runout and low deceleration rate (cf. Ekström and Stark, 2013). It is noted that similar low average velocities were inferred for other rock avalanches emplaced on snow-covered glacier surfaces (e.g. Gordon et al., 1978). The deceleration of the debris is calculated as $D=[(V_{min}-V_{max})/(Time_{Vmin}-Time_{Vmax})]$. Therefore, the deceleration of the debris is $(-64 \text{ m/s})/(-419 \text{ s}) = 0.15 \text{ m/s}^2$. This low deceleration rate is a further indication of the influence of the low friction glacier ice surface; a higher deceleration would reflect a higher friction surface resulting in shorter runout.

DAN-W estimated that the centre of gravity of the rock avalanche deposit is located at an elevation of 2,316 m a.s.l., which is 521 m a.s.l. lower than the pre-event location of the centre of gravity of the initial rock mass (Fig. 5.13). During movement, the centre of gravity of the rock mass was displaced a horizontal distance of 2,620 m. The angle of the line joining the two centres of gravity is termed the travel angle and it has been shown to be equivalent to the true angle of basal friction (φ) of a rock avalanche movement along its path (Cruden, 1980). In the Mount Munday case, $\varphi=11°$ (coefficient of friction=0.194). Comparison

148

with the basic friction angle for granitic gneiss (35°; coefficient of friction=0.70) suggests an equivalent reduction in frictional resistance due to all emplacement effects in the movement of 72 %.

The rock avalanche resistance parameters utilised in the DAN-W simulation above were used in a 3D simulation using DAN 3D (McDougall and Hungr, 2004; Hungr and McDougall, 2009; Sosio et al., 2012). DAN 3D does not require an input path constraint as does DAN-W, since the debris is free to interact with the actual topographic surface over which the rock avalanche travels. Due to the unconstrained topography setup inDAN3D, the Voellmy parameters used above were modified slightly to obtain the best-fit 3D simulation of the rock avalanche (Fig. 5.15). The DAN 3D friction parameter (f) is 0.08 compared to the DAN-W value of 0.085, and the DAN 3D turbulence (ξ) parameter is 1,050 m/s^2 compared to the DAN-W value of 850 m/s^2. These values are similar to those obtained for the best-fit DAN 3D simulation of the Mount Munday case by Sosio et al. (2012), i.e. f=0.07 and ξ=1,000 m/s^2.

As shown in Fig. 5.15, where the simulated emplacement sequence is superimposed on the July 28, 1997 LANDSAT5 image of the rock avalanche, the DAN 3D simulation is reasonably successful in simulating the geometry of the debris sheet. The simulated runout distance (4,593 m) corresponds closely to the actual distance (4,613 m). With respect to the simulated area of the debris sheet, the 4,000 particles (green dots in Fig. 5.15) created in DAN 3D represent the total volume of the source mass divided by the total number of particles. In our simulation, there is no further fragmentation of the particles as they move downslope or entrain from the glacier surface. This results in DAN 3D underestimating the exact extent of the debris sheet and overestimating its depth. However, we note that the simulation results in a debris sheet are of generally unit thickness, i.e. one block in depth indicated by the DAN 3D colour depth scale in Fig. 5.15. In Fig. 5.15, we also note that the simulated flow lines of the particles near the distal tip closely match the flow lines in the actual event (see Figs. 5.1, 5.7, 5.10 and 5.12). The simulation also matches the occurrence

149

and general form of the hand-like depositional feature (see Figs. 5.1, 5.10 and 5.11) close to the source region. The DAN 3D simulation thus confirms the existence of the low frictional glacial surface, which aids in the lateral and downslope spreading of the debris, as well as the unit (or one block) thickness of the deposit.
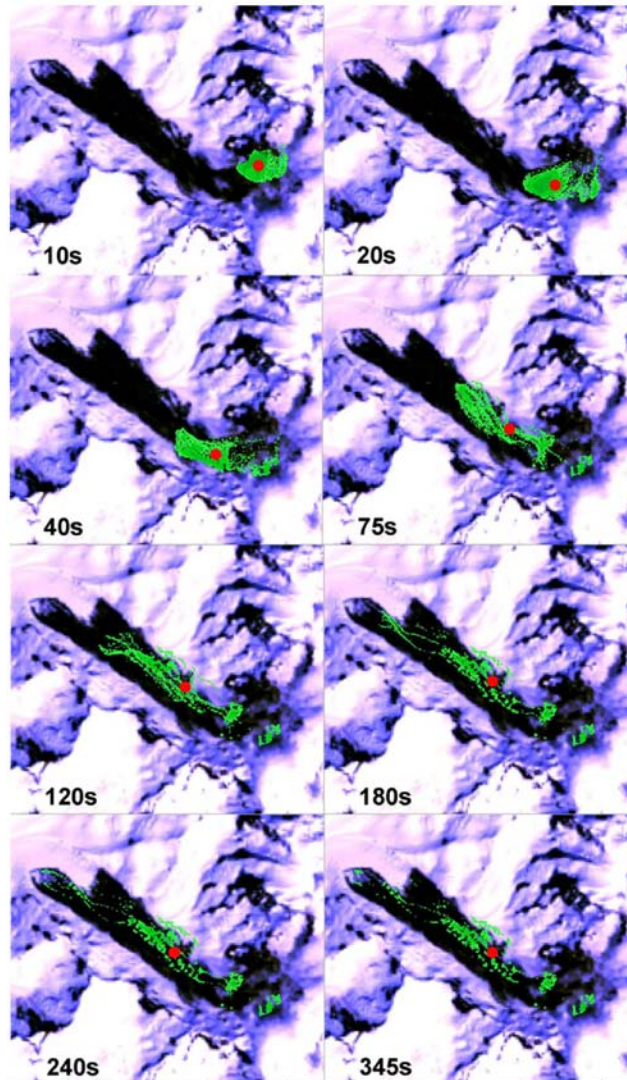
Figure 5.15: DAN 3D simulation of the propagation of the Mount Munday rock avalanche onto Ice Valley Glacier (cf. Fig. 4g in Sosio et al. 2012). Propagation is shown at eight time steps (see lower left corner of each panel) superimposed on the July 28, 1997 LANDSAT5 image showing actual debris sheet outline. The maximum velocities within the debris sheet at these times are 10s=68.6 m/s, 20s=53.2 m/s, 40s=42.6 m/s, 75s=25.4 m/s, 120s=18.3 m/s, 180s=11.0 m/s, 240s=9.4 m/s and 345s=6.8 m/s; 4,000 (the maximum permitted in DAN 3D) particles (*green dots*) were used to generate the debris sheet; the red circle represents the centre of gravity of the rock mass/debris sheet at each time step. Simulation carried out using a Voellmy basal resistance model (see text for details). Mean velocity obtained is 13 m/s over a simulated run out distance of 4,593 m (cf. Figs. 3.13 and 3.14).

The total runout time in DAN 3D dropped to 350 s in comparison to 419 s in the DAN-W 2D simulation, equivalent to a mean velocity of 13 m/s. Movement in the DAN 3D simulation does continue on past 350 s; however, the outline of the slide does not change as only small internal movements are occurring. In DAN- W, the 2D nature of the model pushes those small internal movements towards the front of the mass, continuing the total displacement for a slightly longer period of time (69 s).

5.4.3 Energetics of Rock Avalanche Motion

Assuming an average density of 2,600 kg/m^3 for the granitic gneiss, the total mass of the rock avalanche is estimated as $8.32{\times}10^9$ kg. The total potential energy (PE) released calculated using the equation PE=ΔzgγV (where Δz is the vertical distance between the centres of gravity from the initial to final positions, g is the gravitational constant, γ is the unit weight of the material and V is the failed volume; Erismann and Abele (2001)) in the Mount Munday rock avalanche is $4.33{\times}10^{13}$ J. Thus, the rock avalanche expended a total of ca. $5.11{\times}10^3$ J/kg, the specific energy (defined as energy per unit mass) of the rock avalanche; the specific energy of a rock avalanche can be taken as a measure of the potential energy stored per unit mass in the source rock mass.
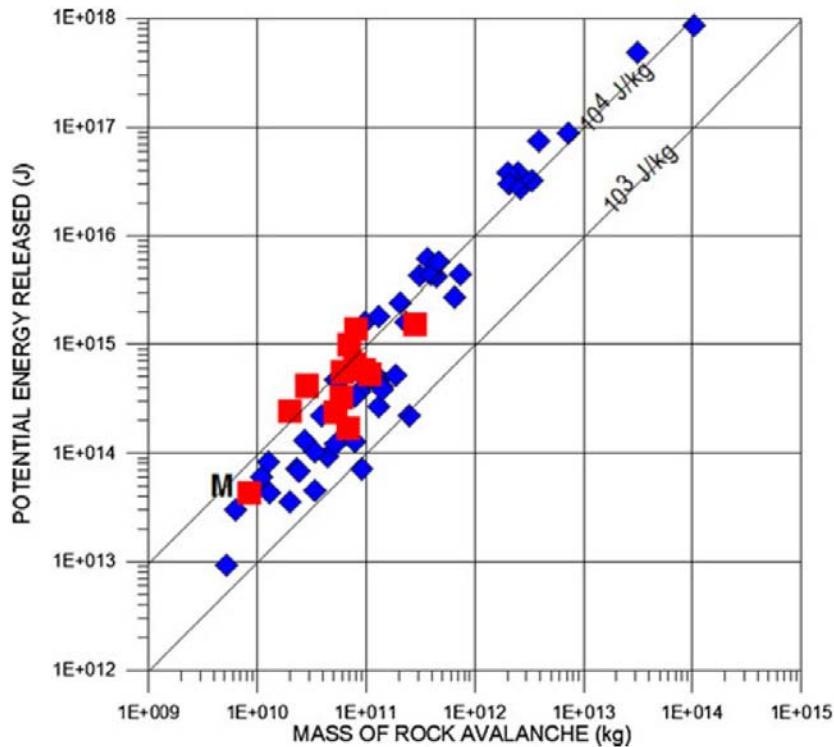
Figure 5.16: Plot of potential energy (joules) released during a rock avalanche v. the mass of the initial failure (kilograms). Blue diamonds are rock avalanches in nonglacial environments and red squares are rock avalanches on glacier surfaces. Data is from Tables 1 and 2 (this paper; M is Mount Munday data point), Table 2 in Lucchitta (1978), Table 3 in Locat et al. (2006), Table S1 in the Supplementary Data of Ekström and Stark (2013) and Table 1 in Roberts and Evans (2013). Contours of specific energy are drawn at 10^3 and at 104 J/kg.

It is of interest to compare the specific energy of other documented rock avalanches both in the glacial and non-glacial environment. Data was abstracted from Table 2 in Lucchitta (1978), who assumed that the vertical displacement in the centre of mass of a rock avalanche was 4/5 the total height of the path, Table 3 in Locat et al. (2006), Table S1 in the Supplementary Data of Ekström and Stark (2013) and Table 1 in Roberts and Evans (2013). We note that some of these sources present very rough rock avalanche path geometry data; in a number of cases, we inserted corrected values from our own analysis of specific rock avalanche paths. In a plot of potential energy (Joules) versus rock avalanche mass (kilograms), we may draw contours of specific energy (Fig. 5.16) with the result that: (a) the specific energy for rock avalanches, ranging in volume from 1 Mm³ to 38 Gm³, varies within a narrow 1-order of magnitude range between 10^3 and 10^4 J/kg; (b) the vertical behaviour of the centre of gravity of rock masses generating rock avalanches on glacier surfaces cannot be

152

distinguished from non-glacial rock avalanches; and (c) specific energy appears to increase with rock avalanche mass. Further implications of Fig. 5.16 for rock avalanche dynamics are currently being examined.

5.5 Characteristics of Rock Avalanche Debris and Fragmentation of Source Rock Mass

5.5.1 Image Analysis of Debris Sheet

Using ImageTool™ image analysis software, a block size analysis of the debris was carried out. Large-scale colour aerial photographs of the Mount Munday rock avalanche were scanned and loaded into ImageTool where they were converted to black and white polarization for analysis (Fig. 5.17). In the polarised imagery, the software detects blocks at or above a given detection threshold, and measures the major and minor axes of the detected blocks, applying an input real-world scale.
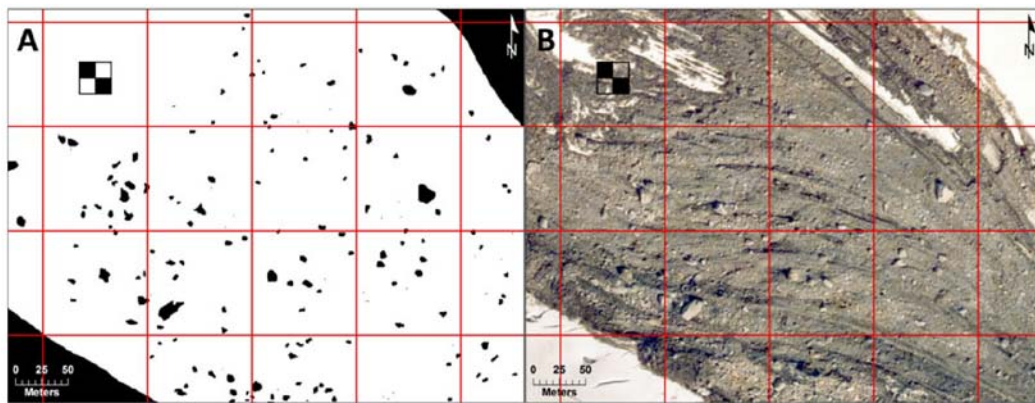
Figure 5.17: Fragmentation of Mount Munday debris sheet. A: Example of ImageTool polarised aerial photograph of debris showing detected, measured and counted boulders in a part of the distal tongue. Detection limit is 2.4 m in size (long axis) or 1.92 m^2 in area. B: Source aerial photograph for image analysis in a. Note that chequered square is scaled 30 m square from source area (see Fig. 3.19). Area of image in A and B is outlined by red square in Fig. 5.10.

In the image analysis of the Mount Munday debris, pixel resolution was 0.64 m^2. The software was calibrated to detect blocks in the processed high-resolution aerial photographs of at least 3 pixels in size (i.e. the length of the long axis ≥ 2.4 m) which represents the

153

threshold of detection. The average major and minor axis lengths of the counted blocks are 6.33 m and 3.75 m, respectively. To estimate the area of each block, we multiplied the length of the major and minor axis measurements calculated by ImageTool. The smallest blocks which could be detected by ImageTool in the debris have a surface area of approximately 1.92 m^2. To estimate the volume of the fragmented blocks, we used unpublished data by S.G. Evans who developed a relationship ($V_B=0.383L_B^{2.859}$; r2=0.867) between boulder volume (V_B) and boulder long axis (L_B) based on the field measurement of the three principle axes of 475 granite boulder fragments. This volume estimate assumes a cuboid boulder shape and should be taken as approximate only. Using this relationship, the smallest detectable blocks had an estimated volume (based on the length of the long axis (L_B)=2.4 m) of 4.7 m^3.

ImageTool identified and measured 2,915 blocks above the detection limit in the rock avalanche debris. The imaged blocks constituted only 3.5% (87,195 m^2) of the total rock avalanche debris area (2.6 km²) and 15.3% (581,231 m^3) of the total debris volume (3.8 Mm³). Therefore, a major part (∼85 %) of the debris volume resulted from the fragmentation of the source rock mass to a fragment volume of less than 4.7 m^3, suggesting a high degree of fragmentation of the source rock mass. The lack of a rollover in the particle size distribution of the measured long axes of the counted blocks (Fig. 5.18) near the detection threshold suggests that we have detected all the blocks up to this limit in the debris (cf. Blenkinsop, 1991) and that the ratio of detectable boulder size to debris sheet thickness is ∼1 or greater.
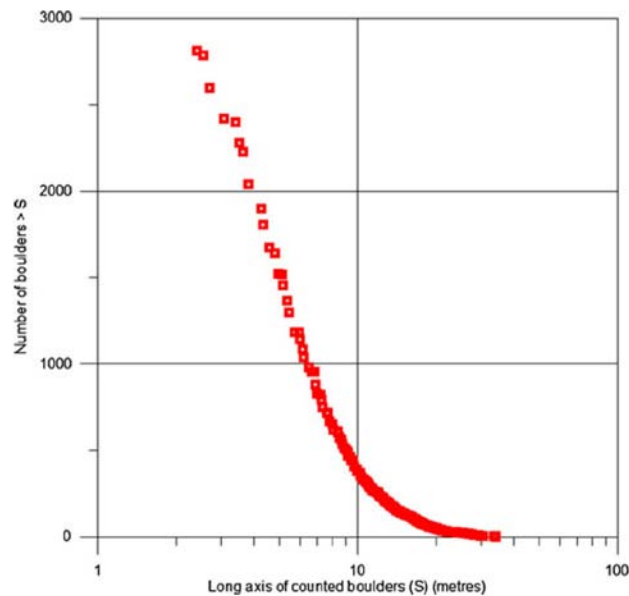
Figure 5.18: Grain size curve of measured blocks (n=2,915) on the surface of the Mount Munday debris sheet as detected by ImageTool in high-resolution aerial photographs. As discussed in text, no rollover is visible near the detection limit (2.4-m long axis) suggesting all boulders above this detection limit have been counted by ImageTool.

The spatial distribution of detected boulder density in the debris sheet (Fig. 5.10) suggests that there is a down-debris decrease in boulder density as well as a lateral decline in boulder density away from the central axis of the debris sheet. Both patterns suggest the highest degree of fragmentation, indicated by boulder density, correlates with the thinnest debris.

5.5.2 Fragmentation in Rock Avalanches and the Mount Munday Case

The image analysis reported above suggested that the Mount Munday event resulted in a high degree of fragmentation of the source rock mass, since the debris contained only a relatively small number of large blocks (Figs. 5.7 and 5.12). Fragmentation in rock avalanches was first discussed by Davies et al. (1999) and was defined (p. 1096) as occurring "in a rock mass when the rock breaks into smaller pieces, that is the number of grains increases. In particular ...[fragmentation describes] the breaking of rocks into pieces smaller than those defined by the joint (discontinuity) system of the parent rock mass. In other words, the process takes place under stresses exceeding the strength of the unjointed (intact) rock." We have not

155

carried out detailed mapping of the source area to characterize discontinuity patterns in the rock mass involved in initial failure. However, to gain some insight into the geometry of discontinuities in the source rock mass, we estimated the dimensions of a scaled 30 m square (the approximate size of the largest boulder in the rock avalanche debris) on a field photograph of the source area (Fig. 5.19).

Figure 5.19: Aerial view (to the northwest) of source area of Mount Munday rock avalanche. Chequered square is a 30-m square approximately scaled to photograph to estimate discontinuity spacing in source area granitic gneiss. Mount Waddington (4,019 m), highest peak in the British Columbia Coast Mountains, is visible on skyline, centre left.

We also added the scaled 30 m square to Fig. 5.17 and the vertical aerial photograph of the distal part of the debris in Fig. 5.12. From a visual comparison of the two images and the 30 m square, we assert that generally the rock avalanche debris has undergone intensive fragmentation to fragment sizes lower that the average discontinuity spacing in the source rock mass (i.e. at depths greater than the frost shattered surface rock). Few boulders in the debris appear bigger than the average discontinuity spacing in the source area (Figs. 5.12 and 5.19). Large boulders are indeed a minor proportion of the debris; in our case, ~85% of the debris volume is fragmented to sizes below 2.4 m in long axis dimension. The reduction ratio (R_r) was defined by Locat et al. (2006) as $R_r = D_{50}/d_{50}$ (where D_{50} and d_{50} are the mean diameter of the source rock mass (represented by the discontinuity spacing) and the mean diameter of the debris, respectively); we roughly estimate $R_r > 50$, a very high value

156

compared to those calculated for nine non-glacial rock avalanches (a range of 0.7–20.7) by Locat et al. (2006; Table 3).

Further, in terms of debris sheet structure, the Mount Munday deposit does not show stratification and related facies associations typical of modern rock avalanche debris in non-glacial settings (e.g. Hewitt, 2002a) or rock avalanche deposits preserved in the geological record (e.g. Yarnold and Lombard, 1969; Yarnold, 1993; Morris and Hebertson, 1996). These authors found rock avalanche deposits to consist broadly of (from the base) a disrupted pulverised breccia zone of matrix-rich (>50 % matrix) concentrated comminution and an overlying matrix-poor zone containing large, fractured blocks making up the rock avalanche surface. McSaveney and Davies (2006) introduced the term 'carapace' to describe the surficial matrix-poor breccia. In biology, a carapace is defined as 'a thick hard protective shell covering (an animal)'. This definition implies a thickness (in vertical dimension) and a covering (in a planimetric sense) and further implies a spatial contiguity in this thickness (as in a tortoise shell).

Dunning (2006) and Dunning and Armitage (2011) distinguish the following facies (from the top) in a rock avalanche deposit: a carapace facies, an underlying body facies (usually the most voluminous facies) and a thin basal facies (lowest in volume in a given deposit). They describe a carapace facies as follows (Dunning and Armitage, 2011, pp. 486–487):

> "The carapace facies is the coarsest unit of a rock-avalanche deposit and is the material composing the surface and near surface, observations suggest a depth of up to 30 % of total-deposit thickness as a maximum in deposits that have not been prematurely stalled by topography. The facies is clast supported… The key point of relevance is that the facies is sharply bounded below, with the boundary defined as the line below which all material is intensely fragmented, matrix supported and showing fragmentation derived features—the body facies."

Dunning (2006) suggests that the carapace is the result of limited fragmentation in a passively transported zone of partly broken rock. We thus note that the carapace facies is: (1) the coarsest unit of a rock avalanche composing the surface of a rock avalanche deposit; (2) is clast supported; (3) sharply bounded at its base by a line below which all material is

intensely fragmented and matrix supported (the body facies); (4) results from limited fragmentation; and (5) may constitute a significant proportion of the total volume of the rock avalanche debris.

Our field observations (see Figs. 5.9 and 5.12) indicate that the characteristics of the Mt. Munday debris sheet differs from the archetypical structure and sedimentology outlined above in two respects. First, a distinctive carapace (or carapace facies) as defined above is absent; the density of boulders in a conventional carapace is much greater than is found on the surface of the Mount Munday debris (e.g. Fig. 5.12). Second, a defined interior (or body facies) is not present. Rather, the debris sheet is a chaotic matrix-rich deposit with no apparent structure. It has properties of both carapace and interior sedimentology suggesting either a mixing of carapace and body facies during emplacement or the absence of distinctive carapace/body facies generating processes. The latter alternative is consistent with a high degree of fragmentation throughout the thickness of the debris sheet.

We suggest that both these alternatives point to a difference in emplacement mechanism and fragmentation process compared to a conventional non-glacial rock avalanche. Indeed, this is alluded to by Dunning and Armitage (2011) who note that 'Deposits that are relatively thin, … through unconfined spreading, may consist almost entirely of the carapace facies' thus linking distinctive debris sheet structure to the process of unconfined spreading. They also note that in deposits that have spread and thinned 'completely unrestricted …it may only be the basal and carapace facies that remain' (Dunning and Armitage, 2011, p. 487). This interpretation of thin debris sheets resulting from unconfined spreading suggests a process of hypofragmentation. In contrast, McSaveney and Davies (2006, p. 297) suggested that the greater degree of comminution in the 1992 Mount Cook rock avalanche resulted in 'greater fragmentation-driven thinning' of the debris sheet, suggestive in our mind of hyper-fragmentation. An evaluation of these alternative hypotheses on the relationship between debris thinning and the degree of fragmentation awaits further investigation. However, we note that such an evaluation will be hindered by the fact that no credible boulder-inclusive

full grain size curve (based on weight, volume or number of grains) for a rock avalanche deposit has been published to date.

5.6 Rock Avalanches on Glacier Surfaces: Debris Sheet Geometry and Fragmentation Effects

Rock avalanche behaviour on glacier surfaces shows important differences from that of rock avalanches in non-glacial environments. First, the runout distance of rock avalanche debris is significantly greater for a given volume (Evans and Clague, 1988; Lipovsky et al., 2008; Schneider et al., 2011; DeBlasio, 2011; Sosio et al., 2012), and second, deposit area is greater for a given volume indicating greater spreading of the debris (Evans and Clague, 1999; Sosio et al., 2012; Uhlmann et al., 2013). These effects result in very thin supra-glacial debris sheets (e.g. Post, 1967; Marangunić and Bull, 1968; McSaveney, 1978, 2002; Cox and Allen, 2009; Shugar and Clague, 2011; Uhlmann et al., 2013). We focus on the second effect concerning debris sheet geometry. Very thin debris sheets on glacier surfaces result from spreading driven by the low friction interface at the base of the debris (e.g. McSaveney, 2002). Laboratory experiments carried out by Dufresne (2012) found that debris travel distance increased and debris sheet thickness thinned during runout on low friction surfaces consistent with the hypothesis of Evans and Clague (1988).

In his examination of debris sheet geometry, Davies (1982) showed that deposit length scaled with volume (V) as $V^{0.33}$. Li (1983), Hungr (1990), Dade and Huppert (1998), and Legros (2002) showed that for non-glacial rock avalanches, deposit area scales with volume (V) as $V^{0.66}$. These exponents are consistent with Galileo-type scaling. However, in later work, Sosio et al. (2012) found that for rock avalanches on glacier surfaces, debris sheet area scaled with volume (V) directly as V~1 indicating the greater spreading and smaller thickness of rock avalanches emplaced on glacier surfaces.

In addition to the Mount Munday data, we assembled a data set of debris sheet geometries from 22 well-documented rock avalanches on glacier surfaces in NW North America (Table

5-2); we excluded rock avalanches with significant channelization in their path (e.g. the 2005 Mt. Steller, Alaska, event) or were constrained in their runout (e.g. the 2007 Mt. Steele, Yukon, event). Deposit area and length were measured from original source maps or remotely sensing imagery. Where debris volume estimates were not given in the source literature, we estimated the volume, V, from the power law equation $V=aA^b$, where A is area, a=58.041 and b=0.787 (r^2=0.79 for n=9 cases obtained from Table 5-2). These data are summarised in Table 5-2. It is noted that a small change in debris sheet thickness results in a substantial change in the estimate of debris volume.

In Fig. 5.20, debris sheet length is plotted against debris volume (Table 5-2) for rock avalanches on glacier surfaces and compared to similar data for non-glacial rock avalanches taken from Davies (1982). A distinct difference is observed in debris sheet length–volume relations between the two groups (Fig. 5.20); debris sheet length for rock avalanches on glacier surfaces scales with volume (V) as $V^{0.7}$ in contrast to Davies's finding of $V^{0.33}$. Davies's result indicates scale-independent self-similar debris sheet shape for non-glacial rock avalanches. Our result indicates that debris sheets of unconfined rock avalanches on glacier surfaces are very thin, are longer for a given volume and are approximately of unit thickness.

Table 5-2: Properties of debris sheets associated with 23 selected rock avalanches onto glacial surfaces, NW North America.

	Rock avalanche		Date	Source	Area (km^2)	Length (km)	Vol. 1 (Mm^3)	Thick. 1 (m)	Vol. 2 (Mm^3)	Thick. 2 (m)	L_N
1	Sherman	AK	1964	Post, 1967	8.25	6.00	12.12	1.65			23.89
2	Schwan 1	AK	1964	Post, 1967	9	6.00			17.25	1.9	23.35
3	Steller 1	AK	1964	Post, 1967	7.5	6.50			14.94	2.0	26.54
4	Sioux 1	AK	1964	Post, 1967	3	4.50			7.26	2.4	23.36
5	Allen 4	AK	1965	Post, 1967	7.5	7.50			14.94	2.0	30.62
6	Fairweather	AK	1965	Post, 1967	8.5	10.50			16.49	1.9	41.48
7	Allen 1	AK	1964	Post, 1967	2	3.00			5.28	2.6	17.32
8	Martin River 2	AK	1964	Post, 1967	11.5	4.00			20.92	1.8	14.60
9	Mount Munday	BC	1997	This paper	2.65	4.60	3.75	1.5			24.67
10	McGinnis Peak N	AK	2002	Jibson et al. (2006)	10.21	11.00	20.4	2			41.42
11	McGinnis Peak S	AK	2002	Jibson et al. (2006)	5.71	11.50	11.4	2			50.43
12	Black Rapids Glacier E	AK	2002	Jibson et al. (2006)	4.64	4.60	13.9	3			21.30
13	Black Rapids Glacier M	AK	2002	Jibson et al. (2006)	4.55	4.50	13.6	3			20.94
14	Black Rapids Glacier W	AK	2002	Jibson et al. (2006)	3.24	3.20	9.7	3			16.28
15	West Fork Glacier N	AK	2002	Jibson et al. (2006)	1.37	3.30	4.1	3			21.03
16	West Fork Glacier S	AK	2002	Jibson et al. (2006)	1.47	4.10	4.4	3			25.66
18	Cascade 1	AK	1979	This paper	4.78	3.51			10.48	2.2	16.11
19	Cascade 2	AK	1979	This paper	4.93	4.07			10.74	2.2	18.54
20	Cascade 3	AK	1979	This paper	2.99	3.78			7.25	2.4	19.64
21	Tweedsmuir	BC	1979	This paper	0.524	0.97			1.84	3.5	7.95
22	Towagh Glacier	BC	1979	This paper	1.15	2.28			3.42	3.0	15.19
23	Lituya Mountain	AK	2012	This paper	8	7.07			15.72	2.0	28.38

Note: Area and length are taken from original sources or measured from aerial photographs and/or satellite imagery. Volume 1 and Thickness 1 are taken from original sources as indicated. Volume 2 is calcualated from area-volume relation as discussed in text and Thickness 2 is obtained by Volume 2 divided by Area. Vol.: Volume; Thick.: Thickness; L_N: Normalised runout ratio (L/V$^{0.33}$); Davies (1982); Davies and McSaveney (1999).
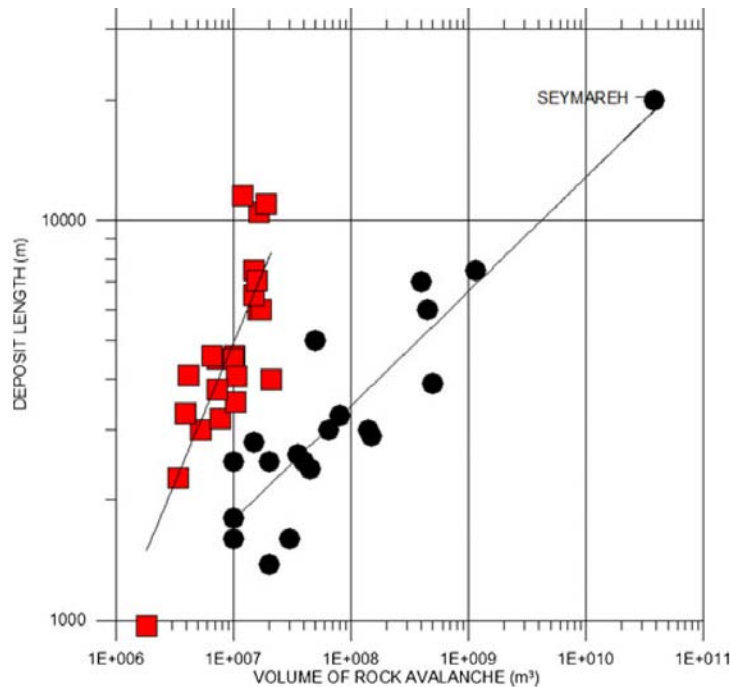
Figure 5.20: Deposit length of rock avalanches on glacier surfaces (*red squares*; data from Table 3-2) and non-glacial rock avalanches (*black circles*; data from Davies (1982)) plotted against rock avalanche volume. Length of non-glacial debris sheets scales with $V^{0.33}$ and debris sheets on glacier surfaces scale with $V^{0.7}$. Seymareh data point added from Roberts and Evans (2013).

Normalised runout ratio (L_N) is a rock avalanche debris sheet parameter defined by Davies and McSaveney (1999) as $L_N = L_S/V^{1/3}$, where L_S is the length of the debris sheet and V is the debris volume. For non-glacial rock avalanches $L_N \sim 10$ (data from Davies 1982). L_N for the glacial rock avalanches listed in Table 5-2 range from 7.9 to 50.3. In Fig. 5.21, L_N for glacial (data from Table 5-2) and non-glacial rock avalanches (data from Davies, 1982) are plotted against actual deposit length. It is noted that L_N for non-glacial rock avalanches are restricted to values less than 14 and are independent of actual deposit length within this range, i.e. they scale precisely with $V^{0.33}$ as found by Davies (1982) (Fig. 5.21). On the other hand, L_N for rock avalanches on glacier surfaces show a positive correlation with actual deposit length above this transition value because of longer runouts in relation to volume. It is suggested that this difference in spreading geometry (Fig. 5.21) reflects a difference in physical processes involved in debris sheet emplacement on glacier surfaces.

162
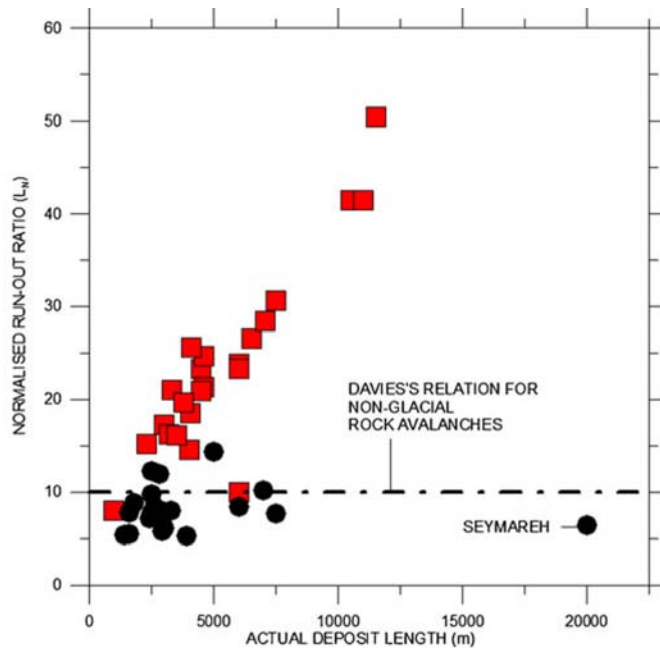
Figure 5.21: Normalised runout ratio (LN) (for definition see text) of rock avalanches on glacier surfaces *(red squares*; data from Table 2) and non-glacial rock avalanches (*black circles*; data from Davies (1982)) plotted against actual deposit length. Davies's relation for non-glacial rock avalanche volume is taken from Davies (1982). Seymareh data point was added from Roberts and Evans (2013).

Recently, Bowman et al. (2012) examined the relationship between the Davies–McSaveney normalised runout ratio (L_N), and fragmentation, expressed as Hardin's relative breakage parameter (B_R) (Hardin 1985). They found L_N in the range of 4.48–7.28 for non-glacial rock avalanches and that this range correlated quite well with values of B_R ranging from 0.34 to 0.58 (Fig. 5.22). As noted above, we obtained values for L_N for rock avalanches on glaciers in the range 7.9–50.3 (Figs. 5.21 and 5.22). When these values for L_N (Table 5-2) are plotted in relation to the data of Bowman et al. (2012), a very high degree of fragmentation is suggested (Fig. 5.22).
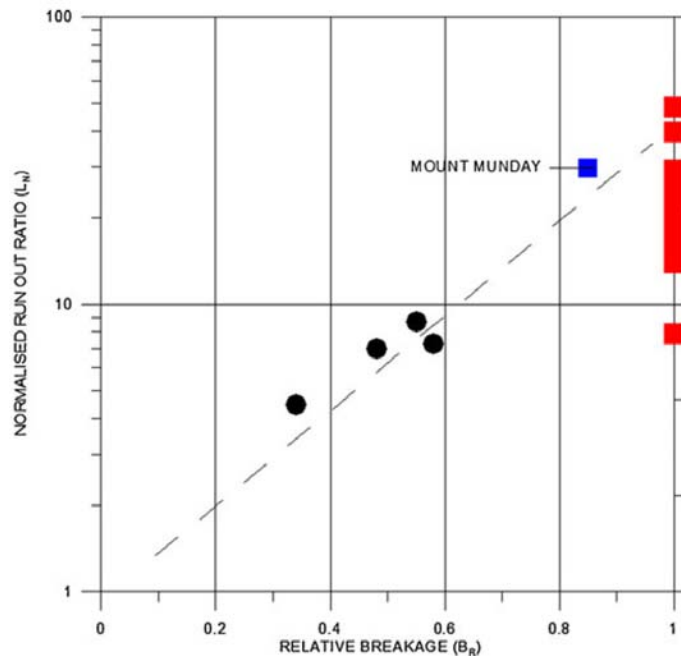
Figure 5.22: Normalised runout ratio (L_N) (for definition see text) for non-glacial rock avalanches plotted against Hardin's relative breakage parameter (B_R) (*black circles*; data from Bowman et al. 2012). Mount Munday data point indicates estimated minimum value of B_R obtained from image analysis of debris, as discussed in text. Values of L_N for rock avalanches on glacier surfaces (*red squares*; data from Table 3-2), for which values of B_R are not available, are plotted on right hand y-axis. Relation to Mount Munday point and visually estimated trend line indicate high degree of fragmentation (high values of B_R) for these events.

Thus, the debris sheet geometry of rock avalanches on glacier surfaces suggests that the rock masses involved suffer a much higher degree of fragmentation than those in non-glacial environments. Unfortunately, the absence in the literature of credible complete block-inclusive grain-size curves of rock avalanche debris in both glacial and non-glacial environments (cf. Crosta et al., 2007) does not allow quantitative support of this statement. However, we note that the absence of a passive coarse-boulder carapace in many rock avalanches on glacier surfaces, including the Mount Munday case documented here, may be taken as one line of positive evidence.

Lastly, we hypothesise that debris sheet thinning is related to the low-friction glacier surface in a process in which the whole thickness of the unconfined debris sheet is fragmented by grain-to-grain collisions during emplacement so that a coarse-boulder carapace does not develop. This effect results in a thin debris sheet that exhibits a greater degree of

164

fragmentation throughout its thickness than in non-glacial rock avalanches and that this results in a high degree of debris spreading not simply related to the high potential energy of the source rock mass in contrast to the suggestion of Dade and Huppert (1998).

5.7 **Summary and Conclusions**

Rock avalanches onto glacier surfaces, involving volumes 1 Mm³ or more, are common occurrences in the glacier environments of NW North America. We have analysed the Mount Munday rock avalanche which occurred in the Coast Mountains of British Columbia in July 1997. It involved the initial movement of 3.2 Mm³ of granitic gneiss from the steep slopes of Mount Munday that underwent a high degree of fragmentation as it was emplaced on Ice Valley Glacier as a thin 2.6 km² debris sheet. An estimated 4.33×10^{13} J of potential energy was expended in the movement and the specific energy of the rock avalanche was 5,204 J/kg, similar to other rock avalanches in both glacial and non-glacial environments. The total height of the path was 850 m, and its length was 4,163 m yielding a fahrböschung of 10°, indicating a long runout in relation to volume. The displacement of the centre of mass of the rock avalanche suggested an operational basal angle of friction for the movement of 11°, a 72% reduction in friction due to all emplacement processes compared to the angle of friction of rock-on-rock. Our analysis of debris sheet surface geomorphology suggested that the mechanism of debris emplacement was predominantly sliding. The success of our simulation of the movement using 2D DAN-W and DAN 3D strongly supports the idea that debris sheet geometry (runout distance and thickness) and behaviour (velocity profile) resulted from movement on a low-friction surface (glacier ice) that resulted in excessive debris thinning and long runout.

Our analysis of the Mount Munday debris sheet geometry, and that of 22 other unconstrained rock avalanches on glacier surfaces in NW North America, indicated that the debris sheets are distinct from those in non-glacial environments in that they are: (a) longer in relation to volume; and (b) more extensive in area in relation to volume. These two effects result in a very thin supra-glacial rock avalanche debris sheet. Using image analysis software, our

analysis of high resolution aerial photography obtained very soon after the Mount Munday event showed that the debris sheet was highly fragmented. We found that ~85 % of the initial source rock volume was fragmented to fragment sizes less than 4.7 m^3 in volume during emplacement.

It is concluded that in the emplacement of rock avalanche debris sheets on glacier surfaces, the low-friction glacier surface drives debris sheet thinning through spreading which in turn results in the fragmentation of its entire thickness so that a conventional passive carapace does not develop. We thus propose low-friction surface-driven fragmentation as a process that contributes to long runout of rock avalanches on glacier surfaces and explains their distinctive debris sheet geometry.

Chapter 6

The July 2007 Rock And Ice Avalanches At Mount Steele, St. Elias Mountains, Yukon, Canada

OVERVIEW: A large rock and ice avalanche occurred on the north face of Mount Steele, southwest Yukon Territory, Canada, on July 24th, 2007. In the days and weeks preceding the landslide, several smaller avalanches initiated from the same slope. The ice and rock debris traveled a maximum horizontal distance 5.76 km with a maximum vertical descent of 2,160 m, leaving a deposit 3.66 km² in area on Steele Glacier. The seismic magnitude estimated from long period surface waves $M_S 5.2$. Modeling of the waveforms suggests an estimated duration of approximately 100 s and an average velocity of between 35 and 65 m/s. This landslide is one of 18 large rock avalanches known to have occurred since 1899 on slopes adjacent to glaciers in western Canada. We describe the setting, reconstruct the event chronology and present a preliminary characterization of the Mount Steele ice and rock avalanches based on field reconnaissance, analysis of seismic records and an airborne LiDAR survey. We also present the results of a successful dynamic simulation for the July 24th event.

6.1 **Introduction**

In July 2007, multiple avalanches involving rock and ice occurred on the steep glaciated northern slope of Mount Steele, Yukon Territory, Canada, depositing a large volume of rock debris and ice on the surface of Steele Glacier (Figs. 6.1 & 6.2). Seismograph records and eyewitness observations indicate at least three rock and ice avalanches occurred between July 22nd and July 24th, 2007. Two or more smaller debris flows occurred on the same slope prior to July 22nd. The largest of the avalanches, referred to hereafter as the "main event", took place at 18:25 hours local time on July 24th (July 25th, 00:57 UTC). It is classified as one of 18 largest rock avalanches onto glaciers that have been documented in the Canadian Cordillera since 1899 (Evans and Clague, 1999) and one of a much larger number that have

167

occurred on glaciers in the mountains of northwest North America since 1964 (Post, 1967; Jibson et al., 2006; Molnia et al., 2006; Gorum et al., 2014).
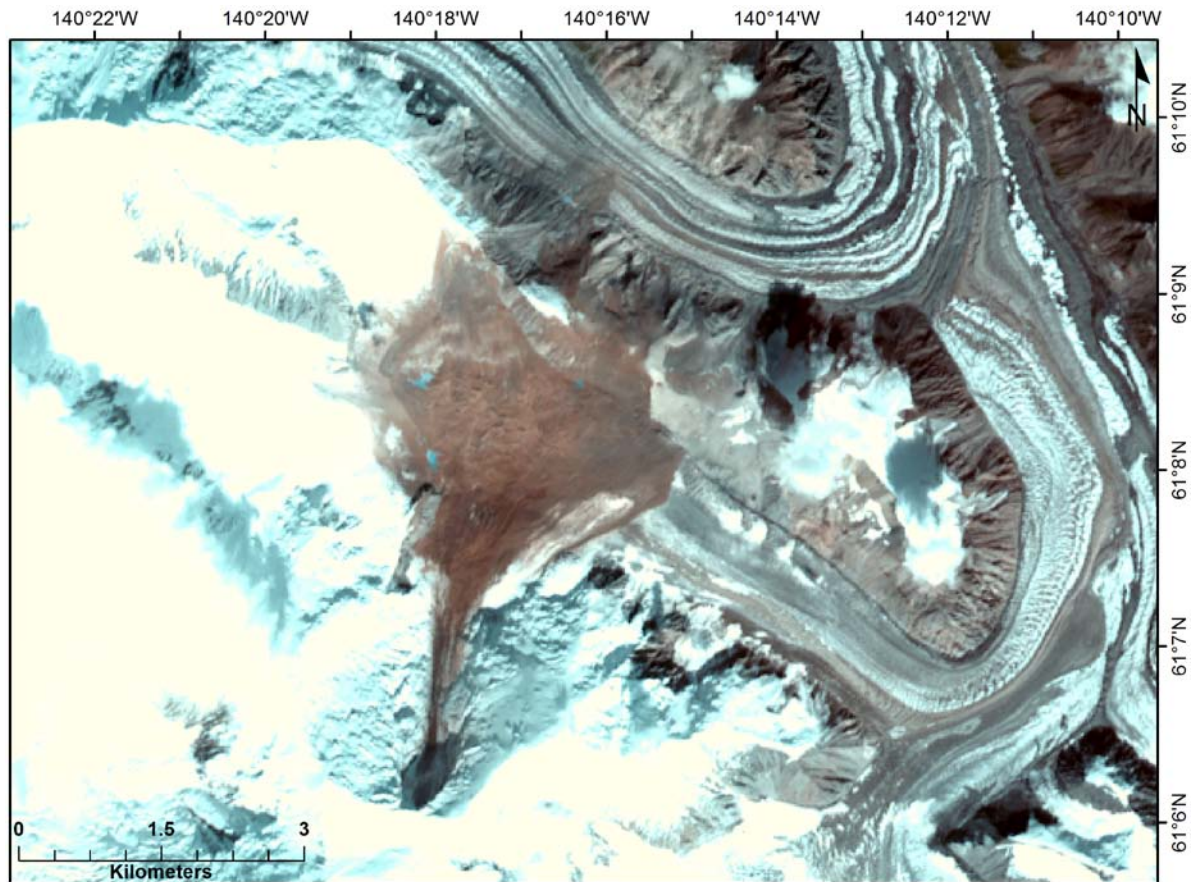
Figure 6.1: SPOT2 satellite image of the Mount Steele rock avalanche, taken July 31st, 2007, one week after then event occured.

Figure 6.2: Oblique aerial photo showing the northeast face of Mount Steele and the July 24th rock avalanche path (photo by: P. von Gaza, August 02, 2007). View is to the west.

The objectives of this report are threefold: (1) to describe the geographic and geologic setting of the July 2007 rock and ice avalanches at Mount Steele; (2) to provide an initial chronology and characterization of the events based on reconnaissance field observations, interpretation of an aerial LiDAR survey and analysis of seismological data; and (3) to discuss the regional and global significance of the avalanches.

6.1.1 Geographic and geologic setting

Standing 5,067 m above sea level (a.s.l.), Mount Steele (61°05′35.4″ N, 140°18′38.4″ W) is the fifth highest mountain in Canada and the tenth highest peak in North America. It is located in Kluane National Park in an uninhabited region of southwest Yukon Territory (Figs. 6.2 & 6.3). The mountain lies within the Icefield Ranges of the St. Elias Mountains, an area of high, rugged, snow and ice-covered mountains surrounded by valley glaciers.
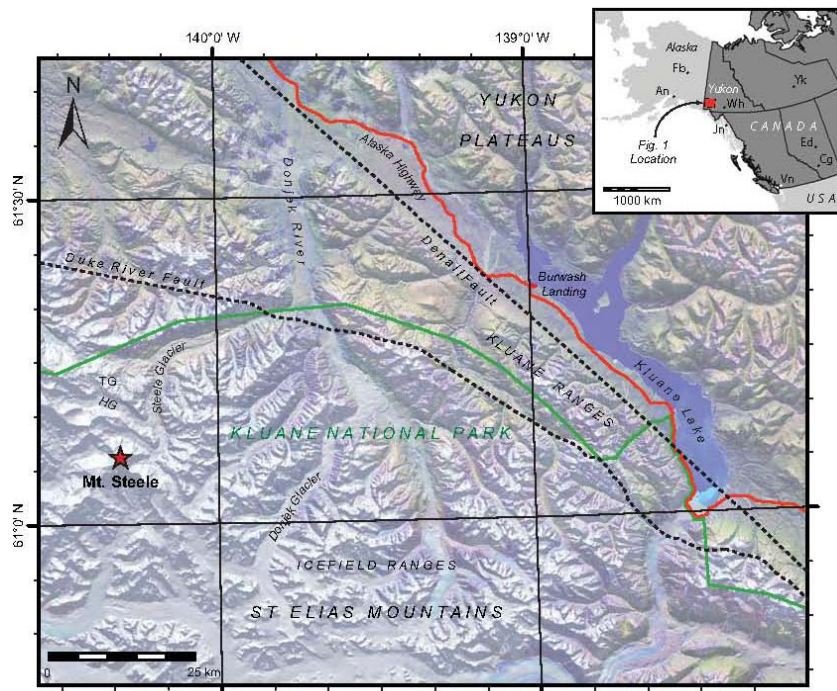
Figure 6.3: Location of Mount Steele in southwesten Yukon Territory, Canada. TG: Trapridge Glacier; SG: Steele Glacier; HG: Hodgson Glacier. Inset cities – Wh: Whitehorse; Yk: Yellowknife; Ed: Edmonton; An: Anchorage; Fb: Fairbanks; Jn: Juneau.

The source of the 2007 ice and rock avalanches is the north face of Mount Steele, which rises over 2,100 m above upper Steele Glacier (Figs. 6.1, 6.2, 6.3, 6.4). This face is almost entirely covered by glacier ice and firn estimated to be 30 m thick on average. Steele Glacier extends approximately 35 km from its source near Mount Steele to its terminus at 1,160 m a.s.l. It has a history of surges, the most recent of which occurred between 1965 and 1968 (Stanley, 1969, 1972). Steele Creek flows from the glacier toe to its confluence with the Donjek River 12 km to the east (Fig. 6.3).

170
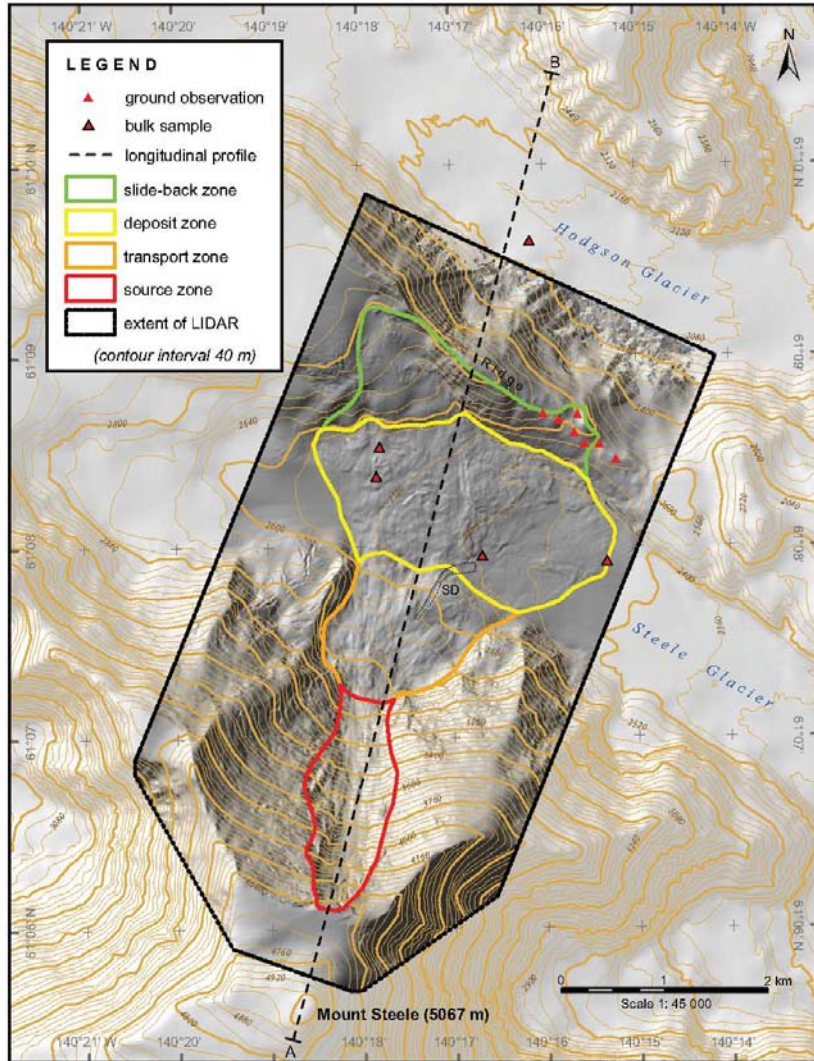
Figure 6.4: Map of the July 24th rock and ice avalanche features. Hillshade image derived from the LiDAR survey described in the text. SD: Secondary debris flow channel. The contours are from the pre-landslide topographic surface, dating to ca. 1951.

The Alaska Highway crosses the Donjek River about 52 km downstream from the glacier

terminus (Fig. 6.3). It is Yukon's main highway and parallels the proposed route of a pipeline

that will carry natural gas southward from the North Slope of Alaska to markets in the conterminous USA.

Burwash Landing (population ca. 100) is the nearest settlement to Mount Steele, 76 km northeast of the peak (807 m a.s.l.), which has a semi-arid continental climate, with mean annual precipitation of 280 mm and mean annual temperature of -3.8°C (Environment Canada normals for 1971–2000). Mean annual temperature decreases with elevation in the eastern and northern parts of the St. Elias Mountains to about -9°C at 2,500 m and -22°C at 5,000 m (Smith et al., 2004). Mean annual temperature at a weather station located at 2,670 m, 52 km southeast of Mount Steele, ranged from -8.8°C to -9.5°C between 2003 and 2005 (C. Zdanowicz, unpublished data).

The St. Elias Mountains are rapidly rising due to plate interactions off the south coast of Alaska (Bruhn et al., 2004). The Denali and Duke River faults extend northwest through the region, east and north of Mount Steele (Fig. 6.3). The Denali fault system within Canada has been inactive during the late Holocene (Clague, 1979), but incurred at least 350 km of right-lateral offset occurred during the Cenozoic (Lowey, 1998). Active seismicity and release of strain along the main Denali Fault in Alaska are transferred to the Totshunda and Duke River fault systems in Canada, resulting in moderate to large earthquakes in the St. Elias Mountains (Horner, 1983; Everard and Savigny, 1994; Haeussler et al., 2004). Rapid uplift and erosion by glaciers, streams, and landslides are also responsible for some of the extreme relief observed in the St. Elias Mountains (Pavlis et al., 2004; Spotila et al., 2004).

The geology of the Mount Steele area has not been mapped in detail, but regional-scale mapping indicates that the rock mass on the north face of Mount Steele mainly consists of granodiorite, diorite and gabbro of the Late Miocene Wrangell Suite (Dodds and Campbell, 1992). The Wrangell Suite intrudes late Proterozoic to Triassic volcanic and sedimentary rocks of the Alexander Terrane (Gordey and Makepeace, 2003; Wheeler et al., 1991; Dodds and Campbell, 1992).

6.1.2 Event chronology

The 2007 rock and ice avalanches occurred on the steep north face of Mount Steele (Figs. 6.1, 6.2, 6.4). Previous mass movements at this site suggest the existence of conditions favourable for slope failure, and photographs taken during scientific expeditions in the late 1930s, for example, show fresh debris below the north face (F. Wood, unpublished data, 1939; Wood, 1972). The bowl-shaped morphology of the north face of Mount Steele suggests that large landslides have occurred there repeatedly in earlier times.

The events in July 2007 have been remarkably well-documented, given the remoteness of the locality and difficulty of access. Glaciologists flying to Trapridge Glacier on July 14th, 2007 took photos of Mount Steele's north face clearly showing fresh debris on the glacier surface. The glaciologists also observed a large crevasse that had developed in the ice on the north face (Fig. 6.7a). Photos of the lower part of the north face taken by a park warden on July 21 show deposits of at least two fresh debris flows. One of the debris flows traveled partway down the tributary glacier, while the other traveled further and reached the southwest margin of Steele Glacier (Fig. 6.8a).

On July 22nd, at approximately 13:25 hours local time (Pacific Daylight Time), the glaciologists at Trapridge Glacier witnessed a large ice avalanche on the north face of Mount Steele. A slab of ice, ca. 3 million cubic metres in volume, broke away along the crevasse noted a week earlier (Fig. 6.7a, b). The slab rapidly fragmented and developed into an avalanche that entrained additional snow and ice as it swept down the north face onto Steele Glacier. The leading edge of the avalanche powder cloud traveled across Steele Glacier, up a 275-m-high ridge and down onto Hodgson Glacier, a total horizontal distance of at least 8 km (Figs. 6.4 and 6.6). The avalanche debris covered an area of about 2 km² on Steele Glacier (Fig. 6.8b), and the distal edge of the main debris lobe was approximately 5 km from the source zone. The scientists photographed the deposit from the air on July 23rd and 24th, and additional small ice and snow avalanches were observed in the source zone during these

visits. They estimated that 95% of the July 22nd avalanche debris was highly fragmented ice and snow and 5% was rock debris; no large chunks of ice or rock were noted.

Seismographs in Alaska and northwestern Canada recorded the July 22nd ice avalanche as a M_L2.1 seismic event. Based on the large difference between surface and body wave magnitudes, it was recognized as a mass movement rather than an earthquake (Ekström et al., 2007).

A larger mass movement (the "main event") occurred at Mount Steele 2 days later, on July 24th at 17:57 hours local time (Figs. 6.7c, 6.8c, 6.8d). It was not directly witnessed but was recorded on seismographs as a M_L3.4 seismic event. The magnitude estimated from long-period surface-waves M_S5.2, and modeling of the waveforms suggests an estimated duration of 100 seconds (Ekström, 2006; Ekström et al., 2007). Another, much smaller mass movement was detected by the Alaska Earthquake Information Centre about 1.5 hours later at the same location (N. Ruppert, personal communication, 2007). A prominent light-coloured (ice-rich) debris lobe located near the east margin of the deposit (Figs. 6.2 and 6.8c) is attributed to this secondary event and suggests that it was likely an ice avalanche.

A total of sixteen earthquakes were recorded within 300 km of Mount Steele between July 1st and 24th, 2007, but none happened at or near the time of the July 22nd or July 24th mass movements. The largest and deepest of the earthquakes (M_L4.1, depth 25 km) occurred on July 9th; its epicentre was 152 km southeast of the mountain. The closest earthquake (M_L2.3) occurred on July 2nd, 109 km east-southeast of Mount Steele. The other earthquakes ranged in size from M_L2.0 to 3.7; their epicentres were 113 to 269 km south and southeast of Mount Steele, and their focal depths ranged from 1 to 15 km.

Analysis of Environment Canada air temperature records from Burwash Landing, located at 807 m elevation 76 km northeast of Mount Steele, indicates that daily average temperatures were up to 2.7°C above the 1971–2000 July monthly normal temperature (12.8°C) for 10

174

days prior to the main event. The average daily temperature for the month of July was 0.6°C higher than normal; the average daily maximum temperature was 0.5°C lower than the 19.3°C normal; and the average daily minimum temperature was 1.5°C higher than the 6.3°C normal.

Following the main event, a number of field parties visited Mount Steele and documented key post-failure landslide characteristics. On July 25th, geologists photographed the landslide debris and reported that "*a lot of dust*" was still in the air at 14:00 hours (J. Spotila, personal communication, 2007). The Yukon Geological Survey conducted a fixed-wing reconnaissance survey on August 2nd and revisited the site by helicopter on August 12th to obtain debris samples and additional photographs. The geologists observed additional small ice and snow avalanches initiating from different parts of the source zone during both visits.

A high-resolution, airborne LiDAR survey was conducted on August 12th by the Geological Survey of Canada in partnership with the Applied Geomatics Research Group (Centre of Geographic Sciences, Nova Scotia Community College). The survey was flown at altitudes between 4,000 and 6,100 m a.s.l. and at a flying speed of 260 km/h (Fig. 6.5).
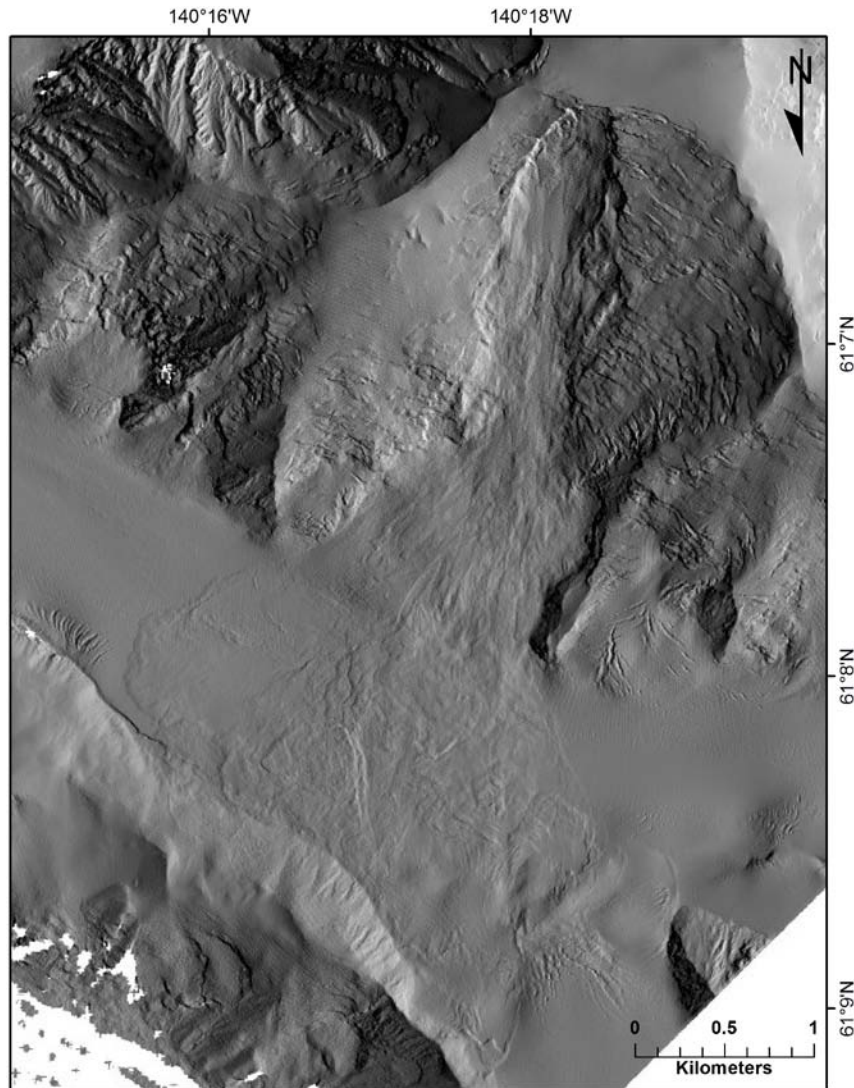
Figure 6.5: Mount Steele rock avalanche hillshade DEM created from the August 12th 2007 LiDAR point cloud.

Over seven million data points were collected along 11 east–west survey lines across the face of Mount Steele and adjacent Steele Glacier (Fig. 6.5). A pulse frequency of 33 kHz, infrared laser wavelength of 1,064 nm and a scan angle of ±24° (48° field of view) were used. A hillshade digital elevation model derived from these data is shown as part of the background image in Fig. 6.4. Both the LiDAR survey data and 1:50,000-scale national topographic data (Natural Resources Canada) were used to characterize the topography and volumes of the landslide source area and deposit.

176

6.2 **Characterisation of the July 24ᵗʰ rock and ice avalanche**

6.2.1 Failure and transport zones

The extreme upper portion of Mount Steele's north face is covered by snow and ice and slopes 23–27° down from the summit (5,067 m a.s.l.) to a bench located at approximately 4,650 m a.s.l. (Figs. 6.1, 6.2). The upper failure zone is delineated by a curved escarpment up to 540 m wide, which exposes approximately 70 m of ice above the bedrock along the edge of the bench. Below it, a steep (average slope 44°) slope descends 1,750 m in elevation to a small tributary glacier that flows into Steele Glacier (Figs. 6.4 and 6.6). The rock and ice that failed during the main event extended from the headscarp down to the top of this tributary glacier.
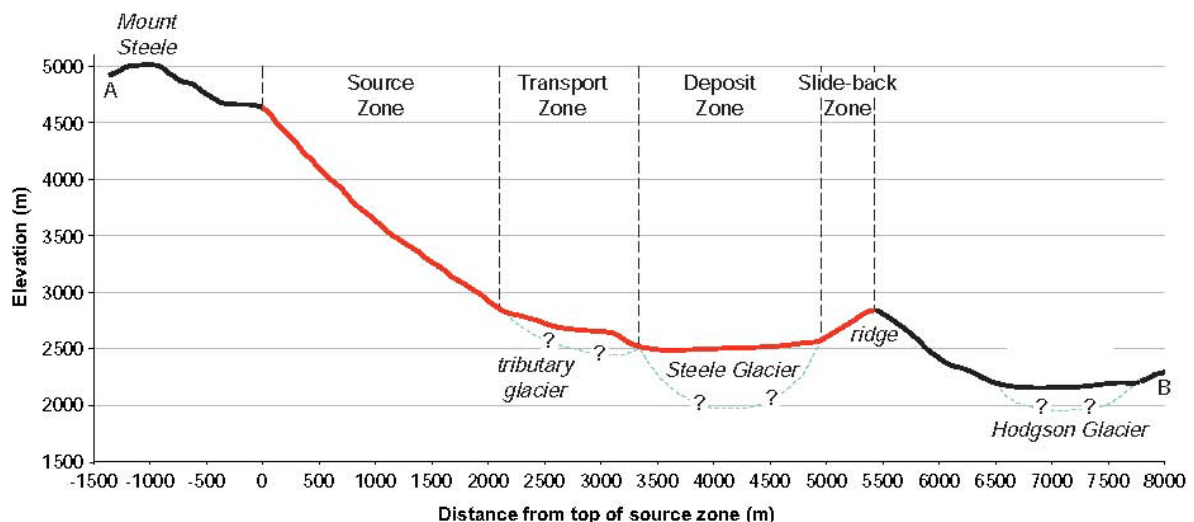
Figure 6.6: Longitudinal profile along line A–B shown in Fig. 3. The travel path of the July 24ᵗʰ rock and ice avalanche is shown by the red line; this path is not equivalent to that used to determine maximum runout.

Detailed examination of the failure zone was impossible due to the high altitude, extreme ruggedness of the terrain, ongoing landslide risk and snow cover. However, pebble- to boulder-sized fragments at the edge of the debris sheet and small rock fragments in bulk samples collected for analysis of particle size and water content indicate that the landslide occurred in light-coloured, hornblende-biotite-quartz diorite and tonalite and plagioclase hornblende-biotite porphyry. The presence of slickensides, sericitic alteration of feldspars

177

and red- to dark-brown oxidization of fracture surfaces suggests that the rocks originated from a fault zone.
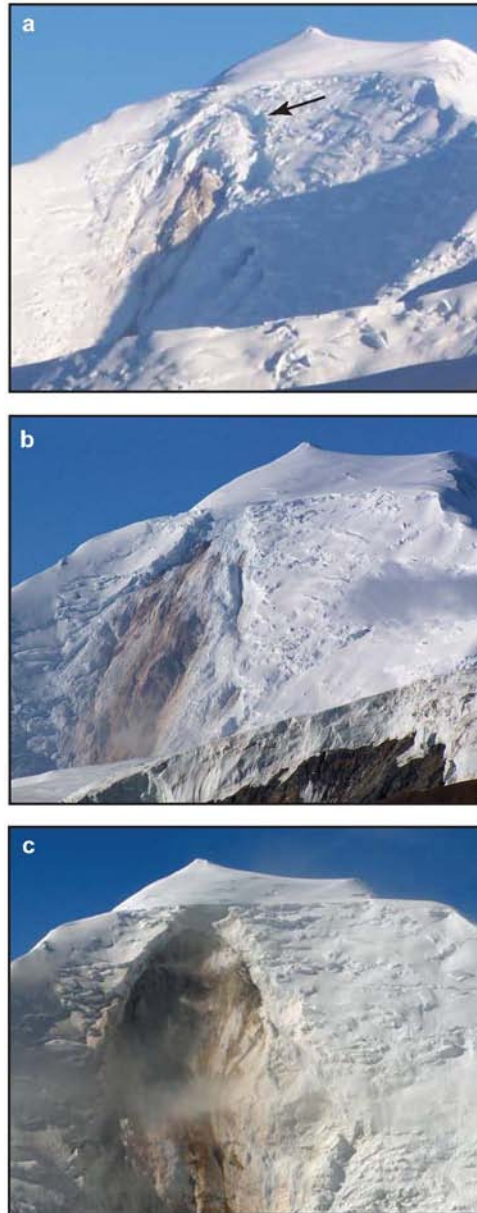
Figure 6.7: Source zone of the ice and rock avalanches on the north face of Mount Steele. a) Crevasse (*arrow*) outlining slab of ice that failed on July 22nd, 2007 (photo taken prior to July 22nd by A. Schaeffer on July 15th, 2007); b) Bedrock exposed after the July 22nd ice avalanche (photo by A. Schaeffer on July 23rd, 2007); c) Source zone scar from July 24th main event, the scar is approximately 500 m wide (photo by P. von Gaza, August 2nd, 2007).

Photographs taken of the failure zone indicate three main sets of discontinuities in the rock mass (Fig. 6.9). The most conspicuous discontinuity set (D1) consists of smooth planes striking parallel to and dipping at the same angle as the slope; some D1 planes may also be daylighting from the slope. The second discontinuity set (D2) dips in the same direction as D1, but at a steeper angle, and therefore does not daylight. The third discontinuity set (D3) is sub-vertical, strikes southwest to northeast, and probably controls the east lateral margin of the main scarp.

The transport zone of the landslide extends a horizontal distance of 1,350 m from the top of the tributary glacier at 2,900 m a.s.l. to the junction of the tributary glacier and Steele Glacier near 2,500 m a.s.l. (Figs. 6.2 and 6.4). Much of the original tributary glacier surface is visible in this zone; thus, only minor deposition was observed and the debris was patchy and thin. Parts of the tributary glacier surface appear scoured in photographs taken shortly after the avalanche, and erosion was probably enhanced by pre-existing longitudinal crevasses. Analysis of the LiDAR data suggests that the most prominent scour is at least 16 m deep, resulting in significant entrainment of materials. The effects on landslide flow, surface roughness, and the configuration of pre-existing longitudinal and transverse crevasses are uncertain.

6.2.2 Deposit zone

The July 24th avalanche deposited a thick sheet of ice and rock debris across the entire 1.5 km width of Steele Glacier. In the distal part of its path, the avalanche reached, but did not significantly overtop, the crest of a 275 m high ridge (Figs. 6.4 and 6.6). Some of the debris at the northwest edge of the deposit and much of the debris that climbed this ridge slid backwards towards Mount Steele after reaching their limits of travel (Fig. 6.8c). We refer to this process as "slide-back". This is important to consider when attempting to estimate the thickness of debris on Steele Glacier, because it led to significant thickening of the debris at the base of the ridge.
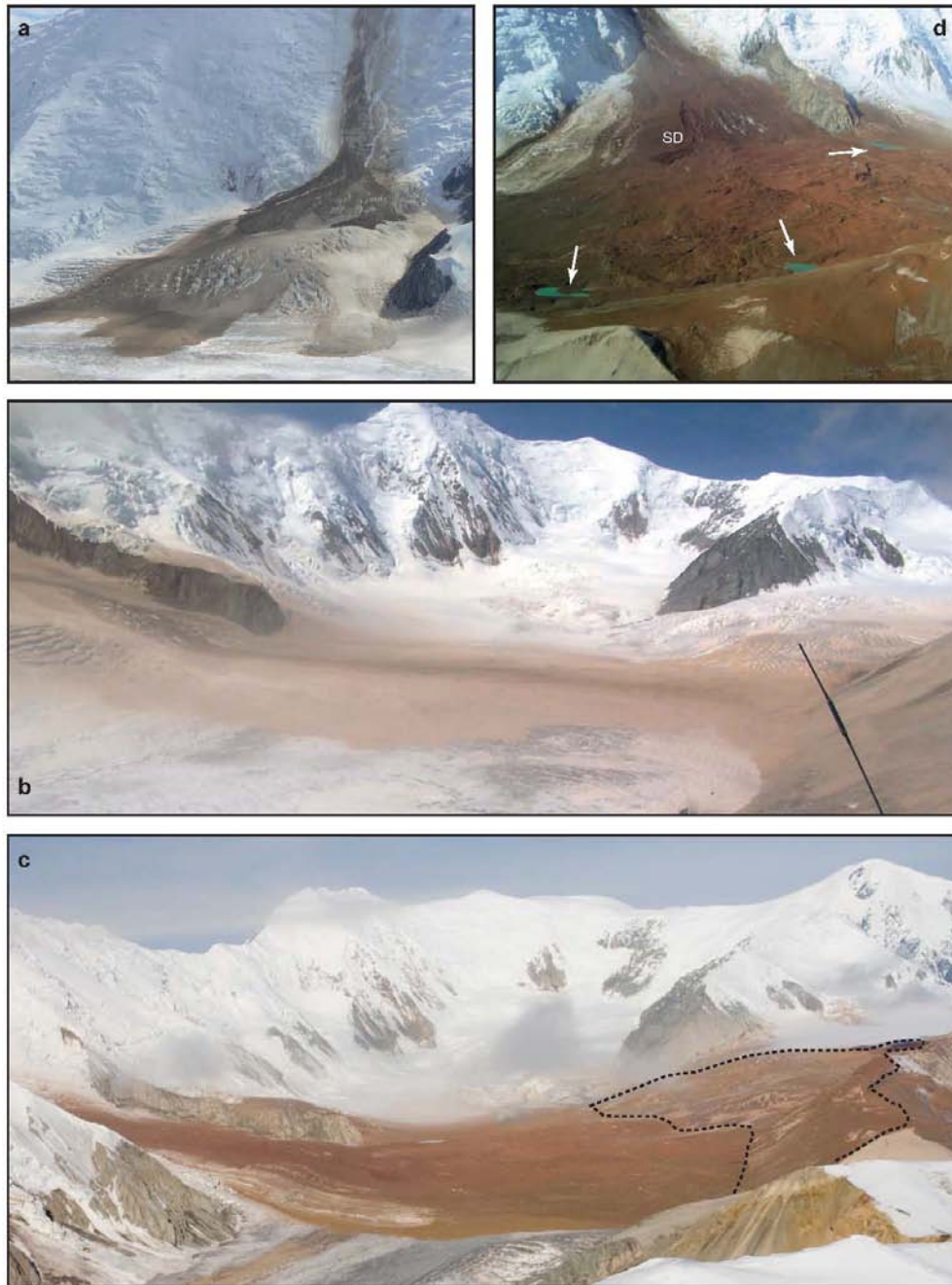
Figure 6.8: Landslide deposits: a) Fresh deposits of two or more small debris flows on the tributary to Steele Glacier, prior to the main event; southern edge of Steele Glacier in the foreground (photo by L. Freese, July 21st, 2007); b) Deposit of July 22nd ice avalanche that extended across Steele Glacier; the deposit contains ca. 95% ice and 5% rock debris (photo by A. Shaeffer, July 24, 2007); c) Debris of July 24th landslide; slide-back zone is delineated by the dashed line; d) Debris of July 24th rock and ice avalanche viewed from above the distal ridge that impeded runout. Note the discontinuous thin debris on ridge crest and tributary glacier, the small ponds formed from ice melt (*arrows*) and secondary debris flow channel (photo by P. Lipovsky, August 2nd, 2007).

180

The debris sheet of the main event covered an area of 5.28 km², fanning out to a width of 3.1 km at the north margin of Steele Glacier (Fig. 6.4). This area includes the total area covered by debris before slide-back. The area of slide-back is about 1.62 km², thus the total area of significant debris cover is about 3.66 km².

The debris was thin on the south flank of the ridge that separates Steele and Hodgson glaciers and in places on Steele Glacier itself, notably where slide-back occurred (Fig. 6.8c). Patchy, thin debris was also present over much of the tributary glacier, but this area is not included in the deposit zone shown in Figure 6.4 since debris transport dominated in this part of the path. In addition, a coating of airborne silt and sand up to 20 cm thick accumulated on the snow and ice on both sides of the ridge crest, and this material was not considered as part of the main debris sheet volume.

The surface of the debris sheet was hummocky, and the local relief of the hummocks, estimated during aerial surveys, was up to 10 m. No surface water was visible within the debris sheet in photographs taken on July 25th, but numerous small ponds had developed on and adjacent to the debris sheet by August 2nd (Fig. 6.8d). Photographs of the Steele Glacier surface taken before the main event indicate very little supraglacial surface water that could have been dammed by the debris and contributed to the ponding, suggesting that the debris contained a significant volume of ice that quickly melted during transport and/or after deposition. Photographs taken less than a day after the main event indicate a prominent secondary debris flow channel near the southern margin of the debris sheet (Fig. 6.8d), further suggesting that the debris was highly saturated when it was deposited.

The debris was found to be much finer than typical rock avalanche deposits (Evans and Clague, 1988, 1999; Jibson et al., 2006). Only scattered boulders were observed during the helicopter and ground surveys, and none was larger than ca. 3 m in size. The high degree of fragmentation suggests that the source rock may have been intensely fractured before it failed.

Bulk samples (3.5–4.0 kg) of surface debris were collected at four locations on August 12th (Fig. 6.4). The solid portion of the samples consists of 58–64% coarse-grained material (>2 mm), the majority of which is pebble-size. The remaining fine-grained material consists of 72–75% sand, 19–21% silt and 7–9% clay. Water constituted 7–35% of the mass of the samples and is assumed to have originally been snow and ice. Based on these data, the debris sheet must have contained significant volumes of snow and ice at the time of the rock avalanche nearly 3 weeks earlier. Several large ice blocks, up to 2 m across, were also observed near the crest of the ridge separating Steele and Hodgson glaciers on August 12.
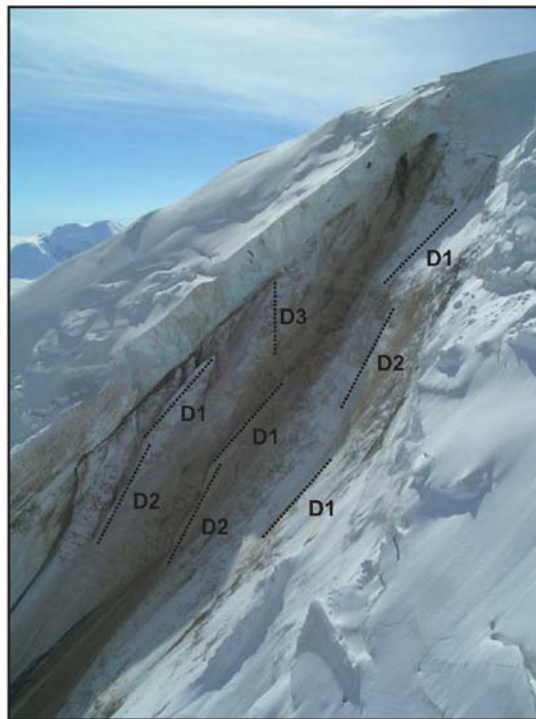
Figure 6.9: Discontinuities (D1, D2, and D3) in the rock mass of the July 24th rock and ice avalanche source zone (photo by P. Lipovsky, August 12th, 2007).

We did not attempt to characterize or map the debris on the ground during the 2007 field season because of the continuing high hazard at the site. The area of the deposit is accurately known from the LiDAR survey, but some uncertainty remains concerning the maximum and mean thicknesses of the debris and therefore its volume. This uncertainty is primarily due to

the fact that the surface elevation and morphology of the Steele Glacier immediately prior to the main event is not adequately known. The only topographic map available for the Mount Steele area was produced from 1951 aerial photography. Subsequent changes in the surface elevation of Steele Glacier are difficult to estimate because of the strong influence of sporadic surging events and recent climatic change. Based on visual inspection during the helicopter survey on August 12th, the debris appeared to range in thickness from 4 to 15 m, suggesting an average thickness of about 7.5 m. LiDAR mapping indicates a greater average thickness, on the order of 22 m. These average thickness values imply a volume range of 27.5 to 80.5 Mm³, respectively, for the main event, and includes a significant volume of snow and ice. These values should be taken as minimum and maximum estimates of the main event deposit volume. Future field and remote sensing work will attempt refine these estimates of debris thickness and volume.

6.3 **Dynamic reconstruction**

The mean velocity of the main event was estimated from seismograms recorded at US Geological Survey seismic stations in Alaska on July 24th. The seismograms indicate that the event lasted for approximately 100 s, a duration which may include a slide-back motion after the maximum runout distance had been reached. The path distance to the distal edge of the slide-back zone varies between 6.5 and 3.5 km depending on whether it is measured from the top of the landslide source zone or the base of the source zone, respectively. The average velocity over the maximum and minimum path distances is therefore between 65 and 35 m/s, respectively. The debris run-up (h) to the summit of the distal ridge was about 275 m (Fig. 6.6). For this run-up geometry, the energy head formula ($v=[2gh]^{1/2}$) gives a minimum velocity (necessary to overtop the ridge) of 73 m/s at a horizontal distance of 5,000 m.

A first-order, 2-D dynamic analysis of the main event along the path shown in Figure 6.6 was carried out using the simulation software DAN-W (Hungr, 1995; Hungr and McDougall, 2008). In the DAN-W model, debris width (taken from Figs. 6.1, 6.4, 6.5) is inputted along the path length of the rock avalanche. The simulation was carried out for material which

originated in the source zone as defined in Figures 6.4 and 6.7, using an initial failure volume of 51 Mm³, in the mid-range of our volume estimates noted above. No entrainment was specified since determination of significant debris entrainment along the path of the main event was difficult to discern. Defining the origin of the landslide as the base of the source zone, the run time and the run-out distance of the debris front were simulated very well (Fig. 6.10) using a Voellmy basal resistance model (Hungr, 1995) with values of 0.052 and 1,525 m/s^2 for the friction (f) and turbulence coefficients (ξ), respectively. These parameter values are comparable to those used to successfully simulate the 1964 Sherman Glacier rock avalanche (f=0.03 and ξ=1,000 m/s^2; Hungr and Evans, 1996). The run-up to the top of the ridge is simulated almost precisely, without overtopping it, and the slide-back is also predicted (Fig. 6.10). The simulated velocity at a horizontal distance of 5,000 m is 42 m/s, which is significantly lower than the 73 m/s estimated from the energy head formula.
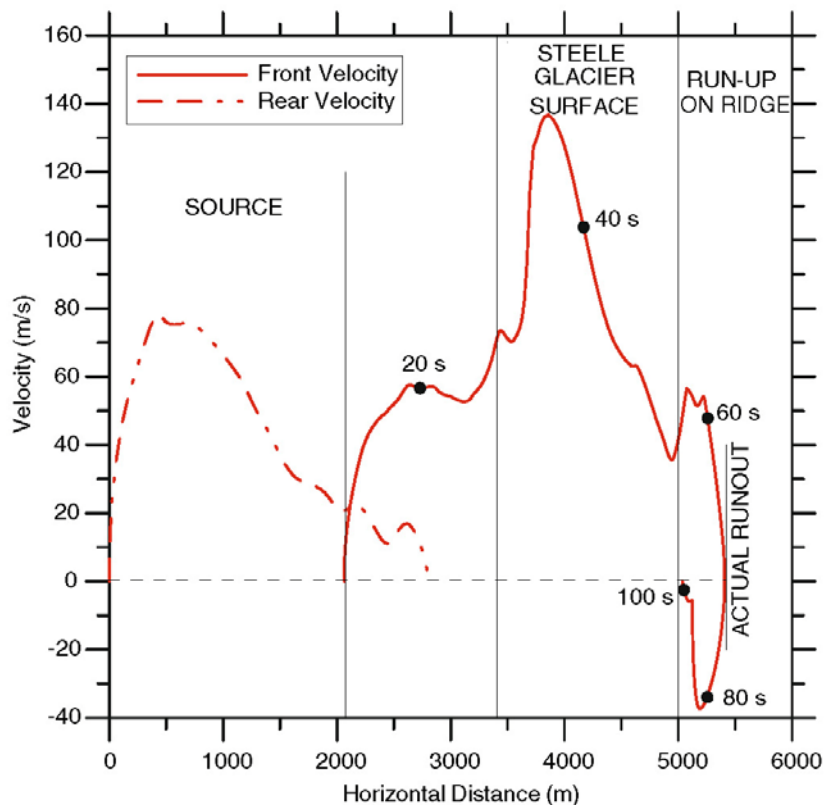
Figure 6.10: Simulated velocity profile of the main event rock and ice avalanche on July 24th, 2007. The velocity of the front and rear of the debris sheet are shown. Note the rapid acceleration of the debris when the front of the sheet encounters the surface of Steele Glacier, followed by rapid deceleration as the debris thins and

184

spreads out on the glacier surface. The black circles represent position and velocity of the debris front at 20 s intervals during movement. Maximum runout was achieved at 69 s, suggesting a simulated mean velocity of 78 m/s. By 100 s, the slideback of debris had reached the base of the ridge. Simulation was carried out using the Voellmy model in DAN-W (Hungr, 1995) with values of 0.052 and 1,525 m/s^2 for the friction and turbulence coefficients, respectively.

The travel angle [fahrböschung = tan^{-1}(H/L)] of the Mount Steele main event is 18°, where H=1,860 m and L=5,760 m. In this case, both H and L were measured to the most distal edge of the slide-back zone (i.e. to the maximum limit of debris travel). It should be noted, however, that the maximum descent from the head scarp to the surface of Steele Glacier is 2,160 m. The H/L ratio for the Mount Steele event is the largest for 20 rock avalanches documented with volumes greater than 1 Mm³ and which occurred onto glaciers in northwest North America (Alaska, Yukon, British Columbia) between 1956 and 2007 (Fig. 6.11; Evans and Clague, 1988, 1999; Jibson et al., 2006; Molnia et al., 2006). The anomalously low mobility of the main event resulted from impact of the debris with the opposing topographic ridge and the spreading of debris on the surface of Steele Glacier. We point out, however, that the debris exhibited reverse mobility by sliding back onto the surface of Steele Glacier. This debris probably collided with material still moving down the path in the initial movement direction. We suggest this process also contributed to the chaotic surface topography of the debris in the deposit zone.

6.4 **Global comparisons of occurrence and behavior**

Rock avalanches onto glaciers are common in high glacierized mountain ranges of the world (Evans and Clague, 1988; Petrakov et al., 2008) and have been well-documented in the European Alps (Eisbacher and Clague, 1984; Porter and Orombelli, 1980), the Southern Alps of New Zealand (McSaveney, 2002), the Himalayas (Hewitt, 2006a,b, 2008, 2009c), the Cordillera of northwest North America (Post, 1967; Evans and Clague, 1999; Jibson et al., 2006; Molnia et al., 2006; Gorum et al., 2014) and the Andes (Hauser, 2002). They form part of a spectrum of complex mass movement processes involving glacial ice (Petrakov et al., 2008) that are significant hazards in some mountain terrain.

Rock avalanches and related mass movements that are contained within the limits of a glacier normally pose little risk to people and infrastructure. In contrast, mass movements that evolve, either instantaneously or after some delay, from rock and ice avalanches onto glacier surfaces and travel beyond glacier limits have caused disasters in populated mountain ranges. One of the most deadly landslides in recent times developed from an earthquake-triggered rock and ice avalanche that fell from the north peak of Nevado Huascaran onto a glacier surface in the Cordillera Blanca, Peru in 1970 (Pflaker and Ericksen, 1978; Evans et al., 2007, 2009a). The landslide obliterated the town of Yungay, claiming thousands of lives (Cluff, 1971; Keefer and Larsen, 2007; Evans et al., 2009a).

Glacier-related mass movements commonly involve flows of highly fragmented, ice-laden debris that can travel long distances reaching very high maximum velocities, that in some cases exceed 100 m/s (Evans et al., 1989; Petrakov et al., 2008). As in the Mount Steele case, melt of ice and snow at the base of the moving mass and that which was incorporated during movement contributes to the high mobility and velocities of these landslides.

The runout of rock avalanches on glaciers is commonly enhanced compared to that of non-glacial rock avalanches of the same volume (Evans and Clague, 1988, 1999). However, the runout of the main event at Mount Steele was significantly less than other rock avalanches of similar volume that have occurred on glaciers (Fig. 6.11; Evans and Clague, 1988, 1999; Jibson et al., 2006; Molnia et al., 2006). In the Mount Steele case, runout was impeded when the landslide encountered a significant topographic barrier; the 275 m high ridge separating Steele and Hodgson glaciers (Figs. 6.1 and 6.4). In addition, the Mount Steele landslide, although initially guided down the north flank of the mountain, subsequently spread over the nearly flat surface of Steele Glacier, rapidly dissipating much of its kinetic energy. The combination of a topographic barrier and rapid unconfined spreading of the debris on the glacier surface explains the relatively short travel distance of the landslide in relation to its volume.
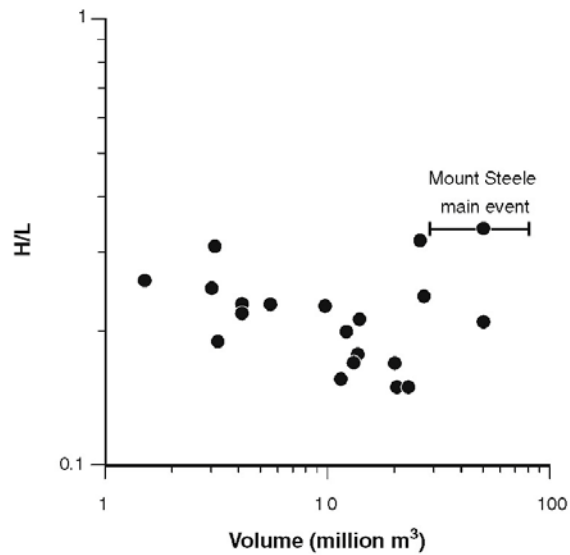
Figure 6.11: Comparison of Mount Steele main event mobility with 20 rock avalanches (volume >1 Mm³) onto glaciers documented in northwest North America (Alaska, Yukon and British Columbia) between 1956 and 2007. H/L is defined in the text, and the volume of the main event is plotted as the mid-point between the minimum and maximum volume estimates described in the text. Data are from Evans and Clague (1988 and 1999), Jibson et al. (2006) and Molnia et al. (2006).

6.5 **Conclusions**

The Mount Steele rock and ice avalanche, which occurred on July 24th, 2007, ranks among one of the largest documented landslides in the mountains of western Canada. It was part of a sequence of slope failures that occurred on the north slope of Mount Steele over a period of several days in July 2007. Further research is needed to determine whether these events were causally related. None of the failures were triggered by earthquakes and weather records from the closest community (Burwash Landing) suggest that air temperatures in July 2007 were not anomalous for the region. The failures occurred on a slope that had been the source of previous slope instability. The fine texture and the red-brown colour of the debris suggest that the igneous rocks in the failure zone are highly sheared and have low rock mass strength, perhaps because they lie within a fault zone.

Despite the remote location, the July events were exceptionally well-documented by eyewitnesses and seismographs. Analysis of seismic records indicates a maximum and minimum mean velocity of 65 and 35 m/s, respectively, for the main event. During this

187

event, ice and rock debris descended a maximum of 2,160 vertical metres and traveled a maximum horizontal distance of 5.76 km. Runout was impeded by a 275 m high ridge on the north side of Steele Glacier; the leading edge of debris just reached the top of the ridge before it slid back onto Steele Glacier. The debris contained much snow and ice derived from the slopes of Mount Steele. The melting of this entrained snow and ice contributed to the fluidity of the debris, its mobility and its high velocity. The Mount Steele landslide is one of a large number of landslides onto glaciers over the past century in northwestern North America, indicating that rock slopes adjacent to glaciers are particularly prone to catastrophic failure. Work is ongoing in order to evaluate the causes of the Mount Steele landslide sequence and to characterize the geometry and behaviour of the July 24th event with more precision.

Chapter 7

Conclusions and Future Work

7.1 Introduction

This thesis represents a large body of work that seeks to describe, quantify, and simulate the behaviour of large rock slope failures (> 1 Mm³), in the form of landslides and rock avalanches. This study focused on regions in northwest North America (British Columbia, Yukon Territory, and Alaska), and on regions in the Himalaya and Pamir Mountain chains (Pakistan, and India). This research looked directly at: 1) the ability to accurately calculate geometrics for large scale landslides and their associated landslide dammed lakes, utilizing data from remotely sensed sources; 2) the attempt to successfully simulate the observed dynamics for both landslide emplacement, debris deposits, and outburst floods; and, 3) attempt to quantify the kinetic and specific energy involved in rock avalanches, and how these energetics relate to fragmentation, and spreading of debris sheets. It has been shown that both of the above study regions are highly dynamic landscapes, where the occurrence of failures per area is higher than non-mountainous regions, and these events are aiding to the shape and profile of the surfaces found today. The combination of landslides and their associated landslide dammed lakes are an important geomorphic process to study, as it has a direct relationship to the hazard and risk faced by local communities living and working in these regions. By understanding the emplacement dynamics of large landslides and/or the outburst flood scenarios from impounded reservoirs, we can attempt to reduce the direct impacts these events have to local communities. The main conclusions of each modular chapter are summarized below.

7.2 Landslides and Landslide Dams in the Pamir and Himalayas

The remains of rockslide dams are widespread throughout the river valleys of the northwest Himalayas (Pakistan and India) and the adjacent Pamir Mountains of Afghanistan and Tajikistan, Central Asia. This region contains in excess of two hundred known rockslide deposits of unknown age that have interrupted surface drainage and previously dammed

major rivers in the region in recent and prehistoric time. Some prehistoric rockslide dams in the northwest Himalayas have impounded massive lakes with volumes in excess of 20 Gm³. The region contains: 1) the highest rockslide dam in the world (the 1911 Usoi rockslide, Tajikistan), which impounds the current largest rockslide-dammed lake (Lake Sarez) on Earth (est. volume 17 Gm³); 2) the largest documented outburst flood (6.5 Gm³) associated with a historical rockslide dam outburst (the 1841 Indus Flood, Pakistan); and, 3) the world's most recent rockslide-dammed lake emergency, the 2010 Attabad rockslide dam on the Hunza River, in the Upper Indus basin, including the newly created Lake Gojal. We used SRTM-3 digital terrain data and various satellite imagery platforms, in combination with historical literature, to analyze three major rockslide damming events as follows: 1) our analysis of the 1841 Indus rockslide-damming event indicates that the volume of the impoundment and subsequent outburst was a minimum of 6.5 Gm³, the largest outburst from a rockslide-dammed lake in historical time; 2) the 1858 Hunza Valley rockslide dam impounded ca. 805 Mm³ before a catastrophic outburst in August 1858, which occurred within 5 km of the current 2010 rockslide emergency at Attabad; and, 3) the development of the 2010 Hunza rockslide-dammed lake is described in detail. Lake Gojal reached a maximum volume of ca. 430 Mm³ before stable overflow through an excavated spillway on the rockslide debris began on May 29, 2010. Stable overflow continues to April 2014, and over that time period the spillway has been expanded and deepened significantly, resulting in a reduction of lake depth and volume, and therefore a lowering of the hazard and risk to downstream communities. The emplacement of rockslide dams and the behaviour of their impounded lakes are critical hazards to communities and the development of infrastructure, including hydroelectric facilities, in the northwest Himalayas (India and Pakistan) and adjacent Pamir Mountains (Afghanistan and Tajikistan).

7.3 **Attabad rockslide and Lake Gojal**

Rockslides and rock avalanches can be found throughout the Indus and Hunza river valleys as both new and dissected historic deposits. Due to the steep walls and narrow canyon topography, they often form valley blocking debris deposits which have the ability to impound significant volumes of surface water into unstable natural reservoirs. Many of these

prehistoric and historic dams have been breached, releasing large quantities of impounded water in short timeframes, catastrophically flooding downstream valleys and communities. They often leave behind distinct topographic evidence in the form of knick-points and low sloping upstream aggregated river systems. Using digital elevation datasets combined with high resolution multi-temporal imagery, we calculated the changing geometrics (e.g. length, area, volume, depth) of Lake Gojal, from its initiation in January 2010, and its slow drawdown from July 2010 until April 2014 utilizing two distinct methods. A first-order calculation was completed using only interpolated contours from the SRTM-3 and ASTER GDEM2 DEMs. It was assumed that these DEM contours would be a satisfactory match to the lake shorelines, however it was discovered that the resulting geometric values calculated from the interpolated elevations were most likely exaggerated, and would only give an approximation, within an order of magnitude of the true values. Therefore, a more rigorous pixel-by-pixel statistical method was also used, which returned favorable values to the field-observed changes. This technique is comparable to the first-order results, but we believe offers a higher degree of accuracy, and includes the ability to quantify errors in the DEM data analysis. The two methods described above returned maximum volumes for Lake Gojal of ca. 430 Mm³ using the contour interpolation method, and ca. 432.8 Mm³ ($\pm$ 29.2 Mm³) for the pixel-by-pixel analysis, covering an area of approximately 10 km². Very similar results, however, the statistical approach allowed for a proper quantification of error, which is between 6% - 7% of the total volume. The ongoing excavation of the spillway by Pakistani authorities from 2010 - 2013 had initially reduced the depth of the lake by about 10 m, decreasing the possible outburst volume by almost 100 Mm³. By April 2014, after additional cycles of excavation and continued erosion of the spillway, Lake Gojal has dropped in elevation to 2398.04 m a.s.l. ($\pm$ 4.13 m at CL(95%)), with a total reservoir volume of ca. 126.5 Mm³ ($\pm$ 13.5 Mm³), approximately 29% of its maximum size, according to our pixel-by-pixel analysis using the SRTM-3 DEM. Therefore, the continued excavation and erosion has eliminated much of the hazard and risk of a catastrophic outburst flood facing the downstream communities. The creation, filling and failure of rockslide dams in the Indus and Hunza river basins happens with a frequency of approximately 1 in 50 years, making them a

191

constant hazard to communities living in these regions, as well as the development of infrastructure, including highways (e.g. Karakorum Highway) and hydroelectric projects (e.g. The Diamer-Basha Dam). Therefore, the quantification and increased understanding of the primary and secondary processes involved in these regions remains of vital importance

7.4 **Yigong Rock-Avalanche and Outburst Flood**

In April 2000, a large-scale rock avalanche dammed the Yigong Zangpo River, forming an extensive rockslide-dammed lake upstream. The impoundment lasted for 62 days before a catastrophic breaching caused by the lake waters overtopping the dam resulted in a massive outburst flood in the Yarlung Zangpo (Tibet) and the Dihang Rivers (India) that travelled downstream to the floodplain of the Brahmaputra in northeastern India. We attempted to reconcile the various inconsistencies in the published literature of the 2000 Yigong landslide, with regards to the path and volume of the rock avalanche, as well as the temporal evolution of the volumes and areas of the natural dam and impounded reservoir. Using digital topographic data (e.g. SRTM-3) and previously published isopleths maps, in conjunction with satellite data from the LANDSAT-7 satellite, we have presented credible and verifiable values for the original landslide source volume (ca. 91 Mm³), the total deposit volume of ca. 115 Mm³, including entrainment and bulking, and the final and outburst volume of Yigong lake (ca. 2.0 Gm³). These values are considerably lower than previously published literature, but still remain as some of the largest values recorded since 1840, and the volume of the Yigong rock avalanche was found not to be exceptional in the literature when compared to similar events worldwide since 1900. The outburst flood of 2.0 Gm³ is second only to the 1841 Indus river outburst which occurred in northern Pakistan. The excavated spillway did not prevent a catastrophic release of lake water, but did significantly reduce the maximum outburst volume by almost 1.0 Gm³. Freely available remotely sensed data, including satellite imagery and digital topographic models, can be reliably used to calculate estimates for the areas and volumes of recent large-scale rock avalanches and newly-formed impounded reservoirs, as well as model their emplacement and outburst dynamics.

7.5 The 1997 Mount Munday Rock Avalanche

Rock avalanches travelling onto glacier surfaces, involving volumes 1 Mm³ or more, are common occurrences in the glacier environments of NW North America, and more than 40 events have been recorded in this region since 1899. This rock avalanche event involved the initial movement of ca. 3.2 Mm³ of granitic gneiss from the steep slopes of Mount Munday that underwent a high degree of fragmentation as it was emplaced onto the surface of Ice Valley Glacier as a thin 2.6 km² debris sheet. The total height of the path was 850 m, and its length was 4,163 m yielding a fahrböschung of 10°. An estimated 4.3×10^{13} J of potential energy was expended in the movement and the specific energy of the rock avalanche was 5,204 J/kg, a comparable value to other rock avalanches in both glacial and non-glacial environments. The mechanism of debris emplacement was predominantly sliding, creating the multiple flow lines/paths observed on the surface of the debris, and the bulldozing of surface snow creating visible trains of debris. We simulated the movement of the rock avalanche using DAN-W and DAN3D, which strongly supports the idea that the debris sheet geometry (runout distance and thickness) and emplacement behaviour (velocity profile) resulted from movement on a low-friction surface (glacier ice) causing excessive debris thinning and spreading, including a longer runout. These types of debris sheets are distinct from those in non-glacial environments in that they are: a) longer in relation to volume; and, b) more extensive in area in relation to volume. These two effects combine to result in a very thin supra-glacial rock avalanche debris sheet, which aids in the analysis of the block fragmentation. We analyzed high resolution aerial photography obtained shortly after the Mount Munday event, which showed that the debris sheet was highly fragmented, with a limited number of large blocks present. We found that ∼85 % of the initial source rock volume was fragmented to block sizes less than 4.7 m^3 in volume during the failure and emplacement process. We believe that low-friction surface-driven fragmentation is a process that at least partially contributes to longer runouts of rock avalanches on glacier surfaces and explains their distinctive thin debris sheet geometry.

7.6 **The 2007 Mount Steele Rock Avalanche**

The Mount Steele rock and ice avalanche occurred on July 24, 2007, ranks among the largest documented landslides in the mountainous region of western Canada. The failure mechanism is not fully understood, but it was not triggered by any known earthquake. Weather records from the closest community of Burwash Landing also suggest that air temperatures in July 2007 were not anomalous for the region. The fine texture and the red-brown colour of the debris suggest that the igneous rocks in the failure zone were highly sheared and likely had a low rock mass strength. The rock avalanche was a combination of both ice and rock debris, which descended a maximum of 2,160 vertical metres and traveled a maximum horizontal distance of 5.76 km. Further runout of the debris sheet was impeded by a 275-m-high ridge on the northeast side of Steele Glacier; the leading edge of debris just reached the top of the ridge before a majority of the mass slid back down onto Steele Glacier, increasing the deposit depths. Analysis of seismic records indicates a maximum and minimum mean velocity of 65 and 35 m/s, respectively, for the rock avalanche event. We believe the melting of the entrained snow and ice, and the large fall height, both contributed to the fluidity of the debris, its mobility and its high velocity.

7.7 **Conclusions**

Remotely sensed data (e.g. satellite imagery, DEMs) can be successfully used to study and quantify large landslides, and their impounded reservoirs in mountainous terrain. This data can also be imported into various simulation models, which can be used to back-analyze specific events, or project a possible future outburst flood simulation. Simulation models (e.g. DAN-W, DAN3D, FLO2D) have been found to successfully replicate the runouts, velocities, volumes, deposit depths and widths, and outburst dynamics (e.g. velocities and downstream depths) of landslides and their impoundments.

Although the utility of remotely sensed data has been shown in this study, it should be considered as a complement, not a supplement, to field excursions and field observed data collection. Mountainous regions are constantly undergoing change, and are not static features on the landscape. Therefore, continued future study, observation, and new computer assisted

techniques are required to continue to advance this field, and not only attract, but enthrall future scientists into landslide research.

The combination of landslides and their associated landslide dammed lakes are an important geomorphic process to study, as it has a direct relationship to the hazard and risk faced by local communities living and working in these regions. By understanding the emplacement dynamics of these large landslides and/or the outburst flood scenarios from impounded reservoirs, we can attempt to reduce the direct impacts these events have to local communities.

7.7.1 Focusing on Geomorphic Processes

The simulation modeling (back-casting or projection) is an important part of landslide research. Models such as DAN-W and DAN3D attempt to simulate the emplacement process and debris deposit geometrics for landslide events. It has been shown that both 2D and 3D models can successfully replicate most of the dynamic processes involved during rock mass emplacement, including velocities, debris depths, and lateral spreading of the debris sheet.

A new technique has been developed to assess the dynamics of fragmentation in rock avalanches in the glacial environment. Much work has been completed on quantifying the smallest grain-sizes in a debris deposit, where the larger blocks are essentially omitted. Using the image techniques described above, a credible grain-size curve for the largest blocks can be obtained, allowing for the creation of a more complete grain-size curve for a particular event. This allows for a more complete understanding of the influence of rock mass type and volume on fragmentation processes during emplacement.

The incorporation of material entrainment and bulking of debris deposits is an important process to quantify when studying large landslides. The entrainment of material can directly influence the emplacement of a rock mass by increasing the overall volume, which can increase the average and maximum velocities of the movement, and allow for a longer runout and further lateral thinning. By increasing the volume of the mass, entrainment also has a direct impact on the energetics of the event, as well as the creation and magnitude of a natural dam, if the rock mass travelled into a narrow river valley.

Downstream floodwave dynamics is an important process to understand giving the direct relationship to hazard and risk for natural dam outbursts. By accurately quantifying the volume of an impoundment, and the downstream valley topography (DEM), floodwave scenarios can be created for various breaching situations, allowing for the delineation of downstream inundation areas. For back-casting historic flood events, flood simulations (e.g. FLO2D) can be successful at recreating the processes involved in replicating the disaster.

This research has also shown the ability to dramatically reduce the hazard and risk to local communities from catastrophic outburst floods through engineering and excavation of the surface on a natural debris dams. For both the Attabad and Yigong landslide dam case studies, excavation through the lowest part of the dam successfully reduced the maximum possible lake depths, therefore reducing the outburst flood depths and velocities.

7.7.2 Focusing on New Methodology

Successful simulations of landslides and outburst floods require detailed inputs to their respective models. One of the newer methods of obtaining this data is through the use of remotely sensed data (e.g. satellite imagery and digital elevation models). This research has shown that one can obtain the necessary geometrics for large landslides or impoundments, solely from these remotely sensed datasets. This can significantly aid research projects where detailed field work is not possible

A new fragmentation analysis method was described above, including the use of aerial photography and computer assisted software. Using a high resolution scan of a single or set of aerial photographs, block fragmentation can be quantified. By polarizing the imagery to a black and white image, allows the blocks to be easily measured and recorded by the image software. This new method can provide researchers with credible grain-size curves for the larger grains and blocks in a debris sheet. It should be noted that this new method requires a thinner debris sheet (unit thickness), which is often found in the glacial environment, to accurately identify all the blocks present at the surface.

A new pixel-by-pixel statistical method of defining the elevation of newly impounded reservoirs from digital elevation models was presented. This technique was found to be of higher accuracy than past methods, such as contour interpolation, and allowed for the

additional calculation of errors in the digital data, providing a more confident result. Overall, it was determined that past methods often exaggerated the volumes of landslide dammed reservoirs, within one order of magnitude.

7.8 **Future Work**

Further analysis and comparison on the errors (horizontal and vertical) involved in using digital elevation models to represent the regional landscape surrounding landslide events is an important area for ongoing research. Some questions which are still requiring details answers: Are these datasets accurate for all sizes and magnitudes of events? Can the accuracy in the DEMs be relied upon, even when local spatial variations are apparent?

More research on the block fragmentation analysis from remotely sensed images of several rock avalanches on glaciers, in combination of ground-truth field excursions to check the validity and accuracy of the new block fragmentation technique present in this thesis. Many scientists have omitted a decent amount of the grain-size curves in the larger fractions by omitting the largest blocks from previous analyses. This needs to be incorporated to obtain a better understanding of the dynamics in rock mass fragmentation, and how it relates to the energetics and total volume.

A collection/inventory of accurate geometric data on as many landslide/rock avalanche events as possible is required, to look at how the kinetic and specific energies of a mass wasting event can control or alter the morphology and geometrics of the resulting deposit (e.g. fragmentation, spreading, runout). This type of research could also improve the regional/global magnitude-frequency plots of various events, which has direct implications to discussions on hazard and risk.

Finally, continued work on the computer modeling and simulation of landslides and their secondary processes over various surficial materials and topographies, at many different magnitudes. This research would attempt to refine the inputs to the various models to a tighter range of values (e.g. frictional and turbulence coefficients), allowing for more accurate back-analyses, and possible projections of future events.

The accurate characterization of landslides/rock avalanches and their secondary effects, such as landslide-dammed lakes is fundamental to understanding the geomorphic processes involved, and implementing the appropriate mitigation strategies to limit the hazard and risk to local communities.

References

Abbott, J. 1848. Inundation of the Indus, taken from the lips of an eye-witness A.D. 1842. Journal of the Asiatic Society of Bengal, 17, 230–232.

Abe, K., Noguchi, S. 1983. Revision of magnitudes of large shallow earthquakes, 1897–1912. Physics of the Earth and Planetary Interiors, 33, 1–11.

Abele, G. 1974. Bergstürze in den Alpen, ihre Verbeitung, Morphologie und Folgeerscheinungen. Wissenschafteliche Alpenvereinsheft, 25, München, 230 p.

Aggarwal, A., Jain, S.K., Lohani, A.K. and Jain, N. 2013. Glacial lake outburst flood risk assessment using combined approaches of remote sensing, GIS and dam break modeling. Geomatics, Natural Hazards and Risk, DOI: 10.1080/19475705.2013.862573.

Agliardi, F., Crosta, G.B., Frattini, P. and Malusà, M.G. 2013. Giant non-catastrophic landslides and the long-term exhumation of the European Alps. Earth and Planetary Science Letters, 365, 263 – 274.

Ali, K.F., de Boer, D.H. 2007. Spatial patterns and variation of suspended sediment yield in the upper Indus river basin, northern Pakistan. Journal of Hydrology, 334, 368–387.

Ali, K.F., de Boer, D.H. 2008. Factors controlling specific sediment yield in the upper Indus river basin, northern Pakistan. Hydrological Processes, 22, 3102–3114.

Archer, D. 2003. Contrasting hydrological regimes in the upper Indus Basin. Journal of Hydrology, 274, 198–210.

Becek, K. 2008. Investigating error structure of shuttle radar topography mission elevation data product. Geophysical Research Letters 35, L15403, doi:10.1029/2008GL034592, 2008.

Becher, J. 1859. The flooding of the Indus. Letter addressed to R.H. Davies, Secretary to the Government of Punjab and its dependencies, Journal of the Asiatic Society of Bengal, 28, 219–228.

Bhatt, B.P., Awasthi, K.D., Heyojoo, B.P., Silwal, T. and Kafle, G. 2013. Using geographic information system and analytical hierarchy process in landslide hazard zonation. Applied Ecology and Environmental Sciences, 1, 14 – 22.

Biedermann, P., Attewill, L. 2002. Evolution of seepage through landslide dams: The case of Usoy Dam in Tajikistan. Paper presented at IAHR Syposium, St. Petersburg, 8 p.

Blenkinsop, T.G. 1991. Cataclasis and processes of particle size reduction. PAGEOPH,136, 59–86.

Bolten, A. and Waldhoff G. 2010. Error estimation of ASTER GDEM for regional applications – comparison to ASTER DEM and ALS elevation models. 3rd ISDE Digital Earth Summit, 12-14 June, 2010, Nessebar, Bulgaria.

Booth, A.M., Lamb, M.P., Avouac, J.P. and Delacourt, C. 2013. Landslide velocity, thickness, and rheology from remote sensing: La Clapière landslide, France. Geophysical Research Letters, 40, 4299 – 4304.

Bowman, E.T., Take, W.A., Rait, K.L., Hann, C. 2012. Physical models of rock avalanche spreading behaviour with dynamic fragmentation. Canadian Geotechnical Journal, 49,460–476.

Bruhn, R.L., Pavlis, T., Plafker, G., Serpa, L. 2004. Deformation during terrane accretion in the Saint Elias orogen, Alaska. Geological Society of America Bulletin, 116, 771–787.

Burgisser, H.M., Gansser, A., Pika, J. 1982. Late Glacial lake sediments of the Indus valley area, northwestern Himalayas. Eclogae Geologicae Helvetiae, 75, 51–63.

Butler, R.W.H., Prior, D.J. 1988. Tectonic controls on the uplift of the Nanga Parbat Massif, Pakistan Himalayas. Nature, 333, 247–250.

Butler, R.W.H., Owen, L., Prior, D.J. 1988. Flashfloods, earthquakes, and uplift in the Pakistan Himalayas. Geology Today, 4, 197–201.

Butt, M.J., Umar, M. and Qamar, R. 2013. Landslide dam and subsequent dam-break flood estimation using HEC-RAS model in Northern Pakistan. Natural Hazards, 65, 241 – 254.

Chen, C.-Y., Chen, T.-C., Yu, F.-C. and Hung, F.-Y. 2004. A landslide dam breach induced debris flow – a case study on downstream hazard areas delineation. Environmental Geology, 47, 91 – 101.

Chen, R-F., Chang, K-J., Angelier, J., Chan, Y-C., Deffontaines, B., Lee, C-T., and Lin, M-L., 2006, Topographical changes revealed by high-resolution airborne LiDAR data: the 1999 Tsaoling landslide induced by the Chi-Chi earthquake. Engineering Geology, 88, 160-172.

Clague, J.J. 1979. The Denali Fault system in southwest Yukon Territory—a geologic hazard? In: Current Research Part A, Geological Survey of Canada, Paper 79-1A, 169–178.

Cluff, L.S. 1971. Peru earthquake of May 31, 1970; engineering geology observations. Bulletin of the Seismology Society of America, 61, 511–533.

Code, J.A., Sirnhindi, S. 1986. Engineering implications of impoundment of the upper Indus river, Pakistan, by an earthquake-induced landslide. In R.L. Schuster (ed.), Landslide Dams: Processes, Risk, and Mitigation, Geotechnical Special Publication No. 3. American Society of Civil Engineers, New York, NY, pp. 97–109.

Cook, N. and Butz, D. 2013. The Atta Abad landslide and everyday mobility in Gojal, northern Pakistan. International Mountain Society, 33, 372 – 380.

Corominas, J. and Moya, J. 2010. Contribution of dendrochronology to the determination of magnitude-frequency relationships for landslides. Geomorphology, 124, 137-149.

Costa, J.E. and Schuster, R.L. 1988. The formation and failure of natural dams. Geological Society of America Bulletin, 100, 1054 – 1068.

Crosta, G.B., Frattini, P., Fusi, N. 2007. Fragmentation in the Val Pola rock avalanche, Italian Alps. Journal of Geophysical Research: Earth Surface, 112, F01006.

Cruden, D.M. 1980. A large landslide on Mars: discussion. Geological Society of America Bulletin, 91, 63.

Dade, W.B., Huppert, H.E. 1998. Long-runout rockfalls. Geology, 26, 803–806.

Davies, T.R.H. 1982. Spreading of rock avalanche debris by mechanical fluidization. Rock Mechanics, 15, 9–24.

Davies, T.R., McSaveney, M.J. 1999. Runout of dry granular avalanches. Canadian Geotechnical Journal, 36, 313–320.

Davies, T.R., McSaveney, M.J., Hodgson, K.A. 1999. A fragmentation-spreading model for long-runout rock avalanches. Canadian Geotechnical Journal, 36, 1096–1110.

DeBlasio, F.V. 2011. Introduction to the physics of landslides. Springer, Heidelberg, 423 p.

De Blasio, F.V. 2014. Friction and dynamics of rock avalanches travelling on glaciers. Geomorphology, 213, 88 – 98.

Delaney, K.B., Evans, S.G. 2008. Application of digital cartographic techniques in the characterisation and analysis of catastrophic landslides; the 1997 Mount Munday rock avalanche, British Columbia. Proceedings 4th Canadian Conference on Geohazards, Québec, p. 141-146.

Delaney, K.B., Evans, S.G., 2011. Rockslide dams in the northwestern Himalayas (Pakistan, India) and adjacent Pamir Mountains (Afghanistan, Tajikistan), Central Asia. In: Evans, S.G., Hermanns, R.L., Strom, A.L., and Scarascia-Mugnozza, G. (Eds), Natural and Artificial Rockslide Dams, Lecture Notes in the Earth Sciences, Springer, Heidelburg, 133, 205 - 242.

Delaney, K.B., and Evans, S.G. 2014. The 1997 Mount Munday landslide (British Columbia) and the behaviour rock avalanches on glacier surfaces. Landslides, DOI: 10.1007/S10346-013-0456-7.

Deline, P. 2009. Interactions between rock avalanches and glaciers in the Mount Blanc massif during the late Holocene. Quaternary Science Reviews, 28, 1070 – 1083.

Dodds, C.J., Campbell, R.B. 1992. Geology of Mount St. Elias map area (115B and F[E1/2]), Yukon Territory. Geological Survey of Canada Open File 2189.

Dong, J.-J., Lai, P.-J., Chang, C.-P., Yang, S.-H., Yeh, K.-C., Liao, J.-J. and Pan, Y.-W. 2014. Deriving landslide dam geometry from remote sensing images for the rapid assessment of critical parameters related to dam-breach hazards. Landslides, 11, 93 – 105.

Dortch, J.M., Owen, L.A., Haneberg, W.C., Caffee, M.W., Dietsch, C., Kamp, U. 2009. Nature and timing of large landslides in the Himalaya and Transhimalaya of northern India. Quaternary Science Reviews, 28, 1037–1054.

Drew, F. 1873. Alluvial and lacustrine deposits and glacial records of the upper-Indus Basin (with discussion). Quarterly Journal of the Geological Society, 29, 441–471 (includes discussion).

Drew, F. 1875. The Jummoo and Kashmir Territories, a Geographical Account. Edwin Stanford, London, 568 p.

Droz, P., Spasic-Gril, L. 2006. Lake Sarez mitigation project: A global risk analysis. Proceedings 22nd Congress on Large Dams, Q.36-R75, Barcelona, Spain.

Droz, P., Fumagalli, A., Novali, F., Young, B. 2008. GPS and INSAR technologies: A joint approach for the safety of Lake Sarez. 4th Canadian Conference on Geohazards, Quebec, QC, Conference CD, 8 p.

Duan, Z. and Bastiaanssen, W.G.M. 2013. Estimating water volume variations in lakes and reservoirs from four operational satellite altimetry databases and satellite imagery data. Remote Sensing of the Environment, 134, 403 – 416.

Dufresne, A. 2012. Granular flow experiments on the interaction with stationary runout path materials and comparison to rock avalanche events. Earth Surface Processes and Landforms, 37, 1527–1541.

Dunning, S.A. 2006. The grain size distribution of rock-avalanche deposits in valley confined settings. Italian Journal of Engineering Geology and Environment, Special Issue 1, 117-121.

Dunning, S.A., Mitchell, W.A., Rosser, N.J., Petley, D.N. 2007. The Hattian Bala rock avalanche and associated landslides triggered by the Kashmir Earthquake of 8 October 2005, Engineering Geology, 93, 130–144.

Dunning, S.A., Armitage, P.J. 2011. The grain-size distribution of rock-avalanche deposits: implications for natural dam stability. In: S.G. Evans, R.L. Hermanns, A. Strom, G Scarascia Mugnozza (eds). Natural and artificial rockslide dams. Lecture notes in Earth Sciences, 133, Springer, Heidelberg, 479-498.

Eisbacher, G.H., Clague, J.J. 1984. Destructive mass movements in high mountains. Geological Survey of Canada Paper 84-16, 228 pp.

Ekström, G. 2006. Global detection and location of seismic sources using surface waves. Bulletin of the Seismology Society of America, 96, 1201–1212.

Ekström, G., Hansen, R.A., Pavlis, G.L., Lipovsky, P.L. 2007. Seismological detection and analysis of recent landslides in Alaska and the Yukon. In: Eos Transactions AGU, 88(52), Fall Meeting Supplement, Abstract S52B-05.

Ekström, G., Stark, C.P. 2013. Simple scaling of catastrophic landslide dynamics. Science, 339, 1416–1419.

Environment Canada. 2012. National Climate Data and Information Archive: Tatlayoko Lake, British Columbia (Station 10880 http://www.climate.weatheroffice.ec.gc.ca/). Accessed October 2012.

Erismann, T.H., Abele, G. 2001. Dynamics of rockslides and rockfalls. Springer, New York, 316 p.

Evans, S.G. 1986. The maximum discharge of outburst floods caused by the breaching of man-made and natural dams. Canadian Geotechnical Journal, 23, 385–387.

Evans, S.G., Clague, J.J. 1988. Catastrophic rock avalanches in glacial environments. In: Bonnard, C. (ed) Proceedings of the 5th International Symposium on Landslides, Lausanne, 2, 1153–1158.

Evans, S.G., Clague, J.J., Woodsworth, G.J., Hungr, O. 1989. The Pandemonium Creek rock avalanche, British Columbia. Canadian Geotechnical Journal, 26, 427–446.

Evans, S.G., Clague, J.J. 1994. Recent climatic change and catastrophic geomorphic processes in mountain environments. Geomorphology, 10, 107–128.

Evans, S.G., Clague, J.J. 1998. Rock avalanche from Mount Munday, Waddington Range, British Columbia, Canada. Landslide News, 11, 23–25.

Evans, S.G., Clague, J.J. 1999. Rock avalanches on glaciers in the Coast and St. Elias Mountains, British Columbia. In: Proceedings of the 13th Annual Vancouver Geotechnical Society Symposium, Vancouver, 115–123.

Evans, S.G., Scarascia-Mugnozza, G., Strom, A., Hermanns, R.L. 2006. Landslides from massive rock slope failure and associated phenomena. In S.G. Evans, G., Scarascia Mugnozza (eds.), Landslides from Massive Rock Slope Failure, NATO Science Series IV, Earth and Environmental Sciences, Vol. 49. Springer, Dordrecht, 3–52.

Evans, S.G., Fidel, S.L., Zegarra, L.J. 2007. Los Movimientos en Masa de 1962 y 1970 en el Nevado de Huascarán, Valle del rio Santa, Cordillera Blanca, Perú. Anexo B4. In: Movimientos en Masa en la Región Andina: Una guía para la evaluación de amenazas. Proyecto Multinacional Andino:Geociencias para las Comunidades Andinas, Publicacion Geologica Multinacional, No. 4, pp 386–404.

Evans, S.G., Bishop, N.F., Fidel Smoll, L., Valderrama Murillo, P., Delaney, K.B., and Oliver-Smith, A. 2009a. A re-examination of the mechanism and human impact of catastrophic

mass flows originating on Nevado Huascarán, Cordillera Blanca, Peru in 1962 and 1970. Engineering Geology, 108, 96 – 118.

Evans, S.G., Roberts, N.J., Ischuk, A., Delaney, K.B., Morozova, G.S. and Tutubalina, O. 2009b. Landslides triggered by the 1949 Khait earthquake, Tajikistan, and associated loss of life. Engineering Geology, 109, 195 – 212.

Evans, S.G., Tutubalina, O.V., Drobyshev, V.N., Chernomorets, S.S., McDougall, S., Petrakov, D.A., and Hungr, O. 2009c. Catastrophic detachment and high-velocity long-runout flow of Kolka Glacier, Caucasus Mountains, Russia in 2002. Geomorphology,105, 314 – 321.

Evans, S.G. and Delaney, K.B. 2011. Characterization of the 2000 Yigong Zangpo river (Tibet) landslide dam and impoundment by remote sensing, In: Evans S.G. et al., (eds.), Natural and artificial rockslide dams, Lecture Notes in Earth Sciences, Springer, Heidelberg, 133, 543-560.

Evans, S.G., Delaney, K.B., Hermanns, R.L., Strom, A., Scarascia-Mugnozza, G. 2011. The Formation and behaviour of natural and artificial rockslide dams; implications for engineering performance and hazard management. In: Evans SG, Hermanns RL, Strom A, Scarascia Mugnozza G (eds), Natural and artificial rockslide dams. Springer, Heidelberg, 133, pp 1–76.

Everall, W.T., 1930. The reconstruction of the Attock Bridge across the River Indus on the North West Railway, India. Minutes of the Proceedings of the Institution of Civil Engineers 230, 234-258.

Everard, K.A., Savigny, K.W. 1994. Neotectonic effects of landslide distributions, Yukon, Canada. In: Oliveira R, Rodrigues, L.F., Coelho, A.G., Cunha, A.P. (eds), Proceedings, 7th International Congress. International Association of Engineering Geology, Lisbon, pp 1811–1820.

Falconer, H. 1841. Letter to the Secretary of the Asiatic Society, on the recent cataclysm of the Indus. Journal of the Asiatic Society of Bengal, 10, 615–620.

Fan, X., van Westen, C.J., Xu, Q., Gorum, T. and Dai, F. 2012. Analysis of landslide dams induced by the 2008 Wenchuan earthquake. Journal of Asian Earth Sciences, 57, 25-37.

Farr, T.G., M. Kobrick, 2000. Shuttle Radar Topography Mission produces a wealth of data, American Geophysical Union Eos, 81, 583-585.

Farr, T.G., Rosen, P.A., Caro, E., Crippen, R., Duren, R., Hensley, S., Kobrick, M., Paller, M., Rodriguez, E., Roth, L., Seal, D., Shaffer, S., Shimada, J., Umland, J., Werner, M., Oskin, M., Burbank, D., Alsdorf, D. 2007. The shuttle radar topography mission. Reviews of Geophysics, 45, RG2004, doi: 10.1029/2005RG000183.

Fischer, L., Amann, F., Moore, J.R. and Huggel, C. 2010. Assessment of periglacial slope stability for the 1988 Tschierva rock avalanche (Piz Morteratsch, Switzerland). Engineering Geology, 116, 32 – 43.

Florsheim, J.L. and Nichols, A. 2013. Landslide area probability density function statistics to assess historical landslide magnitude and frequency in coastal California. Catena, 109, 129-138.

Fort, M., Burbank, D.W., Freytet, P. 1989. Lacustrine sedimentation in a semiarid alpine setting: An example from Ladakh, northwest Himalaya. Quaternary Research, 31, 332–350.

Fort, M., Peulvast, J.-P. 1995. Catastrophic mass-movements and morphogenesis in the Peri-Tibetan ranges: Examples from west Kunlun, east Pamir, and Ladakh. In O. Slaymaker (ed.), Steepland Geomorphology. Wiley, New York, NY, 171–198.

Fujita, K., Suzuki, R., Nuimura, T. and Sakai, A. 2008. Performance of ASTER and SRTM DEMs, and their potential for assessing glacial lakes in the Lunana region, Bhutan Himalaya. Journal of Glaciology, 54, 220 – 228.

Galitzin, M.B. 1915. Sur le tremblement de terre du 18 février 1911. Comptes Rendus des Seances de l'Académie des Sciences, 160, 810–814.

Gaziev, E. 1984. Study of the usoy landslide in Pamir. Proceeding 4th International Symposium on Landslides, Toronto, Vol. 1, 511–515.

Geological Survey of Canada. 2008. Natural Resources Canada, Earthquakes Canada: Earth Science Sector. http://earthquakescanada.nrcan.gc.ca/index_e.php Accessed 1 Oct 2012.

Gladkov, E.G., Eletskii, V.S., Zhabin, V.F. 1990. Prediction of the change in the water level of Lake Sarez and characteristics of seepage through the Usoi Barrier. Hydrotechnical Construction, 24, 25–28.

Gordon, J.E., Birnie, R., Timmis, R. 1978. A major rockfall and debris slide on the Lyell Glacier, South Georgia. Arctic Antarctic and Alpine Research, 10, 49–60.

Gordey, S.P., Makepeace, A.J. 2003. Yukon digital geology, Version 2.0. Geological Survey of Canada Open File 1749 and Yukon Geological Survey Open File 2003-9(D), 2 CD-ROMS.

Gordin, M.D. 2003. Measure of all the Russias: Metrology and governance in the Russian Empire. Kritika, 4, 783–815.

Gorum, T., Korup, O., van Westen, C.J., van der Meijde, M., Xu, C. and van der Meer, F.D. 2014. Why so few? Landslides triggered by the 2002 Denali earthquake, Alaska. Quaternary Science Reviews, 95, 80-94.

Gunn, J.P. 1930. Hydraulic observations on the Shyok Flood of 1929. Minutes of Proceedings of the Punjab Engineering Congress, Lahore, v. 18, p. 53-71 (excluding plates and discussion).

Gunn, J.P., Todd, H.J. and Mason, K. 1930. The Shyok Flood, 1929. Himalayan Journal, II, 35-

47 (with illustration).

Gutenberg, B., Richter, C.F. 1954. Second Edition, Seismology of the Earth and Associated Phenomena. Princeton University Press, Princeton, NJ, 310 p.

Guthrie, R.H., Friele, P., Allstadt, K., Roberts, N., Evans, S.G., Delaney, K.B., Roche, D., Clague, J.J., Jakob, M. 2012. The 6 August 2010 Mount Meager rock slide-debris flow, Coast Mountains, British Columbia: characteristics, dynamics, and implications for hazard and risk assessment. Natural Hazards and Earth System Science, 12, 1227–1294.

Guzzetti, F., Mondini, A.C., Cardinali, M., Fiorucci, F., Santangelo, M. and Chang, K.-T. 2012. Landslide inventory maps: new tools for an old problem. Earth-Science Reviews, 112, 42-66.

Haeussler, P.J., Schwartz, D.P., Dawson, T.E., Stenner, H.D., Lienkaemper, J.J., Sherrod, B., Cinit, F.R., Montone, P., Craw, P.A., Crone, A.J., Personius, S.F. 2004. Surface rupture and slip distribution of the Denali and Totshunda faults in the 3 November 2002 M7.9 earthquake, Alaska. Bulletin of the Seismology Society of America, 94(6B), S23–S52.

Han, Z.S. 2003. Large-scale landslide-debris avalanche in Tibet, China (1) April-June 2000 Yigong Landslide, Tibet China. Landslide News, 14-15, 22-23.

Hardin, B.O. 1985. Crushing of soil particles. Journal of Geotechnical Engineering, 111, 1177–1192.

Harp. E.L. and Jibson, R.W. 1996. Landslides triggered by the 1994 Northridge, California, earthquake. Seismological Society of America, 86, 5319 – 5332.

Harp, E.L., Keefer, D.K., Sato, H.P. and Yagi, H. 2011. Landslide inventories: the essential part of seismic landslide hazard analyses. Engineering Geology, 122, 9 – 21.

Hauser, A. 2002. Rock avalanche and resulting debris flow in Estero Parraguirre and Rio Colorado, Region Metropolitana, Chile. In: Evans, S.G., DeGraff, J.V. (eds) Catastrophic landslides: effects, occurrence and mechanisms. Geological Society of America Reviews in Engineering Geology 15:135–148.

Henderson, W. 1859. Memorandum on the nature and effects of the flooding of the Indus, 10th August 1858, as ascertained at Attock. Journal of the Asiatic Society of Bengal, 28, 199–228.

Heimsath, A.M. and McGylnn, R. 2008. Quantifying periglacial erosion in the Nepal high Himalaya. Geomorphology, 97, 5 – 23.

Hermanns, R.L., Naumann, R., Folguera, A., Pagenkopf, A., 2004. Sedimentologic analyses of deposits of a historic landslide dam failure in Barrancas valley causing the catastrophic 1914 Rio Colorado flood, northern Patagonia, Argentina. Proceedings 9th International Symposium on Landslides, Rio de Janeiro, Balkema, Rotterdam, v. 2, pp. 1439-1445.

Hewitt, K. 1968. Records of natural damming and related events in the upper Indus basin.

Indus Journal of Water Power Development Authority, 10, 11–19.

Hewitt, K., 1982. Natural dams and outburst floods of the Karakoram Himalaya. IAHS Publication 138, 259-269.

Hewitt, K. 1998. Catastrophic landslides and their effects on the upper Indus streams, Karakoram Himalaya, northern Pakistan. Geomorphology, 26, 47–80.

Hewitt, K. 1999. Quaternary moraines vs catastrophic rock avalanches in the Karakoram Himalaya, northern Pakistan. Quaternary Research, 51, 220–237.

Hewitt, K. 2001. Catastrophic rockslides and the geomorphology of the Hunza and Gilgit river valleys, Karakoram Himalaya. Erdkunde, 55, 72–93.

Hewitt, K. 2002a. Styles of rock-avalanche depositional complexes conditioned by very rugged terrain, Karakoram Himalaya, Pakistan. In: Evans, S.G., DeGraff, J.V. (eds) Catastrophic landslides: effects, occurrence and mechanisms. Geological Society of America, Boulder Reviews in Engineering Geology, 15, 345-377.

Hewitt, K. 2002b. Postglacial landform and sediment associations in a landslide-fragmented river system: The TransHimalayan Indus streams, central Asia. In K. Hewitt, M.L. Byrne, M. English, and G. Young(eds.), Landscapes of Transition. Kluwer Academic, Dordrecht, 63–91.

Hewitt, K. 2006a. Disturbance regime landscapes: Mountain drainage systems interrupted by large rockslides. Progress in Physical Geography, 30, 365–393.

Hewitt, K. 2006b. Rock avalanches with complex run out and emplacement, Karakoram Himalaya, inner Asia. In S.G. Evans, G., Scarascia-Mugnozza (eds.), Landslides from Massive Rock Slope Failure, NATO Science Series IV, Earth and Environmental Sciences Vol. 49. Springer, Dordrecht, 521–550.

Hewitt, K. 2006c. Rock avalanche dams on the Transhimalayan Upper Indus streams: A survey and assessment of hazard-related characteristics. Italian Journal of Engineering Geology and Environment, Special Issue 1, 61–65.

Hewitt, K. 2008. Rock avalanches that travel onto glaciers and related developments, Karakoram Himalaya, Inner Asia. Geomorphology, 103, 66-79.

Hewitt, K., Clague, J.J. and Orwin, J.F. 2008. Legacies of catastrophic rock slope failures in mountain landscapes. Earth Science Reviews, 87, 1 – 38.

Hewitt, K. 2009a. Catastrophic rock slope failures and late Quaternary developments in the Nanga Parbat-Haramosh massif, Upper Indus basin, northern Pakistan. Quaternary Science Reviews, 28, 1055–1069.

Hewitt, K. 2009b. Glacially conditioned rock-slope failures and disturbance-regime landscapes, Upper Indus Basin, northern Pakistan. In Knight, J. and Harrison, S. (eds.), Periglacial

and paraglacial processes and environments, Special Publication 320. Geological Society, London, 235–255.

Hewitt, K. 2009c. Rock avalanches that travel onto glaciers and related developments, Karakorum Himalaya, Inner Asia. Geomorphology, 103, 66 – 79.

Hewitt, K. 2010. Gifts and perils of landslides. American Scientist, 98, 410–419.

Hewitt, K., Liu, J., 2010. Ice-dammed lakes and outburst floods, Karakoram Himalaya: historical perspectives on emrging threats. Physical Geography 31, 528-551.

Hewitt, K. 2011. Rock avalanche dams on the Trans Himalayan Upper Indus streams: a survey of late Quaternary events and hazard-related characteristics. In: S.G. Evans, R.L. Hermanns, A. Strom, G. Scarascia Mugnozza (eds). Natural and artificial rockslide dams. Lecture notes in Earth Sciences, 133, Springer, Heidelberg, 177-204.

Holm, K., Bovis, M.J., Jakob, M. 2004. The landslide response of alpine basins to post-Little Ice Age glacial thinning and retreat in southwestern British Columbia. Geomorphology, 57, 201–216.

Horner, R.B. 1983. Seismicity in the St. Elias region of northwestern Canada and southeastern Alaska. Bulletin of the Seismology Society of America, 73, 1117–1137.

Huggel, C., Schneider, D., Miranda, J., Delgado Granados, H. and Kääb, A. 2008. Evaluation of ASTER and SRTM DEM data for lahar modeling: a case study on lahars from Popocatépetl Volcano, Mexico. Journal of Volcanology and Geothermal Research, 170, 99-110.

Huggel, C. 2009. Recent extreme slope failures in glacial environments: effects of thermal perturbation. Quaternary Science Reviews, 28, 1119–1130.

Huggel, C., Fisher, L., Schneider, D. and Haeberli, W. 2010a. Research advances on climate-induced slope instability in glacier and permafrost high-mountain environments. Geographica Helvetica, 65, 146-156.

Huggel, C., Salzmann, N., Allen, S., Caplan-Auerbach, J., Fisher, L., Haeberli, W., Larsen, C., Schneider, D. and Wessels, R. 2010b. Recent and future warm extreme events and high-mountain slope stability. Philosophical Transactions of the Royal Society A, 368, 2435-2459.

Hungr, O. 1990. Mobility of rock avalanches. Report in National Research Institute for Earth Science and Disaster Prevention, 46, 11–20.

Hungr, O. 1995. A model for the runout analysis of rapid flow slides, debris flows and avalanches. Canadian Geotechnical Journal, 32, 610–623.

Hungr, O., Evans, S.G. 1996. Rock avalanche runout prediction using a dynamic model. In: Proceedings of the 7th International Symposium on Landslides, Trondheim, 17–21 June 1996, pp 233–238.

Hungr, O., Evans, S.G. 2004. Entrainment of debris in rock avalanches: an analysis of a long runout mechanism. Geological Society of America Bulletin, 116, 1240–1252.

Hungr, O., McDougall, S. 2009. Two numerical models for landslide dynamic analysis. Computers and Geosciences, 35, 978-992.

Hurst, M.D., Ellis, M.A., Royse, K.R., Lee, K.A. and Freeborough, K. 2013. Controls on the magnitude-frequency scaling of an inventory of secular landslides. Earth Surface Dynamics, 1, 67-78.

Iqbal, M.J., Shah, F.H., Chaudhry, A.U.H. and Baig, M.N. 2014. Impacts of Attabad lake (Pakistan) and its future outlook. European Scientific Journal, 10, 107 – 120.

Ischuk, A. 2006. Usoy natural dam: Problem of security (Lake Sarez, Pamir Mountains, Tadjikistan). Italian Journal of Engineering Geology and Environment, Special Issue 1, 189–192.

Ischuk, A. 2011. Usoi rockslide dam and Lake Sarez, Pamir Mountains, Tajikistan. In: S.G. Evans, R.L. Hermanns, A. Strom, G., Scarascia Mugnozza (eds). Natural and artificial rockslide dams. Lecture notes in Earth Sciences 133, Springer, Heidelberg, 423-440.

Jeffreys, H. 1923. The Pamir earthquake of 1911 February 18, in relation to the depths of earthquake foci. Monthly Notices of the Royal Astronomical Society Geophysics Supplement, 1, 22–31.

Jeffreys, H. 1937. On the materials and density of the earth's crust. Monthly Notices of the Royal Astronomical Society Geophysics Supplement, 4, 50–61.

Jibson, R.W., Harp, E.L. and Michael, J.A. 2000. A method for producing digital probabilistic seismic landslide hazard maps. Engineering Geology, 58, 271 – 289.

Jibson, R.W., Harp, E.L., Schulz, W., Keefer, D.K. 2006. Large rock avalanches triggered by the M 7.9 Denali Fault, Alaska, earthquake of 3 November 2002. Engineering Geology, 83, 144–160.

Jing, C., Shortridge, A., Lin, S. and Wu, J. 2013. Comparison and validation of SRTM and ASTER GDEM for a subtropical landscape in southeastern China. International Journal of Digital Earth, DOI:10.1080/17538947.2013.807307.

Kargel, J.S., Leonard, G., Crippen, R.E., Delaney, K.B., Evans, S.G., Schneider, J. 2010. Satellite monitoring of Pakistan's rockslide-dammed Lake Gojal. EOS, 91, 394–395.

Keefer, D.K., Larsen, M.C. 2007. Assessing landslide hazards. Science, 316, 1136–1138.

Kershaw, J.A., Clague, J.J., Evans, S.G. 2005. Geomorphic and sedimentological signature of a two-phase outburst flood from moraine-dammed Queen Bess Lake, British Columbia, Canada. Earth Surface Processes and Landforms, 30, 1–25.

Khan, M. 1969. Influence of upper Indus basin on the elements of the flood hydrograph at Tarbela-Attock. In: Floods and their computation, IAHS Publication, 85, Vol. 2, 918–925.

Klotz, O. 1915. Earthquake of February 18, 1911. Bulletin of the Seismological Society of America, 5, 206–213.

Korup, O. and Clague, J.J. 2009. Natural hazards, extreme events, and mountain topography. Quaternary Science Reviews, 28, 977–990.

Korup, O., Densmore, A.L., Schlunegger, F. 2010a. The role of landslides in mountain river evolution. Geomorphology, 120, 77–90.

Korup, O., Montgomery, D.R. and Hewitt, K. 2010b. Glacier and landslide feedbacks to topographic relief in the Himalayan syntaxes. Proceedings of the National Academy of Sciences, 107, 5317–532.

Kuhle, M. 2004. The Pleistocene glaciation in the Karakoram-Mountains: Reconstruction of past glacier extensions and ice thicknesses. Journal of Mountain Science, 1, 3–17.

Lang, K.A., Huntingdon, K.W., and Montgomery, D.R. 2013. Erosion of Tsangpo Gorge by megafloods, Eastern Himalaya. Geology, 41, 1003-1006.

Lee, H-Y et al. 2003. Miocene Jiali faulting and its implications for Tibetan tectonic evolution. Earth and Planetary Science Letters, 205, 185-194.

Le Fort, P., Michard, A., Sonet, J., and Zimmermann, J.L. 1983. Petrography, geochemistry and geochronology of some samples from the Karakorum Axial Batholith, Pakistan. In: Shams, F.A. (Ed.), Granites of the Himalayas, Karakorum and Hindu Kush. University of Lahore, Lahore, pp277 – 387.

Legros, F. 2002. The mobility of long run-out landslides. Engineering Geology, 63, 301–331.

Li, P., Shi, C., Li, Z., Muller, J.-P., Drummond, J., Li, X., Li, T., Li, Y. and Liu, J. 2012. Evaluation of ASTER GDEM VER2 using GPS measurements and SRTM VER4.1 in China. ISPRS Annals of the Photogrammetry, Remote Sensing and Spatial Information Sciences, 1-4, 181-186.

Li, T. 1983. A mathematical model for predicting the extent of a major rockfall. Zeitschrift fur Geomorphologie, N.F. 27: 473-482.

Lipovsky, P.S., Evans, S.G., Clague, J.J., Hopkison, C., Couture, R., Bobrowsky, P., Ekström, G., Demuth, M.N., Delaney, K.B., Roberts, N.J., Clarke, G., Schaeffer, A. 2008. The July 2007 rock and ice avalanches at Mount Steele, St. Elias Mountains, Yukon, Canada. Landslides, 5, 445–455.

Locat, P., Couture, R., Leroueil, S., Locat, J., Jaboyedoff, M. 2006. Fragmentation energy in

rock avalanches. Canadian Geotechnical Journal, 43, 830–851.

Lowey, G.W. 1998. A new estimate of the amount of displacement on the Denali Fault system based on the occurrence of carbonate megaboulders in the Dezadeash Formation (Jura-Cretaceous), Yukon, and the Nutzotin Mountains sequence (Jura-Cretaceous), Alaska. Bulletin of Canadian Petroleum Geology, 46, 379–386.

Lucchitta, B.K. 1978. A large landslide on Mars. Geological Society of America Bulletin, 89, 1601–1609.

Macelwane, J.B. 1926. Are important earthquakes ever caused by impact? BulletinSeismological Society of America, 16, 15–18.

Malik, Z.M., Tariq, A., Anwer, J. 2008. Seepage control for Satpara dam, Pakistan. Proceedings of the Institution of Civil Engineers Geotechnical Engineering GE5, 161, 235–246.

Mantovani, F., Soeters, R. and Van Westen, C.J. 1996. Remote sensing techniques for landslide studies and hazard zonation in Europe. Geomorphology, 15, 213 – 225.

Marangunić, C., Bull, C. 1968. The landslide on the Sherman Glacier. In: The great Alaska earthquake of 1964. Part A—Hydrology, Publication 1603, National Academy of Sciences, Washington, D.C., 383-394.

Martha, T.R., van Westen, C.J., Kerle, N., Jetten, V. and Kumar, K.V. 2013. Landslide hazard and risk assessment using semi-automatically created landslide inventories. Geomorphology, 184, 139 – 150.

Mashimbye, Z.E., de Clercq, W.P. and Van Niekerk, A.V. 2014. An evaluation of digital elevation models (DEMs) for delineating land components. Geoderma, 213, 312-319.

Mason, K. 1929. Indus floods and Shyok Glaciers. Himalayan Journal, 1, 10–29.

Mason, K., 1935. The study of threatening glaciers. Geographical Journal 85, 24-35.

Mather, A.E., Hartley, A.J., Griffiths, J.S. 2014. The giant coastal landslides of Northern Chile: Tectonic and climate interactions on a classic convergent plate margin. Earth and Planetary Science Letters, 388, 249 – 256.

McDougall, S., Hungr, O. 2004. A model for the analysis of rapid landslide motion across three-dimensional terrain. Canadian Geotechnical Journal, 41, 1084–1097.

McDougall, S. and Hungr, O. 2005. Dynamic modeling of entrainment in rapid flowslides. Canadian Geotechnical Journal, 42, 1437 – 1448.

McSaveney, M.J. 1978. Sherman Glacier rock avalanche, Alaska, U.S.A. In: Voight, B. (ed), Rockslides and avalanches, Volume 1, Elsevier, Amsterdam, 197–258.

McSaveney, M.J. 2002. Recent rockfalls and rock avalanches in Mount Cook National Park, New Zealand. In: Evans SG, DeGraff JV (eds) Catastrophic landslides: effects, occurrence and mechanisms. Geological Society of America, Reviews in Engineering Geology, 15, 35–70.

McSaveney, M.J., Davies, T.R.H. 2006. Rapid rock mass flow with dynamic fragmentation: inferences from the morphology and internal structure of rockslides and rock avalanches. In: Evans, S.G., Scarascia Mugnozza, G., Hermanns, R.L., Strom, A. (eds), Landslides from massive rock slope failure. NATO Science Series IV Earth and Environmental Sciences v. 49, Springer, Heidelerg, 285-304.

Mergili, M. and Schneider, J.F. 2011. Regional-scale analysis of lake outburst hazards in the southwestern Pamir, Tajikistan, based on remote sensing and GIS. Natural Hazards and Earth System Sciences, 11, 1447-1462.

Mergili, M., Schneider, D., Worni, R. and Schneider, J.F. 2011. Glacial lake outburst floods in the Pamir of Tajikistan: challenges in prediction and modeling. Italian Journal of Engineering Geology and Environment, DOI: 10.4408/IJEGE.2011-03.B-106.

Metternicht, G., Hurni, L. and Gogu, R. 2005. Remote sensing of landslides: an analysis of the potential contribution to geo-spatial systems for hazard assessment in mountainous environments. Remote Sensing of the Environment, 98, 284 – 303.

Meyer, D., Tachikawa, T., Kaku, M., Iwasaki, A., Gesch, D., Oimoen, M., Zhang, Z., Danielson, J., Kreiger, T., Curtis, B., Haase, J., Abrams, M., Crippen, R. and Carabajal, C. 2011. ASTER global digital elevation model verison 2 – summary of validation results. NASA Land Processes Distributed Active Archive Center and the Joint Japan-US ASTER Science Team, US Geological Survey, Earth Resource Observation and Science Center, 27pp.

Molnia, B.F., Agneli, K.M., Bratton, D.A., Keeler, R.H., Noyles, C. 2006. Meltwater induced glacier landslides - Waxell Ridge, AK. Eos 87(52), Fall Meeting Supplement, Abstract C31A-1247.

Montgomerie, T.G. 1860. Memorandum on the great flood of the river Indus which reached Attock on the 10th August 1858. Journal of the Asiatic Society of Bengal, 29, 128–135.

Moore, R.D., Fleming, S.W., Menounos, B., Wheate, R., Fountain, A., Stahl, K., Holm, K., Jakob, M. 2009. Glacier change in western North America: influences on hydrology, geomorphic hazards and water quality. Hydrological Processes, 23, 42–61.

Morris, T.H., Hebertson, G.F. 1996. Large-rock avalanche deposits, eastern Basin and Range, Utah: emplacement, diagenesis, and economic potential. American Association of Petroleum Geology Bulleting, 80, 1135–1149.

Nadim, F., Kjekstad, O., Peduzzi, P., Herold, C. and Jaedicke, C. 2006. Global landslide and avalanche hotspots. Landslides, 3, 159 – 173.

NASA, 2004. ASTER instrument subsystems.
http://ast 905 erweb.jpl.nasa.gov/instrument.asp
Accessed – January 2014.

National Engineering Services of Pakistan (NESPAK). 2014. Hydrology, sedimentation and
flood routing study report for Attabad landslide lake.
http://dc407.4shared.com/doc/8ccvW7qT/preview.html
Accessed – May 2014.

Nichol, J. and Wong, M.S. Satellite remote sensing for detailed landslide inventories using
change detection and image fusion. International Journal of Remote Sensing, 26, 1913 –
1926.

O'Brien, J.S., Julien, P.Y. and Fullerton, W.T. 1993. Two-dimensional water flood and mudflow
simulation. Journal of the Hydraulics Divison, ASCE, 119(HY2), 244 – 261.

O'Connor, J.E., Costa, J.E. 1993. Geologic and hydrologic hazards in glacierized basins in North
America resulting from 19th and 20th century global warming. Natural Hazards, 8, 121–140.

Oldham, R.D. 1923. The Pamir Earthquake of 18th February, 1911. Quarterly Journal of the
Geological Society, 79, 237–245.

Oppikofer, T., Jaboyedoff, M. and Keusen, H.R. 2008: Collapse at the eastern Eiger flank in the
Swiss Alps. Nature Geosciences, 1, 531 – 535.

Ouimet, W.B., Whipple, K.X., Royden, L.H., Sun, Z. and Chen, Z. 2007. The influence of large
landslides on river incision in a transient landscape: Eastern margin of the Tiberan
Plateau (Sichuan, China). GSA Bulletin, 119, 1462 – 1476.

Owen, L.A. 1989. Neotectonics and glacial deformation in the Karakoram Mountains and
Nanga Parbat Himalaya. Tectonophysics, 163, 227–265.

Owen, L.A. 1996. Quaternary lacustrine deposits in a high-energy semi-arid mountain
environment, Karakoram Mountains, northern Pakistan. Journal of Quaternary Science, 11,
461–483.

Owen, L.A., Kamp, U., Khattack, G.A., Harp, E.L., Keefer, D.K., Bauer, M. 2008. Landslides
triggered by the 8 October 2005 Kashmir earthquake. Geomorphology, 94, 1–9.

Pacheco, J.F., Sykes, L.R. 1992. Seismic moment catalog of large shallow earthquakes,
1900 to 1989. Bulletin of the Seismological Society of America, 82, 1306–1349.

Pan, F., Liao, J., Li, X. and Guo, H. 2013. Application of the inundation area – lake level rating
curves constructed from the SRTM DEM to retrieving lake levels from satellite measured
inundation areas. Computers and Geoscience, 52, 168 – 176.

Pavlis, T.L., Picornell, C., Serpa, L., Bruhn, R.L., Plafker, G. 2004. Tectonic processes during

oblique collision: insights from the St. Elias orogen, northern North American Cordillera. Tectonics, 23, 1–14.

Petley, D., Dunning, S.A. and Rosser, N.J. 2005. The analysis of global landslide risk through the creation of a database of worldwide landslide fatalities. In: O. Hungr, R. Fell, R. Couture, E. Eberhardt (Eds.), Landslide Risk Management, A.T. Balkema, Amsterdam, 2005, 367–374.

Petley, D., Rosser, N.J., Karim, D., Wali, S., Al,i N., Nasab, N., Shaban, K. 2010. Non-seismic landslide hazards along the Himalayan arc. In: Williams AL, Pinches GM, Chin CY, McMorran TJ, Massey CI (eds) Geologically active. CRC Press, London, pp 143–154.

Petley, D. 2011. Damming events at Attabad. International Water and Power. http://www.waterpowermagazine.com/features/featuredamming-events-at-attabad-/ Accessed – March 2013.

Petley, D. 2012. Global patterns of loss of life from landslides. Geology, 40, 927 – 930.

Petrakov, D., Chernomorets, S.S., Evans, S.G., Tutubalina, O.V. 2008. Catastrophic multi-phase glacial movement: a special type of glacier hazard. Advances in Geoscience, 14, 211–218.

Pflaker, G., Ericksen, G.E. 1978. Nevados Huascaran avalanche, Peru. In: Voight B (ed) Rockslides and avalanches, Volume 1: natural phenomena. Elsevier, New York, pp 277–314.

Phartiyal, B., Sharma, A., Srivastava, P., Ray, Y. 2009. Chronology of relict lake deposits in the Spiti River, NW trans Himalaya: Implications to Late Pleistocene-Holocene climatetectonic Perturbations. Geomorphology, 108, 264–272.

Porter, S.C., Orombelli, G. 1980. Catastrophic rockfall of September 12, 1717 on the Italian flank of the Mont Blanc massif. Zeitschrift für Geomorphologie, 24, 200–218.

Post, A. 1967. The Alaska earthquake March 27, 1964: effects on hydrologic regimen. U.S. Geological Survey Professional Paper 544-D.

Pudassaini, S.P. and Miller, S.A. 2013. The hypermobility of huge landslides and avalanches. Engineering Geology, 157, 124 – 132.

Preobrajensky, J. 1920. The Usoi Landslide. Geological Committee Papers on Applied Geology, 14, 21 p. (In Russian).

Raetzo, H. 2006. Hazard assessment of Lake Sarez rockslides and Usoy Dam in Pamir Mountains (Tadjikistan). Italian Journal of Engineering Geology and Environment, Special Issue 1, 193–196.

Rahman, S.A., Javed, K. 1975. A study in dam break flood. Proceedings, Pakistan Engineering Congress v. XV, p. 85-127 (Paper 118).

Rautian, T., Leith, W. 2002. Composite regional catalogs of earthquakes from the Former Soviet Union. United States Geological Survey Open File Report 02–500.

Regmi, N.R., Giardino, J.R. and Vitek, J.D. 2013. Characteristics of landslides in western Colorado, USA. Landslides, DOI:10.1007/s10346-013-0412-6.

Ren, J., Shan, X., Shen, J., Deng, G. and Zhang, J. (2001) Geological characteristics and kinematics of the rock-fall landslide in Yi'ong, southeastern Tibet. Geological Review, 47, 642-647 (in Chinese with English abstract).

Richter, C.F. 1958. Elementary Seismology. Freeman, San Francisco, 768 p.

Risley, J.C., Walder, J.S., Denlinger, R.P. 2006. Usoi dam wave overtopping and flood routing in the Bartang and Panj rivers, Tajikistan. Natural Hazards, 38, 375–390.

Roberts, N.J., Evans, S.G. 2013. The gigantic Seymareh (Saidmarreh) rock avalanche, Zagros Fold-Thrust Belt, Iran. Journal of the Geological Society, 170, 685–700.

Roddick, J.A. 1985. Mount Waddington 92N: Geological Survey of Canada Open File 1163.

Rodier, J.A., Roche, M., 1984. World catalogue of maximum observed floods. IAHS Publication 143, 354 p.

Rodriguez, E., Morris, C.S. and Belz, J.E. 2006. A global assessment of the SRTM performance. Photogrammetric Engineering and Remote Sensing, 72, 249 – 260.

Safran, E.B., Anderson, S.W., Mills-Novoa, M., House, P.K. and Ely, L. 2011. Controls on large landslide distribution and implications for the geomorphic evolution of the southern interior Columbia River basin. Geology, 123, 1851 – 1862.

Schiefer, E., Menounos, B., Wheate, R. 2007. Recent volume loss of British Columbian glaciers, Canada. Geophysical Research Letters, 34, L16503.

Schneider, D., Huggel, C., Haeberli, W., Kaitna, R. 2011. Unraveling driving factors for large rock-ice avalanche mobility. Earth Surface Processes and Landforms, 36, 1948–1966.

Schneider, D., Huggel, C., Cochachin, A., Guillén, S. and Garcia, J. 2014. Mapping hazards from glacier lake outburst floods based on modeling of process cascades at Lake 513, Carhuaz, Peru. Advances in Geosciences, 35, 145-155.

Schneider, J.F. 2009. Seismically reactivated Hattian slide in Kashmir, Northern Pakistan. Journal of Seismology, 13, 387–398.

Schneider, J.F., Gruber, F.E. and Mergili, M. 2011. Recent cases and geomorphic evidence of landslide-dammed lakes and related hazards in the mountains of Central Asia. Proceedings of the Second World Landslide Forum, Rome, 1 – 7.

Schulz, W.H., Galloway, S.L., Higgins, J.D. 2012. Evidence for earthquake triggering of large landslides in coastal Oregon, USA. Geomorphology, 141-142, 88 – 98.

Schuster, R.L., Alford, D. 2004. Usoi landslide dam and Lake Sarez, Pamir Mountains, Tajikistan. Environmental and Engineering Geoscience, 10, 151–168.

Schuster, R.L. and Evans, S.G. 2011. Engineering measures for the hazard reduction of landslide dams. In: Evans, S.G., Hermanns, R.L., Strom, A.L., and Scarascia-Mugnozza, G. (Eds), Natural andArtificial Rockslide Dams, Lecture Notes in the Earth Sciences, Springer, Heidelburg,133, 77 – 100.

Searle, M.P. 1991. Geology and tectonics of the Karakoram Mountains. John Wiley and Sons Ltd., Chichester, 358pp.

Seong, Y.B., Bishop, M.P., Bush, A., Clendon, P., Copland, L., Finkel, R.C., Kamp, U., Owen, L.A., Shroder, J.F. 2009. Landforms and landscape evolution in the Skardu, Shigar and Braldu Valleys, central Karakoram, Geomorphology, 103, 251–267.

Shah, F.H., Ali, A. and Baig, M.N. 2013. Taming the monster – Attabad landslide dam. Journal of Environmental Treatment Techniques, 1, 46 - 55.

Shang, Y., Yang, Z., Li, L., Liu, D., Liao, Q., and Wang, Y. (2003) A super-large landslide in Tibet in 2000: background, occurrence, disaster, and origin. Geomorphology, 54, 225-243.

Shang, Y., Park, H-D., Yang, Z., Yang, J. 2005. Distribution of landslides adjacent to the northern side of the Yarlu Tsangpo Grand Canyon in Tibet, China. Environmental Geology, 48: 721-741.

Shreve, R.L. 1966. Sherman landslide, Alaska. Science, 154, 1639–1643.

Shroder, J.F. 1989. Slope failure: Extent and economic significance in Afghanistan and Pakistan. In Brabb, E.E., Harrod, B.L. (eds.), Landslides: Extent and Econmic Significance in the World. Balkema, Rotterdam, 325–341.

Shroder, J.F., Khan, M.S., Lawrence, R.D., Madin, I.P., Higgins, S.M. 1989. Quaternary glacial chronology and neotectonics in the Himalaya of northern Pakistan. In L. Malinconico and R.J. Little (eds.), Tectonics of the western Himalaya, Geological Society of America Special Paper 232, 275–294.

Shroder, J.F., Cornwell, K., Khan, M.S. 1991. Catastrophic break-out floods in the western Himalaya, Pakistan. Geological Society of America Annual Meeting Program with Abstracts, 23, A87.

Shroder, J.F. 1998. Slope failure and denudation in the western Himalaya. Geomorphology, 26, 81–105.

Shroder, J.F., Weihs, B.J. 2010. Geomorphology of the Lake Shewa landslide dam, Badakhshan, Afghanistan, using remote sensing data. Geografiska Annaler, 92A, 469–483.

Shpilko, G. 1914. The Pamir Earthquake of 1911 and its consequences: Chronological reference and report of the works of the Military Detachment of the Pamir. Bulletin Imperial Russian Geographic Society, 50, 68–94.

Shugar, D.H., Clague, J.J. 2011. The sedimentology and geomorphology of rock avalanche deposits on glaciers. Sedimentology, 58, 1762–1783.

Smith, C.A.S., Meikle, J.C., Roots, C.F. (eds). 2004. Ecoregions of the Yukon Territory: biophysical properties of Yukon landscapes. Agriculture and Agri-Food Canada, PARC Technical Bulletin No. 04-01, Summerland, BC, 313 pp.

Smith, L.C. and Pavelsky, T.M. 2009. Remote sensing of volumetric storage changes in lakes. Earth Surface Processes and Landforms, 34, 1353 – 1358.

Sökefeld M. 2012. The Attabad landslide and the politics of disaster in Gojal, Gilgit-Baltistan. In: Luig U, editor. Negotiating Disasters: Politics, Representation, Meaning. Frankfurt, Germany: Peter Lang, pp 175–204.

Sosio, R., Crosta, G.B., Hungr, O. 2008. Complete dynamic modeling calibration for the Thurwieser rock avalanche (Italian Central Alps). Engineering Geology, 100, 11–26.

Sosio, R., Crosta, G.B., Chen, J.H., Hungr, O. 2012. Modelling rock avalanche propagation onto glaciers. Quaternary Science Reviews, 47, 23–40.

Sosio, R., Crosta, G.B., Chen, J.H. and Hungr, O. 2013. Runout prediction of rock avalanches in volcanic and glacial terrains. In Landslide Science and Practice, 3, 285 – 291.

Spotila, J.A., Buscher, J.T., Meigs, A.J., Reiners, P.W. 2004. Long-term glacial erosion of active mountain belts: examples of the Chugach-St Elias Range, Alaska. Geology 32, 501– 504.

Stanley, A.D. 1969. Observations of the surge of Steele Glacier, Yukon Territory, Canada. Canadian Journal of Earth Sciences, 6, 819–830.

Stanley, A.D. 1972. Observations of the surge of Steele Glacier. In: Bushnell, V.C., Ragle, R.H. (eds) Icefield Ranges Research Project scientific results, Volume 3. American Geographical Society and Arctic Institute of North America, 61–69.

Stein, A. 1916. A third journey of exploration in central Asia, 1913–16 (continued). The Geographical Journal, 48, 193–225.

Stein, A. 1928. Innermost Asia-Detailed Report of Explorations in Central Asia, Kan-Su and Eastern Iran. Clarendon Press, Oxford, 1159 p.

Stoffel, M., Tiranti, D. and Huggel, C. 2014. Climate change impacts on mass movements – case studies from the European Alps. Science of the Total Environment, In Press, DOI: 10.1016/j.scitotenv.2014.02.102, 1 – 12.

Stone, R. 2009. Peril in the Pamirs. Science, 326, 1614–1617.

Stucky Consulting Engineers. 2001. Lake Sarez Mitigation Project, Design Report, 149 p.

Suwandana, E., Kawamura, K., Sakuno, Y., Kustiyanto, E. and Raharjo, B. 2012. Evaluation of ASTER GDEM2 in comparison with GDEM1, SRTM DEM and topographic-map-derived DEM using inundation area analysis and RTK-dGPS data. Remote Sensing, 4, 2419 – 2431.

Tewari, P. (2004) A study of soil erosion in Pasighat town (Arunachal Pradesh) India. Natural Hazards, 32, 257-275.

Uhlmann, M., Korup, O., Huggel, C., Fischer, L., Kargel, J.S. 2013. Supra-glacial deposition and flux of catastrophic rock-slope failure debris, south-central Alaska. Earth Surface Processes and Landforms, 38, 675–682.

USGS, 2011. Earth observing 1 (EO-1).
http://eo1.usgs.gov/sensors/ali
Accessed – January 2014.

USGS, 2013. Landsat 8 history.
http://landsat.usgs.gov/about_ldcm.php
Accessed – January 2014.

Van Westen, C.J., Seijmonsbergen, A.C. and Mantovani, F. 1999. Comparing landslide hazard maps. Natural Hazards, 20, 137 – 158.

Viero, A., Furlanis, S., Squarzoni, C., Teza, G., Galgaro, A. and Gianolla, P. 2013. Dynamics and mass balance of the 2007 Cima Una rockfall (Eastern Alps, Italy). Landslides, 10, 393 – 408.

Walder, J.S. and O'Connor, J.E. 1997. Methods for predicting peak discharge of floods caused by failure of natural and constructed earthen dams. Water Resources Research, 33, 2337 – 2348.

Walsh, L.S., Martin, A.J., Ojha, T.P., Fedenczuk, T. 2012. Correlations of fluvial knickpoints with landslide dams, lithologic contcats, and faults in the southwestern Annapurna Range, central Nepales Himalaya. Journal of Geophysical Research, 117, F01012, 24p.

Wang, K., Deng, C. and Zhang, F. 2012. Formation process of Tanggudong landslide and Yuri accumulation body in Yalong River Valley in southwest China. Journal of Engineering Geology, 20, 955 0 970.

Wang, W., Yang, X. and Yao, T. 2011. Evaluation of ASTER GDEM and SRTM and their suitability in hydraulic modeling of a glacial lake outburst flood in southeast Tibet. Hydrological Processes, 26, 213 – 225.

Wang, X., Chen, Y., Song, L., Chen, X., Xie, H. and Liu, L. 2013. Analysis of lengths, water areas and volumes of the Three Gorges Reservoir at different water levels using Landsat

images and SRTM DEM data. Quaternary International, 304, 115 – 125.

Wang, Y., Liao, M., Sun, G. and Gong, J. 2005. Analysis of the water volume, length, total area and inundated area of the Three Gorges Reservoir, China using the SRTM DEM data. International Journal of Remote Sensing, 26, 4001 – 4012.

Wang, Z. (2008) A thunder at the beginning of the 21st Century - the giant Yigong landslide, in *Landslides and Engineered Slopes*, Ed. Z. Chen, J. Zhang, Z. Li, F. Wu, K. Ho, Proceedings, 10th International Symposium on Landslides, Xian, China, v. 2, 2111-2118.

Wang, Z. and Lu, J. (2002) Satellite monitoring of the Yigong landslide in Tibet, China. Proceedings SPIE, v. 4814, 34 DOI:10.11117/12.453739.

Weichert, D.H., Horner, R.B., Evans, S.G. 1994. Seismic signatures of landslides: The 1990 Brenda Mine collapse and the 1965 Hope rockslides. Bulletin of the Seismological Society of America, 84, 1523–1532.

Wen, B., Wang, S., Wang, E., Zhang, J. 2004. Characteristics of rapid giant landslides in China. Landslides, 1, 247-261.

Westoby, M.J., Glasser, N.F., Hambrey, M.J., Brasington, J., Reynolds, J.M. and Hassan, M.A.A.M. 2014. Reconstructing historic glacial lake outburst floods through numerical modeling and geomorphological assessment: extreme events in the Himalaya. Earth Surface Processes and Landforms, DOI: 10.1002/esp.3617.

Wheeler, J.O., Brookfield, A.J., Gabrielse, H., Monger, J.W., Tipper, H.W., Woodsworth, G.J. (compilers). 1991. Terrane map of the Canadian Cordillera, Geological Survey of Canada Map 1713A, scale 1:2,000,000.

Wood, W.A. 1972. Steele Glacier, 1935–1968. In: Bushnell VC, Ragle RH (eds) Icefield Ranges Research Project scientific results, Volume 3. American Geographical Society and Arctic Institute of North America, 1–8.

Xu, Q., and Wang, S.T. 2008. Large scale avalanches of Yigong, Tibet (2000). In: Catastrophic Landslides in China, Eds. Huang, R.Q. and Xu, Q., Science Press, Beijing, p. 406-423

Xu, Q., Wang, S-T., Chai, H-J., Zhang, Z-Y., and Dong, S. 2008. Yigong rock avalanche-flow landslide event, Tibet, China. In: Landslides and Engineered Slopes, Ed. Z. Chen, J. Zhang, Z. Li, F. Wu, K. Ho, Proceedings, 10th International Symposium on Landslides, Xian, China, v. 2, 1675-1680.

Xu, Q., Shang, Y., van Asch, T., Wang, S., Zhang, Z., and Dong, W. 2012. Observations from the large, rapid Yigong rock slide-debris avalnche, southeast Tibet. Canadian Geotechnical Journal, 49, 589-606.

Yang, S.H., Pan, Y.W., Dong, J.J., Yeh, K.C. and Liao, J.J. 2013. A systematic approach for the assessment of flooding hazard and risk associated with a landslide dam. Natural Hazards, 65, 41 – 62.

Yang, X., Yang, Z., Cao, S., Gao, X., Li, S. 2010. Key techniques for the emergency disposal of Quake Lakes. Natural Hazards, 52, 43-56.

Yarnold, J.C., Lombard, J.P. 1969. A facies model for large rock-avalanche deposits formed in dry climates. In: P. Abbott and I.E. Colburn (eds), Conglomerates in basin analysis: a symposium dedicated to A.O. Woodford. Society of Economic Paleontologists and Mineralogists Pacific Section, 62, 9-31.

Yarnold, J.C. 1993. Rock-avalanche characteristics in dry climates and the effect of flow into lakes: insights from mid-Tertiary sedimentary breccias near Artillery Peak, Arizona. Geological Society of America Bulletin, 105, 345–360.

Zech, R., Abramowski, U., Glaser, B., Sosin, P., Kubik, P.W., Zech, W. 2005. Late Quaternary glacial and climatic history of the Pamir mountains derived from cosmogenic ^{10}Be exposure ages. Quaternary Research, 64, 212–220.

Yin, Y., Wang, F., Sun, P. 2009. Landslide hazards triggered by the 2008 Wenchuan earthquake, Sichuan, China. Landslides, 6, 139 – 151.

Yin, Y. and Xing, A. 2012. Aerodynamic modeling of the Yigong gigantic rock slide-debris avalanche, Tibet, China. Bulletin Engineering Geology & Environment, 71, 149-160.

Yuan, Z., Chen, J., Owen, L.A., Hedrick, K.A., Caffee, M.W., Li, W., Schoenbohm, L.M., Robinson, A.C. 2013. Nature and timing of large landslides within an active orogen, eastern Pamir, China. Geomorphology, 182, 49 – 65.

Yuliang, Q., Shnagmin, Z., Zhen, L., and Bei, J. 2009. Application of China-Brazil earth resources satellite in China. Advances in Space Research, 43, 917-922.

Zhou, C.H., Yue, Z.Q., Lee, C.F., Zhu, B.Q., and Wang, Z.H. 2001. Satellite image analysis of a huge landslide at Yi Gong, Tibet, China. Quaternary Journal of Engineering Geology and Hydrogeology, 34, 325-332.

Zhu, P.Y. and Li, T. 2000/2001. Flash flooding caused by landslide dam failure. Newsletter of ICIMOD, 38, 4-5.

Zhu, P.Y., Wang, C.H., and Wang, Y.C. 2003. Large-scale landslide-debris avalanche in Tibet, China. Formation of an exceptionally serious outburst flood from a landslide dam in Tibet. Landslide News, 14-15, 23-25.